Solid-state NMR Studies of Organotin compounds and of titania pigments

Bai, Haiping

Bai, Haiping (1991) *Solid-state NMR Studies of Organotin compounds and of titania pigments*, Durham theses, Durham University. Available at Durham E-Theses Online: http://etheses.dur.ac.uk/6286/

Solid-State NMR Studies of Organotin Compounds and of Titania Pigments

by

Haiping Bai, B.Sc.

**A Thesis submitted in partial fulfilment
of the requirements for the degree of
Doctor of Philosophy**

Department of Chemistry

**The University of Durham
1991**

Memorandum

The research presented in this Thesis has been carried out at the Department of Chemistry of the University of Durham between October 1988 and March 1991. It is the original work of the author unless stated otherwise. None of this work has been submitted for any other degree.

The copyright of this Thesis rests with the author. No quotation from it may be published without her prior written consent, and information derived from it should be acknowledged.

To my family

知不知上
不知知病

录老子句
公元前五百年

Those who realize they don't know, know.
Those who imagine they know, don't know.

Lao zi

500 B.C.

Acknowledgements

Firstly I would like to thank my supervisor, Professor Robin K. Harris, for his invaluable help and guidance throughout my Ph.D. course in Durham. I would like also to thank my research colleagues for their assistance in various aspects of my work: Dr. Alan Kenwright for stimulating discussions on NMR problems; Dr. David Apperley for help with experimental issues and the theory of quadrupolar effect; Barry Say for his expert help concerning the use of spectrometers; Nicola Davies for her assistance with experimental work. I am also grateful to those individuals and companies who supplied me with samples for study. For financial support I would like to thank the British Council and the Government of the People's Republic of China.

My fellow research students Anita and Matthew helped me greatly after my arrival in Britain, and my colleagues Tim, Rob, Peter, Youssef, Elizabeth, Maria, Daniele, Shuwei and Roberto helped to produce a lively and friendly working atmosphere. Thanks also go to all my friends in Collingwood College who provided extra-curricular entertainment, and to my Chinese countrymen who provided the opportunity of enjoying conversation in our own language.

Finally, of course, I must thank my family, my friend Chris, and his family, for their support and patience during my time in Durham.

Publications

David Apperley, Bai Haiping and Robin K. Harris
'Tin-chlorine coupling in magic-angle spinning NMR spectra', *Molecular Physics*, Vol. **68**, No. 6, 1277 (1989). (Also presented as a poster at the 10th ISMAR conference in Morzine, France, July 1989.)

Haiping Bai and Robin K. Harris
'Solid-state ^{119}Sn NMR studies of coordination in triorganyl tin fluorides', Accepted for publication in *Journal of Organometallic Chemistry*

Haiping Bai and Robin K. Harris
'The effects of interplay of shielding, dipolar and indirect coupling tensors in the tin-119 NMR spectra of solid triorganyl tin fluorides', Accepted for publication in *Journal of Magnetic Resonance*

Haiping Bai and Robin K. Harris
Poster 'NMR studies of the surface of TiO_2 pigments' Presented at the 10th ISMAR conference in Morzine, France, July 1989

Contents

Chapter I

Introduction

Significant advances in the development of high-resolution NMR techniques for solids have taken place in the past 15 years. The most promising development is the successful application in the solid-state of the suite of techniques comprising magic-angle spinning (MAS), cross-polarization (CP) and high-power proton decoupling (HPPD) [1-4]. Combined, these techniques provide near liquid-like spectra for a wide range of solid compounds. CPMAS (with HPPD) experiments can yield dilute spin (e.g.^{13}C) spectra of organic solids with line widths as narrow as 2 Hz [5]. The resolution of individual chemical shifts provides a method for obtaining information about solid-state structure and dynamics on the atomic level. Moreover, the methods may be applied to amorphous materials, thus being complementary to standard X-ray studies.

Organometallic chemistry has always been a subject of considerable interest, and solution-state NMR has been used widely to probe the structures of organometallic systems [6-8]. The potential of high-resolution solid-state ^{119}Sn NMR spectroscopy in the understanding of chemical structure and bonding in organotin chemistry is becoming clear [9-18]. The ^{119}Sn NMR spectra for solids provide a wealth of information on both coordination and the size of the crystallographic asymmetric unit. The anisotropic nature of NMR interactions is also retained in the solid-state spectra.

The main work presented in this thesis is representative of the continuing investigations in this developing area. Chapter 2 outlines the theoretical aspects of solid-state NMR, while Chapter 3 briefly describes the experimental considerations. Chapter 4 investigates the triorganyl tin fluorides (R_3SnF) and Chapter 5 studies the chlorine quadrupolar effect in the Sn-119 spectra for chlorine-containing organotin compounds. Chapter 6 provides the first example of the application of high-resolution solid-state NMR to organooxotin compounds. Chapter 7 illustrates the use of a computational method to obtain shielding anisotropy and asymmetry from a slow magic-angle spinning spectrum. Chapter 8 shows the preliminary results of the application of high-resolution solid-state NMR to solid surfaces of commercial titania pigments.

References

1. (a) E.R. Andrew, A. Bradbury and R.G. Eades, *Nature*, London, **182**, 1659 (1958). (b) I.J. Lowe, *Phys. Rev. Lett.*, **2**, 285 (1959).
2. A. Pines, M.G. Gibby and J.S. Waugh, *J. Chem. Phys.*, **59**, 569 (1973).
3. J. Schaefer, E.O. Stejskal and R. Buchdahl, *Macromolecules*, **8**, 291 (1975).
4. S.R. Hartmann and E.L. Hahn, *Phys. Rev.*, **128**, 2042 (1962).
5. S. Yannoni, *Acc. Chem. Res.*, **15**, 201 (1982).
6. R.K. Harris and B.E. Mann, *NMR and the Periodic Table.*
7. G.A. Webb (ed.), *Annu. reports on NMR Spectros.*, Vol. **8** and Vol **16**, Academic Press.
8. J. Mason, *Multinuclear NMR*, Plenum Press.
9. E.T. Lippmaa, A.A. Madis, T.J. Pehk and G. Engelhardt, *J. Amer. Chem. Soc.*, **100**, 1929 (1978).
10. R.K. Harris, K.J. Packer and P. Reams, *J. Magn. Reson.*, **61**, 564 (1985).

11. R.K. Harris, T.N. Mitchell and G.J. Nesbitt, *Magn. Reson. Chem.*, **23**, 1080 (1985).

12. R.K. Harris, P. Reams and K.J. Packer, *J. Mol. Struct.*, **141**, 13 (1986).

13. R.K. Harris, K.J. Packer, P. Reams and A. Sebald, *J. Magn. Reson.*, **72**, 385 (1987).

14. R.K. Harris and A. Sebald, *J. Organomet. Chem.*, **331**, C9 (1987).

15. R.K. Harris and A. Sebald, *Magn. Reson. Chem.*, **25**, 1058 (1987).

16. R.K. Harris, A. Sebald, D. Furlani and G. Tagliavini, *Organomet.*, **7**, 388 (1988).

17. B. Wrackmeyer, C. Stader and K. Horchler, *J. Magn. Reson.*, **83**, 601 (1989).

18. I.D. Gay, C.H.W. Jones and R.D. Sharma, *J. Magn. Reson.*, **84**, 501 (1989).

Chapter II

Solid-state NMR theory

2.1 Introduction

Nuclear Magnetic Resonance (NMR) involves the study of magnetic energies of those nuclei which possess nuclear magnetic moments, in the presence of a magnetic field $\mathbf{B}_0$. The nuclear magnetic moment μ, arising from the motion of a charged particle, is usually expressed in terms of the magnetogyric ratio (γ) [1]:

$$\mu = \gamma \mathrm{P} \tag{2.1.1}$$

where P is the spin angular momentum ($\mathrm{P} = \hbar\sqrt{\mathrm{I}(\mathrm{I}+1)}$) and I is the spin quantum number, which is a property of a given nucleus. Only those nuclei with non-zero spin quantum number I are suitable for NMR studies. The nuclear spin properties for some selected nuclei (relevant to this work) can be found in Table 3.2.1.

The basic NMR theory has been described in many books and reviews and will not be discussed in any detail here. The interactions between spin and magnetic field and among spins are usually expressed by Hamiltonians ($\mathcal{H}$). The equations of the interactions which are of interest in this work will be outlined in Section 2.2, followed by the calculation of the interplay of shielding, dipolar and indirect couplings for an AX_2 system. Finally, the quadrupolar effect of an S ($>\frac{1}{2}$) nucleus on the appearance of a spin-$\frac{1}{2}$ spectrum will be given.

2.2 Nuclear spin Hamiltonian

The nuclear spin Hamiltonian consists of a number of terms that describe physically different interactions of the nuclear spins [2]. The terms include Zeeman, chemical shielding, dipolar, spin-spin (scalar) coupling and quadrupolar interactions. Some of them cause shifts, while others cause line-broadening of NMR signals. Their relative importance depends on the nucleus being investigated. The nuclear spin Hamiltonian terms are summarized as follows:

Term	Description of interaction
$\mathcal{H} = \mathcal{H}_{\mathrm{Z}}$	Zeeman interaction with the external field $\mathbf{B}_0$
$\mathcal{H}_{\mathrm{rf}}$	Interaction with the external radio frequency field $\mathbf{B}_1$
$\mathcal{H}_{\mathrm{CS}}$	Magnetic shielding of the nucleus by surrounding electrons
$\mathcal{H}_{\mathrm{D}}$	Direct dipole-dipole interaction with other spins
$\mathcal{H}_{\mathrm{J}}$	Indirect spin-spin coupling with other spins
$\mathcal{H}_{\mathrm{Q}}$	Quadrupolar interaction with the electric field gradient

The first two terms $\mathcal{H}_{\mathrm{Z}}$ and $\mathcal{H}_{\mathrm{rf}}$ may be called external Hamiltonians, because they account for the interactions of the nuclear magnetic moment with the applied field $\mathbf{B}_0$ and the time-dependent radio frequency field $\mathbf{B}_1$ respectively. The remaining terms are associated with the spin system and are independent of experimental conditions; thus they are called internal Hamiltonians.

The Zeeman Hamiltonian $\mathcal{H}_{\mathrm{Z}}$ may be written as follows [2]:

$$\hbar^{-1}\mathcal{H}_{\mathrm{Z}} = -\gamma_{\mathrm{I}} B_z I_z = -2\pi\nu_0 I_z \qquad (2.2.1)$$

Where $\mathbf{B}_0$ is chosen as $(0,0,B_z)$; γ_{I} is the magnetogyric ratio of the nucleus being studied and $\nu_0 = \gamma_{\mathrm{I}} B_z / 2\pi$, is the Larmor frequency of the nucleus.

The radio frequency Hamiltonian $\mathcal{H}_{\mathrm{rf}}$ is usually applied perpendicular to the static magnetic field and parallel to the x axis. The expression is [2]:

$$\hbar^{-1}\mathcal{H}_{\mathrm{rf}} = -\gamma_{\mathrm{I}} B_1(t)\ cos[\omega t + \varphi(t)] I_x \qquad (2.2.2)$$

where $B_1(t)$ is the time-dependent amplitude of the rf field; $\varphi(t)$ and $\omega/2\pi$ describe the phase and the carrier frequency of the field. The above equation implies that an rf irradiation may be modulated in both its amplitude and phase.

All the internal Hamiltonians have a common structure [2,3], which may be expressed as (in Cartesian terms):

$$\hbar^{-1}\mathcal{H}^{\lambda} = C^{\lambda} \sum_{\alpha,\beta=1}^{3} I_{\alpha} R^{\lambda}_{\alpha\beta} A^{\lambda}_{\beta} = C^{\lambda} \sum_{\alpha,\beta=1}^{3} R^{\lambda}_{\alpha\beta} T^{\lambda}_{\beta\alpha} \tag{2.2.3}$$

The coefficients C^{λ} are constants for each interaction mechanism. I_{α} and A^{λ}_{β} are nuclear spin vector operators. $R^{\lambda}_{\alpha\beta}$ is a second-rank tensor describing the geometrical configurations of the molecule. $T^{\lambda}_{\alpha\beta}$ is a vector constructed from two vectors, one of which is always a spin vector, whereas the other one can be the same vector in the case of quadrupolar interaction or another spin vector in the case of the dipolar couplings.

For each $\mathbf{R}^{\lambda}$ there exists a frame of the principal axis system (PAS) which is fixed in the molecular frame. Every $\mathbf{R}^{\lambda}$ tensor becomes diagonal in its own PAS and the diagonal elements R_{xx}, R_{yy} and R_{zz} are called principal components. The axes are chosen so that:

$$|R_{zz} - R| \geq |R_{xx} - R| \geq |R_{yy} - R| \tag{2.2.4}$$

where R is the trace of the tensor $\mathbf{R}$, $\frac{1}{3}\mathrm{Tr}\mathbf{R}$. In PAS, the second-rank tensor $\mathbf{R}$ can be written as:

$$\mathrm{R}_{\mathrm{PAS}} = \begin{pmatrix} R_{xx} & & \\ & R_{yy} & \\ & & R_{zz} \end{pmatrix} = R\mathbf{1} + \beth \begin{pmatrix} -\frac{1}{2}(1+\eta) & & \\ & -\frac{1}{2}(1-\eta) & \\ & & 1 \end{pmatrix} \tag{2.2.5}$$

where $\mathbf{1}$ is the unity matrix; $\beth = R_{zz} - R$, and $\eta = (R_{yy} - R_{xx})/\beth$, $(0 \leq \eta \leq 1)$. $\beth$ is the anisotropy and η is the asymmetry of the tensor.

In solution, anisotropic interactions are averaged to zero by rapid molecular tumbling (although such tumbling may be unable to completely reduce broadening for quadrupolar nuclei), leaving only the isotropic contribution (R). However, in the solid-state, no such averaging takes place and for powder samples all possible orientations are equally probable, the anisotropic contributions being predominant.

The anisotropic nature of spin interactions may be more conveniently expressed by irreducible spherical tensors. The common form of the Hamiltonians in a spherical basis will be [2,3]:

$$\hbar^{-1}\mathcal{H}^{\lambda} = C^{\lambda}\sum_{l}\sum_{m=-l}^{l}(-1)^{m}R^{\lambda}_{l-m}T^{\lambda}_{lm} \tag{2.2.6}$$

where R^{λ}_{l-m} derive from the $R^{\lambda}_{\alpha\beta}$ and T^{λ}_{lm} from the $T^{\lambda}_{\alpha\beta}$. For a symmetric 2nd-rank cartesian tensor $R^{\lambda}_{\alpha\beta}$, only those R^{λ}_{l-m} with l =0, 2 will be non-zero. Moreover, in its own PAS, only components with $m = 0$ and ± 2 are non-zero. If ρ_{lm} denote the components of spherical tensor operator R_{lm} in their respective PAS, the following results will be created:

$$\rho_{00} = \frac{1}{3}\mathrm{Tr}\mathbf{R} = R \tag{2.2.7}$$

$$\rho_{20} = \sqrt{\frac{3}{2}}(R_{zz} - R) = \sqrt{\frac{3}{2}}\,\beth \tag{2.2.8}$$

$$\rho_{2\pm 1} = 0 \tag{2.2.9}$$

$$\rho_{2\pm 2} = \frac{1}{2}(R_{yy} - R_{xx}) = \frac{1}{2}\eta\,\beth \tag{2.2.10}$$

For a given system, all the interactions have to be dealt with in the same frame. The laboratory frame is usually chosen as such a common frame, because the two nuclear spin vectors I_{α}, A^{λ}_{β}, which make the operator T^{λ}_{lm}, are basically connected to that frame [3]. R^{λ}_{lm} can be expressed in the laboratory frame through Wigner rotation matrices $\mathcal{D}^l_{m'm}(\alpha^\lambda, \beta^\lambda, \gamma^\lambda)$ [4] as:

$$R^\lambda_{lm} = \sum_{m=-l}^{l} \mathcal{D}^l_{m'm}(\psi^\lambda, \theta^\lambda, \phi^\lambda)\rho^\lambda_{lm'} \tag{2.2.11}$$

where ψ^λ, θ^λ, ϕ^λ are the Euler angles, as displayed in Figure 2.2.1. $\mathcal{D}^0_{00}$ is a unity constant, therefore $R_{00} = \rho_{00}$. The elements of the matrices $(\mathcal{D}^2_{m'm})$ which are relevant to this work are presented as follows:

$$\begin{aligned}
\mathcal{D}^2_{00}(\psi, \theta, \phi) &= \frac{1}{2}(3\cos^2\theta - 1) \\
\mathcal{D}^2_{01}(\psi, \theta, \phi) &= -\sqrt{\frac{3}{8}}\sin 2\theta e^{i\psi} \\
\mathcal{D}^2_{0-1}(\psi, \theta, \phi) &= \sqrt{\frac{3}{8}}\sin 2\theta e^{-i\psi} \\
\mathcal{D}^2_{02}(\psi, \theta, \phi) &= \sqrt{\frac{3}{8}}\sin^2\theta e^{i2\psi} \\
\mathcal{D}^2_{0-2}(\psi, \theta, \phi) &= \sqrt{\frac{3}{8}}\sin^2\theta e^{-i2\psi} \\
\mathcal{D}^2_{20}(\psi, \theta, \phi) &= \sqrt{\frac{3}{8}}\sin^2\theta e^{i2\phi} \\
\mathcal{D}^2_{-20}(\psi, \theta, \phi) &= \sqrt{\frac{3}{8}}\sin^2\theta e^{-i2\phi}
\end{aligned} \tag{2.2.12}$$

To transfer I_α from the cartesian system to the spherical system, the following definitions have been used [2]:

$$\begin{aligned}
I_\pm &= I_x \pm I_y \\
I_{+1} &= -\frac{1}{\sqrt{2}}I_+ \\
I_0 &= I_z \\
I_{-1} &= +\frac{1}{\sqrt{2}}I_-
\end{aligned} \tag{2.2.13}$$

The expressions of the coefficients C^λ and the tensor components T^λ_{lm} and ρ^λ_{lm}, for chemical shielding (CS), dipolar interaction (D), indirect coupling (J) and quadrupolar interaction (Q), are summarised in Table 2.2.1.

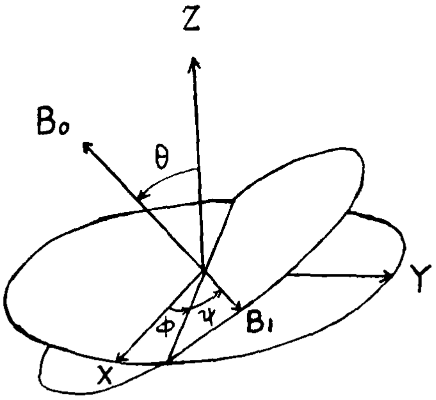

Figure 2.2.1: Coordination of the principal axis system (X,Y,Z) with respect to the laboratory frame ($\mathbf{B}_1$ is chosen in the plane perpendicular to $\mathbf{B}_0$). ψ, θ and ϕ are the Euler angles [5].

2.2.1 Chemical shielding

The chemical shielding arises from the local magnetic field generated at the nucleus by the circulation of the surrounding electrons induced by the applied field. The general equation for the shielding Hamiltonian, in irreducible spherical notation, can be derived from the previously mentioned relevant equations and Table 2.2.1:

$$\hbar^{-1}\mathcal{H}^{cs} = C^{cs}\ [\rho^{cs}_{00}T^{cs}_{00} + \sum_{m=-2}^{2}(-1)^m \sum_{m'=-2}^{2} \mathcal{D}^2_{m'-m}\rho^{cs}_{2m'}T^{cs}_{2m}] \tag{2.2.14}$$

Since the contribution of the chemical shift Hamiltonian is very small compared to that of the Zeeman interaction, its influence may be truncated to a 1st-order effect (secular term), which involves only I_0 terms, i.e. $m = 0$ terms (the observed shielding constant is generally the secular term). Hence the above equation can be immediately written as (dropping the index cs):

$$\hbar^{-1}\mathcal{H} = \gamma_I[\rho_{00}T_{00} + \rho_{20}\mathcal{D}^2_{00}T_{20} + \rho_{2\pm2}(\mathcal{D}^2_{-20} + \mathcal{D}^2_{20})T_{20}] \tag{2.2.15}$$

Referring to Table 2.2.1 and the Wigner equations, Equation 2.2.15 may be recast

Table 2.2.1: **Irreducible spherical tensor operators (T^{λ}_{lm}, ρ^{λ}_{lm}) of the interaction Hamiltonian $\mathcal{H}^{\lambda}$ with λ = CS, D, J, Q. Also the expressions for the coefficient C^{λ} [2,3]**

Tensors	chemical shielding (CS)	Dipolar coupling (D)	scalar coupling (J)	Quadrupolar coupling (Q)
T_{00}	$I_z B_0$	$\mathbf{I}\cdot\mathbf{S}$	$\mathbf{I}\cdot\mathbf{S}$	$\mathbf{S}^2$
T_{20}	$\sqrt{\frac{2}{3}} I_z B_0$	$\frac{1}{\sqrt{6}}(3I_zS_z - \mathbf{I}\cdot\mathbf{S})$	$\frac{1}{\sqrt{6}}(3I_zS_z - \mathbf{I}\cdot\mathbf{S})$	$\frac{1}{\sqrt{6}}(3S_z^2 - \mathbf{S}^2)$
$T_{2\pm1}$	$\mp\frac{1}{2} I_\pm B_0$	$\mp\frac{1}{2}(I_zS_\pm + S_\pm I_z)$	$\mp\frac{1}{2}(I_zS_+ + S_\pm I_z)$	$\mp\frac{1}{2}(S_zS_\pm + S_\pm S_z)$
$T_{2\pm2}$	0	$\frac{1}{2} I_\pm S_\pm$	$\frac{1}{2} I_\pm S_\pm$	$\frac{1}{2} S_\pm^2$
ρ_{00}	σ^{iso}	0	J^{iso}	0
ρ_{20}	$\sqrt{\frac{3}{2}} \sqsupset$	$-2\sqrt{\frac{3}{2}} r_{\mathrm{IS}}^{-3}$	$\sqrt{\frac{3}{2}} \sqsupset_{\mathrm{J}}$	$\sqrt{\frac{3}{2}} eq_{zz}$
$\rho_{2\pm1}$	0	0	0	0
$\rho_{2\pm2}$	$\frac{1}{2} \sqsupset \eta$	0	$\frac{1}{2} \sqsupset_{\mathrm{J}} \eta_{\mathrm{J}}$	$\frac{1}{2} eq_{zz}\eta_{\mathrm{Q}}$
C^{λ}	γ_{I}	$\frac{\mu_0}{4\pi}\gamma_I\gamma_S h$	2π	$\frac{eQ}{2S(2S-1)\hbar}$

as:

$$\hbar^{-1}\mathcal{H} = 2\pi\nu_0\ [\sigma^{iso} + \frac{1}{2}\ \beth\ (3\cos^2\theta - 1) + \frac{1}{2}\ \beth\ \eta\sin^2\theta\cos 2\phi] I_z \qquad (2.2.16)$$

Where $\nu_0 = B_0\gamma_I/2\pi$, the Larmor frequency of the nucleus; σ^{iso} is the isotropic shielding value; $\beth$ and η denote the anisotropy and asymmetry of the shielding tensor respectively; θ and ϕ are two of the Euler angles which describe the relative orientations between the PAS of the shielding tensor and the laboratory frame (Figure 2.2.1).

It is therefore the case that the shielding constant is directly related to the orientations of the molecules under investigation, with respect to the applied field $\mathbf{B}_0$. Heavy nuclei such as ^{119}Sn and ^{207}Pb usually have large anisotropies, and the principal values of the shieldings may be obtained from slow MAS experiments (see below).

2.2.2 Dipolar interactions

The presence of neighbouring magnetic nuclei alters the local field of a nucleus, and therefore changes its energies. The Hamiltonian used to describe this direct dipolar interaction may be written as (in a spherical basis):

$$\hbar^{-1}\mathcal{H}^{\mathrm{D}} = C^{\mathrm{D}}[\rho^{\mathrm{D}}_{00}T^{\mathrm{D}}_{00} + \sum_{m=-2}^{2}(-1)^m \sum_{m'=-2}^{2}\mathcal{D}^2_{m'-m}\rho^{\mathrm{D}}_{2m'}T^{\mathrm{D}}_{2m}] \qquad (2.2.17)$$

Recalling from Table 2.2.1 and other relevant equations, the dipolar Hamiltonian for two heteronuclear spins, applicable to this work, yields (dropping the index D):

$$\begin{aligned}\hbar^{-1}\mathcal{H} &= -2\sqrt{\frac{3}{2}}(\frac{\mu_0}{4\pi})\gamma_{\mathrm{I}}\gamma_{\mathrm{S}}\hbar r_{\mathrm{IS}}^{-3}\sum_{m=-2}^{2}(-1)^m\mathcal{D}^2_{0-m}T_{2m} \\ &= -2\pi\mathrm{D}(3\cos^2\theta - 1)I_zS_z \qquad (2.2.18) \\ &\quad - 2\pi\frac{3}{2}\mathrm{D}\sin\theta\cos\theta\ [(I_zS_+ + S_+I_z)e^{-i\psi} + (I_zS_- + S_-I_z)e^{i\psi}]\end{aligned}$$

where $\mathrm{D} = \frac{\mu_0}{4\pi}\gamma_{\mathrm{I}}\gamma_{\mathrm{S}}\hbar r_{\mathrm{IS}}^{-3}$, the dipolar coupling constant; ψ and θ are the two Euler angles. This equation is derived by assuming that only the secular part, I_z, of spin vector $\mathbb{I}$ is important, and that all components of $\mathbb{S}$ spin should be taken into account. This assumption is made for the situation where the rare spin under study ($\mathrm{I} = \frac{1}{2}$) is coupled to a quadrupolar nucleus S ($\mathrm{S} > \frac{1}{2}$); a quadrupolar spin is quantised by both the Zeeman and the quadrupolar interactions [6], so all components must be considered.

However, if the two nuclei under investigation are both spin-$\frac{1}{2}$, then only the first term, secular term, of Equation (2.2.18) is of importance. The effect of the dipolar interaction on the NMR spectrum will thus only depend on θ, the angle between the internuclear vector and the applied field. When the two nuclei are orientated at 54.7° to the magnetic field $\mathbf{B}_0$, leading to $< 3\cos^2\theta - 1 >= 0$, the dipolar contribution will disappear. This angle is called the 'magic-angle' and is extremely useful for high-resolution solid-state NMR. On the other hand, the dipolar interaction may be observed in NMR spectra in solids, the dipolar constant D may thus be obtained, and then the interatomic distance $\mathrm{r_{IS}}$ may be derived.

It is clear that even under MAS condition the second part of Equation (2.2.18) will not be averaged out, hence residual dipolar interaction will still exist. Detailed calculation of the quadrupolar effect in a solid-state NMR spectrum is given below in section 2.4.

2.2.3 Indirect spin-spin (J) coupling

Indirect spin-spin coupling, also known as scalar or J coupling, describes the interactions between nuclear spins via the surrounding electrons in the system. Whereas direct dipolar coupling contains structural information in the form of interatomic distance, J coupling contains bond-related structural information. The Hamiltonian has the form:

$$\hbar^{-1}\mathcal{H}^{\mathrm{J}} = 2\pi[\rho^{\mathrm{J}}_{00}T^{\mathrm{J}}_{00} + \sum_{m=-2}^{2}(-1)^m \sum_{m'=-2}^{2} \mathcal{D}^2_{m'-m}\rho^{\mathrm{J}}_{lm'}T^{\mathrm{J}}_{2m}] \qquad (2.2.19)$$

For directly-bonded atoms it is generally assumed that J coupling is dominated by electrons which directly take part in the chemical bond. Those electrons usually form an electron-pair sigma single bond; the J coupling tensor should therefore be (at least approximately) axially symmetric (i.e. $\eta_J = 0$) [7]. The unique axis normally lies parallel to the internuclear axis. When this assumption is assured, the truncated Hamiltonian can be immediately written as:

$$\hbar^{-1}\mathcal{H}^J = 2\pi[J^{iso} + \frac{1}{2}\daleth_J(3\cos^2\theta - 1)]I_zS_z \qquad (2.2.20)$$

where $\daleth_J = J_{33} - J^{iso}$, is the anisotropy of the J coupling tensor. However, since J tensor is axially symmetric, the anisotropy can be expressed as:

$$\begin{aligned}\daleth_J &= J_{33} - J^{iso} = J_{\parallel} - \frac{1}{3}(2J_{\perp} + J_{\parallel}) \\ &= \frac{2}{3}(J_{\parallel} - J_{\perp}) = \frac{2}{3}\Delta J \end{aligned}\qquad (2.2.21)$$

In many cases, as in this chapter, ΔJ is called J-coupling anisotropy. Hence, the Hamiltonian can be recast as:

$$\hbar^{-1}\mathcal{H} = 2\pi[J^{iso} + \frac{1}{3}\Delta J(3\cos^2\theta - 1)]I_zS_z \qquad (2.2.22)$$

where θ is the angle between the unique J coupling axis (internuclear vector) and the applied field. This Hamiltonian is identical to the first term of the direct dipolar interaction (Equation 2.2.18), except for the isotropic value J^{iso}. It is therefore expected that the anisotropic part of J coupling (ΔJ) will behave exactly the same as the direct dipolar coupling (D).

2.2.4 Quadrupolar interaction

In addition to a nuclear magnetic moment, a nucleus with $S > \frac{1}{2}$ possesses an ellipsoidal distribution of charge, known as the electric quadrupolar moment. In the laboratory frame, the expression for the Hamiltonian may have the following form:

$$\hbar^{-1}\mathcal{H}^Q = \frac{eQ}{2S(2S-1)\hbar}\sum_{m=-2}^{2}(-1)^m\sum_{m'=-2}^{2}\mathcal{D}^2_{m'-m}\rho^Q_{lm'}T^Q_{2m} \qquad (2.2.23)$$

Inserting the T_{2m}^{Q}, ρ_{2m}^{Q} terms described in Table 2.2.1 and the Wigner equations into the above equation, with the assumption that the electric field gradient is axially symmetric, i.e. $\eta_{\mathrm{Q}} = 0$, the final expression for the quadrupolar interaction may be stated as follows:

$$\hbar^{-1}\mathcal{H} = \frac{\chi}{16S(2S-1)}[2(3\cos^2\theta - 1)(3S_z^2 - \mathbf{S}^2) + 3\sin 2\theta e^{-i\psi}(S_+S_z + S_zS_+)$$

$$+3\sin 2\theta e^{i\psi}(S_-S_z + S_zS_-) + 3\sin^2\theta e^{-i2\psi}S_+^2 + \sin^2\theta e^{i2\psi}S_-^2] \qquad (2.2.24)$$

Where $\chi = e^2Qq/\hbar$, the quadrupolar coupling constant; ψ, θ are the Euler angles which describe the relative orientations of the electric field gradient and the laboratory frame ($\mathbf{B}_0$ in z-direction).

It may be worthy of mention here that when a quadrupolar nucleus is coupled to a spin-$\frac{1}{2}$ nucleus, the dipolar interaction between them may be affected by the quadrupole moment, thus altering the spin-$\frac{1}{2}$ NMR spectrum. More details about such quadrupolar effects can be found in section 2.4.

2.3 Interplay of shielding, dipolar and indirect coupling tensors

For a heteronuclear spin system (AX), the Hamiltonian of the A nucleus in the presence of chemical shielding, dipolar and indirect interactions becomes:

$$\begin{aligned} h^{-1}\mathcal{H}_A =& \nu_0[\sigma_A^{iso} + \frac{1}{2}\beth_A(3\cos^2\theta^{\mathrm{cs}} - 1) + \frac{1}{2}\beth_A\eta_A\sin^2\theta^{\mathrm{cs}}\cos 2\phi^{\mathrm{cs}}]I_{zA} \\ &- \mathrm{D}(3\cos^2\theta^{\mathrm{D}} - 1)I_{zA}I_{zX} \qquad (2.3.1) \\ &+ [J^{iso} + \frac{1}{3}\Delta\mathrm{J}(3\cos^2\theta^{\mathrm{J}} - 1)]I_{zA}I_{zX} \end{aligned}$$

This equation is the sum of Hamiltonians given by Equations (2.2.16), (2.2.18) and (2.2.22). It is assumed that both nuclei are spin-$\frac{1}{2}$, so only the secular term (I_zS_z) of the dipolar Hamiltonian is included.

Suppose both σ and J tensors are axially symmetric and their principal axes are coincident along the relevant internuclear vector (and perpendicular to it), and thus are coaxial with the D tensor as well, then η_A will be zero and $\theta^{\mathrm{cs}} = \theta^{\mathrm{D}} = \theta^{\mathrm{J}} = \theta$. Equation (2.3.1) may be then rewritten as:

$$\begin{aligned} h^{-1}\mathcal{H}_A =& \nu_0[\sigma_A^{iso} + \frac{1}{2}\beth_A(3\cos^2\theta - 1)]I_{zA} \\ &+ [J^{iso} - D'(3\cos^2\theta - 1)]I_{zA}I_{zX} \end{aligned} \tag{2.3.2}$$

where $\nu_0 = \gamma_A B_0/2\pi$ and $D' = D - \frac{1}{3}\Delta \mathrm{J}$.

The extension of the above theory to an AX_2 system is straightforward, provided the X nuclei are equivalent, and the system is linear, i.e. there is only one tensor $\mathbf{J}_{AX}$. The Hamiltonian determining the A-spin spectrum for an AX_2 system will thus be:

$$\begin{aligned} h^{-1}\mathcal{H}_A =& \nu_0[\sigma_A^{iso} + \frac{1}{2}\beth_A(3\cos^2\theta - 1)I_{zA} \\ &+ [J^{iso} - D'(3\cos^2\theta - 1)]I_{zA}(I_{zX_1} + I_{zX_2}) \end{aligned} \tag{2.3.3}$$

This Hamiltonian gives rise to eight energy levels due to the possible A, X_1 and X_2 spin states. The eight eigenstates and their corresponding energy levels are as follows:

Energy levels for an axially symmetric AX_2 system

eigenstate	m_A	$\sum m_X$	energy level
$\beta\beta\beta$	$-\frac{1}{2}$	-1	$E(1) = -\frac{1}{2}\nu_0[\sigma^{iso} + \frac{1}{2}\beth(3\cos^2\theta - 1)] + \frac{1}{2}[J^{iso} - D'(3\cos^2\theta - 1)]$
$\beta\beta\alpha$	$-\frac{1}{2}$	0	$E(2) = -\frac{1}{2}\nu_0[\sigma^{iso} + \frac{1}{2}\beth(3\cos^2\theta - 1)] + 0$
$\beta\alpha\beta$	$-\frac{1}{2}$	0	$E(3) = -\frac{1}{2}\nu_0[\sigma^{iso} + \frac{1}{2}\beth(3\cos^2\theta - 1)] + 0$
$\beta\alpha\alpha$	$-\frac{1}{2}$	$+1$	$E(4) = -\frac{1}{2}\nu_0[\sigma^{iso} + \frac{1}{2}\beth(3\cos^2\theta - 1)] - \frac{1}{2}[J^{iso} - D'(3\cos^2\theta - 1)]$
$\alpha\beta\beta$	$+\frac{1}{2}$	-1	$E(5) = +\frac{1}{2}\nu_0[\sigma^{iso} + \frac{1}{2}\beth(3\cos^2\theta - 1)] - \frac{1}{2}[J^{iso} - D'(3\cos^2\theta - 1)]$
$\alpha\beta\alpha$	$+\frac{1}{2}$	0	$E(6) = +\frac{1}{2}\nu_0[\sigma^{iso} + \frac{1}{2}\beth(3\cos^2\theta - 1)] + 0$
$\alpha\alpha\beta$	$+\frac{1}{2}$	0	$E(7) = +\frac{1}{2}\nu_0[\sigma^{iso} + \frac{1}{2}\beth(3\cos^2\theta - 1)] + 0$
$\alpha\alpha\alpha$	$+\frac{1}{2}$	$+1$	$E(8) = +\frac{1}{2}\nu_0[\sigma^{iso} + \frac{1}{2}\beth(3\cos^2\theta - 1)] + \frac{1}{2}[J^{iso} - D'(3\cos^2\theta - 1)]$

where β refers to the spin state $-\frac{1}{2}$, whereas α refers to $+\frac{1}{2}$. Due to the selection rule $\Delta m_A = \pm 1$ and $\Delta \sum m_X = 0$, transitions allowed are between energy levels:

$$\begin{aligned} E(4) - E(8) &= \nu^+ \\ E(2) - E(6) = E(3) - E(7) &= \nu^0 \\ E(1) - E(5) &= \nu^- \end{aligned} \tag{2.3.4}$$

where each transition, denoted by ν^+ or ν^0 or ν^-, is assigned to either 'plus' or zero or 'minus' according to its X_2 spin state $\sum m_X = -1, 0, +1$ respectively. The transition frequencies are therefore expressed as:

$$\begin{aligned} \nu^+ &= -\nu_0[\sigma^{iso} + \frac{1}{2} \beth\, (3\cos^2\theta - 1)] - [J^{iso} - D'(3\cos^2\theta - 1)] \\ \nu^0 &= -\nu_0[\sigma^{iso} + \frac{1}{2} \beth\, (3\cos^2\theta - 1)] \\ \nu^- &= -\nu_0[\sigma^{iso} + \frac{1}{2} \beth\, (3\cos^2\theta - 1)] + [J^{iso} - D'(3\cos^2\theta - 1)] \end{aligned} \tag{2.3.5}$$

It is obvious that the intensity ratio among the three resonances is 1:2:1. It may be seen that Equation (2.3.5) is, in reduced form as:

$$\begin{aligned} \nu^+ &= -\nu_0\sigma^{iso} + (D' - \frac{1}{2}\nu_0 \beth)(3\cos^2\theta - 1) - J^{iso} \\ \nu^0 &= -\nu_0\sigma^{iso} - \frac{1}{2}\nu_0 \beth\, (3\cos^2\theta - 1) \\ \nu^- &= -\nu_0\sigma^{iso} - (D' + \frac{1}{2}\nu_0 \beth)(3\cos^2\theta - 1) + J^{iso} \end{aligned} \tag{2.3.6}$$

These relationships are given for the case where γ_A is positive. When γ_A is negative, the three transitions have the following form:

$$\begin{aligned} \nu^+ &= -\nu_0\sigma^{iso} - (D' + \frac{1}{2}|\nu_0| \beth\,)(3\cos^2\theta - 1) + J^{iso} \\ \nu^0 &= -\nu_0\sigma^{iso} - \frac{1}{2}|\nu_0| \beth\, (3\cos^2\theta - 1) \\ \nu^- &= -\nu_0\sigma^{iso} + (D' - \frac{1}{2}|\nu_0| \beth\,)(3\cos^2\theta - 1) - J^{iso} \end{aligned} \tag{2.3.7}$$

Comparing Equations (2.3.6) and (2.3.7) it is clear that the spectra are invariant to a change in the sign of γ_A, but the 'minus' and 'plus' states of nuclei X_2 are interchanged. However, such inversion will not have any effect on the appearance of the NMR spectrum. It can also be seen from the above equations that the anisotropy in J (ΔJ) cannot be distinguished from D experimentally. Only when r_{AX} is known can ΔJ be derived.

2.4 Dipolar interaction between spin-$\frac{1}{2}$ and spin-$\frac{3}{2}$ nuclei

The dipolar Hamiltonian of an IS system, where I = $\frac{1}{2}$ and S = $\frac{3}{2}$, can be expressed in the laboratory frame using Equation (2.2.18) as (under magic-angle condition):

$$h^{-1}\mathcal{H}^{\mathrm{D}} = -\frac{3}{2}D\sin\theta\cos\theta[(I_zS_+ + S_+I_z)e^{-i\psi} + (I_zS_- + S_-I_z)e^{+i\psi}] \qquad (2.4.1)$$

The energies of the spin states are immediately available as:

$$< \psi_m, m_z|\mathcal{H}^{\mathrm{D}}|\psi_m, m_z > \qquad (2.4.2)$$

Where $|m_z >$ are the eigenfuntions of the Zeeman interaction, $\mathcal{H}_{\mathrm{ZI}}$, of the I spin and eigenfunctions $|\psi_m >$ are solutions to:

$$\mathcal{H}^{\mathrm{ZS}} + \mathcal{H}^{\mathrm{Q}}|\psi_m >= E_m|\psi_m > \qquad (2.4.3)$$

where E_m denote the corresponding eigenvalues. The resonance frequency of the nuclei I, ν_m, influenced by the I-S dipolar interaction will thus be ($\Delta m_z = \pm 1$):

$$\nu_m = \frac{3}{2}\mathrm{D} < \psi_m|\sin\theta\cos\theta(S_+e^{-i\psi} + S_-e^{i\psi})|\psi_m > \qquad (2.2.4)$$

where m is the spin state of the S nucleus, and ψ, θ relate the dipolar principal axis system to the laboratory axis system through rotations about the dipolar y and z axes respectively. In order to apply a perturbation approach, the Zeeman interaction is considered large enough so that the quadrupolar Hamiltonian can be estimated using perturbation theory. The four eigenfunctions, $|\psi_m>$, can then be regarded as linear combinations of the eigenfunctions, $|m>$, of the Zeeman term:

$$|\psi_m> = \sum_{n=-\frac{3}{2}}^{\frac{3}{2}} C_{mn}|n> \tag{2.4.5}$$

The coefficients C_{mn} can be derived by standard perturbation theory provided that the magnitude of the quadrupolar interaction is not too great. The theory allows an approximation to the coefficients C_{mn} of the linear expansion to be obtained [8]:

$$C_{mn} =^0 C_{mn} +^1 C_{mn}+ \tag{2.4.6}$$

where

$$\begin{aligned} {}^0C_{mn} &= \delta_{mn} \\ {}^1C_{mn} &= -\frac{< n|\mathcal{H}^{Q}|m >}{E_n - E_m} & \qquad if\ m \neq n \\ {}^1C_{mm} &= 0 \end{aligned}$$

The second and higher order corrections are neglected. The quadrupolar Hamiltonian under MAS conditions and with no asymmetry may be written as (according to Equation 2.2.24):

$$\begin{aligned} \hbar^{-1}\mathcal{H}^{Q} = \frac{\chi}{16}[2\sin\theta\cos\theta[e^{-i\psi}(S_+S_z + S_zS_+) + e^{i\psi}(S_-S_z + S_zS_-)] \\ + \sin^2\theta[e^{-i2\psi}S_+^2 + e^{i2\psi}S_-^2]] \end{aligned} \tag{2.4.7}$$

This equation is valid provided that the quadrupolar axis system is coincident with the dipolar axis system. Inserting Equation (2.4.7) into Equation (2.4.6) and using the well-known relations:

$$S_z|\ m >= m\ |m > \tag{2.4.8}$$

$$S_{\pm}|m >= \sqrt{S(S+1) - m(m \pm 1)}\ |m \pm 1 > \tag{2.4.9}$$

The C_{mn} may be calculated and the $|\psi_m>$ can then be written as:

$$|\psi_{\frac{3}{2}}>=|\frac{3}{2}>+a_1\,|\frac{1}{2}>+a_2\,|-\frac{1}{2}> \tag{2.4.10}$$

$$|\psi_{\frac{1}{2}}>=-a_1^*\,|\frac{3}{2}>+|\frac{1}{2}>+a_2\,|-\frac{3}{2}> \tag{2.4.11}$$

$$|\psi_{-\frac{1}{2}}>=-a_2^*\,|\frac{3}{2}>+|-\frac{1}{2}>+a_1\,|-\frac{3}{2}> \tag{2.4.12}$$

$$|\psi_{-\frac{3}{2}}>=-a_2^*\,|\frac{1}{2}>+a_1^*\,|-\frac{1}{2}>+|-\frac{3}{2}> \tag{2.4.13}$$

where $a_1 = -(\sqrt{3}\chi/4\nu_S)\sin\theta\cos\theta\exp(i\psi)$, $a_2 = -(\sqrt{3}\chi/16\nu_S)\sin^2\theta\exp(i2\psi)$. The asterisk defines a complex conjugate and ν_S is the resonance frequency of the S spin. Referring to the previous expressions results in a general form:

$$\nu_m = \frac{9D\chi}{4\nu_S}(\frac{5}{4}-m^2)\sin^2\theta\cos^2\theta \tag{2.4.14}$$

where $D = \frac{\mu_0}{4\pi}\gamma_I\gamma_S\hbar r_{IS}{}^{-3}$, the dipolar coupling constant; $\chi = \frac{e^2Qq}{h}$, the quadrupolar coupling constant; r_{IS} is the distance between nuclei I and S. If indirect I-S J coupling is also included, the resonance frequency will be:

$$\nu_m = -mJ^{iso} + \frac{9D'\chi}{4\nu_S}(\frac{5}{4}-m^2)\sin^2\theta\cos^2\theta \tag{2.4.15}$$

where $D' = D - \Delta J/3$, the pseudo-coupling constant.

2.5 High-resolution solid-state NMR

Solid-state NMR spectra tend to have very broad featureless lines if no special techniques are applied. These usually result from dipolar interactions with other nuclei (including protons) and from shielding anisotropy. Dipolar interactions may be removed by the magic-angle spinning experiment, which involves fast rotation of the sample about an axis inclined at 54.7° (the magic-angle, which enables $<3\cos^2\theta-1>=0$), to the magnetic field [9,10]. In principle, this technique not only averages the dipolar interaction to its isotropic value (zero) but also averages the chemical shielding and spin-spin indirect coupling to their isotropic values (σ^{iso}, J^{iso}). However, this can only be achieved provided the spinning speed exceeds the size of the interaction, or the combined effects from the interplay of two or more interactions.

In practice, generally attainable MAS speeds have a limit of ca. 5 kHz, though modern commercial probes can reach up to 15 kHz. Such speeds may be sufficient to average inhomogeneously broadened systems with no protons [11]. However, for a system when the heteronuclear dipolar coupling involves protons, the size of the dipolar interactions well exceeds the above mentioned attainable spinning speed [12]. This problem has been solved by high-power proton decoupling (HPPD) [13]. The process of decoupling is carried out by a double resonance technique, i.e. two radio frequencies are needed. One of them strongly irradiates the resonance of protons, whereas the other is set on the resonance of the nucleus in question.

Magic-angle spinning and high-power proton decoupling are two very powerful techniques for line-narrowing in the solid-state. However, in some cases these two means are unable to completely remove the effect of shielding anisotropy, whose linewidth may be greater than the spinning speeds. The resulting spectrum contains a series of peaks spaced at the spinning frequency with the centreband (invariant to spinning speed) at the isotropic chemical shift. The intensities of the peaks are related to the chemical shielding anisotropy, which can be derived from spinning sideband analysis (see Chapter 7).

Another widely-used technique in solid-state NMR is cross-polarization (CP), which very substantially increases the signal-to-noise in the spectra of those magnetically dilute (rare) spin systems [14]. Many nuclei with high NMR interest are rare spins (e.g. ^{13}C, ^{119}Sn, etc); they usually have low natural abundance (e.g. ^{13}C 1.1 %) and very long spin-lattice relaxation times. CP enhances the magnetisation of the rare spins from that of the abundant spins (usually protons) and, as a result, the intensity of the spectrum of rare spin systems effectively depends on the relaxation of the proton spin system. The spin-lattice relaxation times of protons are often much shorter than those of rare spins. Hence, the recycle time needed for efficient spectral accumulation is, in general, much shorter for a CP experiment than for a conventional pulse-FT experiment.

References

1. R.K. Harris, *Nuclear Magnetic Resonance Spectroscopy*, Longman Scientific & Technical, (1986).

2. U. Haeberlen, *High Resolution NMR in Solids, Selective Averaging*, Academic Press, (1976).

3. M. Mehring, *Principles of High resolution NMR in Solids*, Springer-Verlag, (1983).

4. A.R. Edmonds, *Angular Momentum in Quantum Mechanics*, Princeton Univ. Press, (1957).

5. P.C. Taylor, J.F. Baugher and H.M. Krit, *Chem. Revs*, **75**, 203 (1975).

6. J. Schaefer, E.O. Stejskal and R. Buchdahl, *Macromolecules*, **10**, 384 (1977).

7. P.C. Taylor, J.F. Baugher and H.M. Kriz, *Chem. Revs*, **75**, 203 (1975).

8. P.N. Tutunjian and J.S. Waugh, *J. Chem. Phys.*, **76**, 1223 (1982).

9. E.R. Andrew, A. Bradbury and R.G. Eades, *Nature*, London, **182**, 1659 (1958).

10. I.J. Lowe, *Phys. Rev. Lett.*, **2**, 285 (1959).

11. E.R. Andrew, *Internat. Rev. Phys. Chem.*, **1**, 195 (1981).

12. C.S. Yannoni, *Acc. Chem. Res.*, **15**, 201 (1982).

13. C.A. Fyfe, *Solid State NMR for Chemists*, C.F.C. Press, (1983).

14. A. Pines, M.G. Gibby and J.S. Walsh, *J. Chem. Phys.*, **59**, 569 (1973).

Chapter III

Experimental Descriptions

3.1 Spectrometer systems

Two spectrometer systems, a Bruker CXP-200 and a Varian VXR-300, were used for the majority of the work outlined in this thesis. The CXP-200 was equipped with a 4.7 Tesla wide-bore (89.5 mm) magnet, with a proton resonance frequency of 200.13 MHz. Two broad-band, dual-channel double-bearing probes were usually used on the CXP-200 machine. The frequency range covered by the two probes is 20 $\sim$ 90 MHz. The double-bearing probes provided a very stable spinning system for magic-angle spinning studies. The spinning speeds could reach up to 5 kHz, provided that the rotor was full and homogeneously packed. The rotors were made from zirconia with a 7 mm diameter. Further details about the spectrometer can be found in [1]. Most of the H-1, C-13, F-19, P-31, Sn-119 and Pb-207 spectra presented in this thesis were run on this spectrometer.

The VXR-300 is a spectrometer equipped with a 7.1 Tesla narrow-bore (89 mm) magnet with a proton resonance frequency of 299.95 MHz. The probes used for MAS experiments were also double-bearing and were designed by Doty Scientific. Spinning speeds of up to 15 kHz could be obtained by a specially designed fast spinning probe with 5 mm o.d. rotors. The spectrometer was used to perform Al-27, Si-29 and Pb-207 studies. Many Sn-119 spectra were obtained from the VXR-300 as well as from the CXP-200 because a second field was necessary for a thorough investigation of the organotin compounds. Variable temperature operation was also carried out on the VXR-300 machine.

The ^{1}H relaxation time measurements were performed on a home-made WRAC spectrometer, which has a proton resonance frequency of 60.00 MHz. A full description of the spectrometer may be found in [2].

3.2 Nuclei of interest

The main materials studied were three different series of organotin compounds, namely R_3SnF, R_2SnCl_2 (including R'_2SnCl_6, where R$'$ is a cation) and organooxotin compounds. Undoubtedly, ^{119}Sn NMR studies comprise the majority of the work presented in this thesis. ^{13}C spectra of these samples were also taken to assist the structural elucidation. The other samples being investigated were TiO_2 pigments, which were coated with P_2O_5, or Al_2O_3 or/and SiO_2. It is very easy for the samples to adsorb water molecules and hydroxyl groups on their surfaces. The structure of the coatings and the way that the H_2O molecules and OH groups adsorbed on the surfaces are apparently important to the understanding of the pigments. Therefore, ^{1}H, ^{31}P, ^{27}Al and ^{29}Si NMR studies were carried out for the samples. The properties of those nuclei being investigated are listed in Table 3.2.1.

3.3 Chemical shift references

Chemical shifts are commonly measured relative to a standard substance; the definition of chemical shift is:

$$\delta/\text{ppm} = \frac{\nu - \nu_{ref}}{\nu_{ref}} \times 10^6 \tag{3.3.1}$$

where ν denotes the resonance frequency of the observed line, and ν_{ref} refers to the resonance frequency of a reference line. Therefore, a positive chemical shift δ suggests that the observed resonance frequency is higher than that of the standard material, whereas a negative chemical shift suggests otherwise. The high-frequency-positive convention has been adopted throughout this thesis where the symbol δ is used. Shielding (denoted by σ) has the opposite sign convention.

In solid-state NMR, a secondary reference is usually used when the standard substance is a liquid (except for ^{27}Al). This is because liquid references are not

Table 3.2.1: NMR properties of selected nuclei [3]

Isotope	Spin	% Natural abundance	Magnetogyric ratio $\gamma/10^7$ rad T^{-1} s^{-1}	Quadrupolar moment 10^{28} Q/m^2	NMR[(a)] frequency Ξ /MHz	Chemical shift reference
^1H	$\frac{1}{2}$	99.985	26.7520	-	200.13	TMS
^{13}C	$\frac{1}{2}$	1.108	6.7283	-	50.32	TMS
^{19}F	$\frac{1}{2}$	100	25.1810	-	188.34	$CFCl_3$
^{27}Al	$\frac{5}{2}$	4.308	6.9760	0.15	52.15	$Al(H_2O)_6^{3+}$
^{29}Si	$\frac{1}{2}$	4.7	−5.3188	-	39.76	TMS
^{31}P	$\frac{1}{2}$	100	10.8410	-	81.01	H_3PO_4
^{35}Cl	$\frac{3}{2}$	75.53	2.6240	−0.1	19.63	-
^{37}Cl	$\frac{3}{2}$	24.47	2.1842	-7.9×10^{-2}	16.34	-
^{117}Sn	$\frac{1}{2}$	7.61	−9.5780	-	71.30	Me_4Sn
^{119}Sn	$\frac{1}{2}$	8.58	−10.0210	-	74.63	Me_4Sn
^{207}Pb	$\frac{1}{2}$	22.6	5.5400	-	41.87	Me_4Pb

(a) The frequency is calculated at 4.7 Tesla.

practical for routine use since the shimming conditions for solids and liquids are generally different. Tetramethyl silane, TMS, is the accepted standard reference sample for ^1H, ^{13}C and ^{29}Si. Secondary references are silicone gum for both ^1H (at 0.6 ppm) and ^{29}Si (at −22.7 ppm) and adamantane for ^{13}C (the higher frequency line is 38.5 ppm). The secondary reference for ^{19}F is C_6F_6, which is indirectly referenced to $CFCl_3$. The chemical shift of C_6F_6 is −163.4 ppm with respect to $CFCl_3$ solution. All ^{31}P NMR data are indirectly referenced to 85% aqueous phosphoric acid (H_3PO_4). Brushite ($CaHPO_4{\cdot}2H_2O$) powder is used as a secondary reference. Its chemical shift is 1.2 ppm relative to H_3PO_4 solution.

^{119}Sn chemical shifts have been referenced to Me_4Sn. Two secondary references were used: one was tetraphenyltin (Ph_4Sn) on the CXP-200, and the other one was tetracyclohexyltin, $(C_6H_{11})_4Sn$, on the VXR-300. The chemical shifts of these two compounds with respect to Me_4Sn are -121.0 and -97.4 ppm respectively. For ^{27}Al NMR, the standard reference is $Al(H_2O)_6^{3+}$ solution. Me_4Pb was used as the standard reference for ^{207}Pb. The secondary reference chosen was tetraphenyllead, Ph_4Pb, whose chemical shift is -156.5 ppm relative to the standard reference. All the above discussed standard references are summarised in Table 3.2.1.

3.4 Pulse sequences

NMR pulse sequences have been the major power of modern FT NMR, which involves the use of pulses of varying duration, phase, frequency and amplitude. With these techniques the behaviour of nuclear spins can be manipulated and therefore certain NMR parameters may be obtained. The basic techniques have become generally well-known and it is unnecessary to repeat here. What follows in this section is a brief description of pulse sequences, illustrated in Figure 3.4.1, which are relevant to this work.

3.4.1 Single-pulse excitation (SPE)

The simplest of all pulse sequences is shown in Figure 3.4.1(a), which combines a 90° single pulse and high-power proton decoupling (HPPD). The duration of the 90° pulse was generally set at ca. $4\mu s$. This sequence, together with magic-angle spinning, was used to obtain ^{31}P spectra for TiO_2 pigments. However, for compounds without protons, such as K_2SnCl_6, the proton decoupling was switched off and only a 90° pulse was used. Since the resonance frequencies of ^{1}H and ^{19}F are very close, it is not feasible to decouple ^{1}H while obtaining ^{19}F signals, so during the acquisition of ^{19}F spectra no decoupling field was used. The recycle delay is usually $\sim 5T_1(X)$.

3.4.2 Cross-polarization

As described in Chapter 2, cross-polarization (CP) is used to derive the magnetization of dilute spins from abundant spins, e.g. protons. Figure 3.4.1(b) shows the pulse sequence which allows the transfer of magnetization between different spin systems. After the 90° pulse on the proton channel, the ^{1}H magnetization is spin-locked by an on-resonance pulse in the y-direction. At the same time, a strong on-resonance pulse is applied to the X spins (^{13}C, ^{31}P, ^{119}Sn etc). The magnitudes of the two fields are chosen to fulfill the Hartmann-Hahn condition [4]:

$$\gamma_H H_{1H} = \gamma_X H_{1X} \tag{3.4.1}$$

In the time period τ, known as contact time, the magnetization of ^{1}H spins will transfer to that of dilute spins through dipolar interactions. During the acquisition of the rare spin signal, the proton channel is still locked for proton decoupling.

In practice, the Hartmann-Hahn condition is achieved by changing the power of the X spin channel using a reference sample, until the FID of the reference sample reaches a maximum. The contact time is generally between 1 and 10 ms and the recycle delay is $\sim 5T_1(^{1}H)$. The second 90° pulse on the proton channel is a flip-back pulse [5], which is used to reduce the recycle time.

3.4.3 Non-quaternary suppression

Figure 3.4.1(c) shows the pulse sequence of non-quaternary suppression (NQS), also known as dipolar-dephasing. This sequence, designed by Opella and Frey [6], is usually used for ^{13}C studies, though it can be applied to any nuclei directly coupled to protons. The purpose of this sequence is to assist in assignment of solid-state NMR spectra. Between the contact time and FID aquisition time, there is a decoupling 'window'. During the 'window' period, the transverse magnetization of the protonated ^{13}C nuclei will, in principle, decay much more rapidly than those with no directly bonded protons. This is because protonated carbons have strong (C, H) interactions, whereas quaternary carbons have no such interactions. Hence the FID obtained will contain mainly signals from non-protonated carbons. Comparing CP and NQS spectra, thus, can provide information on the assignment of carbon signals, especially where many carbons are involved.

The main reason for the rapid decay of protonated ^{13}C in NQS spectra is the strong (C, H) interactions. However, in some cases, the (C, H) interactions may be partially averaged due to fast internal rotation, for example CH_3 groups. When this happens, most of the transverse magnetization of the carbons will remain after the dipolar-dephasing period. Hence, methyl carbon resonances are usually contained in the NQS spectra.

3.4.4 Proton relaxation time measurements

$T_1(^1H)$ measurement

The method used for the $T_1(^1H)$ is the saturation-recovery method, whose pulse sequence is shown in Figure 3.4.1(d). The pulse spacing t_1 should be set to $T_2 < t_1 << T_1$ [7]. The series of 90° pulses set the magnetization of the spins to zero. During the τ period, the magnetization recovers and this recovery will be sampled at different τ times. The relaxation behaviour will thus be measured.

$T_{1\rho}(^1H)$ measurement

Figure 3.4.1(e) is the pulse sequence for $T_{1\rho}$ measurement. The 90° pulse is followed by a change in phase (90°) of the radio-frequency field. The magnetization (M_y) is therefore locked along the r.f. field B_1. However, M_y will still decay with time since the static field $\mathbf{B_0}$ is several orders of magnitude greater than B_1. As the time τ increases the FID signal detected will decrease. The decaying rate is the $T_{1\rho}$ [7].

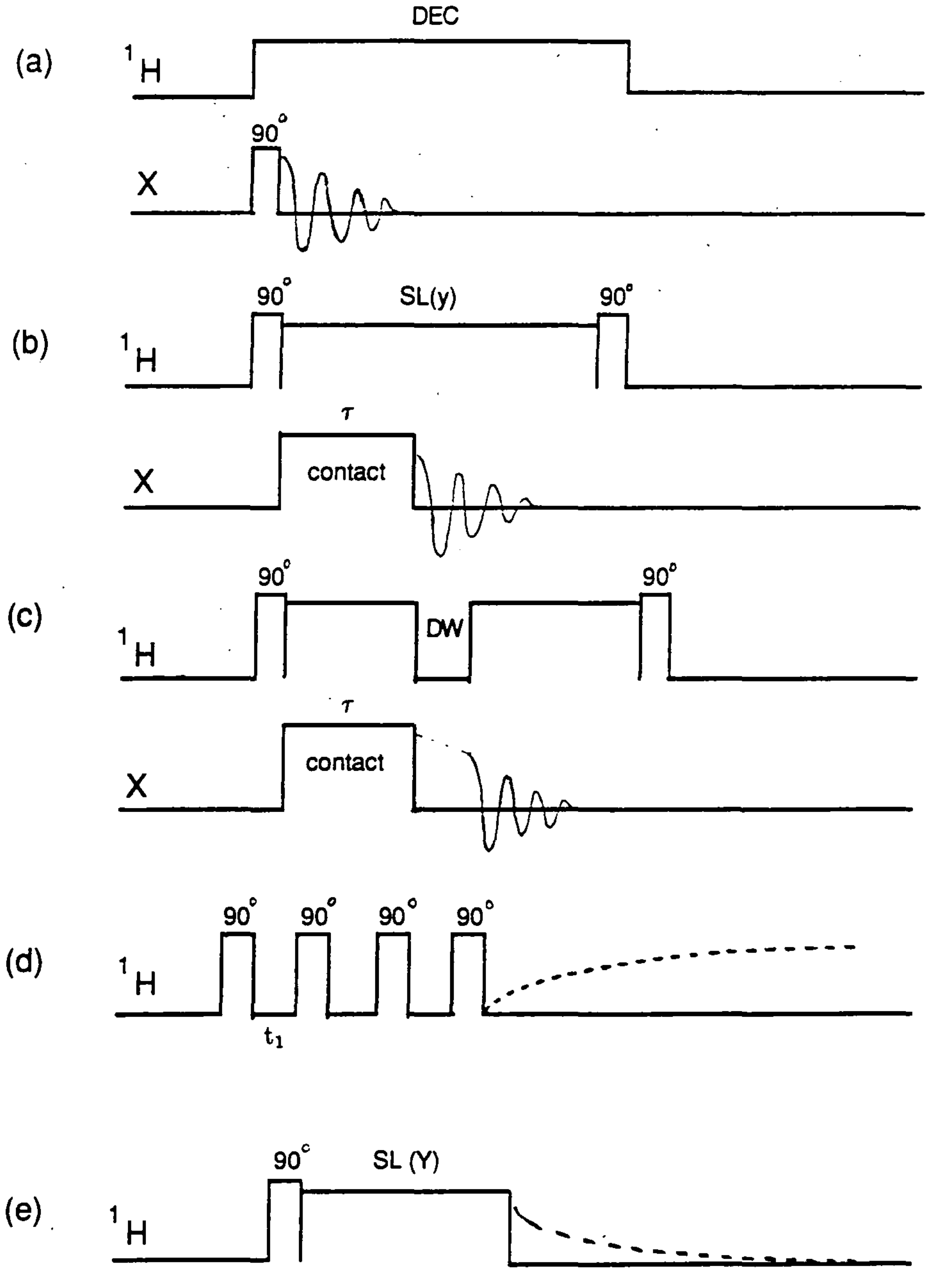

Figure 3.4.1: Pulse sequences: (a) SPE; (b) CP; (c) NQS; (d) $T_1(^1H)$; (e) $T_{1\rho}(^1H)$. Key: DEC = decoupling; SL = spin-lock; DW = decoupling window.

3.5 Magic-angle setting

When the angle between the rotor axis and the magnetic field $\mathbf{B}_0$ is set to 54.7°, the angle is the so-called magic-angle, at which most dipolar coupling, shielding anisotropy and anisotropy in spin-spin coupling will be averaged to zero (see Chapter 2). Solid KBr was used to adjust the angle by observing ^{79}Br FID signals and maximizing the number of spin echoes. The accuracy of this method can normally reach ± 0.1°.

3.6 Sample listing

The following samples were studied during the course of this work and the sources of the compounds are given accordingly.

Compounds	Sources
Triorganotin fluorides	
Me_3SnF	P. Granger
n-Bu_3SnF	Pilkington Bros. PLC
i-Bu_3SnF	Dr. H. Reuter (Institut für Anorganische Chemie, der Universität Bonn)
Ph_3SnF	
Mes_3SnF	"
Neo_3SnF	"
Organooxotin compounds	
$[MeSn(O)O_2CMe]_6$	Prof. P.R. Holmes (University of Massachusettes at Amherst, USA)
[n-$BuSn(O)O_2CMe]_6$	
[n-$BuSn(O)O_2P(C_6H_{11})_2]_4$	"
[(n-$BuSn(OH)O_2PPh_2)_3O][Ph_2PO_2]$	"

Compounds	Sources
Chlorine-containing oganotin compounds	
$(acac)_2SnCl_2$	Prof. P. Finocchiaro (University of Catania, Italy)
$(bzac)_2SnCl_2$	"
$(NH_4)_2SnCl_6$	Dr. K.B. Dillon (University of Durham, England)
$(MeNH_3)_2SnCl_6$	"
$(Ph_4P)_2SnCl_6$	"
K_2SnCl_6	"
$(Bu_4N)_2SnCl_6$	Dr. M.J. Taylor (University of Auckland, New Zealand)
Titania pigments	
anatase TiO_2 coated with $P_2O_5.K_2O$	Tioxide Laboratories (Stockton, Cleveland)
rutile TiO_2 coated with P_2O_5, K_2O	"
rutile TiO_2 coated with Al_2O_3, SiO_2	"
rutile TiO_2 coated with Al_2O_3, organic	"

References

1. Bruker Spectrospin Ltd., *Pulse NMR Spectrometer CXP Users Manual.*

2. R.K. Harris, A.M. Kenwright, A. Royston and B.J. Say, *Meas. Sci. Technol.*, **1**, 1304 (1990).

3. R.K. Harris, *Nuclear Magnetic Resonance Spectroscopy*, Langman Scientific & Technical, (1986).

4. S.R. Hartmann and E.L. Hahn, *Phys. Rev.*, **128**, 2042 (1962).

5. J. Tegenfeldt and U. Haeberlen, *J. Magn. Reson.*, **36**, 453 (1979).

6. S.J. Opella and M.H. Frey, *J. Amer. Chem. Soc.*, **101**, 5854 (1979).

7. E. Fukushima and S.B.W. Roeder, *Experimental Pulse NMR, A Nuts and Bolts Approach*, Addison Wesley, (1981).

Chapter IV

Sn-119 and C-13 NMR studies of triorganyl tin fluorides

4.1 Introduction

With the development of cross-polarization (CP) and magic-angle spinning (MAS), high-resolution NMR studies of solids became one of the most important tools to investigate chemical structure and bonding in solid organic and organometallic chemistry. This chapter will focus on the study of triorganyl tin fluorides, R_3SnF, using high-resolution solid-state NMR techniques. Both Sn-119 and C-13 CPMAS studies were undertaken. Though much more attention is given to ^{119}Sn NMR, the ^{13}C work was also included since carbon is the favourite dilute nucleus being studied, and is thus well documented. Measurement of ^{1}H relaxation times were also carried out which may give some extra information.

There has been considerable interest in the nature of bonding in solid triorganyl halides, and much X-ray work has been done to reveal the structures of triorganyl tin fluorides, though the NMR studies of these compounds are limited. So far, only tri-methyl tin fluoride and tri-n-butyl tin fluoride have been studied by solid-state NMR [1,2], and the ^{119}Sn chemical shift and the tin-fluorine coupling constant of tri-neophyl tin fluoride in solution were recorded some years ago [3,4].

The X-ray result of tri-methyl tin fluoride reported by Clark et al. [5] is presented in Figure 4.1.1. It showed that the crystal structure of Me_3SnF consisted of chains of trimethyltin groups and fluorine atoms, with fluorine-bridges and pentacoordination at tin. However, some ambiguities remained in the X-ray studies. This kind of chain-like five-coordination conformation was supported by Mössbauer studies [6,7] and earlier solid-state ^{119}Sn NMR research [1]. The same structure was also found for a similar compound, tri-n-butyl tin fluoride [2,8].

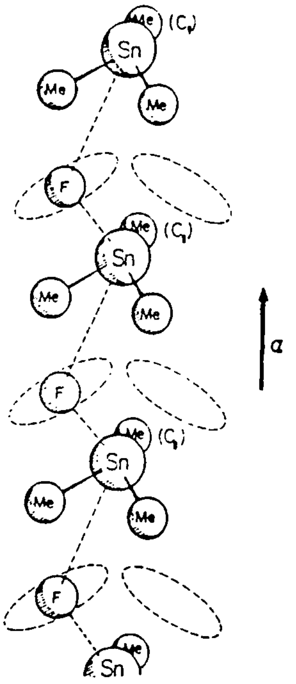

Figure 4.1.1: Crystal structure of Me_3SnF [5].

Recently, Reuter has found by X-ray structure analysis [9] that tri-benzyl tin fluoride has a nearly linear fluorine-tin-fluorine chain and the tin atoms lie in between two fluorine atoms (within experimental error) as shown in Figure 4.1.2. However, the same author has shown [10] that tri-mesityl tin fluoride has tetracoordinated tin with two molecules in the asymmetric unit. The bonded tin-fluorine distance is ca. 1.96 Å, whereas the nearest non-bonded Sn-F is ca. 4.46 Å apart. The crystal structure is displayed in Figure 4.5.8.

The above studies have been found to be very valuable in the understanding of the structures of organic tin fluorides. This chapter presents further work on this group of compounds, dealing specifically with Me_3SnF, n-Bu_3SnF, i-Bu_3SnF, Ph_3SnF, Mes_3SnF (Mes=mesityl) and Neo_3SnF(Neo=neophyl). The first compound was provided by P. Granger and n-Bu_3SnF was supplied by Pilkington Bros. PLC. The last four ones were given by Dr. Reuter along with the X-ray information.

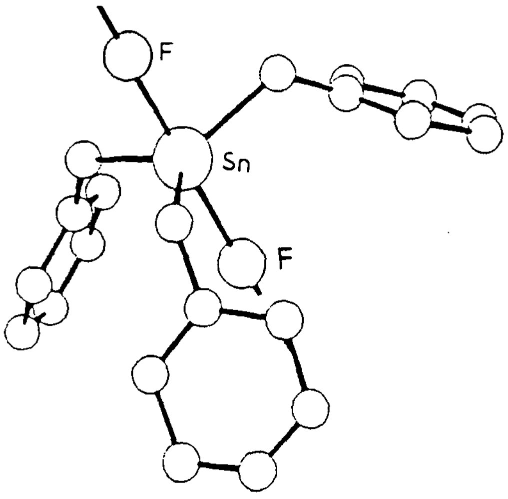

Figure 4.1.2: Crystal structure of Bz_3SnF [9]

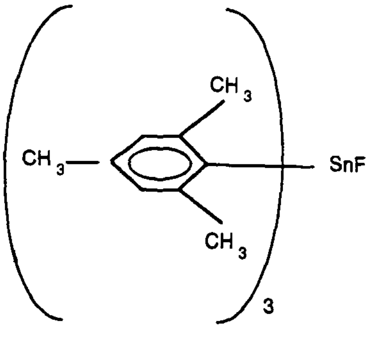

Mes_3SnF

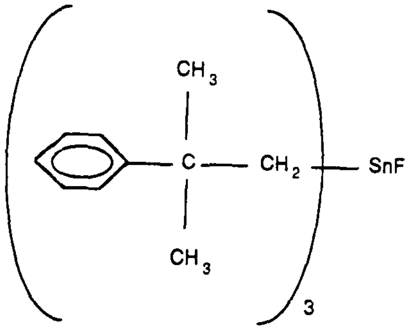

Neo_3SnF

4.2 The coordination number

High-resolution ^{119}Sn NMR spectra were recorded for all the six triorganyl tin fluorides. Though the formulae of the compounds are the same, some of the ^{119}Sn CPMAS spectra appear to be substantially different.

Figure 4.2.1 shows the ^{119}Sn CPMAS spectra of i-Bu_3SnF and Mes_3SnF, obtained with high-power proton decoupling, on the same scale. It is apparent that whereas the spectrum of tri-i-butyl tin fluoride demonstrates some complexity, Mes_3SnF gives a rather simple spectrum. The complexity of the former arises from two properties of the spectrum: (1) the triplet splitting for the centreband (indicated by arrows, obtained by varying the spinning speed); (2) each of the split lines possesses a wide spread of spinning sidebands.

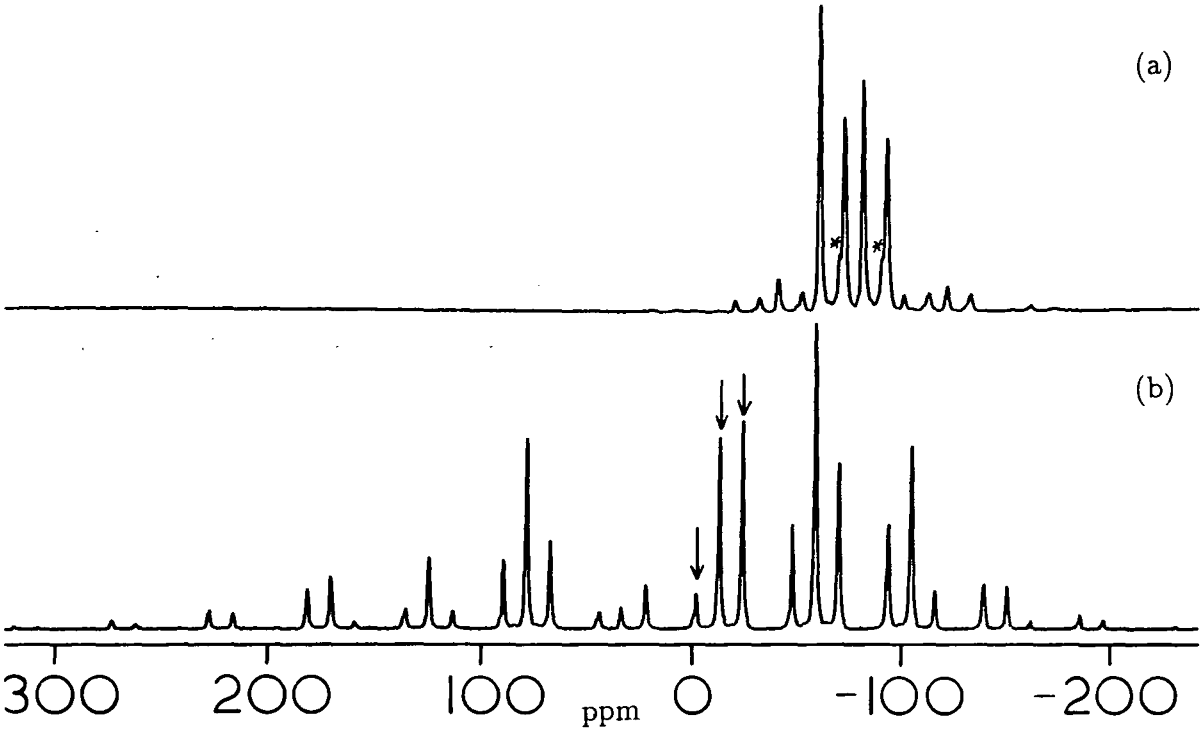

Figure 4.2.1: ^{119}Sn CPMAS spectra of (a) Mes_3SnF and (b) i-Bu_3SnF obtained at 111.86 MHz. Spectrometer operating conditions: Contact time 2ms (a) and 5ms (b); Recycle delay 1s (both); Number of transients 5800 (a) and 2000 (b): Spinning speed 4400 (a) and 5130 (b) Hz.

Summing over the intensities of all the spinning sidebands for each manifold gives the relative intensity ratio of the subspectra as 1:2:1. This triplet splitting indicates that ^{119}Sn nucleus is equally coupled to two equivalent fluorine nuclei (on the NMR timescale). This interpretation implies that tin is five-coordinated in the solid state with tin lying in the middle of the linear fluorine-tin-fluorine chain. The above explanation is fully consistent with the known crystal structure of tri-benzyl tin fluoride [9] and with the incomplete X-ray study of Me_3SnF [5].

The extensive spinning sideband manifolds are the result of large shielding anisotropy of tin atoms, which may be regarded as characteristic of pentacoordination of tin. While the middle spinning sidebands represent the shielding tensors directly, the other two manifolds represent effective shielding tensors, which contain the interplay of various tensors: shielding, dipolar and indirect coupling tensors. An extensive study of the spinning sideband manifolds can be found in Section 5.

On the other hand, the spectrum of Mes_3SnF shows four main lines with few spinning sidebands. It is found by multi-field studies that there are two doublet splittings present. Since scalar coupling is invariant in Hz to magnetic field, spectra obtained at two different fields will give information about such splittings. The two doublets reflect the fact that two chemical shifts exist. Thus the NMR analysis, in conformity with the X-ray work [10], gives the evidence that two molecules of Mes_3SnF exist in the asymmetric unit. Also, the doublet splittings indicate that there is only one fluorine nucleus coupled to tin, which implies the tin has coordination number four. The spectrum also contains two additional weak lines (indicated by $*$), centred at $\delta = -79.9$ ppm. They may arise from a polymorphic form of the molecule, but this suggestion can not be confirmed.

^{119}Sn CPMAS spectra of Me_3SnF, n-Bu_3SnF, Ph_3SnF and Neo_3SnF were also obtained. Tri-methyl tin fluoride and tri-n-butyl tin fluoride have similar spectra to tri-i-butyl tin fluoride in all respects, except for the values of isotropic chemical shift, as shown in Figures 4.2.2(a)(b). The spectrum of tri-phenyl tin fluoride (Figure 4.2.3), too, shows the characteristic pattern of pentacoordination though the spectrum is not of high quality because the CP does not give as significant an improvement as for the other compounds (see Section 7). Figure 4.2.4 shows the spectrum of Neo_3SnF, giving very weak shielding anisotropy. Multi-field studies revealed that four main doublets exist as indicated in the spectrum. There are also some impurities in the spectrum, whose origin is unclear. The Sn-119 NMR studies thus show that the tri-neophyl tin fluoride has the characteristics of a monomeric

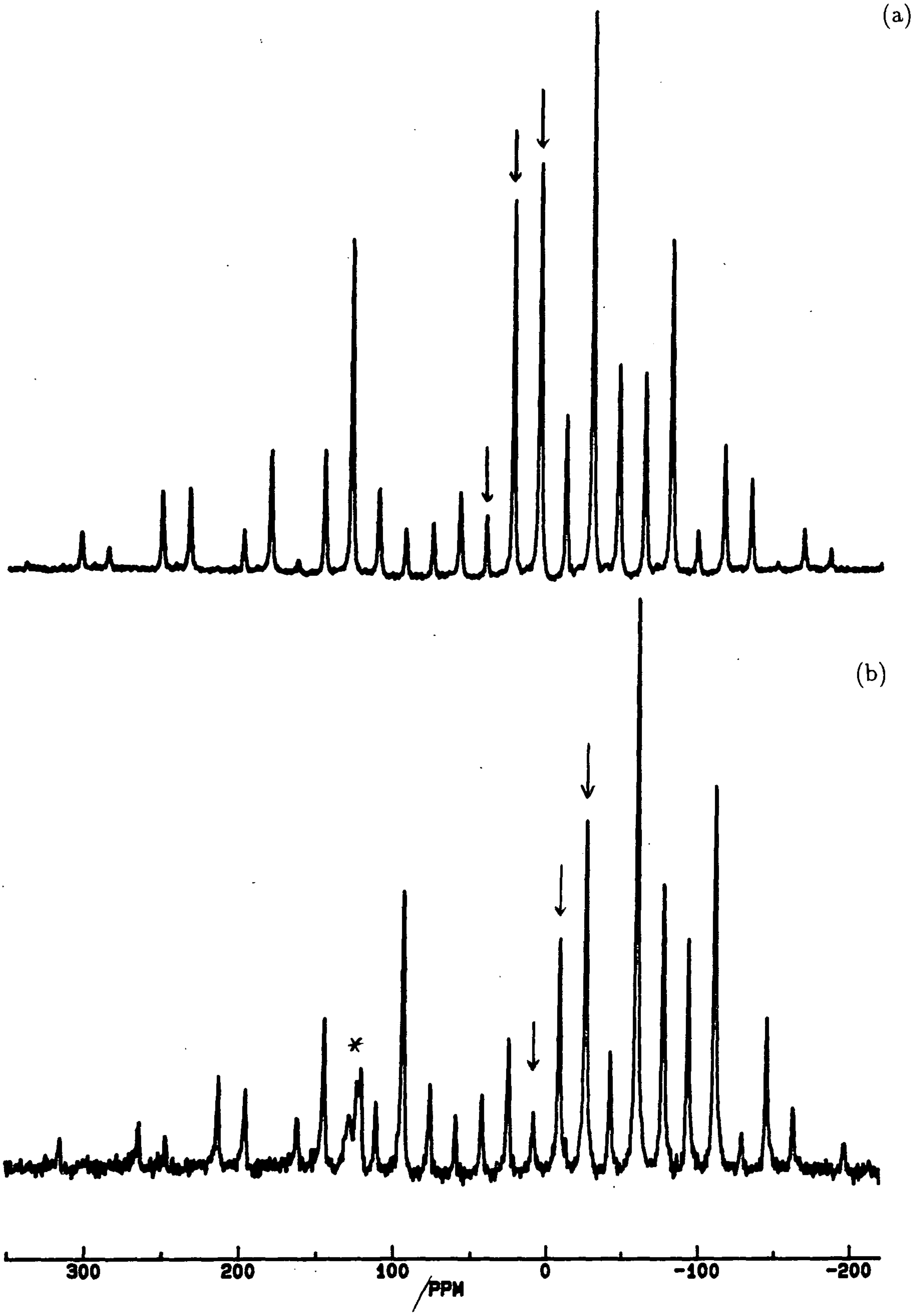

Figure 4.2.2: ^{119}Sn CPMAS spectra of Me_3SnF (a) and n-Bu_3SnF (b) obtained at 74.63 MHz. Spectrometer operating conditions: Contact time 5ms (both); Recycle time 10s (a) and 5s (b); Number of transients 6294 (a) and 9906 (b); Spinning speed 3910 Hz (a) and 3820 Hz (b). The peak marked with * is the impurity.

structure, which implies that the tin atoms are tetracoordinated. However, it is also clear that the compound is not pure.

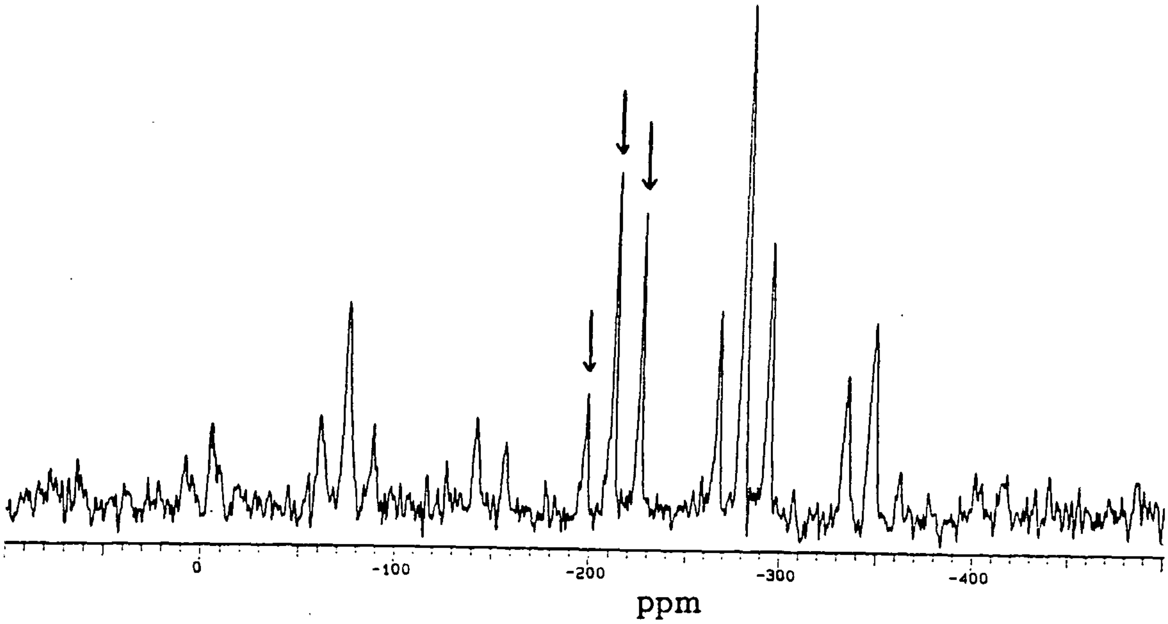

Figure 4.2.3: ^{119}Sn CPMAS spectrum of Ph_3SnF obtained at 111.86 MHz. Spectrometer operating conditions: Contact time 5ms; Recycle time 30s; Number of transients 1904; Spinning speed 8100 Hz.

4.3 Isotropic chemical shifts

The isotropic chemical shifts for the six compounds are listed in Table 4.3.1. It can be seen that the values cover a wide range, and the difference in coordination number is not immediately clear. However, it is well acknowledged through solution studies that a significant change of ^{119}Sn chemical shift to lower frequencies occurs when the coordination number at tin increases. The order of change in tin-119 resonance was found to be ca. 150 ppm per unit change of coordination in solution-state [11].

Table 4.3.1: ^{119}**Sn chemical shifts and** $^{1}J_{SnF}$ **coupling constants of triorganyl tin fluorides** R_3SnF

R	δ_{Sn} /ppm	$\lvert J_{SnF}\rvert$ /Hz	σ^*
Me	23.8	1300	0.00
i-Bu	− 13.2	1260	− 0.125
n-Bu	− 8.9	1295	− 0.130
Ph	− 211.9	1530	0.60
Mesityl	− 82.0 − 70.5	2250 2300	- -
neophyl	161.0 157.0 89.8 72.5	2263 2260 2293 2265	- - - -
Estimated error	± 0.5	± 15	-

As demonstrated in the previous section, four of the six compounds: Me_3SnF, i-Bu_3SnF, n-Bu_3SnF and Ph_3SnF, have chain polymer structures. All of them show only one chemical shift, which suggests that the crystallographic asymmetric unit is a single group. However, their chemical shift values are quite different. The effect of changing the organic group R on ^{119}Sn chemical shifts has been recognised by many authors [12,13,14]. It is understood that as the electron withdrawing ability of the alkyl group R increases, the tin atom becomes less shielded and thus increases the ^{119}Sn chemical shift. However, when the alkyl group attached to tin is replaced by phenyl, other effects will predominate, leading the ^{119}Sn chemical shift to lower frequencies (see below).

It is generally believed that the dependence of ^{119}Sn chemical shifts upon the organic groups bonded to tin may result from a change in the paramagnetic term, σ_p, which is a dominating factor contributing to the tin shielding. The expression for the paramagnetic term of shielding may be written as follows [15]:

$$\sigma_p^{loc} = -\frac{\mu_0 e^2 \hbar^2}{6\pi m^2 \Delta E}(< r^{-3} >_{np} \mathrm{P}_\mu + < r^{-3} >_{nd} \mathrm{D}_n) \qquad (4.3.1)$$

Where μ_0, e, $\hbar$ and m are the usual constants; ΔE is a mean electronic excitation energy, which may be treated as constant for a series of closely related tin compounds; r is defined as the separation between the tin nucleus and the valence p (and d) electrons, and $< r^{-3} >_p$ and $< r^{-3} >_d$ are the average values of r_p^{-3} and r_d^{-3} respectively; P_μ and D_μ refer to the electron imbalance associated with the tin atom's valence p and d orbitals respectively. The values of P_μ and D_μ depend on the ^{119}Sn coordination number, hybridization of the atomic orbitals in bonding and ionicity of the bonds. Large values of P_μ and D_μ correspond to highly imbalanced p and d electron distributions. If the electron shells are symmetric, the values of P_μ and D_μ will be zero.

Hence, when the electron withdrawal ability of the R group increases, the electron imbalance of tin atom P_μ and D_μ will increase accordingly, therefore the paramagnetic term will become larger in magnitude, i.e. the ^{119}Sn magnetic shielding will decrease, leading to an increase in chemical shifts. The Taft σ^* constants in Table 4.3.1 [16] reflect the inductive effect of the R groups and so the electronegativities. Methyl group has a larger value of σ^* constant than that of butyl, so Me_3SnF gives a more positive value (ca. 35 ppm) of ^{119}Sn chemical shift. The electronegativities of i-Bu and n-Bu groups are very close; so are the Sn-119 chemical shifts of i-Bu_3SnF and n-Bu_3SnF. However, the chemical shift of n-Bu_3SnF is somewhat greater than that of i-Bu_3SnF, which is contrary to what one would expect. Nevertheless, a rough correlation exists between the tin chemical shift and the electron withdrawal capacity of alkyl group R, as in the case of solution.

However, when the phenyl group is considered, the ^{119}Sn signal moves to a much lower frequency (ca. −212 ppm), which is inconsistent with the fact that the phenyl has a greater electron withdrawal ability ($\sigma^* = 0.60$). This phenomenon can be attributed to the involvement of π-bonding between tin and the aromatic group [13,17,18]. Such bonding will reduce the electronic imbalance $P\mu$ and $D\mu$ on the tin nucleus and so reduce the paramagnetic term in magnitude, as a result, tin experiences more shielding.

Compared with the other compounds, the chemical shifts of Mes_3SnF and Neo_3SnF appear to be anomalous. However, when the mesityl group is regarded as a substituted phenyl group, and the fact that the ^{119}Sn chemical shift difference between them is of ca. 130 ppm, it is clear that Ph_3SnF is pentacoordinated whereas $mesityl_3SnF$ is four-coordinated. Also, the neophyl group is a substituted methyl group, and as the Me_3SnF shift is ca. 23.8 ppm, a four-coordinated trineophyl tin fluoride would be expected to have a shift of ca. 160 ppm. This is in fact the case. The chemical shift of Neo_3SnF in solution-state was found to be 139.0 ppm [3], which is within the region found for solid-state. However, it seems likely that there is some kind of structural difference between the solution and solid states since their chemical shifts are not quite the same.

The great difference in ^{119}Sn isotropic chemical shifts for different coordination at tin enables ^{119}Sn NMR to be used as a probe to investigate the coordination number of the organic tin compounds in the solid-state.

4.4 The tin-fluorine scalar coupling constants

The important property of scalar coupling is that the coupling (J coupling) constant remains unchanged at different magnetic fields. Hence it can easily be measured by running the samples at two different fields. Figure 4.4.1 shows the ^{119}Sn spectra of Mes_3SnF obtained at 74.63 MHz on a CXP-200 spectrometer and at 111.86 MHz on a VXR-300 spectrometer respectively. Both spectra are on the same scale of ppm. Measuring the distances between the four main peaks, in units of Hz, gives the result that the distance between line 1 and line 3 is same for

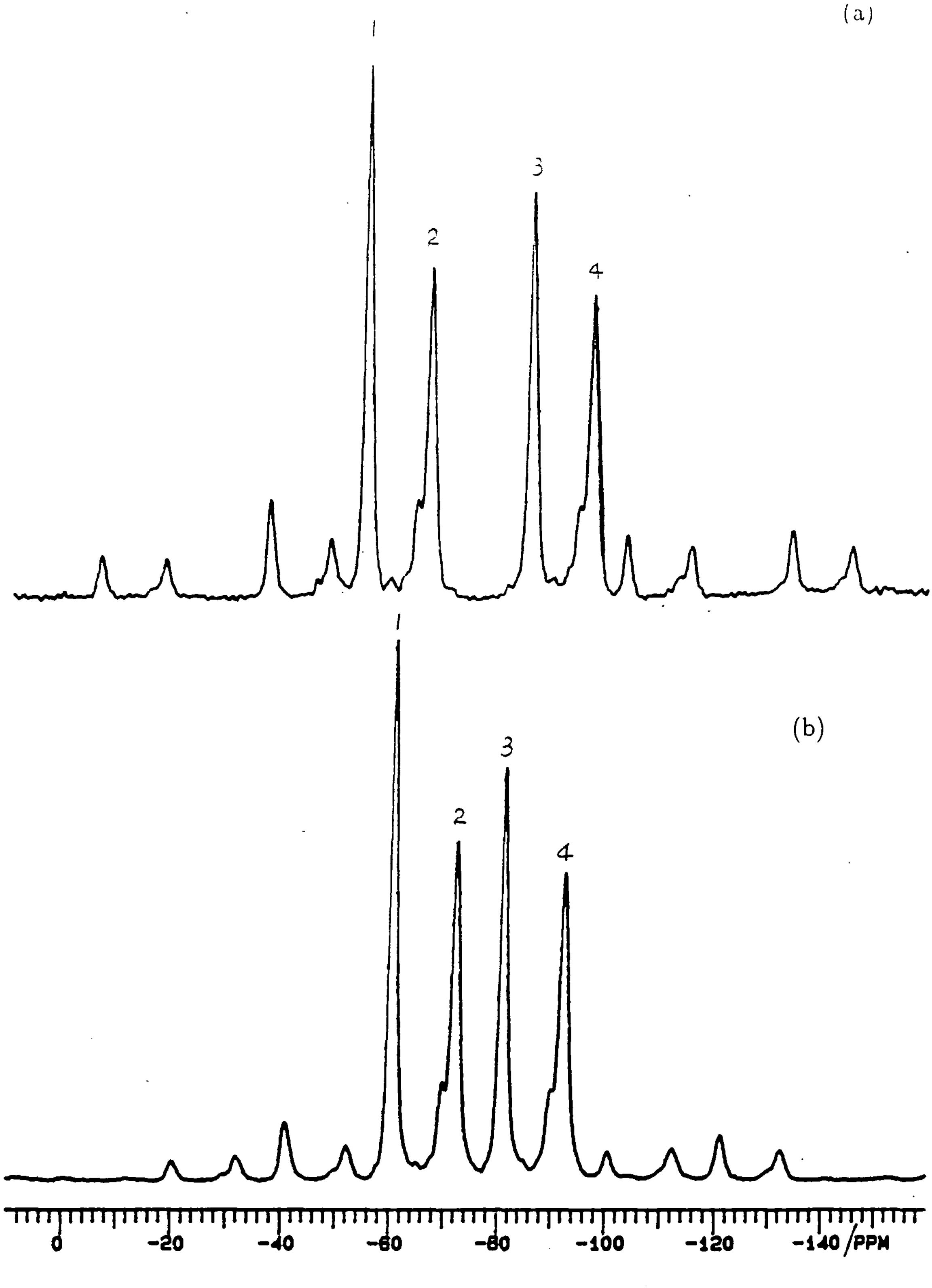

Figure 4.4.1: ^{119}Sn CPMAS spectra of tri-mesityl tin fluoride obtained at (a) 74.63 MHz and (b) 111.86 MHz. Spectrometer operating conditions: Contact time 5ms (a) and 2ms (b); Recycle time 5s (a) and 1s (b); Number of transients 8626 (a) and 5800 (b); Spinning speed 3630 Hz (a) and 4420 Hz (b).

both spectra, as is the difference between line 2 and line 4. Hence two doublet splittings are found, whose isotropic scalar coupling constants are 2300 ± 15 Hz and 2250 ± 15 Hz respectively. All the spectra of triorganyl tin fluorides being studied have been repeated on both spectrometers (CXP-200, VXR-300). Their isotropic indirect coupling constants are presented in Table 4.3.1.

The indirect coupling constant could be either positive or negative. However, the proton-decoupled CPMAS experiment only provides the magnitude of the coupling constant but not the sign; therefore the data in Table 4.3.1 just give the absolute values. Pople and Santry [19] calculated the reduced coupling constant ^{1}K between carbon and fluorine nuclei using molecular orbital theory. The reduced coupling constant K_{AB}, which depends only on the electronic environment, is defined as:

$$\mathrm{K}_{AB} = (2\pi/\hbar\gamma_A\gamma_B)\mathrm{J}_{AB} \tag{4.4.1}$$

They found that the coupling depends predominantly on the contact term, and the expression of the contact contribution is given by :

$$\mathrm{K}_{AB} = \frac{64\pi^2}{9}\beta^2(S_A|\delta(\mathbf{r}_A)|S_A)(S_B|\delta(\mathbf{r}_B)|S_B)\pi_{SA,SB} \tag{4.4.2}$$

As can be seen from the equation, the sign of K_{AB} is determined by the sign of the mutual polarisability term $\pi_{SA,SB}$. Since the fluorine 2s orbital is sufficiently low in energy, the mutual polarisability between $2s_F$ and $2s_C$ will have the limiting form [19]:

$$\pi_{SA,SB} = \frac{4\lambda^2\mu^2\chi^2}{E_2 - E_3} < 0 \tag{4.4.3}$$

This will lead to a negative value of $^1\mathrm{K}(^{13}\mathrm{C},^{19}\mathrm{F})$. Their calculation also indicates that the X-Y reduced coupling constants for first-row elements are likely to be negative if one of the nuclei is ^{19}F. A qualitative extension of the theory leads one to expect that the $^1\mathrm{K}(^{119}\mathrm{Sn},^{19}\mathrm{F})$ has a negative sign, provided the contact term still dominates. A survey of the coupling constants [14] suggested that for one-bond couplings, $^1K(^{119}SnX)$ is negative if X has lone pair electrons, and indeed ^{19}F has a lone pair electrons.

Equation 4.4.2 also implies general parallels between the behavior of the reduced coupling constant involving ^{119}Sn and the corresponding ones involving ^{13}C and ^{29}Si. The reduced coupling constant $^1K(^{29}Si,^{19}F)$ was found to be negative experimentally [20], in agreement with the sign predicted by Pople and Santry's calculation.

However, few J coupling data of triorganyl tin fluorides have been reported. It may be worthy of mention here that as tin has a negative magnetogyric ratio and fluorine has a positive value, the signs of $^1K(^{119}Sn,^{19}F)$ and $^1J(^{119}Sn,^{19}F)$ are opposite. McFarlane and Wood [4] measured both the sign and magnitude for Neo_3SnF in concentrated $CDCl_3$ solution by performing ^{19}F and ^{119}Sn double-irradiation experiments. The result was that $^1J(^{119}Sn,^{19}F)$ has a positive sign (negative reduced coupling) and the magnitude is 2298 Hz. The magnitudes of the same parameter are found to be between ca. 2260 and ca. 2295 Hz in the solid-state for tri-neophyl tin fluoride as shown in Table 4.3.1.

The slight difference in J coupling magnitude between solid and solution states of Neo_3SnF indicates that there are no major changes in the tin electronic environment between the two states. Hence it is reasonable to assume that the $^1J(^{19}F,^{119}Sn)$ constant of tri-neophyl tin fluoride in the solid state has a positive sign as well. Since the magnitudes of $^1J(^{119}Sn,^{19}F)$, shown in Table 4.3.1, are large regardless of the coordination (i.e. no values near zero), it is reasonable to suppose that the coupling constant of the triorganyl tin fluorides always has the same sign.

There are substantial differences in tin-fluorine coupling constants between the four-coordinated tin and the pentacoordinated tin nuclei in the compounds studied here. This may be explained by the fact that when fluorines are "shared" between tin atoms the s electron densities at nuclei Sn and F (Equation 4.4.2) will decrease largely, thus leading to a substantial lowering of $^1J(^{119}Sn,^{19}F)$ for the chain systems.

The coupling constant of Ph_3SnF, which has a chain-like structure, is close to that of other bridging polymers. Thus the isotropic indirect coupling constants provide clearer evidence than chemical shifts that Ph_3SnF has a characteristic pentacoordinated tin. Hence J coupling is extremely useful for structure elucidations. The correlation between $^1J(^{119}Sn,^{19}F)$ and the electronegativity of the alkyl group R is obvious. The more electron-withdrawing ability the alkyl group has, the larger the value of $^1J(^{119}Sn,^{19}F)$ as demonstrated in Table 4.3.1.

4.5 Interplay of shielding, direct and indirect coupling tensors

4.5.1 Introduction

One of the advantages solid-state NMR has is that the three principal components of the shielding tensor can be obtained, whereas in solution they are averaged by molecular tumbling to the isotropic value σ_{iso}. The chemical shift tensor provides potential information about the bonding and structure, especially regarding the local chemical environment of the nucleus. In a MAS spectrum, a single resonance line is produced for each chemically different nucleus in the crystallographic asymmetric unit of a microcrystalline compound, unless there is indirect spin-spin coupling to other magnetic nuclei. When the rotor speeds are less than shielding anisotropies, spinning sideband manifolds should be observed. The spinning sidebands can be analysed to yield the values for shielding tensor elements [21,22]. However, when heteronuclear indirect coupling exists multiplet splittings are normally expected. Under slow MAS conditions, each split signal has a spinning sideband manifold which is governed by an effective tensor involving a combination of σ, $\mathbf{J}$ and $\mathbf{D}$. This situation has been reported for the $(^{13}C,^{19}F)$ and $(^{13}C,^{31}P)$ pairs of nuclei by Zilm and Grant [23], Harris, Packer and Thayer [24] respectively.

In the case of the AX_2 spin system (where the X nuclei are equivalent), triplet splittings with their corresponding spinning sideband manifolds are produced. The simplest situation involving an AX_2 system is: (1) two X spins are magnetically equivalent; (2) the molecular system is linear and axially symmetric: (3) the principal axes of J and σ are coincident, with their unique axis along the dipolar direction. When these conditions are assured, the effective tensor of the A spin for each of the three manifolds may be expressed by (see Chapter 2, note that the shielding is the negative of corresponding resonance frequency):

$$\mathrm{T}_A^{eff(+)} = \nu_A \sigma_A^{iso} + (\mathrm{D}' + \frac{1}{2}|\nu_A| \sqsupset_A)(3\cos^2\theta - 1) - \mathrm{J}_{AX}^{iso} \qquad (4.5.1)$$

$$\mathrm{T}_A^{eff(0)} = \nu_A \sigma_A^{iso} + \frac{1}{2}|\nu_A| \sqsupset_A (3\cos^2\theta - 1) \qquad (4.5.2)$$

$$\mathrm{T}_A^{eff(-)} = \nu_A \sigma_A^{iso} - (\mathrm{D}' - \frac{1}{2}|\nu_A| \sqsupset_A)(3\cos^2\theta - 1) + \mathrm{J}_{AX}^{iso} \qquad (4.5.3)$$

where:

labels +, 0, − refer to X_2 spin states of +1, 0, −1 respectively;

$\nu_A = (\gamma_A/2\pi)\ B_0$, the larmor frequency;

σ_A^{iso} is the isotropic value of the shielding tensor;

$\sqsupset_A$ defines the anisotropy of the shielding tensor;

J^{iso} is the isotropic value of the indirect coupling tensor;

$D' = D - \Delta J/3 = D - (J_\perp - J_\parallel)/3$, D is the dipolar coupling constant;

θ is the angle between the internuclear vector and $\mathbf{B}_0$.

These relationships are given when γ_A is negative and γ_B is positive, as in the case of γ_{Sn} and γ_F. Since θ could lie in any orientation, each of these three equations represents an axially symmetric subspectrum. In fact, the central manifold $\mathrm{T}_A^{eff(0)}$ is governed by the shielding tensor alone. Thus the shielding tensor can be easily determined by analyzing the middle spinning sideband manifold. As only the axial symmetric case is considered, the shielding tensor can be expressed as $\sigma_\perp$ and $\sigma_\parallel$, the extrema of the central resonance, then the extrema of the two outer manifolds may be expressed as:

$$T_{\perp}^{eff(+)} = \sigma_{\perp} - (\mathrm{D}' + \mathrm{J}) \tag{4.5.4}$$

$$T_{\parallel}^{eff(+)} = \sigma_{\parallel} + (2\mathrm{D}' - \mathrm{J}) \tag{4.5.5}$$

$$T_{\perp}^{eff(-)} = \sigma_{\perp} + (\mathrm{D}' + \mathrm{J}) \tag{4.5.6}$$

$$T_{\parallel}^{eff(-)} = \sigma_{\parallel} - (2\mathrm{D}' + \mathrm{J}) \tag{4.5.7}$$

After some rearrangment, the above equations may be rewritten as:

$$|\mathrm{D}' + \mathrm{J}| = |T_{\perp}^{eff(+)} - \sigma_{\perp}| = |\sigma_{\perp} - T_{\perp}^{eff(-)}| \tag{4.5.8}$$

$$|2\mathrm{D}' - \mathrm{J}| = |T_{\parallel}^{eff(+)} - \sigma_{\parallel}| = |\sigma_{\parallel} - T_{\parallel}^{eff(-)}| \tag{4.5.9}$$

It is clear from Equations 4.5.4–4.5.7 that the effective tensor components $\mathrm{T}^{eff(\pm)}$ are the combination of shielding (σ) and coupling (**D**, **J**) tensors, hence the values of $\mathrm{T}^{eff(\pm)}$ derived from spectra obtained at different magnetic fields will be different. However, Equations 4.5.8 and 4.5.9 show that the values of $|\mathrm{D}' + \mathrm{J}|$ and $|2\mathrm{D}' - \mathrm{J}|$ should be same (in units of Hz) for different fields.

The schematic powder pattern of the A nucleus in the above discussed AX_2 spin system is shown in Figure 4.5.1. The middle subspectrum has the intensity twice as much as that of the other subspectra. The extrema of the three subspectra are equally separated, and the separations are $|\ \mathrm{D}' + \mathrm{J}\ |$ and $|\ 2\mathrm{D}' - \mathrm{J}\ |$ respectively as indicated in Figure 4.5.1(a). If the scalar coupling constant J^{iso} equals zero, but the value of D' is non-zero, the powder patterns of the three subspectra will be different, though they have the same chemical shift (Figure 4.5.1(b)). On the other hand, when $\mathrm{J}^{iso} \neq 0.0$ and $\mathrm{D}' = 0.0$, the patterns will be the same, but the two outer subspectra will be shifted in opposite directions by $|\mathrm{J}^{iso}|$ as shown in Figure 4.5.1(c). Figure 4.5.1(d) shows that If both J^{iso} and D' are zero, the three subspectra will be identical, which implies that only shielding interaction occurs.

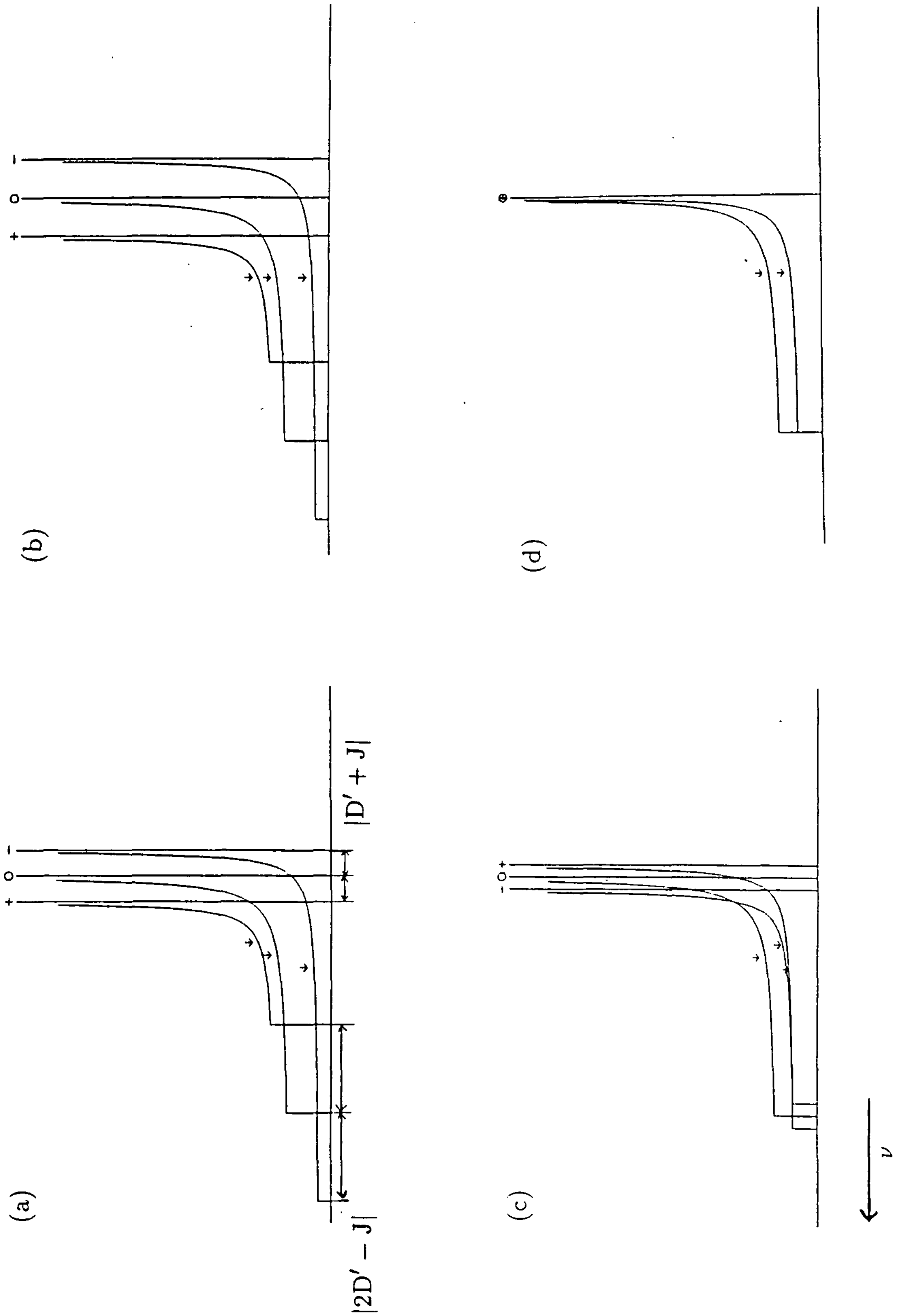

Figure 4.5.1: NMR solid-state powder patterns for the A nuclei of an AX$_2$ system. (a) influenced by dipolar interaction and the anisotropy of spin-spin coupling (D′), by axially symmetric shielding anisotropy (⊐), and by isotropic spin-spin coupling (J^{iso}); the +, 0 − lables are associated with the X$_2$ spin states of +1, 0 −1 respectively. (b) influenced by ⊐ and D′. (c) influenced by ⊐ and J^{iso}. (d) influenced only by ⊐.

The above discussion clearly demonstrates that while the pseudo-dipolar constant D′ governs the patterns of the subspectra, the isotropic J coupling constant governs the positions of the subspectra. However, the NMR spectrum does not provide the information as to which outer subspectrum corrsponds to $T^{eff(+)}$ and which corresponds to $T^{eff(-)}$. The absolute signs of J^{iso} and D′ can not be determined from the ^{119}Sn spectrum either. Figure 4.5.2 illustrates the behavior of the powder patterns as the signs of $\sqsupseteq$, D′ and J^{iso} vary. It is clear that whatever the signs of $\sqsupseteq$, D′ and J^{iso}, the effective anisotropies of the three subspectra always have the same sign. Moreover, the signs of the effective anisotropies only depend on the sign of the shielding anisotropy $\sqsupseteq$, but are independent of the signs of D′ and J^{iso}.

The above studies demonstrate that if the assumptions of coaxial and axially symmetric tensors are correct, the extrema of the shielding tensor should be in the middle of those of the two effective tensors. This fact provides a check on the effective tensor values if the system under investigation is consistent with the above discussion. We will find later in this chapter that the tin-fluorine-tin bridge systems agree with this presumption.

4.5.2 Results and discussion

Figure 4.5.3 shows the typical proton-decoupled ^{119}Sn CPMAS spectra of trimethyl tin fluoride, obtained at 74.63 MHz (a) and 111.86 MHz (b) respectively, with the same scale. Since the rotor speed of the higher field machine (VXR-300) can reach 10 kHz, the spectrum obtained at this speed demonstrates clearly the triplet splittings and the separate spinning sideband manifolds. The isotropic chemical shifts of the two spectra have the same value in ppm (within experimental error), as expected, and have the same isotropic J coupling constants in Hz.

Several different spectra were obtained for this compound at different spinning speeds and different magnetic fields (CXP-200 and VXR-300). Each of the spin-

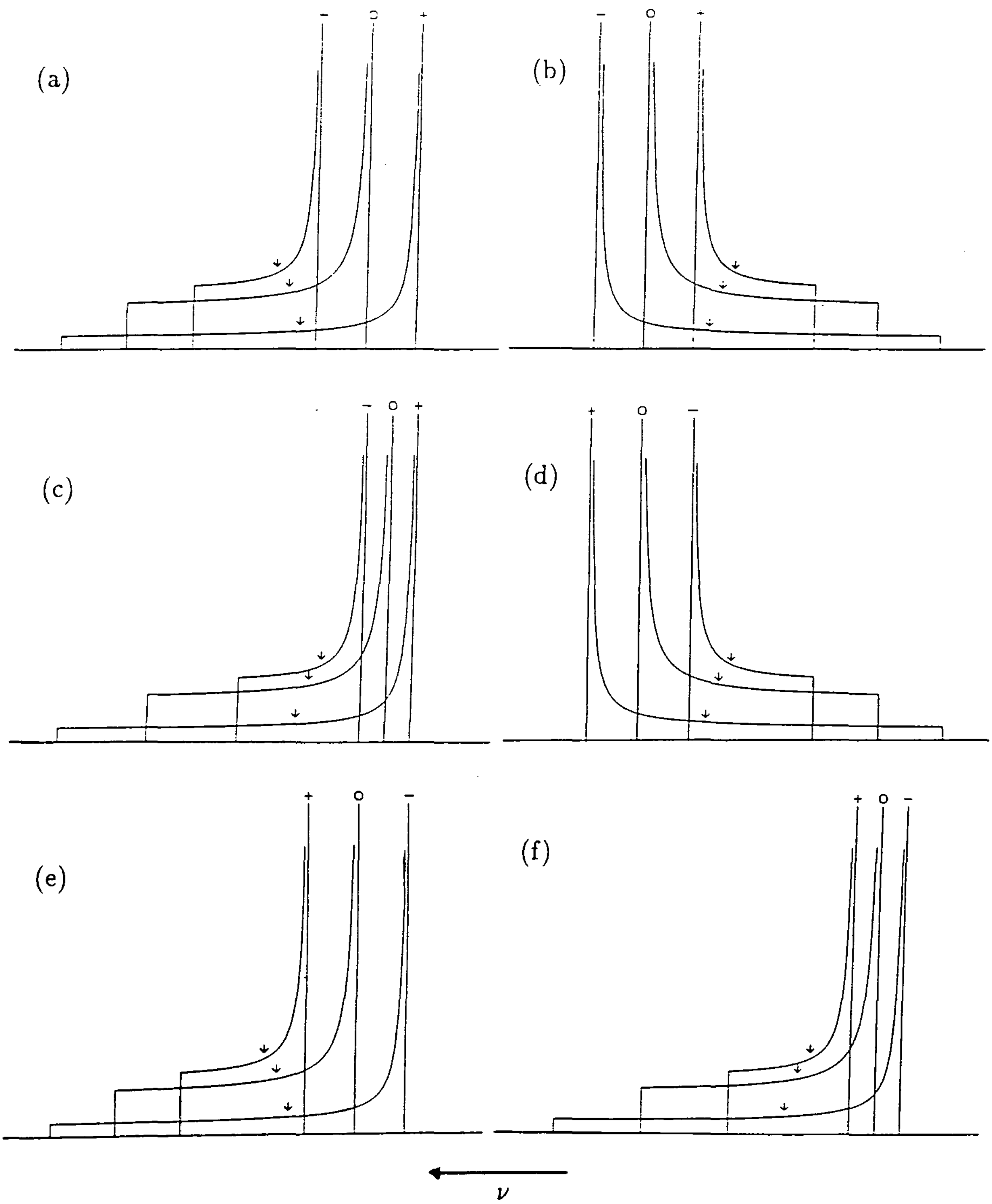

Figure 4.5.2: NMR solid-state powder patterns for A nuclei of an AX_2 system. The terms ℶ, D′, J^{iso} and the labels +, 0, − have the same significance as in Figure 4.5.1. (a) ℶ, D′, J^{iso} are negative. (b) ℶ is positive; D′, J^{iso} are negative. (c) ℶ, J^{iso} are negative; D′ is positive. (d) ℶ, D′, J^{iso} are positive. (e) ℶ is negative; D′, J^{iso} are positive. (f) ℶ and D′ are negative; J^{iso} is positive.

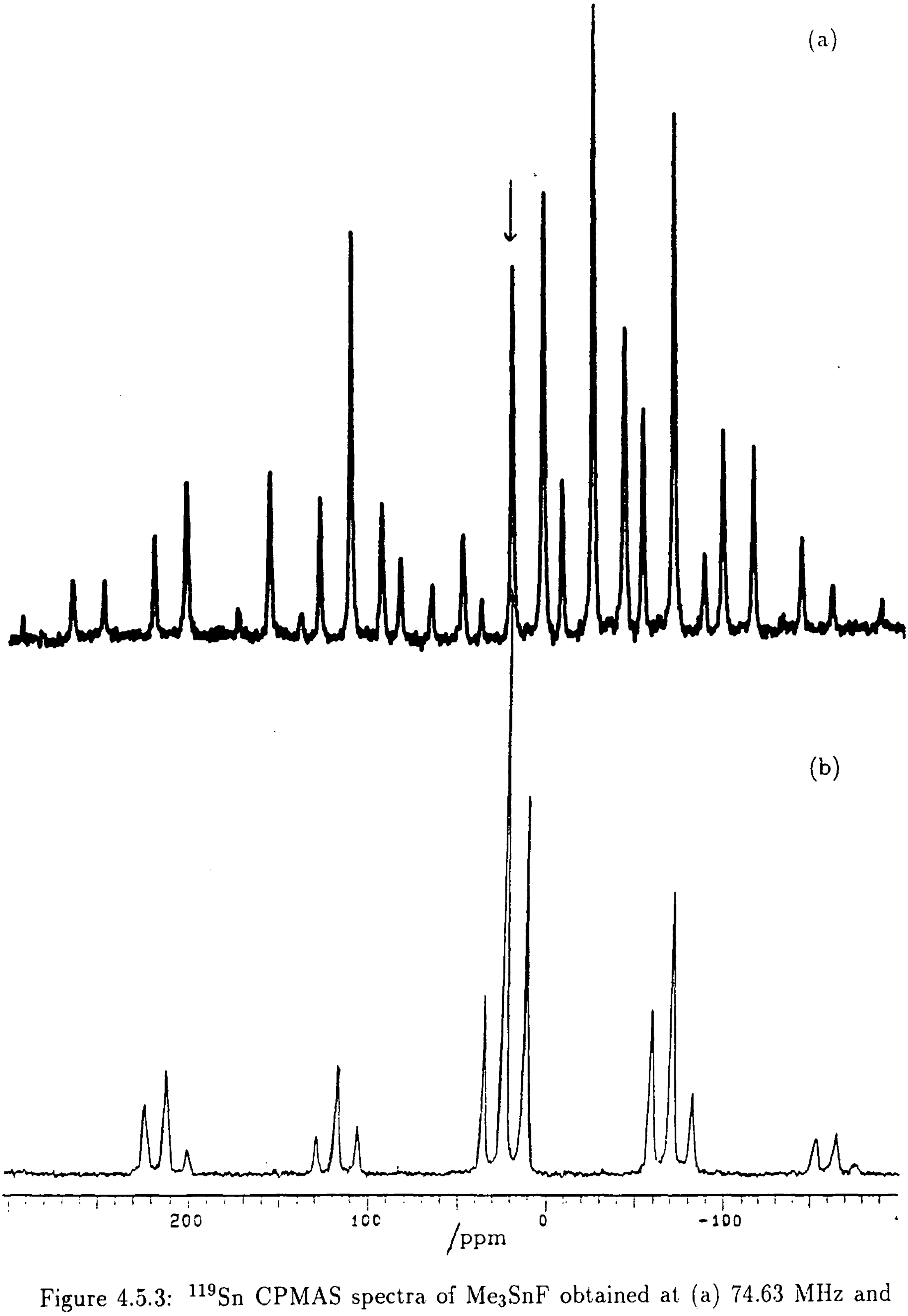

Figure 4.5.3: ^{119}Sn CPMAS spectra of Me_3SnF obtained at (a) 74.63 MHz and (b) 111.86 MHz. The arrow indicates the chemical shift. Spectrometer operating conditions: Contact time 5ms (both); Recycle time 10s (a) and 120s (b); Number of transients 1290 (a) and 448 (b); Spinning speed 3410 Hz (a) and 10400 Hz (b).

ning sideband manifolds was analyzed by an iterative fitting computer program. A full discussion about the program is given in Chapter 7. The resulting values of the effective shielding tensors for these spectra are presented in Table 4.5.1. The shielding tensors, resulting from fitting the central manifolds, are approximately the same for both fields, whereas the effective tensors derived from different magnetic fields are different as predicted in the preceeding section. It is obvious that while most of the tensors have axial symmetry, some of them have near-axial symmetry. However, as discussed in Chapter 7, the iterative fitting program is unable to distinguish between axially symmetric ($\eta = 0.0$) and near-axially symmetric ($\eta < 0.2$) systems. Hence all the tensors are regarded as having axial symmetry, and the perpendicular tensor components $\sigma_{\perp}$ are considered to be $\frac{1}{2}(\sigma_{11} + \sigma_{22})$ for tensors with $0.0 < \eta < 0.2$. One of the iterative fitting outputs is given in Figure 4.5.4, showing that the asymmetry parameter is zero. The average values of the results clearly demonstrate that the extrema of the shielding tensor (the middle spinning sidebands) lie in the middle of those of the two effective tensors, within experimental error. These data, together with the fact that the tin nucleus is equally coupled to two fluorine nuclei, confirms that the previous procedures dealing with AX_2 system are acceptable for this chain polymer system. P. Reams [25] also studied this compound and derived the tentative data for the shielding tensor by the moment method. The data given in this thesis are more accurate since a more sophisticated computer program has been used.

The spinning sideband analysis was also carried out for compounds: n-Bu_3SnF, i-Bu_3SnF and Ph_3SnF, and the average values of the results are summarized in Table 4.5.2. It is clear that all the compounds have axially symmetric tensors, and the differences in effective tensor components between the three spinning sideband manifolds are equal (within experimental error), confirming that the chain polymer systems of triorganyl tin fluorides are in accordance with the preceeding analytical procedures. The central spinning sideband manifolds show that the shielding anisotropies and asymmetries of the four fluorine-bridge compounds are very close,

Table 4.5.1: Spinning sideband analysis for Me_3SnF

	ν /Hz	$\delta_{\mathrm{Sn}}^{eff}$ /ppm	$\beth^{eff}$ /ppm	η^{eff}	$\sigma_{\perp}^{eff}$ /ppm	$\sigma_{\parallel}^{eff}$ / ppm
CXP200	3410	6.7	−113	0.00	50	−120
	3910	6.7	−115	0.00	51	−121
	5140	6.2	−123	0.00	56	−130
	5940	6.3	−128	0.00	58	−134
	Average	6.5 ± 0.3	−120 ± 8	0.00 ± 0.00	54 ± 4	−126 ± 8
VXR300	5030	12.1	−161	0.00	68	−173
	10400	12.7	−143	0.00	59	−155
	Average	12.4 ± 0.3	−152 ± 9	0.00 ± 0.00	64 ± 5	−164 ± 9
CXP200	3410	24.1	−221	0.18	87	−245
	3910	24.1	−227	0.17	90	−251
	5140	23.5	−218	0.00	85	−241
	5940	23.7	−225	0.00	89	−248
	Average	23.9 ± 0.4	−223 ± 5	0.09 ± 0.09	88 ± 3	−246 ± 5
VXR300	5030	23.3	−220	0.09	85	−243
	10400	24.3	−197	0.00	74	−221
	Average	23.8 ± 0.5	−209 ± 11	0.05 ± 0.04	80 ± 6	−232 ± 11
CXP200	3410	41.5	−329	0.00	123	−370
	3910	41.6	−330	0.00	123	−371
	5140	41.0	−320	0.00	119	−361
	5940	41.1	−319	0.00	118	−360
	Average	41.3 ± 0.3	−325 ± 6	0.00 ± 0.00	121 ± 3	−366 ± 6
VXR300	5030	34.6	−292	0.00	112	−327
	10400	36.0	−253	0.00	91	−289
	Average	35.3 ± 0.7	−273 ± 20	0.00 ± 0.00	101 ± 11	−308 ± 19

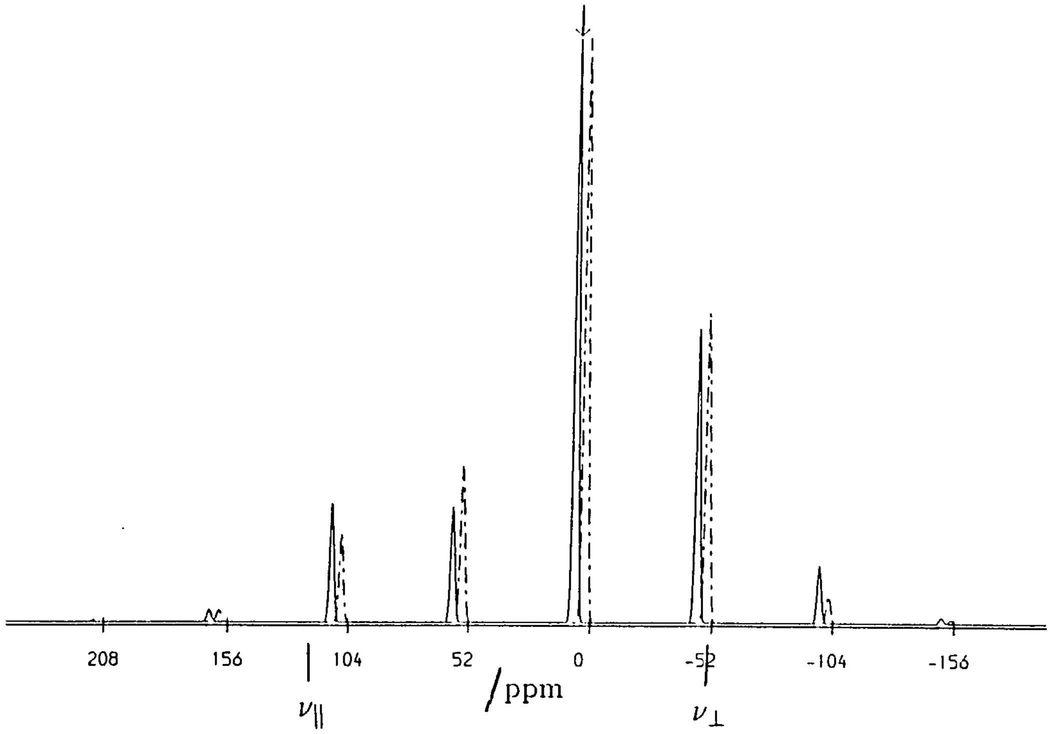

Figure 4.5.4: One of the iterative fitting results of Me_3SnF. Conditions: chemical shift 6.7 ppm; spinning speed 3910 Hz; spectrometer frequency 74.63 MHz. The results: shielding anisotropy = -115 ppm; shielding asymmetry = 0.00.

implying that shielding tensors, as well as coupling constants, are very powerful in the determination of molecular structures.

Calculations of the pseudo-dipolar constants D′ were made using Equations 4.5.8 and 4.5.9. Mathematically there should be four sets of results derived from the equations. However, the magnitude of J^{iso} can be measured directly from the spectra. Moreover the absolute sign of $^1J(^{119}Sn,^{19}F)$ is deduced to be positive from the discussion in the previous section. Hence only one set of results, with J being positive and of the same magnitude as the measurement, was found to be correct. The resulting data for D′ can be found in Table 4.5.2.

In principle, the coupling anisotropies ΔJ can be derived once the data for D′

Table 4.5.2: Tin-119 NMR data for solid fluorine-bridge triorganyl tin fluorides R_3SnF

R	$\delta_{\mathrm{Sn}}^{eff}$ /ppm	$\sqsupset^{eff}$ /ppm	η^{eff}	$\sigma_{\perp}^{eff}$ /ppm	$\sigma_{\parallel}^{eff}$ /ppm	D′ /kHz
$Me_3SnF^{(a)}$	6.5	−120	0.00	54	−126	−4.02
	23.9	−223	0.09	88	−246	
	41.3	−325	0.00	121	−366	
$n\text{-}Bu_3SnF^{(a)}$	−26.3	−130	0.09	92	−103	−3.78
	−8.9	−230	0.00	124	−221	
	8.5	−333	0.00	158	−341	
$i\text{-}Bu_3SnF^{(a)}$	−24.2	−125	0.00	86	−100	−3.74
	−13.2	−208	0.00	117	−195	
	−2.1	−294	0.00	149	−292	
$Ph_3SnF^{(b)}$	−225.5	−188	0.00	321	37	−3.26
	−211.9	−255	0.00	340	−43	
	−198.1	−306	0.00	351	−108	
Estimated error	± 0.5	± 5	± 0.1	± 5	± 5	± 0.35

(a) Data at 74.63 MHz; (b) Data at 111.86 MHz

are determined, provided that the values of (Sn,F) distances, r_{SnF}, are known (e.g. from X-ray studies). The relationship between ΔJ and r_{SnF} can be written in the following form:

$$\Delta J = 3(D - D') = 3(\frac{\mu_0}{4\pi}\gamma_{Sn}\gamma_F\hbar\frac{1}{r_{SnF}^3} - D') \qquad (4.5.10)$$

However, it appears that accurate values of r_{SnF} for the pentacoordinated R_3SnF systems are not yet available. For example, the (Sn,F) distance for Me_3SnF was reported [5] to be 2.15 Å and 2.45 Å respectively by different authors. For Bz_3SnF, the results [9] suggested r_{SnF} equals 2.12 Å and 2.21 Å: the same within experimental error. Thus a graph showing the relationship between the anisotropy $\Delta J(Sn,F)$ and the Sn-F distance, r_{SnF}, for the four polymeric compounds studied in this chapter was plotted (according to Equation 4.5.10), appearing in Figure 4.5.5. It seems clear that values of $\Delta J(Sn,F)$ are modest, e.g. less than ca. 3 kHz in magnitude, as the distances of polymeric R_3SnF usually lie in the region between 2.1 and 2.5 Å. The sign of ΔJ may change from negative ($D < D'$) to positive ($D > D'$) as the distance r_{SnF} increases. A small change in r_{SnF}, e.g. ± 0.1 Å, will lead to a relatively large change in $\Delta J(Sn,F)$ of ca. 0.8 kHz. Hence the estimated values of $\Delta J(Sn,F)$ will only be improved when the (Sn,F) distances are determined accurately by X-ray diffraction. However, as the estimated errors in D' are found to be ca. 0.35 kHz, the error in ΔJ would still be as large as ca. 1.0 kHz even if the measurement of r_{SnF} is very accurate (because $\Delta J \sim 3D'$). The graph shown in Figure 4.5.5 results from the suggestion that the AX_2 system is symmetric; however, if the NMR results are averages arising from unsymmetric fluorine bridges, the calculations may be more complicated.

The spinning sideband analysis was also performed for tri-mesityl tin fluoride to complete the data. However, the results are not very accurate because there are only a few spinning sidebands, which are weak and difficult to measure accurately. The resulting data are shown in Table 4.5.3, and one of the resulting powder patterns, plotted from the data given in Table 4.5.3, is presented in Figure 4.5.6.

It should be noticed that this compound is monomeric as stated earlier and the tin is tetracoordinated. The monomeric structure implies that there is only one fluorine atom coupled to tin, so it is a case of an AX system. Detailed discussion about an AX system influenced by dipolar, shielding and indirect coupling was described by Zilm and Grant [23] and Harris et al [24] some years ago. In view of the likely inaccuracies, no detailed calculation will be given here. However, some qualitative information can still be obtained. It is apparent that the shielding tensor is relatively small and has high asymmetry, in contrast to the polymeric

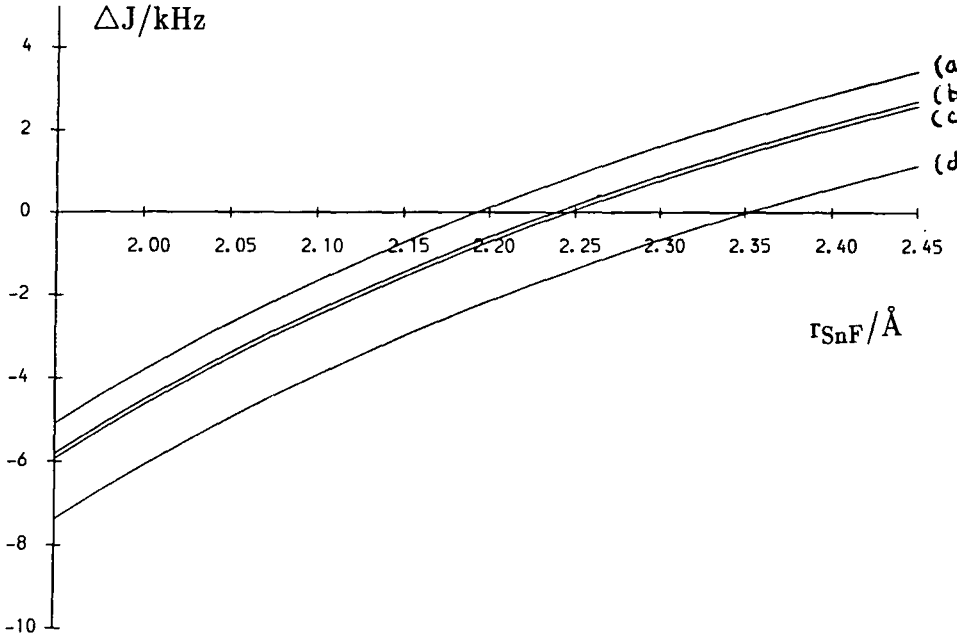

Figure 4.5.5: Graphs showing the relationship between the anisotropy ΔJ(Sn,F) and the Sn–F distance r_{SnF}, according to equation 4.5.10. (a) Me_3SnF; (b) n-Bu_3SnF; (c) i-Bu_3SnF; (d) Ph_3SnF.

Table 4.5.3: Results of spinning sideband analysis for $Mesityl_3SnF$

δ_{Sn} /ppm	Doublet peaks /ppm		$\beth^{eff}$ /ppm	η^{eff}	σ_{11}^{eff} /ppm	σ_{22}^{eff} /ppm	σ_{33}^{eff} /ppm
−82.0	CXP	−96.96	64.1	0.66	43.6	86.2	161.0
		−66.80	−59.5	0.57	113.6	79.5	7.3
	VXR	−92.28	42.3	0.78	54.7	87.6	134.6
		−72.11	−39.6	0.39	99.7	84.1	32.5
−70.5	CXP	−85.69	73.3	0.40	30.3	70.8	156.0
		−54.91	−50.0	0.56	98.9	61.9	4.2
	VXR	−80.87	48.0	0.59	42.7	71.0	128.9
		−60.33	−28.5	0.43	80.7	68.5	31.8

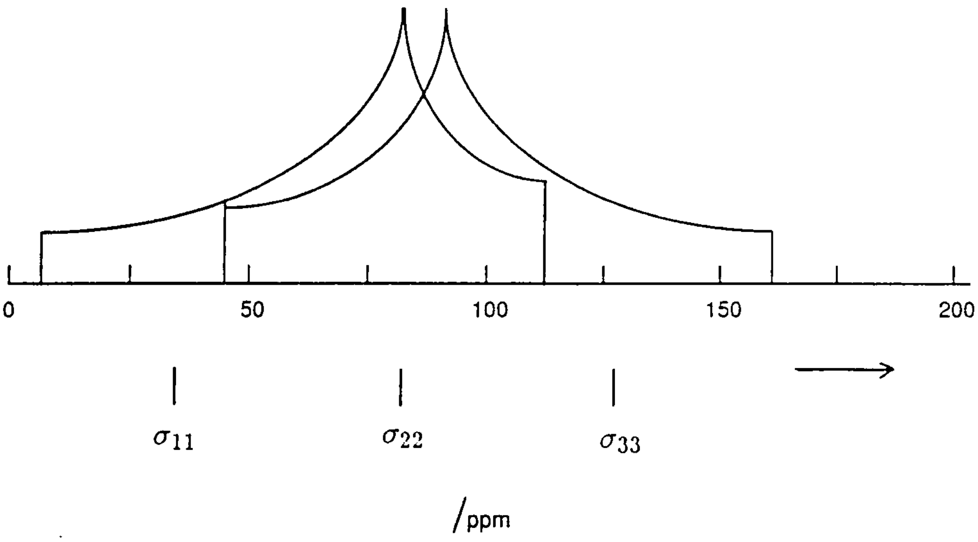

Figure 4.5.6: Schematic powder pattern, derived from data given in Table 4.5.3, of one of the resonances ($\delta_{\mathrm{Sn}} = -82.0$ ppm) of tri-mesityl tin fluoride, obtained on a CXP-200 spectrometer. The calculation of the positions of the three shielding tensor components is given below in the text.

cases. The effective anisotropies of the two subspectra have opposite signs, which implies that of the two effective tensor components $\sigma_{22}^{eff(+)}$ and $\sigma_{22}^{eff(-)}$, one of them moves to higher frequency, whereas the other one moves to lower frequency as demonstrated in Figure 4.5.6. This is due to the influence of dipolar interaction between tin and fluorine. The influence of (A,X) dipolar interaction for an AX system is illustrated in Figure 4.5.7(a), which shows that the dipolar powder pattern of spin A consists of the superposition of two subspectra (Pake doublet), labelled as '+' and '−' according to the spin state of nucleus X ($\pm \frac{1}{2}$). Figure 4.5.7(b) presents the powder pattern when the AX system is influenced by both dipolar interaction and shielding anisotropy. It is clear that the anisotropies of the two subspectra have opposite sign, contrary to an AX_2 system.

Some molecular symmetry may be suggested from the X-ray structure of

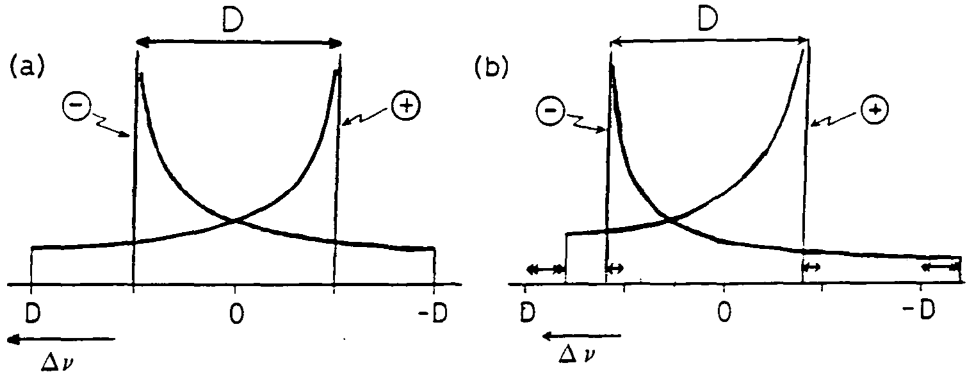

Figure 4.5.7: NMR solid-state powder patterns. (a) For the A spins of an AX system, with (A,X) dipolar interaction alone. (b) For A spins influenced by both (A,X) dipolar interaction and axially symmetric shielding anisotropy. The subspectrum marked with '+' is associated with X spin state of $+\frac{1}{2}$, whereas the subspectrum marked with '−' is associated with X spin state of $-\frac{1}{2}$. The small separations marked by single- and double-headed arrows are $|\nu_0\delta_A/2|$ and $|\nu_0\delta_A|$ respectively. It is assumed that the symmetry axis of the shielding is in the interatomic direction.

Mes$_3$SnF, shown in Figure 4.5.8. The three alkyl groups are equivalent and the tin and fluorine atoms lie in a reflection plane. Such is the case discussed in Zilm and Grant's paper [23]. In the paper, ν_{33} was chosen as perpendicular to the reflection plane and the effect of different ϕ on the A spectrum (ϕ is the angle between ν_{11} and the internuclear axis) was discussed. Figure 4.5.9, quoted from the original paper by Zilm and Grant, shows the powder patterns with respect to angle ϕ. The results obtained for Mes$_3$SnF, Figure 4.5.6, are apparently close to the situation when $\phi = 90°$. This interpretation implies that ν_{22} is along the dipole vector of tin and fluorine, as shown in Figure 4.5.8.

The effective tensor components in Table 4.5.3 may be used to calculate the pseudo-dipolar coupling constant D′, the shielding anisotropy $\beth$ and asymmetry η, though large errors may be expected. The equations given by Harris [24] have

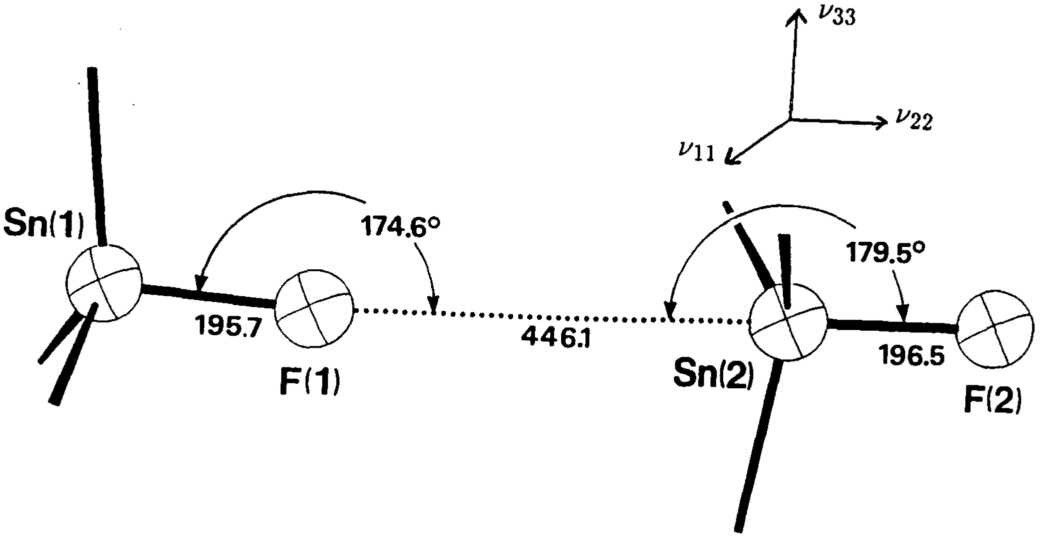

Figure 4.5.8: Crystal structure of tri-mesityl tin fluoride [10].

the form:

$$D' = T_3^+ - T_3^- - J^{iso} = (T_1^- + T_2^-) - (T_1^+ + T_2^+) + 2J^{iso} \tag{4.5.10}$$

$$2\nu_b = (T_1^+ + T_1^- + T_2^+ + T_2^-) \tag{4.5.11}$$

$$2\nu_{33} = T_3^+ + T_3^- \tag{4.5.12}$$

$$\alpha^+ = T_1^+ - T_2^+ \tag{4.5.13}$$

$$\alpha^- = T_1^- - T_2^- \tag{4.5.14}$$

$$(\alpha^+)^2 + (\alpha^-)^2 = 2\nu_a^2 + \frac{9}{2}D'^2 \tag{4.5.15}$$

where

$$\nu_a = \nu_{22} - \nu_{11}$$

$$\nu_b = \nu_{22} + \nu_{11}$$

The $T_{1,2,3}^{\pm}$ refer to the effective tensor components in a resonance frequency convention, so as ν_{11}, ν_{22} and ν_{33} which describe the shielding tensor. Hence the

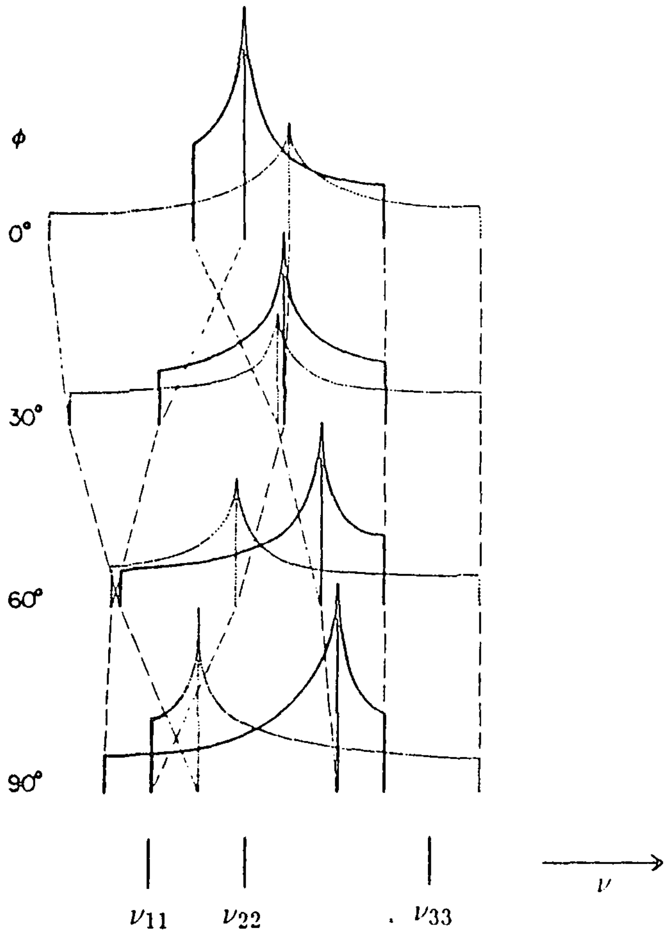

Figure 4.5.9: The effect of ϕ on the A half of an AX spin system. The shielding tensor is given by ν_{11}, ν_{22} and ν_{33}. ν_{33} is along the z axis. When $\phi = 90°$, ν_{22} is along the dipolar vector [23].

values of the $T^{\pm}$ should have opposite signs to those of the corresponding $\sigma^{eff\pm}$, which are defined under a shielding convention, i.e. $T^{\pm} = -\sigma^{eff\pm}$. Also, Equations 4.5.10 to 4.5.15, as stated in references [23,24], are given with the order: $T_1^+ > T_2^+ > T_3^+$ and $T_1^- > T_2^- > T_3^-$. The rearranged values of the subspectra extrema, T^+ and T^-, according to the above discussions, are given in Table 4.5.4. However, it may be worthy of mention here that NMR techniques are unable to determine which of the subspectra corresponds to T^+ and which corresponds to T^-. During the calculations, both possibilities were tried and the assignment of '+' and '−' which produces the more likely results of D$'$ and ν_{ii} was chosen. With the data given in Table 4.5.4 and the Equations of 4.5.10 to 4.5.15, the pseudo-dipolar coupling constant D$'$ and the shielding tensor components ν_{11}, ν_{22} and ν_{33} can be calculated (indicated in Figure 4.5.6). After converting the values to shielding convention, i.e. $\sigma_{11} = -\nu_{11}$, $\sigma_{22} = -\nu_{22}$ and $\sigma_{33} = -\nu_{33}$, the anisotropy $\beth = \sigma_{33} - \sigma^{iso}$ and the asymmetry $\eta = (\sigma_{22} - \sigma_{11})/(\sigma_{33} - \sigma^{iso})$ can immediately be derived. The resulting values of the shielding tensors for both molecules in the asymmetric unit are given in Table 4.5.5.

Table 4.5.4: Effective tensor components for tri-mesityl tin fluoride

δ_{Sn} /ppm	Individual peaks /ppm$^{(a)}$	
−82.0	T_1^+	−7
	T_2^+	−80
	T_3^+	−114
	T_1^-	−44
	T_2^-	−86
	T_3^-	−161
−70.5	T_1^+	−4
	T_2^+	−62
	T_3^+	−99
	T_1^-	−30
	T_2^-	−71
	T_3^-	−156
Estimated error		± 10

(a): Data at 74.63 MHz.

Table 4.5.5: Sn-119 NMR data for trimesityl tin fluoride$^{(a)}$

δ_{Sn} /ppm	D$'$ /kHz	σ_{11} /ppm	σ_{22} /ppm	σ_{33} /ppm	$\beth^{eff}$ /ppm	η	ΔJ /kHz
− 82.0	1.27	27	81	138	56	0.9	− 21
− 70.5	1.97	26	57	128	58	0.5	− 23
(± 0.5)	(± 0.35)	(± 10)	(± 10)	(± 10)	(± 10)	(± 0.2)	(± 1.0)

(a): Data at 74.63 MHz; The values in parentheses are the estimated errors.

The results for D$'$ are 1.27 kHz for the molecule with resonance at $\delta = -82.0$ ppm and 1.97 kHz for the molecule with chemical shift of -70.5 ppm. It is as expected that the values of the pseudo-dipolar constants for the two independent molecules are different, given the fact that their chemical shifts have more than 10 ppm difference. The dipolar distances between tin and fluorine for the two molecules are 1.957 Å and 1.965 Å respectively, giving dipolar constants of -5651 Hz and -5582 Hz. As the two dipolar coupling constants are very close and the attempt to link the resonances with the molecules, i.e. the Sn-F distances, is not satisfactory, it seems reasonable to use their average value, -5617 Hz, to calculate the anisotropies of **J** coupling tensors. The derived results for ΔJ are ca. -21 kHz for $\delta_{Sn} = -82.0$ ppm and ca. -23 kHz for $\delta_{Sn} = -70.5$ ppm. The estimated errors are given in Table 4.5.5.

The calculated ΔJ values for Mes_3SnF are extremely large in magnitude, especially when compared with those for fluorine-bridge triorganyl tin fluorides, which have a magnitude of less than ca. 3 kHz. However, the data still follow the trend according to Figure 4.5.5, which shows that values of ΔJ become more negative as the distance, r_{SnF}, decreases. In fact, the graph shows that when $r_{SnF} = 1.96$ Å, ΔJ for Ph_3SnF is ca. -7.5 kHz. Given the fact that Mes_3SnF is four-coordinated while polymeric Ph_3SnF is pentacoordinated, the ΔJ results for the monomeric Mes_3SnF are reasonable, though undoubtedly substantial errors may exist due to the large errors which occurred during the spinning sideband analysis. Such calculations were not performed for Neo_3SnF because of its lack of spinning sidebands and the existence of the impurities.

4.6 C-13 Study of the triorganyl tin fluorides

The spectra of high-resolution solid state ^{13}C are often characterized by individual isotropic chemical shifts, each of which is assigned to a certain chemically different carbon atom in the unit cell. Hence the study of C-13 as a second nucleus is valuable because it can provide confirmation of the structures obtained from the Sn-119 studies, and even some extra information. Moreover, the coupling constants between ^{13}C and ^{119}Sn may be measured more easily from C-13 spectra than from those of Sn-119. The assignment of the carbon signals and their corresponding data for fluorine-bridged triorganyl tin fluorides are recorded in Table 4.6.1. The spectra discussed in this section are either proton-decoupled CPMAS or NQS (see Chapter 3).

As shown in Fig 4.6.1, the ^{13}C spectrum for Me_3SnF is very well-resolved. The peak at 2.5 ± 0.5 ppm is the isotropic chemical shift of methyl carbon. The two outer peaks are the result of scalar coupling between carbon and tin or fluorine nuclei. However, as fluorine has a natural abundance of 100%, a carbon-fluorine coupling will result in a total doublet splitting, rather than a major peak with a weak doublet, in the carbon spectrum. The natural abundances of ^{119}Sn and ^{117}Sn are 8.6% and 7.6% respectively, and the relative intensity ratio of the doublet and main peak is approximately 14%. Hence the coupling is between the methyl carbons and the tin atoms, with the isotropic value being 520 ± 10 Hz. The single value of the ^{13}C isotropic chemical shift indicates clearly that the three methyl groups are equivalent on an NMR time scale.

N-tributyl tin fluoride has a ^{13}C spectrum consisting of one well-resolved methyl carbon signal at 14.5 ± 0.5 ppm and three methylene resonances at 27.9

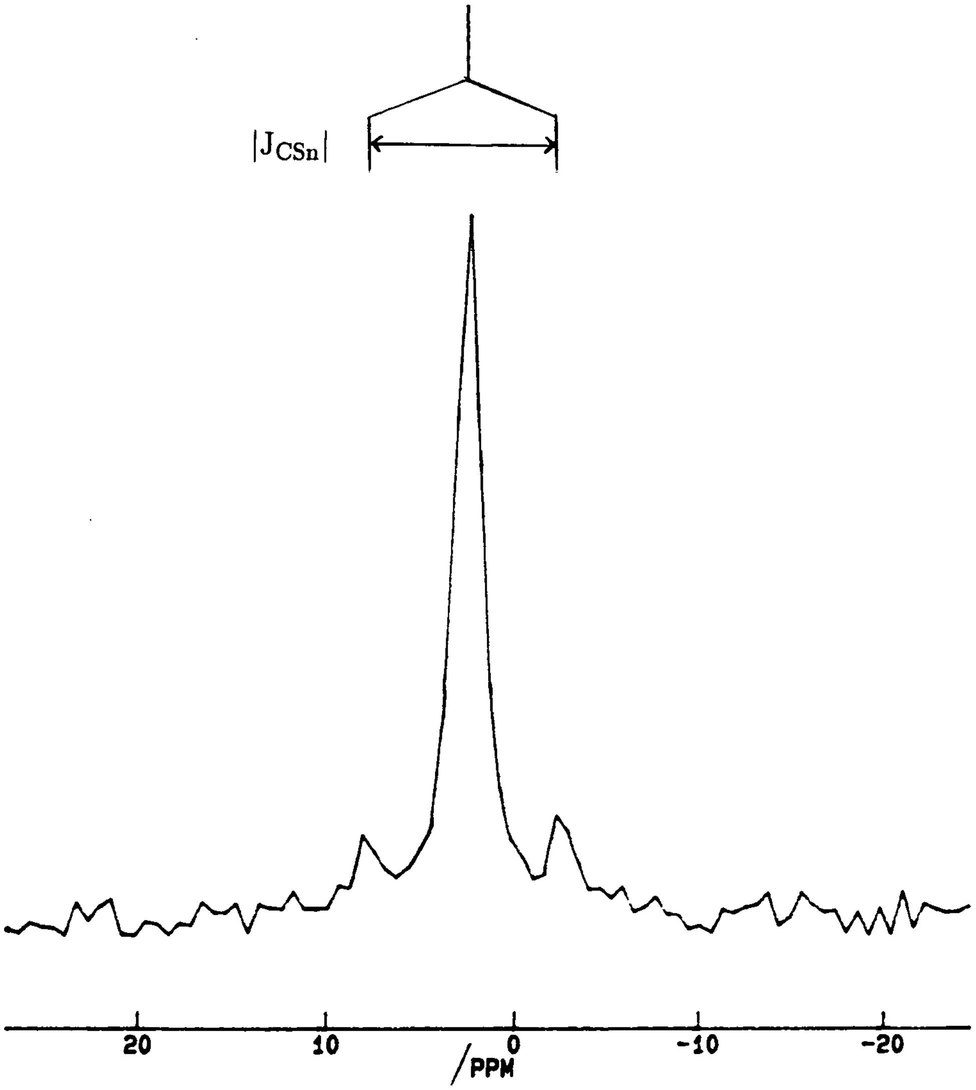

Figure 4.6.1: ^{13}C CPMAS spectrum of Me_3SnF at 50.32 MHz. Spectrometer operating conditions: contact time 10ms; recycle delay 10s; number of transitions 960; spinning speed 2815 Hz.

± 0.5, 28.8 ± 0.5 and 29.9 ± 0.5 ppm respectively. This is illustrated in Figure 4.6.2. The three methylene carbon peaks become clearer after resolution enhancement. The other peaks, marked with *, are considered as impurities, based on their intensities and the obvious impurity signal appearing in the ^{119}Sn spectrum (fig. 4.2.2(b)). Thus, like methyl groups in Me_3SnF, the three n-butyl groups in n-Bu_3SnF are identical.

Table 4.6.1: ^{13}C data for fluorine-bridge R_3SnF

R	δ_{Sn} /ppm	$^1J(Sn,C)$ /Hz	$^3J(Sn,C)$ /Hz	Linewidth /Hz	Assignment
Me	2.5	520	-	110	$^{13}CH_3$–
n-Bu	14.5			20	$^{13}CH_3$–
	27.9	-	-	-	CH_3-CH_2-CH_2-$^{13}CH_2$–Sn
	28.8	-	-	-	CH_3-$^{13}CH_2$-CH_2-CH_2–Sn
	29.9	-	-	-	CH_3-CH_2-$^{13}CH_2$-CH_2–Sn
i-Bu	26.7	-	-	28	–$^{13}CH_2$–
	28.3	-	60	8	$^{13}CH_3$–
	34.1	-	-	90	–^{13}CH–
Ph	129.0	-	-	160	meta
	130.6	-	-	50	para
	136.0	-	-	140	ortho
	142.1	800	-	50	ipso
Estimated error	± 0.5	± 10	± 10	± 20	-

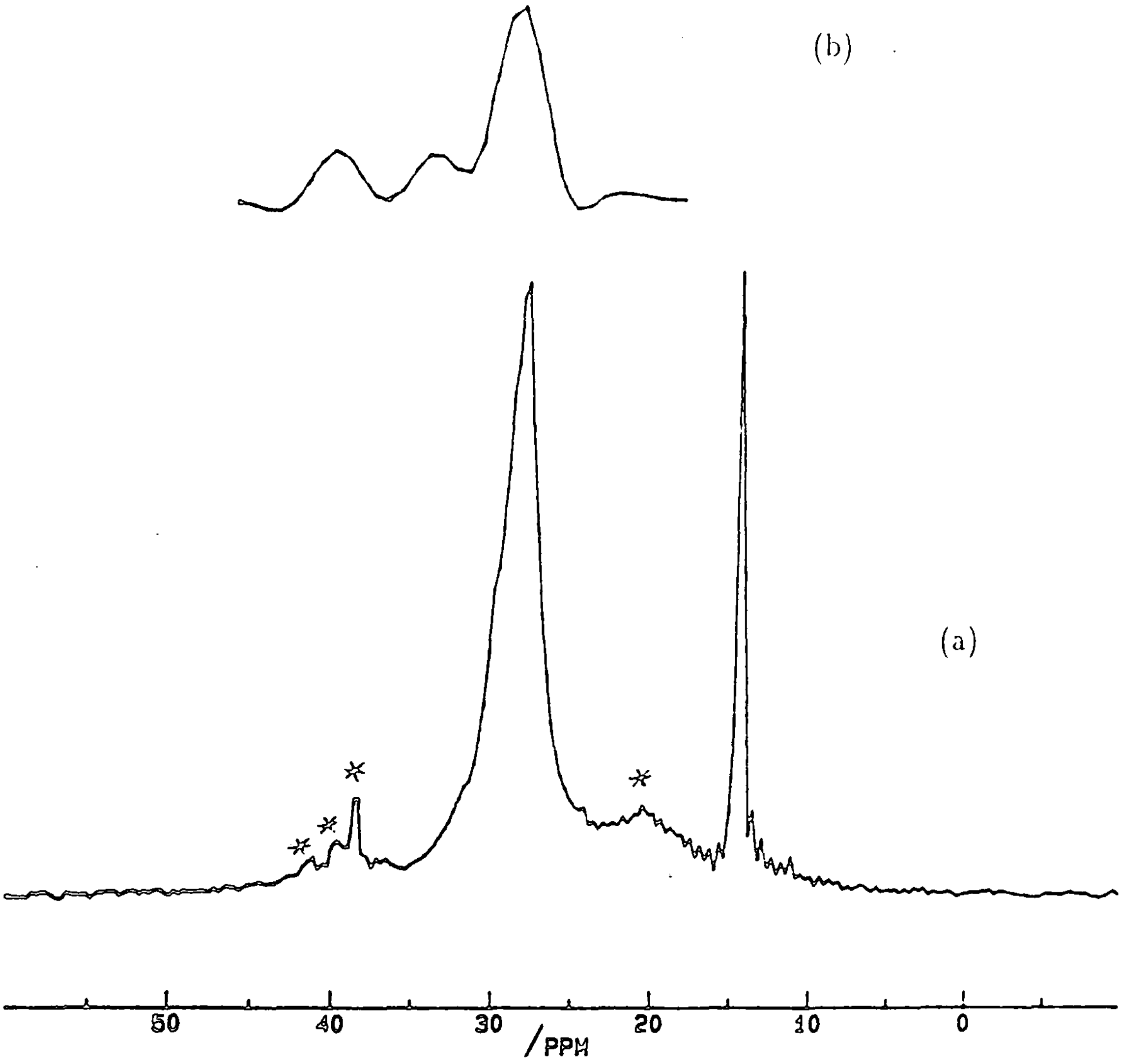

Figure 4.6.2: (a) ^{13}C CPMAS spectrum of n-Bu_3SnF at 50.32 MHz. Spectrometer operating conditions: contact time 1ms; recycle delay 5s; number of transitions 1608; spinning speed 2735 Hz. (b) After resolution enhancement; only part of the spectrum is shown.

The ^{13}C spectrum of i-Bu_3SnF appears unusual, given the two surprisingly broad lines at 26.7 ± 0.5 ppm and 34.1 ± 0.5 ppm respectively, as shown in Figure 4.6.3 (a). Figures 4.6.3 (b)-(d) depict the ^{13}C NQS spectra, which preferentially contain quaternary or methyl carbons, of the same compound. The observed

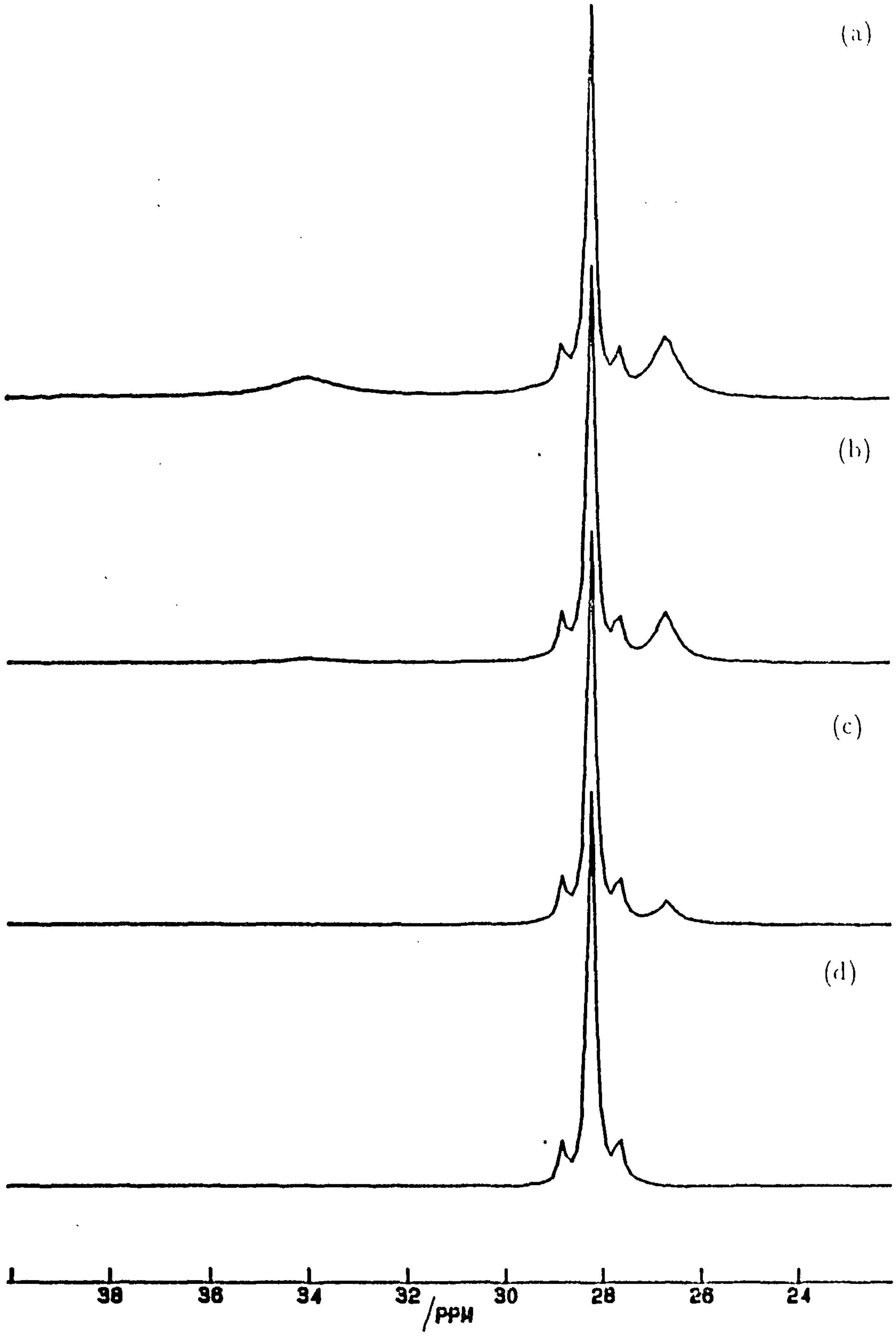

Figure 4.6.3: ^{13}C spectra of i-Bu_3SnF at 50.32 MHz. (a) CPMAS, spectrometer operating conditions: contact time 3ms; recycle delay 3s; number of transitions 330; spinning speed 3300 Hz. (b), (c) and (d) are NQS experiments with decoupling window: 30μs, 50μs and 80μs respectively.

spectra imply that the two broad lines, which disappear gradually in the NQS spectra, are the resonances of methylene and methine carbons. The signal of methyl carbon is at 28.3 ppm with a doublet splitting of ca. 60 Hz. The splitting is a consequence of the three-bond scalar coupling between the methyl carbons and the tin nucleus.

Two possible reasons may result in the linebroadening: (1) strong (F,F) dipolar interaction, which will influence the carbon-fluorine dipolar interaction even under magic-angle spinning [26]; and (2) the existence of molecular motion, which may increase the transverse relaxation (T_2) of the systems, and thus broaden the linewidth [27,28]. As for cause (1), if the average (F,F) distance of fluorine-bridge Me_3SnF, r_{FF} = 4.6 Å, is used for the calculation of the dipolar coupling constant (since it is not available for i-Bu_3SnF), the D_{FF} will be ca. 1.0 kHz. This value is apparantly quite small (MAS spinning speed reaches ca. 3.0 kHz), so cause (1) is unlikely, and thus molecular motion seems likely the reason. Rothwell and Waugh [27] calculated the linewidth of dipolar coupled spin systems as a function of $\omega_1\tau_c$, where ω_1 is the intensity of the radio frequency irradiation for decoupling and τ_c is the correlation time of the dipolar coupling. They found that when $\omega_1\tau_c \approx 1$, i.e. when the time between rotational jumps is comparable to ω_1^{-1}, the resonance lines will be very broad. For compound i-Bu_3SnF, it is believed that the CH_2 and CH groups may undergo some rotational jumping, whose rates may be comparable to the frequency of the coherent motion induced by the proton-decoupling field. Hence, Figure 6.4.3 shows great linewiths of signals which are assigned to the methylene and methine carbons.

Figures 4.6.4 (a) and (b) show the centrebands of ^{13}C NQS and ^{13}C CPMAS spectra of Ph_3SnF respectively. It is apparent that the signal at 142.1 ± 0.5 ppm is the quaternary (ipso) carbon because the peak remains in the NQS spectrum. Since only one quaternary carbon is expected, the two weak signals must be due to the scalar coupling between carbon and tin nuclei, the magnitude of the coupling constant being 800 ± 10 Hz.

It is obvious that line overlappings occur in the ^{13}C CPMAS spectrum, which was thus analyzed by a deconvolution program. It is found that there are two broad lines at 129.0 ± 0.5 and 136.0 ± 0.5 ppm with linewidths of ca. 160 and ca. 140 Hz respectively. These two signals may be assigned to the meta carbons and ortho carbons of the phenyl groups respectively. The lines are unexpectedly broad, suggesting that the aromatic rings may rotate about the axis which connects the para and ipso carbons. This suggestion may receive support from the fact that only meta and ortho resonances are broadened. The reason why molecular motion could cause line broadening has been given earlier. The rotational rates of the aromatic rings may be in the same region as the frequency of the proton-decoupling field. Such motion probably is the cause of the linebroadening for meta and ortho carbons. The line at 130.6 ppm can be assigned as the resonance of the para carbon, given its narrow linewidth and its position in the spectrum.

The above discussion of the ^{13}C spectra clearly shows that the three organyl groups in each of the four compounds are identical on an NMR time scale. This interpretation, together with the linear tin-fluorine-tin chain structures, is consistent with the conclusion that these five-coordinated tin organic compounds are of trigonal bipyramidal conformations.

Figure 4.6.5 is the ^{13}C spectrum of tri-mesityl tin fluoride, with the expanded centrebands above it. Apparently, the two peaks at 128.7 ± 0.5 ppm and 129.6 ± 0.5 ppm are the resonances of meta carbons of the aromatic group. Considering the ^{119}Sn NMR studies, which have revealed that two molecules exist in the asymmetric unit of Mes_3SnF, the two meta carbon signals are probably from the two different molecules. The rest of the spectrum shows some complexity, which is difficult to explain. However, the group of lines between 137 ppm and 147 ppm can be assigned to the quaternary carbons of the phenyl group, while the other lines are assigned to the methyl carbons, since all of these peaks remain in the NQS spectra

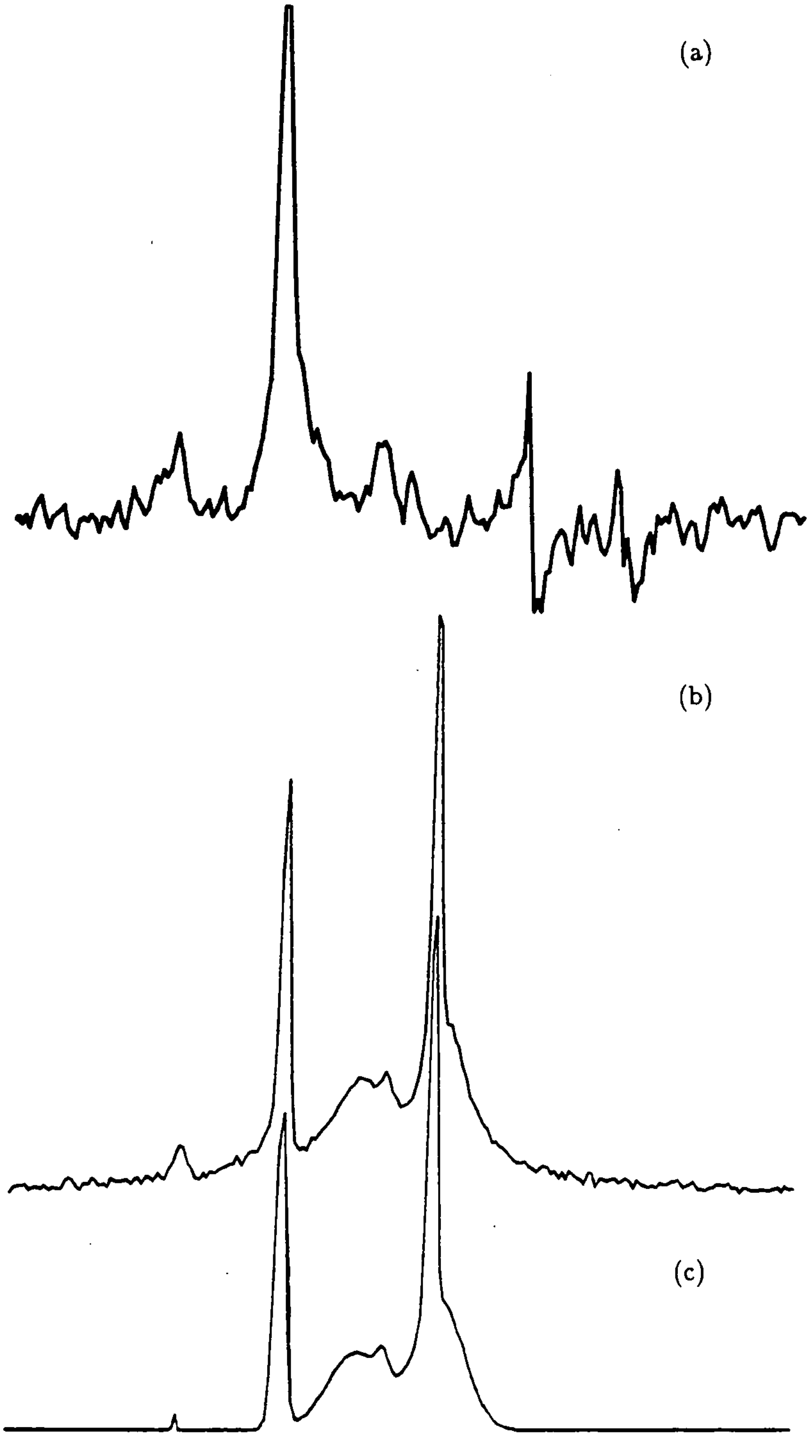

Figure 4.6.4: ^{13}C spectra of Ph_3SnF at 50.32 MHz. (a) NQS (with MAS) spectrum: contact time 5ms, decoupling window 50 μs, recycle time 50s, number of transitions 1110, spinning speed 3500 Hz. (b) CPMAS spectrum: contact time 5ms; recycle delay 50s; number of transitions 1112; spinning speed 3490. (c) Simulated spectrum.

(not shown). Attempts have been made to record the ^{13}C spectrum on a VXR-300 spectrometer, but the spectrum obtained shows no resolution improvement. Also, no scalar coupling constant was found, which should be unchanged in units of Hz at different magnetic fields. In Reuter's paper [10], it is implicit that the 27 carbons in each of the molecules are different. Hence it is understandable that the ^{13}C spectrum is too complicated to fully explain.

The magic-angle CP ^{13}C spectra of tri-neophyl tin fluoride is shown in Figure 4.6.6. The spinning sidebands are due to the aromatic ring carbons. The centrebands indicated by arrows are obtained by varying the rotor spinning speeds. NQS experiments were also carried out to assist in the assignment of the signals, and the resulting spectra (only centrebands) are plotted in Figures 4.6.7 (a)-(d).

The two peaks at 150.7 ± 0.5 ppm and 151.6 ± 0.5 ppm, with relative intensity of approximately 2:1, are the quaternary aromatic carbons. This implies that at least two types of molecule exist in the molecular asymmetric unit, whereas the three neophyl groups of each molecule are the same, to the extent that can be distinguished by NMR. The resonances at 126.5 ± 0.5 ppm and 128.2 ± 0.5 ppm are those of the protonated phenyl carbons: para, meta and ortho; which have strong dipolar couplings with the directly bonded protons. The two lines are relatively broad, arising from the slightly different chemical shifts of the para, meta and ortho carbons of the two molecules.

In the case of the aliphatic carbons, three main signals remain in the NQS spectra. The quaternary carbon line at 38.1 ± 0.5 ppm has almost twice the linewidth as that of the quaternary carbon in the aromatic ring and appears to have a shoulder at the high frequency side. This implies that there are two unresolved peaks present; which is consistent with the fact that two molecules exist as suggested from the aromatic carbon signals. The lines at 28.7 ± 0.5 and 33.3 ± 0.5 ppm are assigned to the methyl carbons of the two molecules respectively. The fact that the resonances of methyl carbons from different molecules are well

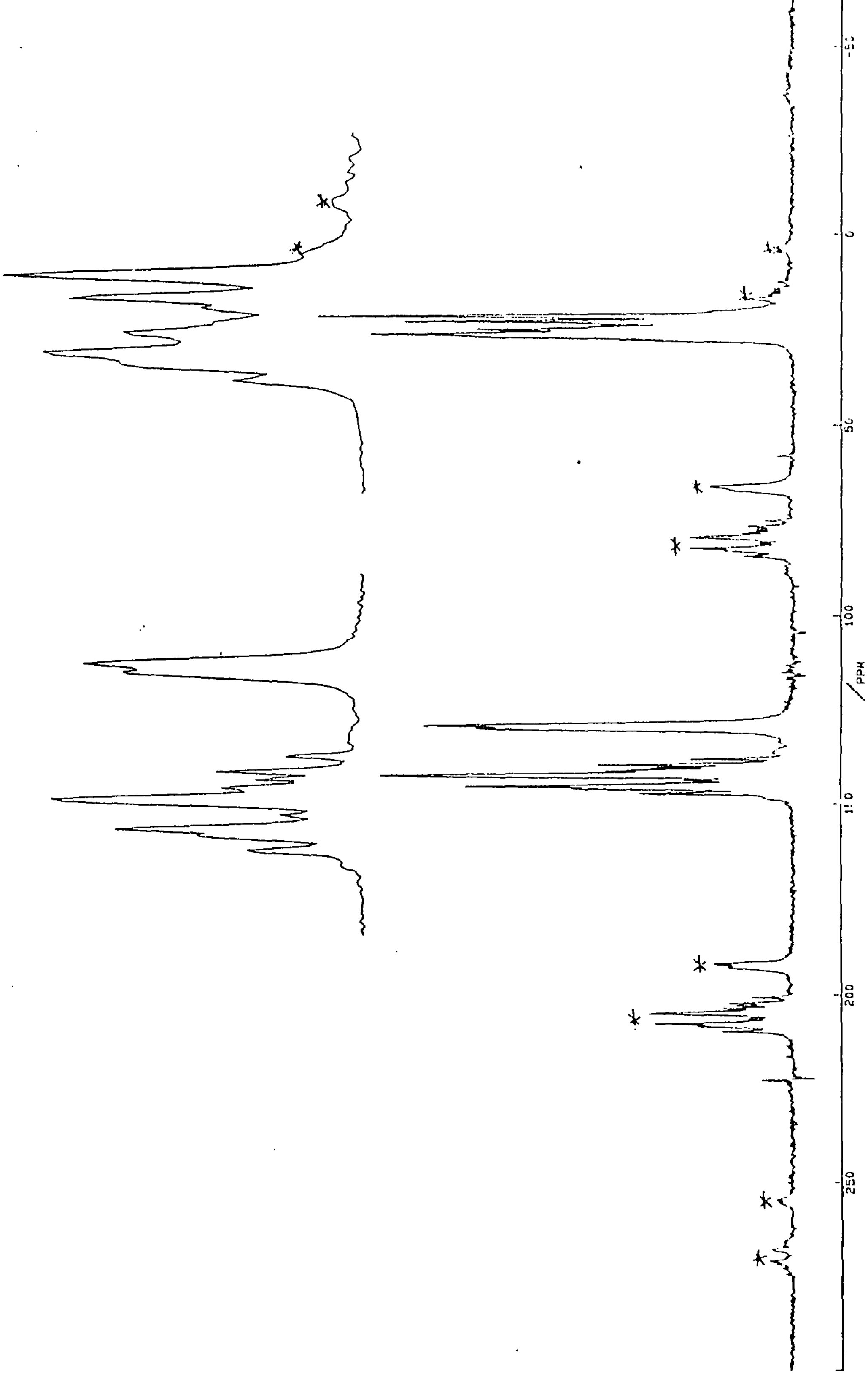

Figure 4.6.5: ^{13}C CPMAS spectrum of tri-mesityl tin fluoride at 50.32 MHz. The centrebands are expanded, and the lines marked with * are spinning sidebands. Spectrometer operating conditions: contact time 3ms; recycle delay 3s; number of transitions 1934; spinning speed 3156.

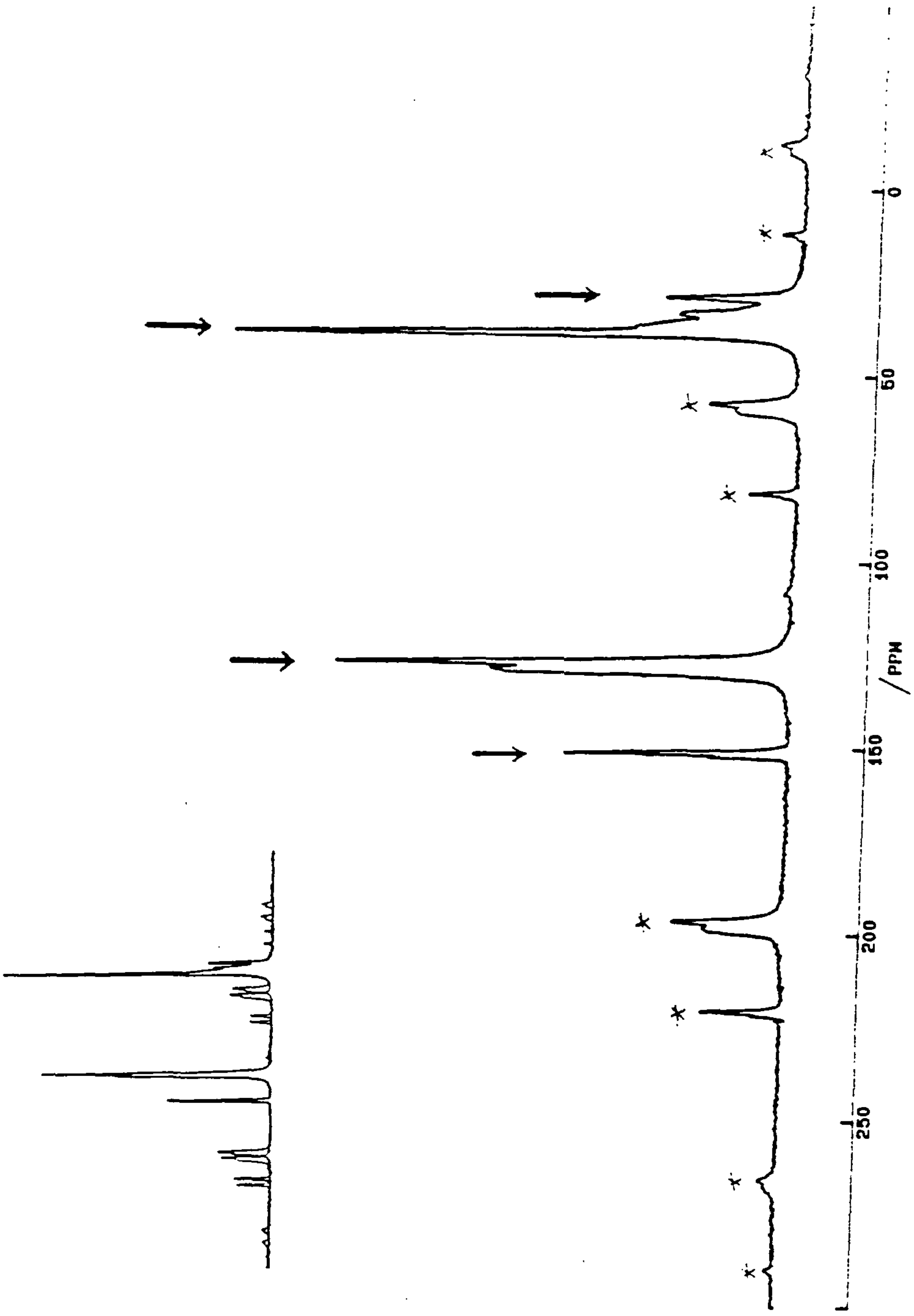

Figure 4.6.6: ^{13}C CPMAS spectrum of tri-neophyl tin fluoride at 50.32 MHz. The centrebands are indicated with arrows, and the peaks marked with $*$ are spinning sidebands. Spectrometer operating conditions: contact time 1ms; recycle delay 1s; number of transitions 3200; spinning speed 3460 Hz. The two spectra on the left corner are those obtained at different spinning speeds. The resonances which are coincident for both spectra are centrebands, whereas the others are spinning sidebands.

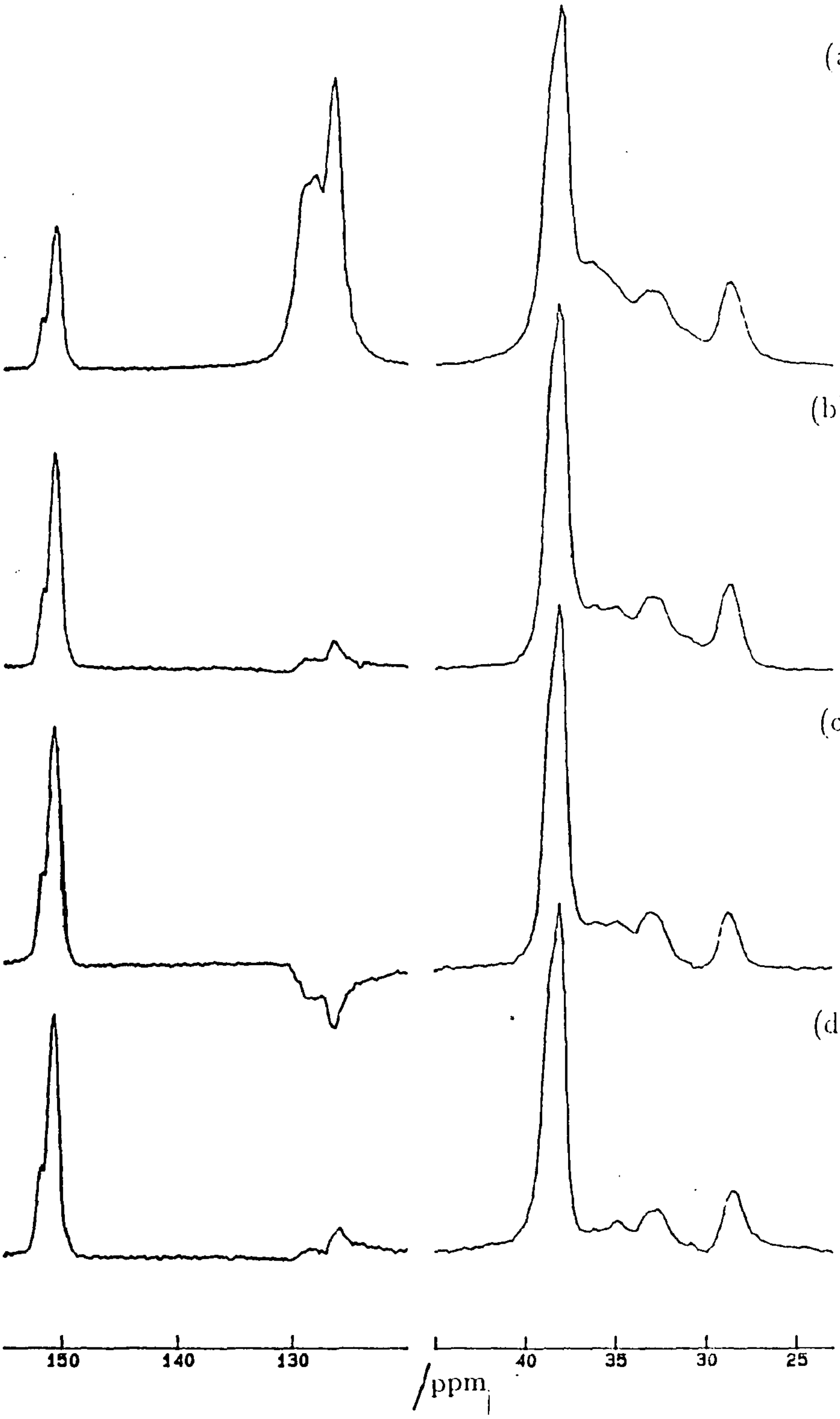

Figure 4.6.7: (a) The centreband of ^{13}C CPMAS spectrum of Figure 4.6.6. (b), (c) and (d): ^{13}C NQS spectra of Neo_3SnF obtained by magic-angle spinning and at 50.32 MHz. Only centrebands are shown. The decoupling windows are 50μs, 70μs and 100μs respectively.

separated indicates that methyl carbons are more sensitive to the differences between the molecules than the other carbons. The two methylene carbon signals, whose intensities gradually decrease, lie at ca. 35.8 ± 0.5 ppm and 36.2 ± 0.5 ppm respectively.

The ^{13}C spectra give the impression that the compound is neat and pure. However, this is contradictary to the ^{119}Sn NMR spectrum (Fig 4.2.4) which demonstrates extra broad lines of uncertain origin. The provider of the compound, Dr. Reuter, mentioned in one of his letters that his recent work on the crystal structure of the neophyl tin fluoride was unsuccessful. It would seem, then, that the purity of the compound is ambiguous.

4.7 ^{1}H Relaxation Measurement and ^{19}F Static Studies

Though relaxation times usually reflect the molecular motions, proton $T_{1\rho}$ is also an important factor in investigations of magnetically dilute spin systems through cross-polarization (see Chapter 2). The CP technique derives the magnetization of the rare spins, i.e. ^{119}Sn or ^{13}C, from the ^{1}H spins, leading to a substantial improvement of the S/N in the spectra of these dilute nuclei. Furthermore, as the magnetization of the rare spins arise entirely from the contact with the protons, the recycle time needed for a good spectrum will be that of protons. The proton spin-lattice relaxation time is, in general, much shorter than that of ^{119}Sn or ^{13}C, so a better spectrum will be obtained in a given period of time. In this section, discussion will focus on the effectiveness of cross-polarization. The results of the $T_1(^{1}H)$ and $T_{1\rho}(^{1}H)$ measurements, obtained by a saturated method on a home-made WRAC spectrometer, for the polymeric Me_3SnF and Ph_3SnF are shown in Table 4.7.1, and the outputs of the ^{1}H relaxation time measurement are presented in Figure 4.7.1 and Figure 4.7.2 respectively. While the relaxation measurements for Me_3SnF were very successful, the measurements for Ph_3SnF were difficult as reflected in the outputs. Long T_1 and short $T_{1\rho}$ of Ph_3SnF are considered to be the cause.

Table 4.7.1: ^{1}H relaxation data

compound	T_1 (^{1}H) / s	$T_{1\rho}$ (^{1}H) / ms
Me_3SnF	25	32
Ph_3SnF	36	11
Estimated error	± 3	± 3

It will be ideal for CP if a system has a relatively long $T_{1\rho}(^1H)$ but relatively short $T_1(^1H)$, though the latter cannot be shorter than the former. Typical contact times during the CP process are in the range of 1-10 ms, so for an effective cross-polarization, $T_{1\rho}(^1H)$ has to be much longer than 10 ms. However, the proton $T_{1\rho}$ of tri-phenyl tin fluoride has the value of only ca. 10 ms. Together with the very long proton T_1 (ca. 36.0 s), it is obvious that the cross-polarization would not be effective at all, unless the cross-polarization rate is very fast (which is unlikely given the distance of protons from the tin). In fact, the ^{119}Sn spectrum of Ph_3SnF (Fig 4.2.3) has much worse resolution than the others, and attempts to observe the spectrum on the CXP-200 proved unsuccessful. Figure 4.2.3 was obtained on the VXR-300.

Tri-methyl tin fluoride has a relatively long $T_{1\rho}(^1H)$ of ca. 32 ms; hence the CP procedure successfully produces the ^{119}Sn spectrum (Fig 4.2.2(a)). The other compounds being studied in this chapter also have relatively favourable proton relaxation times for cross-polarization. It seems unnecessary to discuss them further.

Attempts were made to obtain ^{19}F spectra for these triorganyl tin fluorides, in the hope of gaining structural information about the fluorine nucleus. The typical static spectra for this group of compounds, obtained with single-pulse at 188.3 MHz on the CXP-200 machine, are shown in Figures 4.7.3 (a) and (b). One extremely broad line, with width of ca. 17 kHz, is detected for i-Bu_3SnF, whereas tri-mesityl tin fluoride has a spectrum with linewidth of ca. 20 kHz (apparently

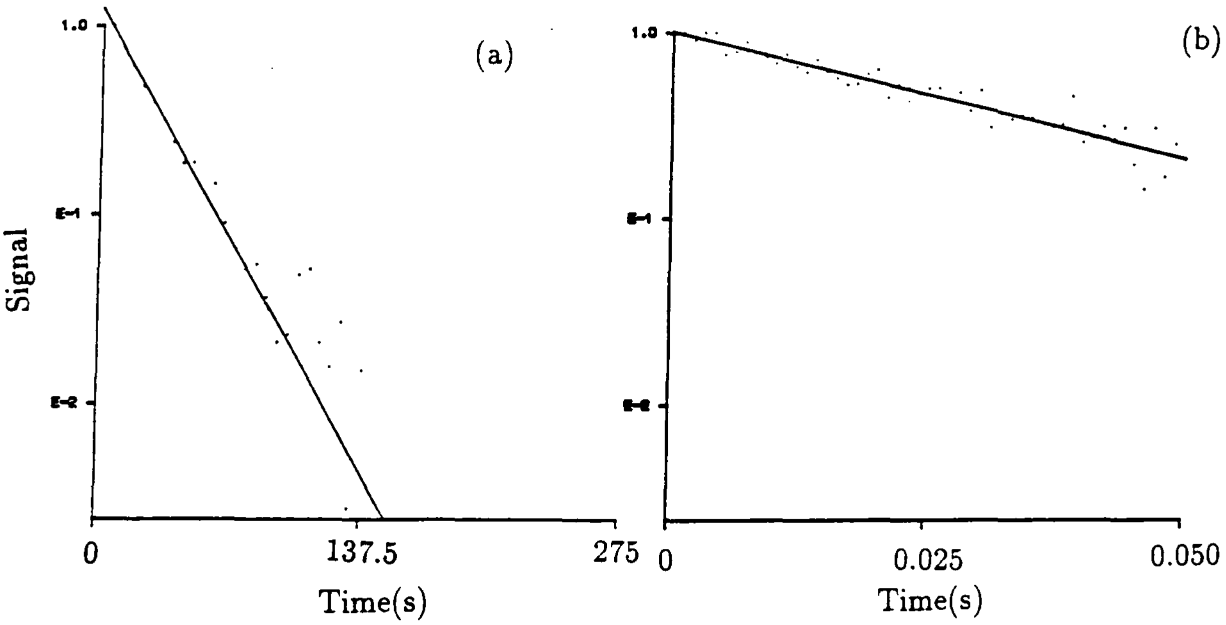

Figure 4.7.1: ^{1}H relaxation time measurement of Me_3SnF at room temperature by a saturated method. (a) T_1 and (b) $T_{1\rho}$. Spectrometer frequency 59.95 MHz; spin lock 40 kHz; number of transitions 4; number of points 50.

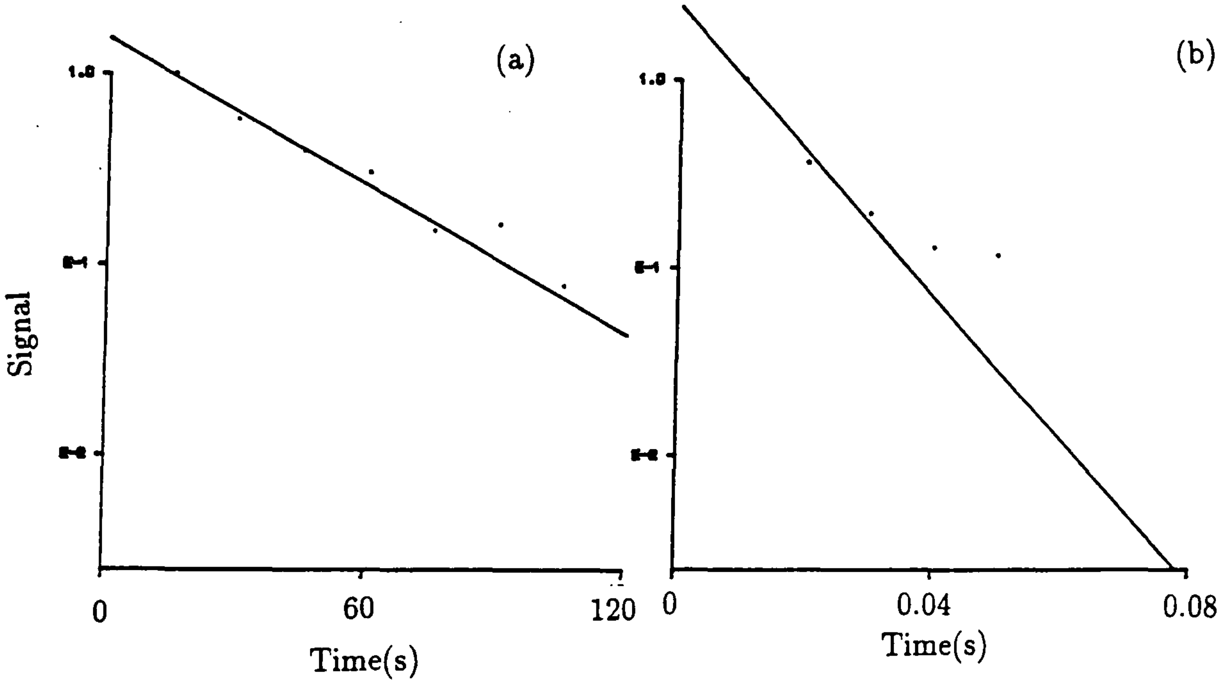

Figure 4.7.2: ^{1}H relaxation time measurement of Ph_3SnF at room temperature by a saturated method. (a) T_1 and (b) $T_{1\rho}$. Spectrometer frequency 59.95 MHz; spin lock 40 kHz; number of transitions 2; number of points 8.

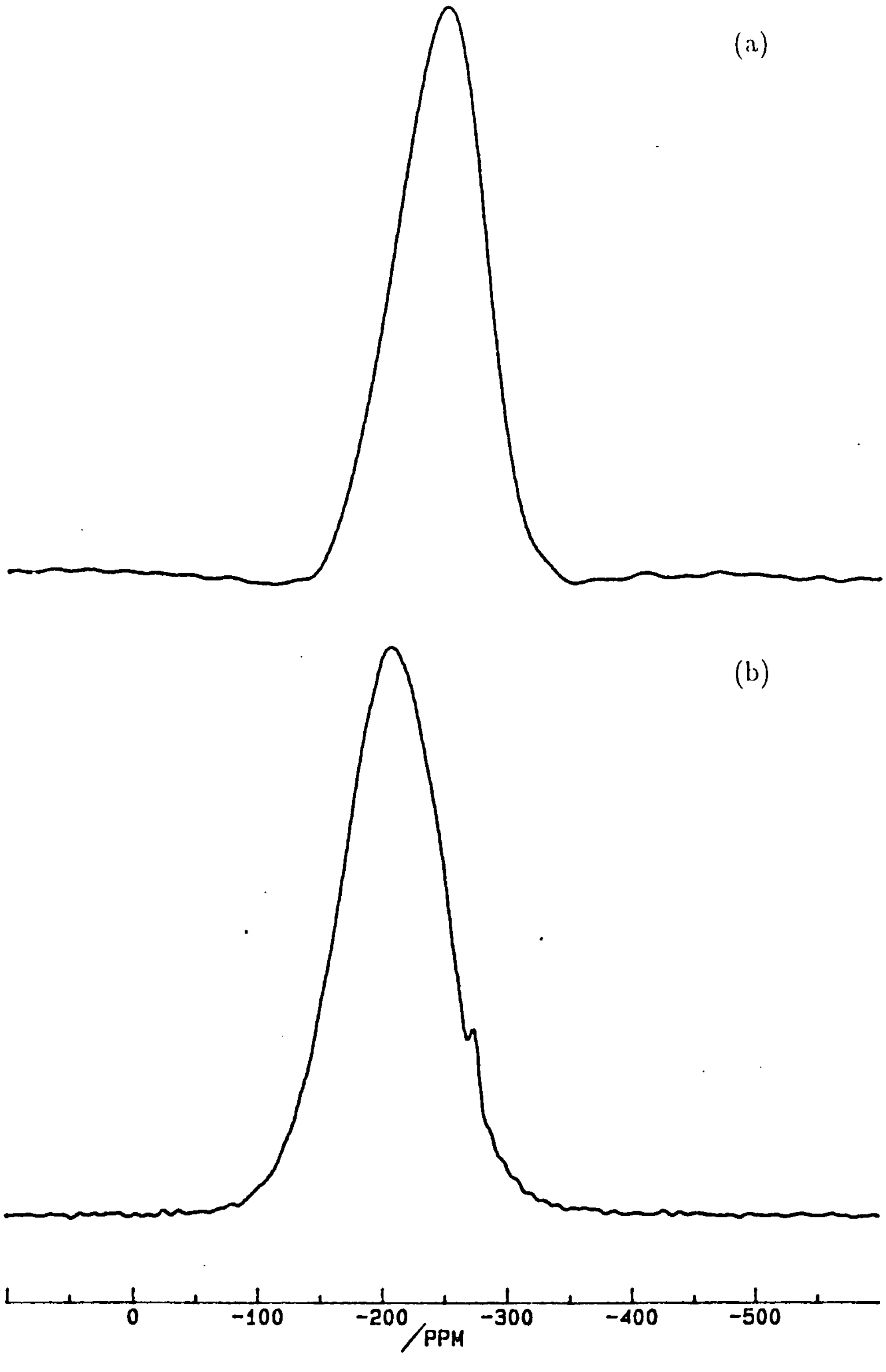

Figure 4.7.3: ^{19}F static spectra obtained by single-pulse and at 188.3 MHz. (a) i-Bu_3SnF and (b) Mes_3SnF. Spectrometer operating conditions: recycle delay 5s (a) and 20s (b); number of transitions 200 (a) and 2810 (b).

with a small shoulder at ca. −272.4 ppm). The line broadening mechnism could be fluorine-proton and/or fluorine-fluorine dipolar interactions, and it is also possible that several lines overlap together to produce a featureless spectrum. Hence little information has been obtained from these static ^{19}F spectra. Experiments with combined magic-angle rotation and multiple-pulse sequences may provide more information, however, such experiments are not feasible for ^{19}F in the Durham laboratory at the moment.

References

1. R.K. Harris, K.J. Packer and P. Reams, *Chem. Phys. Lett.*, **115**, 16 (1985).
2. R.K. Harris, P. Reams and K.J. Packer, *J. Mol. Structure*, **141**, 13 (1986).
3. W. McFarlane and R.J. Wood, *J. Organometal. Chem.*, **40**, C17 (1972).
4. W. McFarlane and R.J. Wood, *Chemical Communications*, 262 (1989).
5. (a) H.C. Clarke, R.J. O'Brien and J. Trotter, *J. Chem. Soc.*, 2332 (1964).
   (b) K. Yasuda, Y. Kawasaki, N. Kasai and T. Tanaka, *Bull. Chem. Soc. Jpn.*, **38** 1216 (1965).
6. H.A. Stöckler and H. Sano, *Phys. Rev.*, **165**, 406 (1968).
7. R.H. Herker and S. Chandra, *J. Chem. Phys.*, **54**, 1847 (1971).
8. Austral. Dept. Stand. Labs. Ann. Rept., 37 (1967/8).
9. H. Reuter, *Ph.D. Thesis*, Univ. Bonn, (1986).
10. H. Reuter and H. Puff, *J. Organomet. Chem.*, **379**, 223 (1989).

11. A.G. Davies, P.G. Harrison, J.D. Kennedy, R.J. Puddephatt, T.N. Mitchell and W. McFarlane, *J. Chem. Soc.*, **A**, 1136 (1969).

12. W. McFarlane, J.C. Maine and M. Delmas, *J. C. S. Dalton*, 1862 (1972).

13. P.J. Smith and A. D. Tupciauskas, *Annual Reports on NMR Spectroscopy*, Vol. **8**, 311 (1978).

14. R.K. Harris and B.E. Mann, *NMR and the Periodic Table*, p345.

15. C.J. Jameson and H.S. Gutowsky, *J. Chem. Phys.*, **40**, 1714 (1964).

16. R.W. Taft Jr., *Steric Effects in Organic Chemistry*, M.S. Newman (ed.) Wiley, (1956).

17. J.M. Angelelli, J.C. Maire and Y. Vignollent, *Annales Fac. Sci. Marseille*, **43 A**, 47 (1970).

18. M.J. Mays and S.M. Pearsom, *J. Chem. Soc. A.*, 136 (1969).

19. J.A. Pople and D.P. Santry, *Molecular Phys.*, **8**, 1 (1964).

20. S. S. Danyluk, *J. Amer. Chem. Soc.*, **86**, 4504 (1964).

21. M.M. Maricq and J.S. Waugh, *J. Chem. Phys.*, **70**, 3300 (1979).

22. J. Herzfeld and A.E. Berger, *J. Chem. Phys.*, **73**, 6021 (1980).

23. K.W. Zilm and D.M. Grant, *J. Amer. Chem. Soc.*, **103**, 2913 (1981).

24. R.K. Harris, J. Packer, A.M. Thayer, *J. Magn. Reson.*, **62**, 284 (1985).

25. P. Reams, *Ph.D. Thesis*, Univ. of Durham (1986).

26. R.K. Harris, *Nuclear Magnetic Resonance Spectroscopy*, Longman Scientific & Technical (1986).

27. W.P. Rothwell and J.S. Waugh, *J. Chem. Phys.*, **74**, No.5, 2721 (1981).

28. J.R. Lyerla, C.S. Yannoni and C.A. Fyfe *Acc. Chem. Res.*, **15**, 208 (1982).

Chapter V

Tin-chlorine coupling in Sn-119 solid-state NMR spectra

5.1 Introduction

In solid-state NMR, magic-angle spinning sufficiently eliminates dipolar broadening, provided both spins are quantised along the magnetic field. However, if one of the spins is a quadrupole-moment-bearing nucleus ($S > \frac{1}{2}$), and the quadrupolar interaction is not negligible compared to the Zeeman interaction, MAS fails to completely remove the dipolar coupling (see Chapter 2). This is because a quadrupolar nucleus, subjected to both quadrupole and Zeeman interactions, is not quantized along the magnetic field. The residual dipolar coupling thus will have effects in the spin-$\frac{1}{2}$ NMR spectra. This phenomenon was first observed for the ^{13}C–^{14}N pair of nuclei [1–3], where an asymmetric doublet was found for carbons coupled to nitrogen nuclei in the presence of magic angle sample spinning. Since then most discussions of such quadrupolar effects have been concentrated on ^{13}C–^{14}N cases [4–15], however, similar effects among other pairs of nuclei such as ^{31}P–^{63}Cu, ^{31}P–$^{35/37}$Cl and ^{119}Sn–$^{35/37}$Cl also have been found [16–18], though very rarely.

Considerable attention has been given to the theoretical calculations of this quadrupolar effect. The problem has been generally solved by computer diagonalization of the full Hamiltonian of the quadrupole spin, followed by calculation of the dipolar interaction using a first-order treatment. It has been found that the line shapes of such spin-$\frac{1}{2}$ NMR spectra are associated with: (1) the magnitude and sign of the quadrupolar coupling constant; (2) the asymmetry of the electric field gradient (EFG) at the quadrupole nucleus; (3) the internuclear distance; (4)

the magnitude of the applied magnetic field; (5) the orientation of the internuclear vector in the principal axis frame of the EFG.

However, it has recently been shown that the major features of residual dipolar splittings may be reproduced by a relatively simple first-order perturbation theory addressed by A.C. Olivieri et al. and R.K. Harris [13,18]. J.G.Hexem and co-workers also used a perturbation approach to calculate a specific case [10].

Olivieri and co-authors studied the ^{13}C–^{14}N cases in which asymmetric splittings are induced in the ^{13}C signals by neighbouring ^{14}N (S=1) nuclei. They found that valuable structural information, regarding the quadrupole tensor at the ^{14}N nucleus and carbon-nitrogen distances, is contained in ^{13}C CPMAS spectra as unaveraged splittings. An equation, which correlates the values of the splittings with molecular structural factors, was then established.

A similar approach has been adopted by Harris to investigate the spectrum of ^{119}Sn bonded to chlorine, where second-order effects arising from residual dipolar coupling to ^{35}Cl and ^{37}Cl are apparent. In the paper, the influence of indirect (Sn,Cl) coupling was also included. A simple diagram was given, which described the appearance of a spin-$\frac{1}{2}$ spectrum influenced by a spin-$\frac{3}{2}$ nucleus. The appearance of the spectrum changes as the magnitude of the quadrupolar coupling constant χ increases.

This chapter will give new examples of the phenomenon and extend the perturbation approach to cases where more than one chlorine nucleus is coupled to tin. The discussion includes the comparison of the simulated powder patterns with the experimental ^{119}Sn spectra. Structural information such as the chemical shifts, the isotropic values and the anisotropies of the scalar coupling constant are extracted from the spectra, provided the (Sn, Cl) distance is known. All the samples are studied at two different magnetic fields, since the spectra are influenced by the magnitude of the field. Section 2 will discuss the samples of (acac)$_2$SnCl$_2$ and

$(bzac)_2SnCl_2$, where evidence of the quadrupolar effects is obvious. The results of this work have been published in *Molecular Physics*, Volume 68, No.6, 1277–1286 (1989). Sections 3 and 4 deal with a series of R_2SnCl_6 compounds. It will be seen that the quadrupolar effects are not observed for this group of materials, though the (Sn,Cl) scalar couplings are present. Low temperature experiments were carried out for compound $(Bu_4N)_2SnCl_6$, because fast anion motion is believed to exist in this sample. All the chemical shifts are referenced to Me_4Sn throughout this chapter.

5.2 The chlorine quadrupolar effects in the ^{119}Sn spectra of $(acac)_2SnCl_2$ and $(bzac)_2SnCl_2$

5.2.1 Introduction

Detailed theoretical calculations of the dipolar interaction between spins S ($S = \frac{3}{2}$) and I ($I = \frac{1}{2}$), influenced by the quadrupole interaction of the S nucleus, were described in Chapter 2 using a first-order perturbation approach. The main results of the calculations will be discussed in this section. Under the assumption that both direct and indirect dipolar interactions are present, and the quadrupolar coupling for the S spin is relatively strong but not too great compared with the Zeeman interaction, the resonance frequencies of the I nucleus in an I-S spin system can be expressed as:

$$\nu_m = -m\mathrm{J}^{iso} + \frac{9\mathrm{D}'\chi}{4\nu_s}(\frac{5}{4} - m^2)\sin^2\theta\cos^2\theta \qquad (5.2.1)$$

where

m defines the four spin states of the S nucleus;

$\mathrm{D}' = \mathrm{D} - \Delta\mathrm{J}/3$, the pseudo-dipolar coupling constant (Hz);

$\mathrm{D} = \frac{\mu_0}{4\pi}\gamma_I\gamma_S\hbar\frac{1}{r^3}$, the dipolar coupling constant (Hz);

χ is the quadrupolar coupling constant (Hz);

ν_s denotes to the resonance frequency of the S spin (Hz);

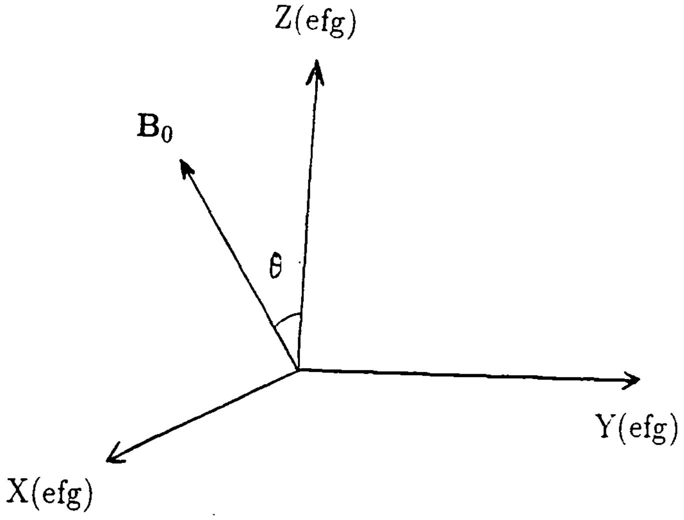

Figure 5.2.1: Orientation of the external field $\mathbf{B}_0$ in the principal axis system of electric field gradient (EFG) at the quadrupolar nucleus.

θ is the angle between the external field $\mathbf{B}_0$ and the z-direction of the principal axis system of the quadrupole tensor (see Fig 5.2.1).

It should be noticed that this equation is only valid, provided that both the quadrupole coupling tensor and the scalar coupling tensor are axially symmetric, with their unique axes coincident with the internuclear vector. It is apparent that the first term of Equation 5.2.1 is due to the isotropic scalar coupling whereas the second term is contributed by the second-order effect, which is caused by the dipolar interaction to a quadrupole nucleus S. The centres of gravity of these resonance bands will be found by performing a powder average:

$$\frac{\int_0^{2\pi}\int_0^{\pi}\nu_m \sin\theta d\theta d\phi}{\int_0^{2\pi}\int_0^{\pi}\sin\theta d\theta d\phi} \qquad (5.2.2)$$

The result is the isotropic value:

$$\bar{\nu}_m = -mJ^{iso} + \frac{3D'\chi}{10\nu_s}(\frac{5}{4} - m^2) \qquad (5.2.3)$$

It is clear that the dipolar frequency shifts depend on $(\frac{5}{4} - m^2)$, which gives values of $+1$ and -1 for spin states $m = \pm\frac{1}{2}$ and $m = \pm\frac{3}{2}$ respectively. The magnitude of these shifts is therefore the same for all four lines but the directions are opposite for the outer and inner lines, as depicted in Figure 5.2.2. It can also be seen that the appearance of the spectrum is independent of the sign of J^{iso}, but depends on the signs of D', χ and ν_s. When the value of $\frac{D'\chi}{\nu_s}$ is positive, the outer lines ($m = \pm\frac{3}{2}$) will move towards lower frequencies and the inner ones ($m = \pm\frac{1}{2}$) towards higher frequencies and vice versa. Hence the sign of the second-order shift Δ may be readily obtained from the spectrum. The magnitude of J^{iso} can be obtained from the spacing of the two central lines (when the magnitude of the second-order shift is smaller than $\frac{1}{2}|J^{iso}|$), which is invariant to the applied magnetic field. The chemical shift may be derived from the average position of all four lines.

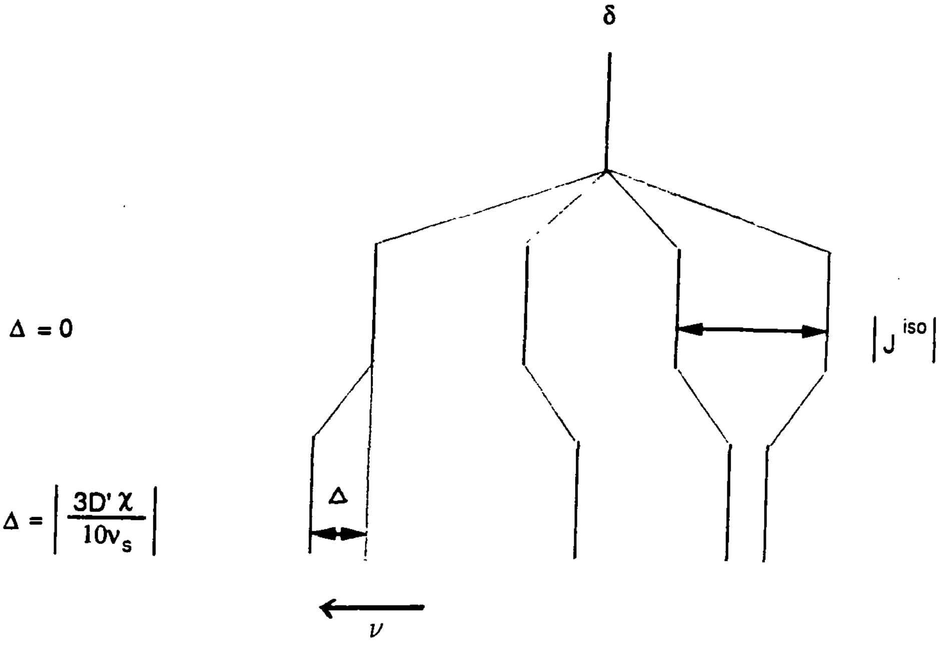

Figure 5.2.2: Schematic diagram of the NMR spectrum of a spin-$\frac{1}{2}$ nucleus I affected by a quadrupolar nucleus S. The shift $\Delta = \frac{3D\chi}{10\nu_s}$ is drawn as negative.

If the anisotropic term ΔJ is neglected in Equation 5.2.3, the sign of the dipolar shift ($\Delta = \frac{3D\chi}{10\nu_s}$) will be only governed by γ_I and χ; since γ_s occurs in both D and ν_s it cannot affect the sign of the shift. Therefore, when the sign of shift Δ is determined from the appearance of the spectrum, the sign of χ may be be immediately obtained (since the sign of γ_I is always known), which is usually unobtainable from NQR spectroscopy. Furthermore, if the distance between the two nuclei is known, the absolute value of the quadrupolar coupling constant χ may be derived. Its magnitude then can be compared with the value given by NQR study, if known.

However, in many cases the effects of ΔJ should be taken into account. If the value of ΔJ is such that D′ and D have opposite signs, then the sign of the shift Δ will be changed. The direction of the shift ($\Delta = \frac{3D'\chi}{10\nu_s}$) will depend on the relative signs of D′, χ and ν_s. In the Sn–Cl cases, Δ is negative if (a) D′ and D have the same sign and χ is positive, or (b) D′ and D have opposite sign and χ is negative. The magnitudes of quadrupolar coupling constants can usually be obtained independently from NQR spectra, but their signs are often not obtainable. However, it is generally believed [19] that the values for single-bonded chlorines are negative. Thus when χ is known and both sign and magnitude of the second-order shift are obtained from the spectrum, D′ will be calculated, since the resonance frequency of S nucleus ν_s is known in all relevant cases. Furthermore, if the Sn–Cl interatomic distances can be determined from crystallography, the dipolar coupling constants D may be calculated and hence ΔJ can be derived.

This treatment may be extended to systems where a spin-$\frac{1}{2}$ nucleus is coupled to two or more equivalent spin-$\frac{3}{2}$ nuclei. For an IS_2 system, four asymmetric quartets of lines are calculated as above and then the same pattern is applied for each of the four lines (i.e. the pattern for an IS case is convoluted with itself). The positions of these signals can be written as:

$$\bar{\nu}_{m,n} = -(n+m)J^{iso} + \frac{3D'\chi}{10\nu_s}(\frac{5}{2} - m^2 - n^2) \qquad (5.2.4)$$

This equation shows that if one of the quadrupolar nuclei is in the spin states of $\pm\frac{1}{2}$ and the other in $\pm\frac{3}{2}$ (m = $\pm\frac{1}{2}$, n = $\pm\frac{3}{2}$ or m = $\pm\frac{3}{2}$, n = $\pm\frac{1}{2}$) the resonance frequencies are equal to $\pm J^{iso}$ and $\pm 2J^{iso}$. When the chemical shift δ is considered,

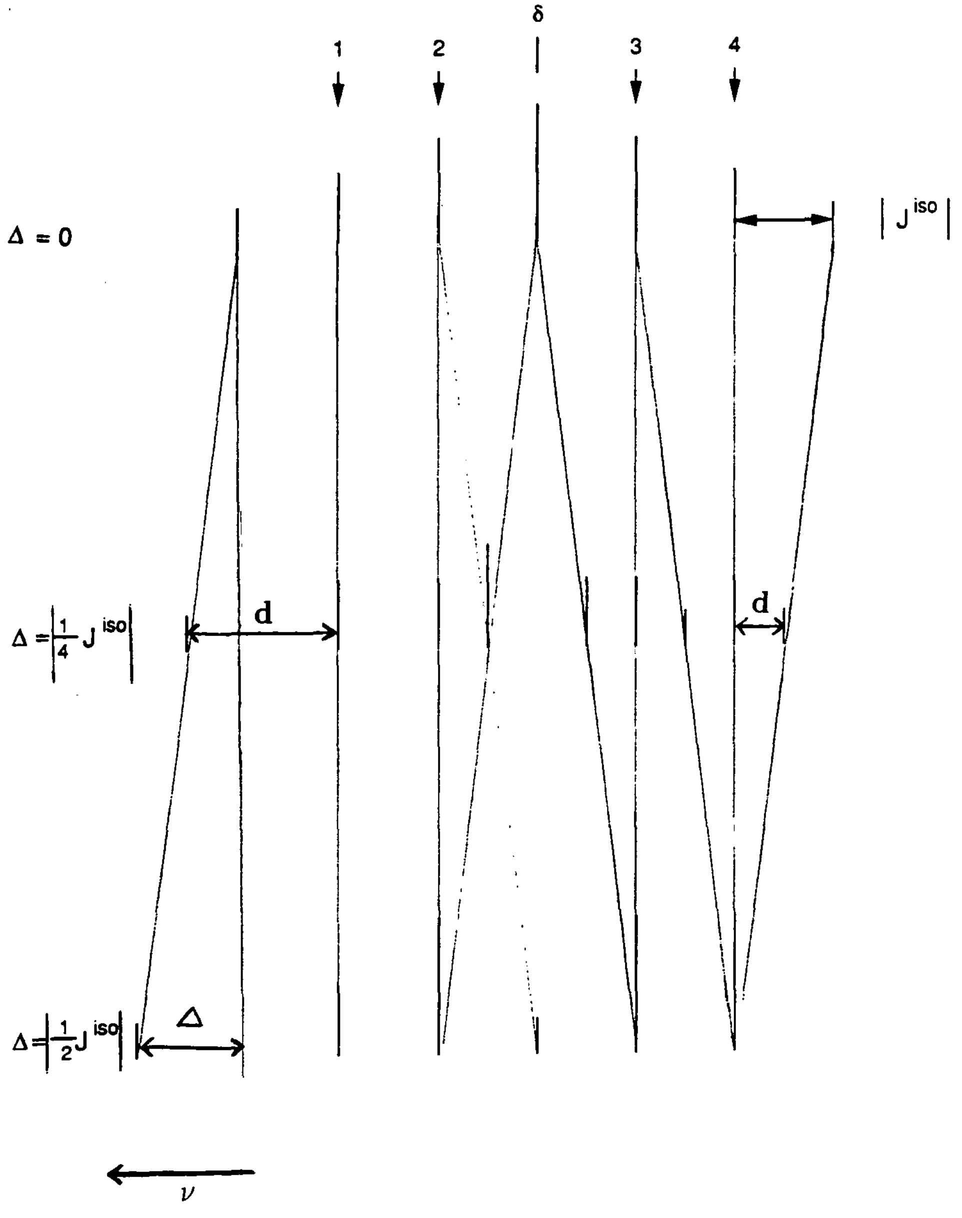

Figure 5.2.3: Schematic diagram of the NMR spectrum of a spin-$\frac{1}{2}$ nucleus I affected by two equivalent quadrupolar nuclei S_2. The shift $\Delta = \frac{3D'\chi}{5\nu_s}$ is drawn as negative.

there should always be lines at $\nu_I\delta \pm J^{iso}$ and $\nu_I\delta \pm 2J^{iso}$. Such lines are most easily recognized by their invariance to the magnetic field of the spectrometer, since scalar coupling is independent of the magnitude of the applied field. Measurement of spectra at two different fields is thus desirable. These four lines are each doubly degenerate and together constitute half the total intensity. The other lines have second-order shifts, whose values equal to $\mp \frac{3D'\chi}{5\nu_s}$ for spin states of $(\pm\frac{3}{2}, \pm\frac{3}{2})$ and $(\pm\frac{1}{2}, \pm\frac{1}{2})$ respectively. Figure 5.2.3 clearly demonstrates the appearance of spectra for an IS_2 system as the magnitude of the shift (Δ) changes from 0 to $\frac{1}{2}|J^{iso}|$.

Once the four constant lines are recognised by multi-field studies, the magnitude of the isotropic coupling constant J^{iso} is immediately known to be the distance between the first and second lines, and also the distance between the third and fourth lines (see Fig 5.2.3). The chemical shift can be determined straightforwardly from the mid-point of the invariant lines. The influence of the signs of D', χ and ν_s on the appearance of the spectrum is the same as that for the IS system. When $|\Delta| < \frac{1}{2}|J^{iso}|$ the frequency shifts can be found from the spectrum by subtracting the measured value of $|J^{iso}|$ from d (the distance between the two highest-frequency lines or the two lowest-frequency lines). These two separations should have the same values, so measurement of them may be used to check whether the system is consistent with the calculation. Once the dipolar shift is measured directly from the spectrum, the parameter $D'\chi$, which is constant for a given molecule, may be calculated. Then a spectrum may be simulated and compared to the experimental result.

5.2.2 Calculation of powder patterns

The resonance frequency described by Equation 5.2.1 is in fact a function of θ, which is the angle between the external field $\mathbf{B}_0$ and the internuclear vector $\mathbf{r}$ (where $\mathbf{r}$, $\mathbf{J}$, χ are colinear). In magic-angle spinning experiments, this angle is time-dependent. Such a time dependence can be introduced explicitly through the following well-known relation:

$$\cos\theta = \cos\theta_m \cos\beta + \sin\theta_m \sin\beta \cos(\omega_r t + \alpha) \tag{5.2.5}$$

where θ_m refers to the magic angle (54.7°); β defines the angle between **r** and the rotation axis; ω_r is the sample spinning frequency; and α is the azimuthal angle of **r** with respect to the rotation axis at time t=0. In the presence of a quadrupole interaction comparable to the Zeeman interaction, the zero-order average-Hamiltonian theory, which is used to include the effects of rotation on the quadrupolar coupling over the period of rotation, is not valid. However, the average dipolar shift over the rotation period can be derived by numerically integrating over the azimuthal angle ($\phi = \omega_r t + \alpha$) for a large number of values in the range of 0° to 360° with constant β, as described in detail by Zumbulyadis et al. [8]. Equation 5.2.1 is then rewritten as:

$$\nu_m(\beta) = \frac{1}{2\pi}\sum_{\phi=0}^{360} \nu_m(\beta,\phi)\Delta\phi \tag{5.2.6}$$

Here, $\nu_m(\beta)$ is the averaged second-order shift of the spinning sample in which the interatomic vector **r** is inclined at an angle β to the MAS axis; $\Delta\phi$ is the value of the increment as ϕ increases from 0° to 360°. However, in a powder sample all values of β are equally probable. Each orientation β gives rise to its own resonance signal in the spectrum. The intensity each orientation contributes to the spectrum is proportional to $\sin\beta$. These theoretical lines are then convoluted with a Gaussian function to give the line shapes which can be compared with the experimental results. Therefore, each 'line' discussed in the previous section is indeed a powder pattern. If each of these line shapes is treated with the same procedure once more, a calculated spectrum for an IS_2 system will be established.

A computer program (for both IS and IS_2 sysytems) using FORTRAN77 based on the above discussion has been written by varying ϕ in steps of 5° between 0° and 360° and varying β in steps of 2° in the range of 0° and 90°. Figure 5.2.4 demonstrates the powder patterns before convolution with a Gaussian function.

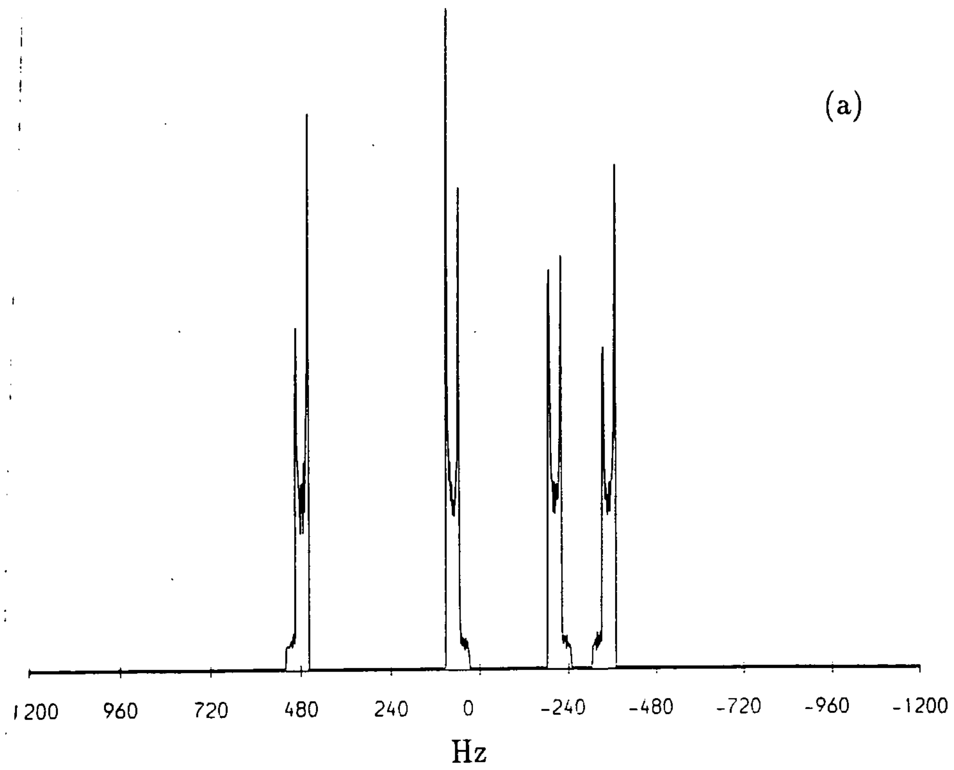

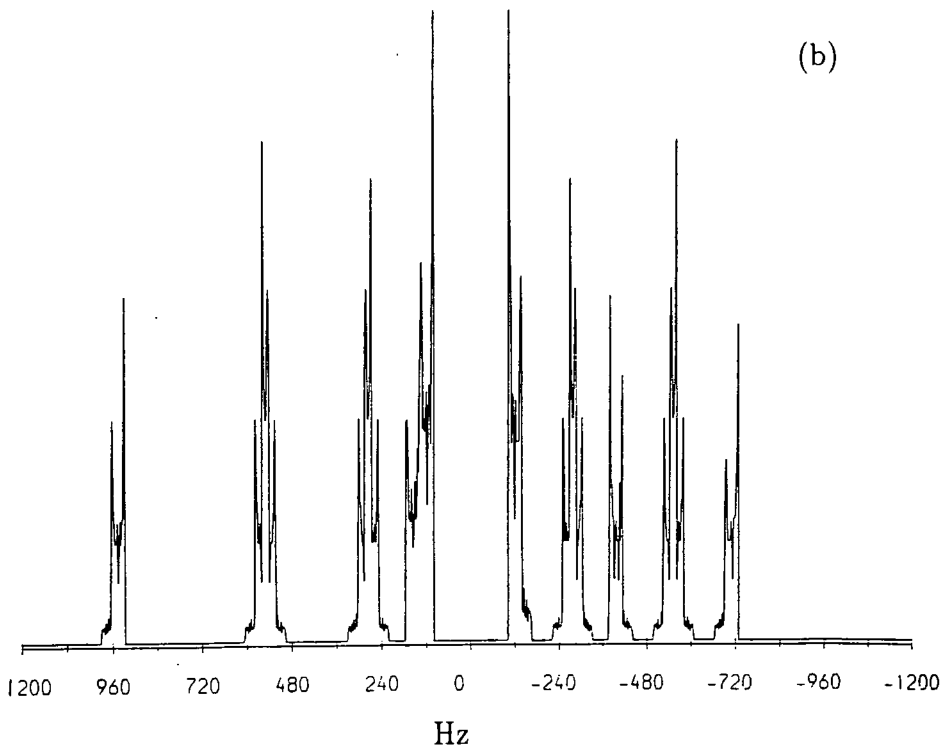

Figure 5.2.4: Powder patterns for a spin-$\frac{1}{2}$ nucleus coupled to (a) one spin-$\frac{3}{2}$ nucleus and (b) two equivalent spin-$\frac{3}{2}$ nuclei, predicted by first-order perturbation theory, with $|J^{iso}| = 240$ Hz and second-order shift $\Delta = 60$ Hz. Gaussian convolutions are not used.

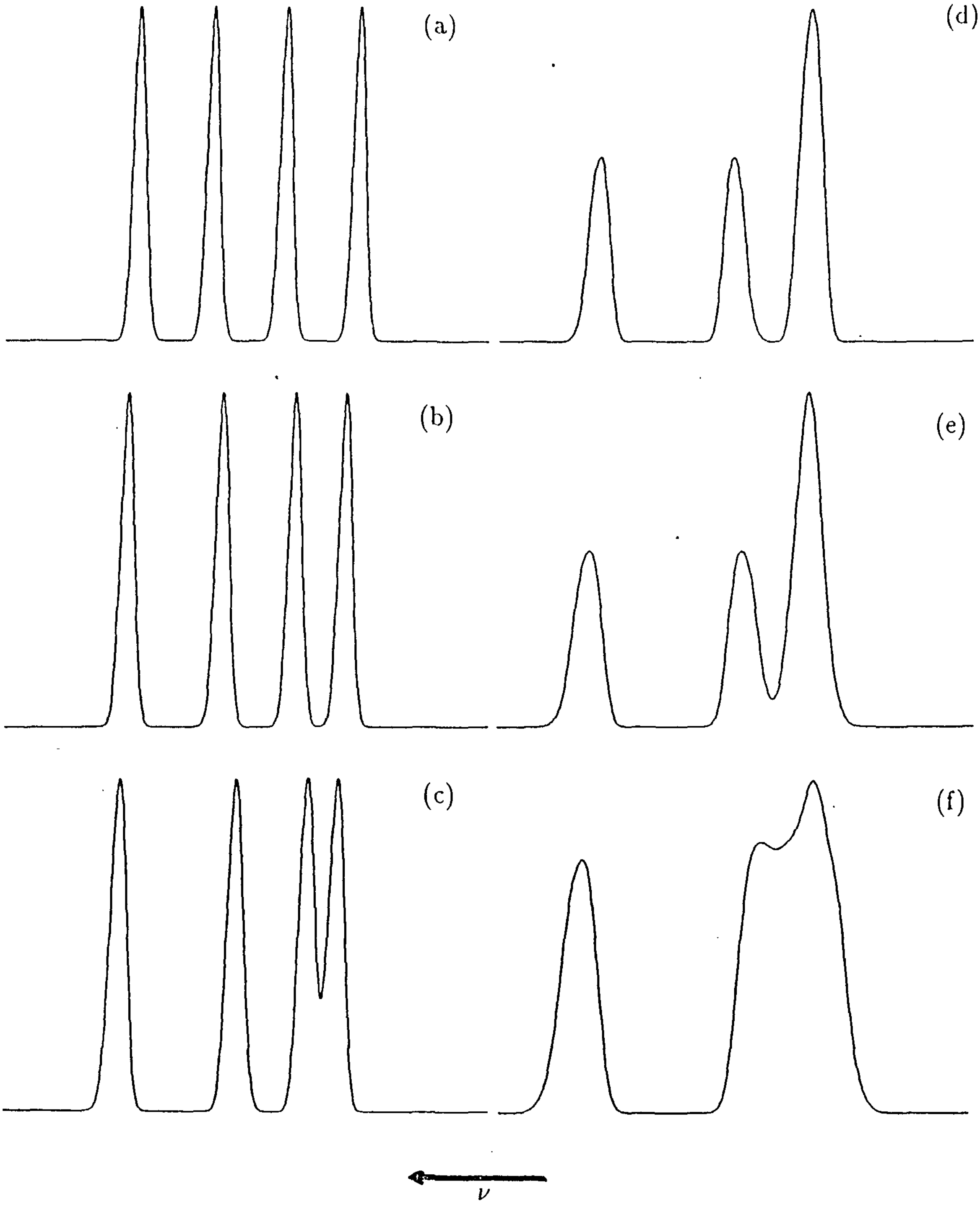

Figure 5.2.5: Powder patterns for an IS system as for Figure 5.2.4(a), but after Gaussian convolution. The calculated spectra are a function of the second-order shift $\Delta = \frac{3D'\chi}{10\nu_s}$ in the unit of $|J^{iso}|$. The magnitudes of the shifts are: (a) 0, (b) $\frac{1}{8}$, (c) $\frac{1}{4}$, (d) $\frac{3}{8}$, (e) $\frac{1}{2}$, (f) $\frac{5}{8}$.

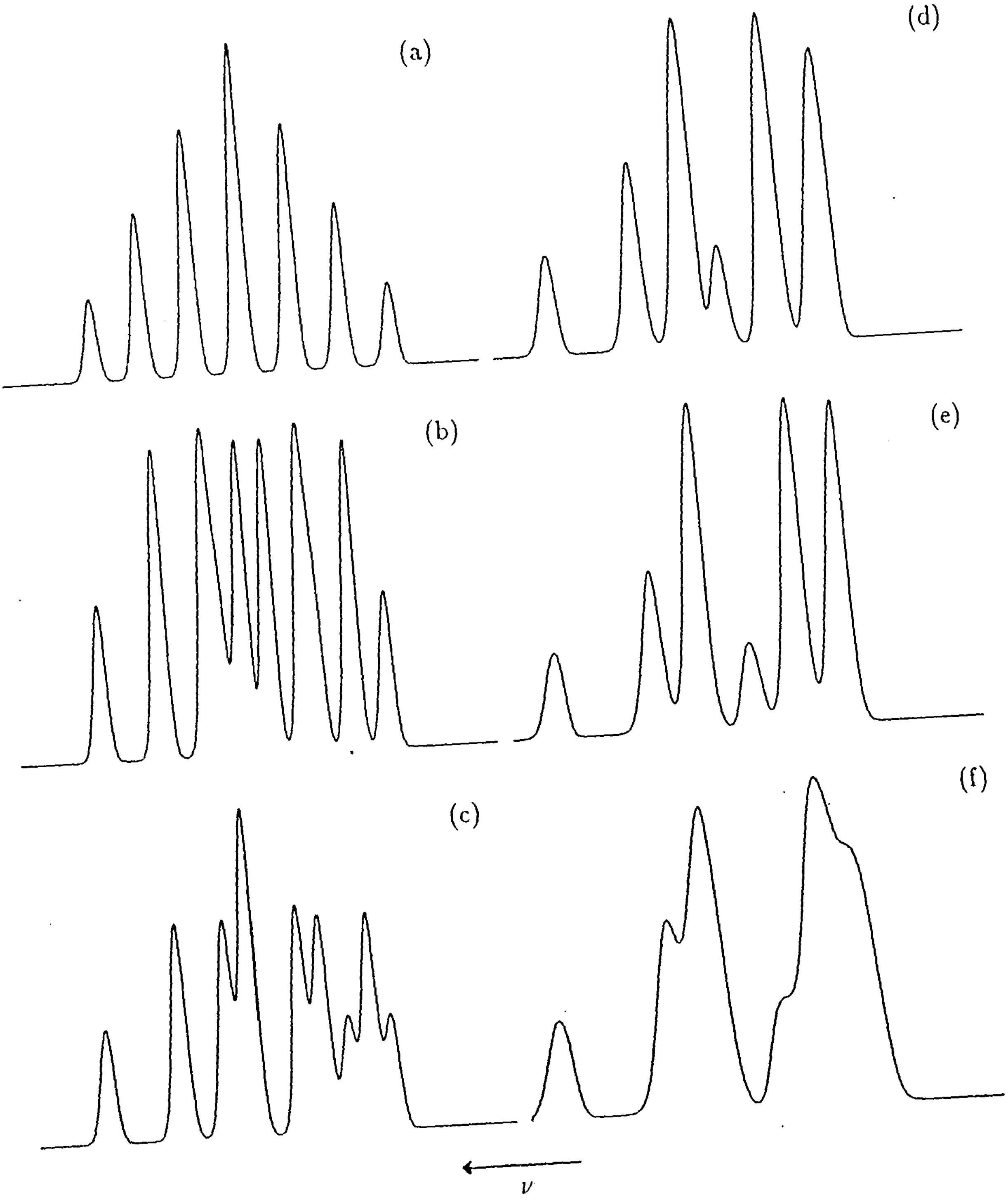

Figure 5.2.6: Powder patterns as for Figure 5.2.5, but for an IS_2 system.

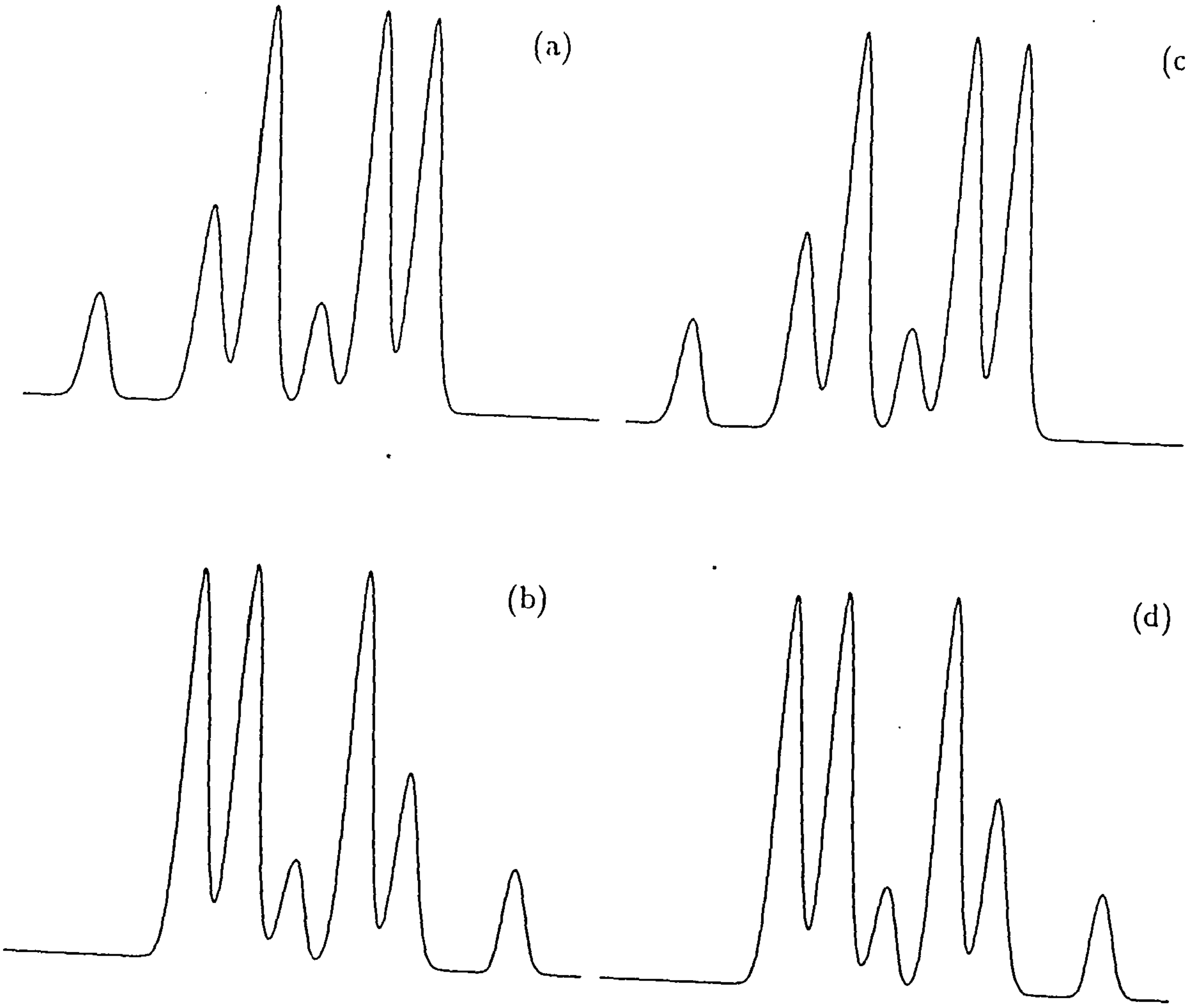

Figure 5.2.7: NMR solid-state powder patterns for an IS_2 spin system, with the second-order shift $|\Delta| = \frac{1}{2}|J^{iso}|$. (a) $D'\chi < 0$ and $J^{iso} > 0$; (b) $D'\chi < 0$ and $J^{iso} < 0$; (c) $D'\chi > 0$ and $J^{iso} < 0$; (d) $D'\chi > 0$ and $J^{iso} > 0$;

The linewidth of each of these lines is governed by the second term of Equation 5.2.1, and thus is equal for all of them. Also, the larger the value of $\frac{D'\chi}{\nu_s}$, the wider each line will be. Figures 5.2.5 and 5.2.6 show the typical calculated powder patterns for IS and IS_2 systems respectively. It is straightforward to interpolate linearly between these various possibilities. These spectra were simulated by varying the value of D' (varying the second-order shift) with constant isotropic J coupling. It is apparant that as the dipolar shift increases the lineshapes get broader. The effect of the signs of J^{iso} and $\frac{D'\chi}{\nu_s}$ on the appearance of the spectra is illustrated in Figure 5.2.7. It can be seen that the sign of $\frac{D'\chi}{\nu_s}$ decides the direction of the shift, but change of sign of isotropic J coupling does not alter the spectrum, confirming that MAS NMR can only determine the sign of $\frac{D'\chi}{\nu_s}$ but not that of J^{iso}.

5.2.3 Results and discussions

The proton-decoupled ^{119}Sn CPMAS spectrum of cis-$(acac)_2SnCl_2$ obtained at 74.63 MHz using a Bruker CXP-200 spectrometer is displayed in Figure 5.2.8. The centreband, indicated in the spectrum and recognised by the first moment method, is expanded in Figure 5.2.10 (a). The splitting pattern is not that expected from simple isotropic indirect coupling of the tin to two equivalent chlorines, which should have a symmetric pattern of a 1: 2: 3: 4: 3: 2: 1 septet. Instead, the spectrum has at least ten resolved or partially resolved lines with an individual linewidth of ca. 60 Hz. Hence, second-order effects may be involved, arising from the quadrupolar nature of the chlorines. This suggestion is confirmed by the spectrum obtained at a different field (111.86 MHz), as shown in Figure 5.2.11 (a) (only the centreband is plotted).

The crystal structure of cis-dichloro-(2,4,pentanedionato)tin, cis-$(acac)_2SnCl_2$, has been studied by X-ray diffraction, and is presented in Figure 5.2.9 [20]. The chloro groups are in *cis* positions in the distorted octahedral coordination of the tin atom. The other four positions are occupied by the oxygen atoms of the two bidentate 2,4-pentanedionate ligands. The molecule is required by the space group,

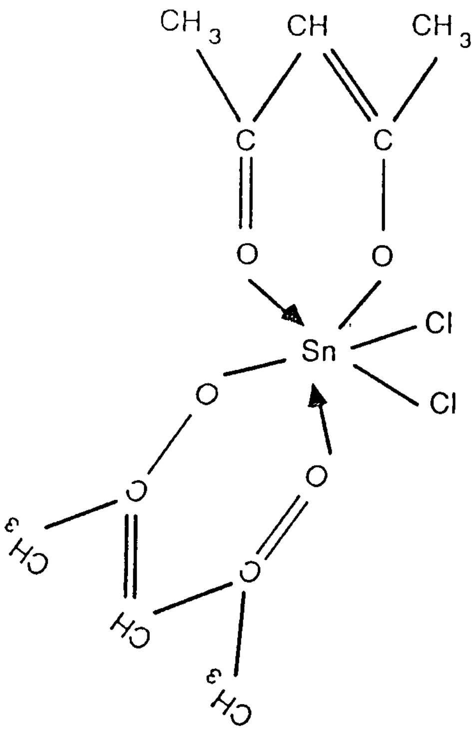

$(acac)_2SnCl_2$

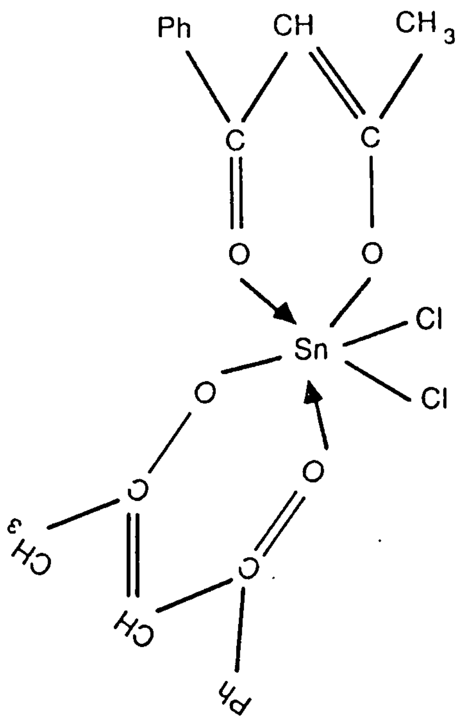

$(bzac)_2SnCl_2$

and the molecular symmetry is D_2. Hence the two acac groups are identical, so as the two chlorine atoms in a given molecule. The ^{13}C NMR spectrum (Figure 5.2.12) demonstrates three narrow lines which are obviously assigned to the three different carbons in the acac groups. This observation is fully consistent with the above described structure, and also shows that there is only one molecule present in the asymmetric unit. Hence, C-13 studies provide further evidence that the complicated patterns in the ^{119}Sn spectra are due to the second-order effect of the chlorine nuclei.

In fact, if one looks closely, the pattern shown in Figure 5.2.10 (a) is not dissimilar from that of Figure 5.2.6 (c), with a second-order shift of $|J^{iso}/4|$. It is found that the four lines which are indicated by arrows in both spectra (Figures 5.2.10(a) and 5.2.11(a)) are invariant to the applied magnetic field. The isotropic

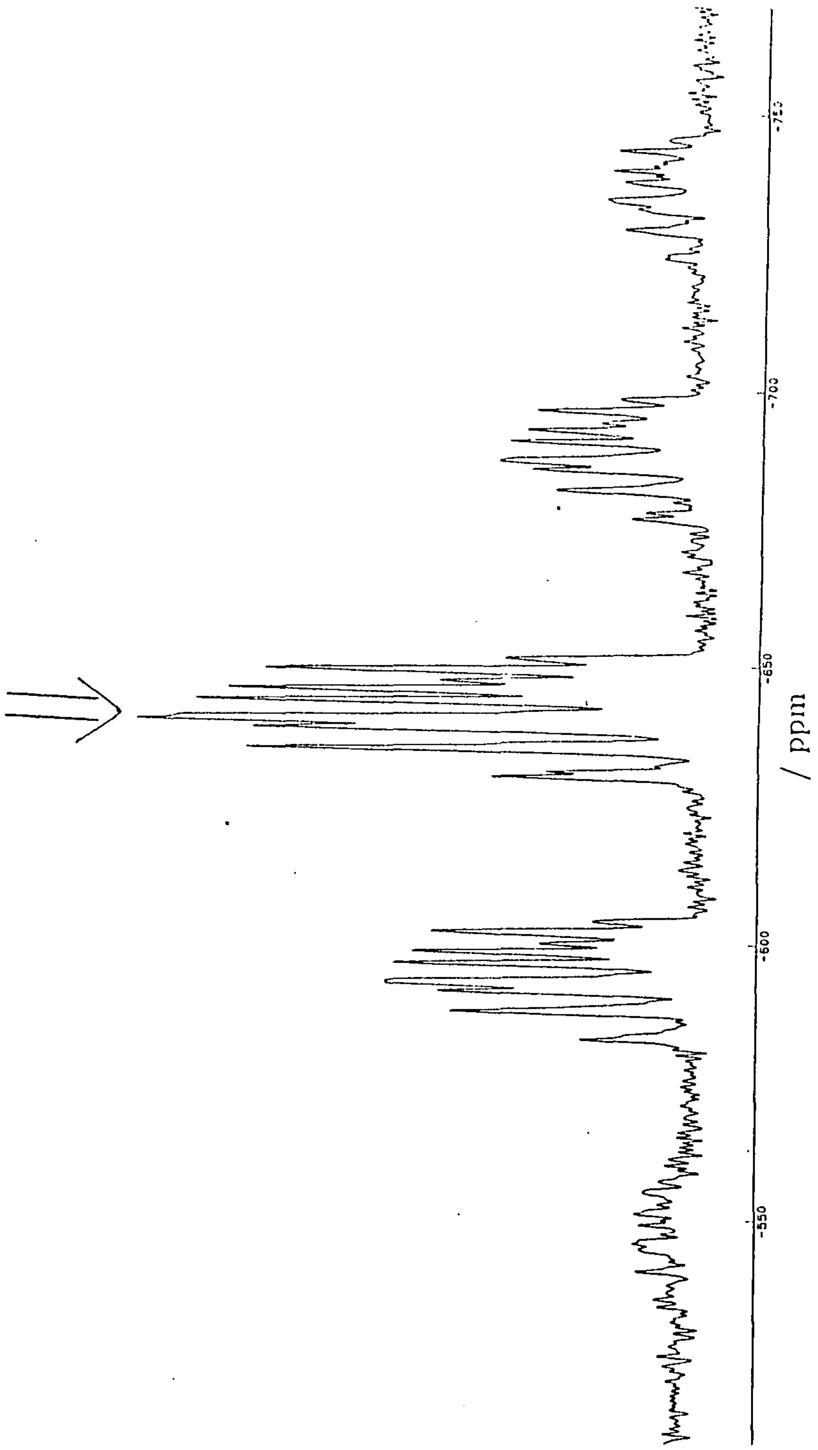

Figure 5.2.8: ^{119}Sn CPMAS spectrum of cis-(acac)$_2$SnCl$_2$ obtained at 74.63 MHz. The centreband is indicated by the arrow. Spectrometer operating conditions: contact time 3ms, recycle delay 15s, number of transitions 5922, spinning speed 3515 Hz.

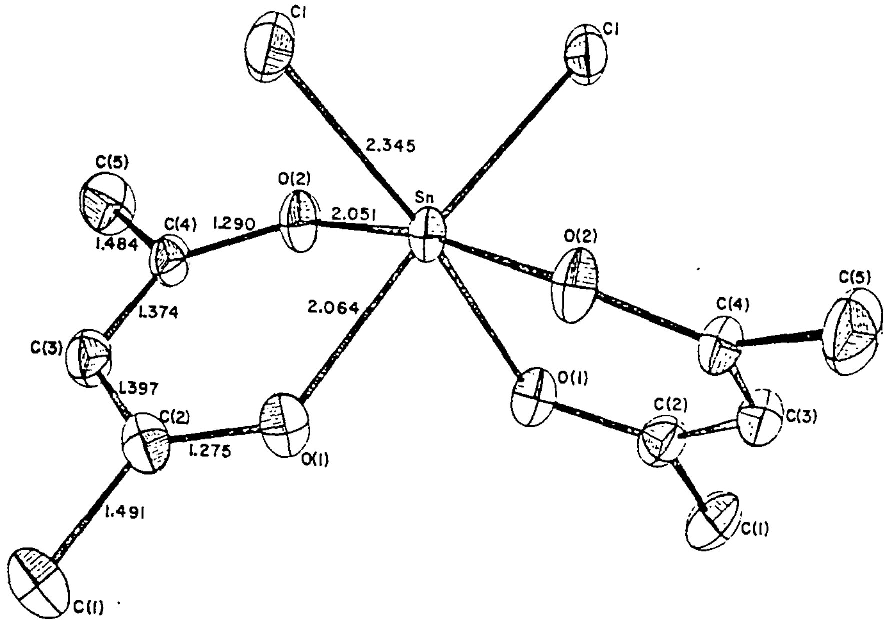

Figure 5.2.9: Crystal structure of cis-$(acac)_2SnCl_2$ [20].

scalar coupling constant is immediately measured to be $|J^{iso}| = 276 \pm 10$ Hz, slightly larger than for Ph_3SnCl and Bz_3SnCl [21]. The second-order shifts (Δ) obtained for spin states $(+\frac{3}{2},+\frac{3}{2})$ and $(-\frac{3}{2}, -\frac{3}{2})$, the two outer lines, are found to be the same within experimental error. The value measured for Figure 5.2.10(a) is -106 ± 10 Hz, while for Figure 5.2.11(a) is -61 ± 10 Hz, leading to $D'\chi = (-3.3 \pm 0.3)\times 10^9$ Hz^2 ($D'\chi = \frac{5}{3}\Delta\nu_{Cl}$). This parameter was then used in the calculation of the theoretical spectra for both 74.63 MHz and 111.86 MHz. The simulated spectra for the two spectrometer frequencies are shown in Figures 5.2.10 (b) and 5.2.11 (b). The close similarity of the calculated patterns and the experimental line shapes for both magnetic fields confirms that the asymmetric splittings of the ^{119}Sn NMR spectrum are caused by quadrupolar interactions of two equivalent chlorine nuclei in the compound. The chemical shift is found to be $\delta_{Sn} = -642.2 \pm 0.5$ ppm. The small spinning sidebands shown in Figure 5.2.8 suggest a modest shielding anisotropy for the tin nucleus. Detailed analysis of the sideband manifolds will be given in the next section.

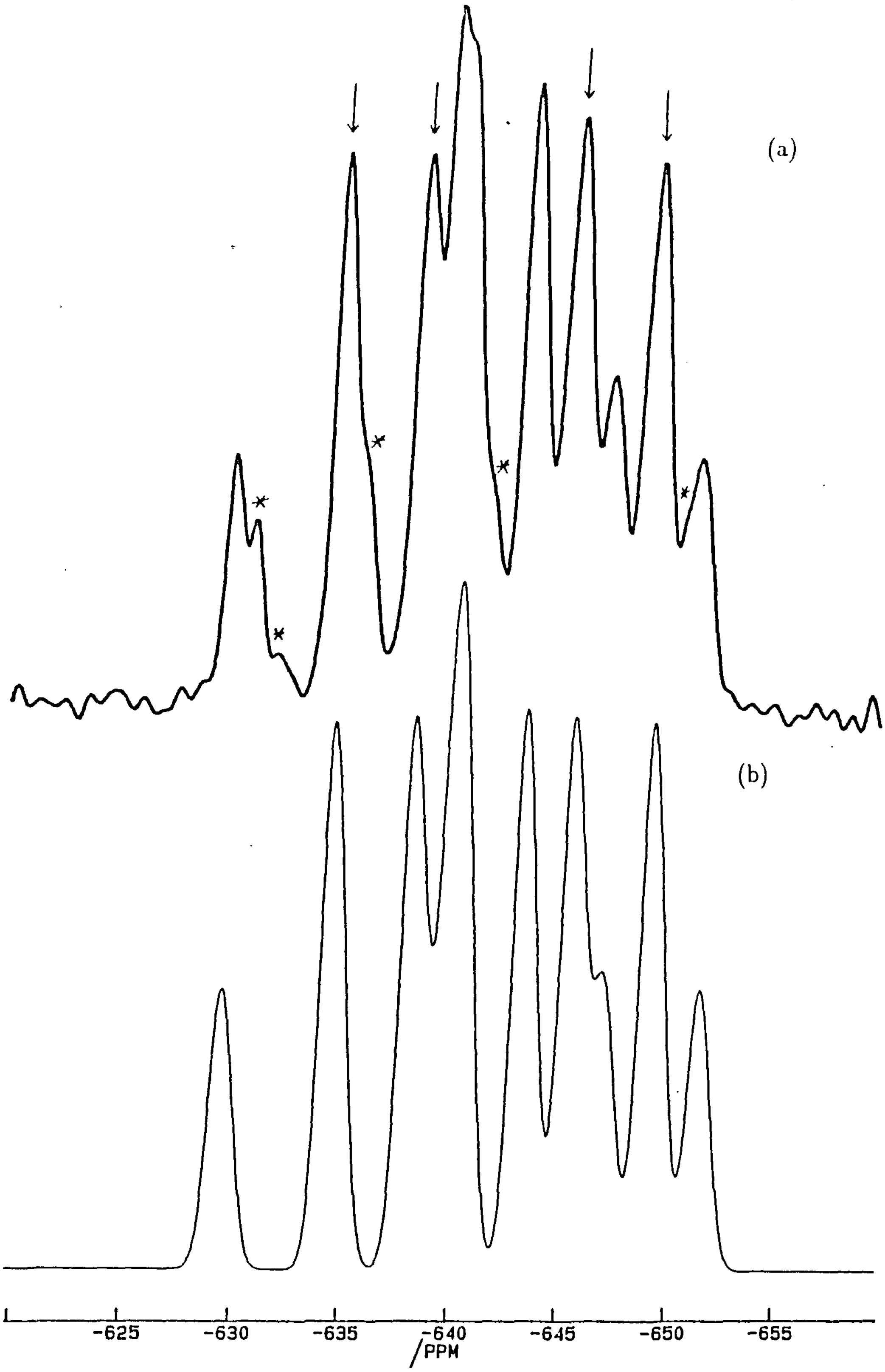

Figure 5.2.10: (a) Expanded centreband of Figure 5.2.8. The lines marked with arrows are those at $\nu_I\delta \pm |J^{iso}|$ and $\nu_I\delta \pm 2|J^{iso}|$. The lines indicated by $*$ are those remained unsolved as described in the text. (b) Simulated powder pattern with $|J^{iso}| = 276$ Hz and $D'\chi = -3.3 \times 10^9$ Hz^2.

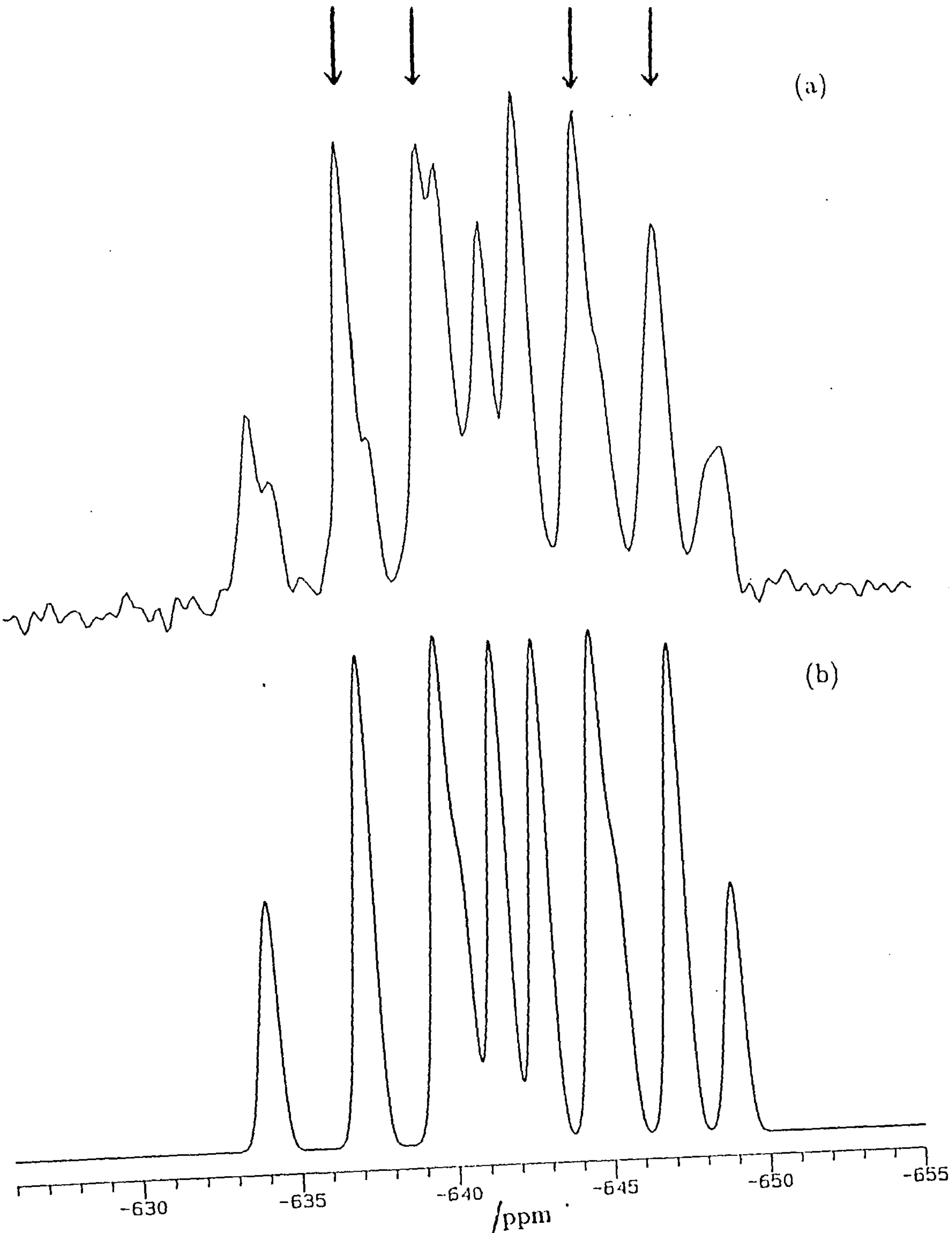

Figure 5.2.11: (a) ^{119}Sn CPMAS spectrum of cis-(acac)$_2$SnCl$_2$ obtained at 111.86 MHz (centreband only). The four lines indicated by arrows are the constant lines as for Figure 5.2.9(a). Spectrometer operating conditions: contact time 3ms, recycle delay 10s, number of transitions 1000, spinning speed 4680 Hz. (b) Simulated powder pattern with $|J^{iso}| = 276$ Hz and $D'\chi = -3.3 \times 10^9$ Hz^2.

The internuclear distance r_{SnCl} for cis-$(acac)_2SnCl_2$ is reported [20] to be 2.345 Å which leads to $D = -340$ Hz. However, the value of χ does not appear to be available in the literature. An attempt to record the NQR spectrum of this sample has been made, but no signal could be obtained. If the correlation between χ and r_{SnCl} reported in [22] is used, the magnitude of the quadrupolar coupling constant for this compound is suggested to be $|\chi| = 39.2$ MHz. If a negative value of χ is assumed (reasonable for single-bonded chlorine), the pseudo-dipolar coupling constant D' will be $+84 \pm 8$ Hz, and $\Delta J(Sn,Cl)$ should be at -1270 ± 25 Hz.

Comparison of Figures 5.2.10 (a) and (b) and also of Figures 5.2.11 (a) and (b) shows that some minor experimental peaks do not appear in the simulated spectra. Possible reasons for this situation are:

(1) Impurities in the sample;
(2) Artefacts in the spectra;
(3) The existence of stereoisomers in the same sample;
(4) The existence of two isotope chlorine nuclei (^{35}Cl and ^{37}Cl);
(5) The existence of non-axial symmetry of the electric field gradient at chlorine;
(6) Possible departure from the perturbation theory.

The sample, as provided, is attested as chemically pure by Professor Finocchiaro. Moreover, a freshly recrystallized sample provided by Professor Finocchiaro gave essentially the same spectrum. In order to check both (1) and (2), a ^{117}Sn CPMAS spectrum was recorded at 70.40 MHz. The spectrum is indistinguishable from the ^{119}Sn spectrum. Hence, causes (1) and (2) are extremely unlikely to be the reasons. The simple ^{13}C spectrum shown in Figure 5.2.12 suggests that there are unlikely to be stereoisomers (cause 3) present in the same sample, though no other simple method can be used to test this.

The isotope effect of chlorine ^{35}Cl and ^{37}Cl can be checked by calculations, since their magnetogyric ratios and quadrupole moments are known. The splitting between the two highest-frequency lines is ca. 71 Hz, which leads to a shift ratio of

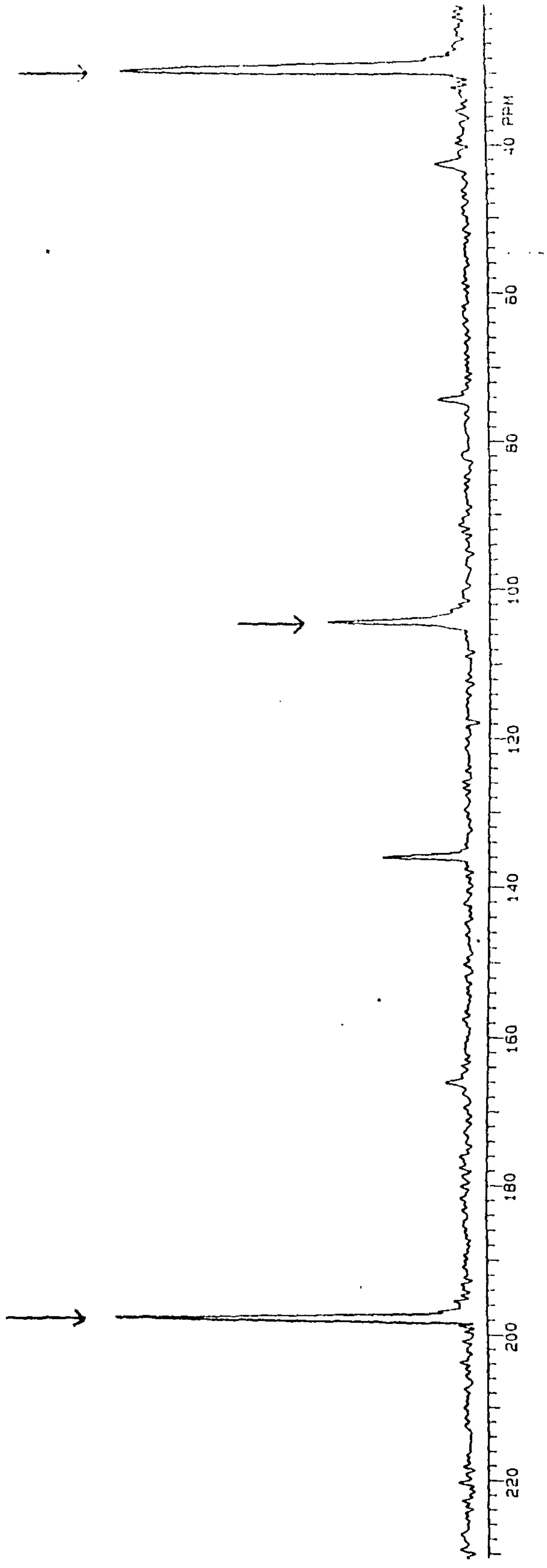

Figure 5.2.12: ^{13}C CPMAS spectrum of cis-(acac)$_2$SnCl$_2$ obtained at 75.43 MHz. Spectrometer operating conditions: contact time 1ms, recycle delay 20s, number of transitions 600, spinning speed 2260 Hz.

ca. 3.05. The second-order shift of the lines is proportional to $(\frac{D'\chi}{\nu_s})$. If the isotopic effect on D' can be ignored, the shift is then proportional to $\frac{|Q|}{\gamma_{Cl}}$, where Q and γ_{Cl} are the quadrupole moment and magnetogyric ratio of chlorine respectively. For chlorine-35, $\frac{|Q|}{\gamma_{Cl}}$ is calculated to be 5.1 $\times 10^{10}$, whereas for chlorine-37 this value equals to 4.8 $\times 10^{10}$. The ratio of these two values is thus 1.06, which is not enough to account for the splitting. The isotope effects on J^{iso} and δ_{Sn} are unlikely to be important, since there are no potential splittings for the four constant lines which are only influenced by the isotropic scalar coupling constant and the chemical shift. Of course, there should also be an isotope effect on D', but the splitting is too great to be accounted for this alone. So cause (4) may be ruled out.

So far in this thesis, the calculation has been based on the assumption that an axially symmetric quadrupole coupling constant is present. A.C Olivieri has carried out a more complete calculation [13,14], which takes into account the asymmetry of the electric field gradient (EFG). A computer simulation program based on his equations was written to check cause (5). The calculated line shape for an IS system is depicted in Figure 5.2.13. The input splitting value is the same as that for Figure 5.2.10 (b), with $\alpha^J = \alpha^D = 0$, $\beta^J = \beta^D = 90°$ and $\eta = 1.0$. These values are considered to give maximum shoulder splittings. Though the line shape is closer to the experimental spectra, the shoulder of the lowest-frequency line is obviously in the opposite direction. This fact demonstrates that non-axially symmetric quadrupole coupling can not be alone used to explain the situation. Furthermore, another simulation carried out by a computer program using the full diagonalization method written by Paul Jonsen [23] gave essentially the same powder pattern as by the perturbation approach. So cause (5) is unlikely as well.

Thus the origin of the additional lines remains unsolved, though many attempts have been made to explain the discrepencies. There are also minor differences between the calculated and experimental spectra in Figures 5.2.10 and 5.2.11. These may be attributed to inadeqacies in the level to which the perturbation

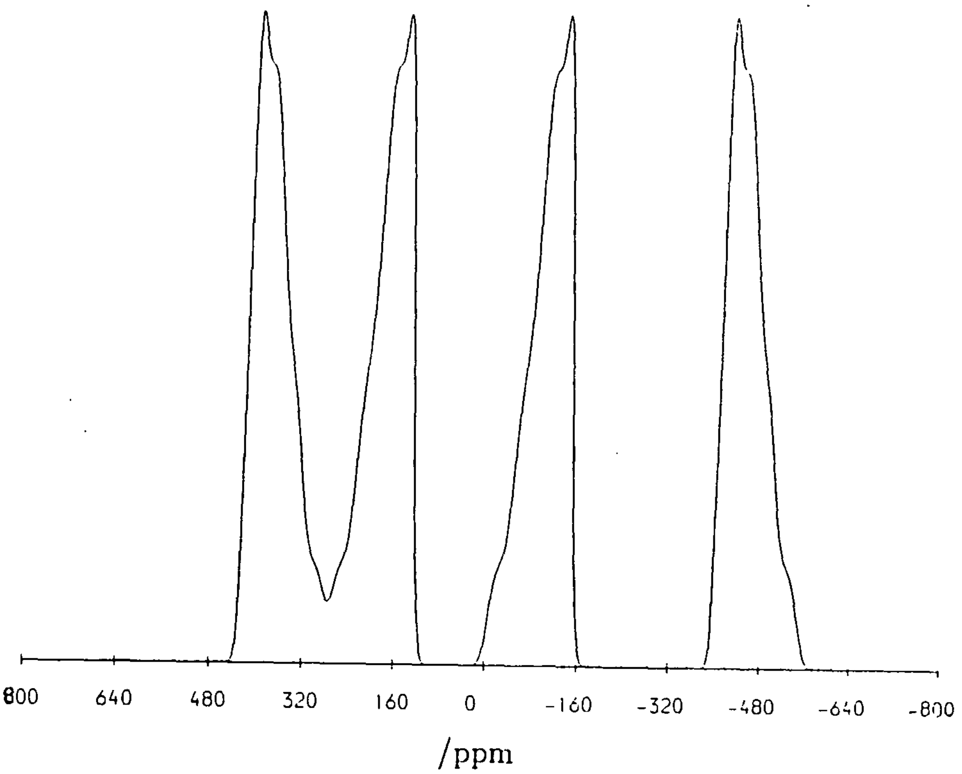

Figure 5.2.13: Simulated spectrum for an IS system based on Olivieri's equations, with $\alpha^J = \alpha^D = 0$, $\beta^J = \beta^D = 90°$ and $\eta = 1.0$. The zero point is regarded as the chemical shift.

approach was taken.

^{119}Sn CPMAS spectra at 74.63 and 111.86 MHz for bis(benzoylacetonato)tin dichloride, (bzac)$_2$SnCl$_2$ (II), have also been obtained by CPMAS as shown in Figures 5.2.14 (a) and 5.2.15 (a). Only centrebands are shown because of the high noise level of the spectra and few spinning sidebands present. The patterns are very similar to those for (acac)$_2$SnCl$_2$, but the peaks are closer together producing less well-resolved spectra. However, the ranges of signals for both (acac)$_2$SnCl$_2$ and (bzac)$_2$SnCl$_2$ are found to be the same at about 2000 Hz, indicating similar magnitudes of interaction between tin and chlorine. Actually, it is not difficult to find the four invariable lines (as indicated by arrows) in Figure 5.2.14 (a),

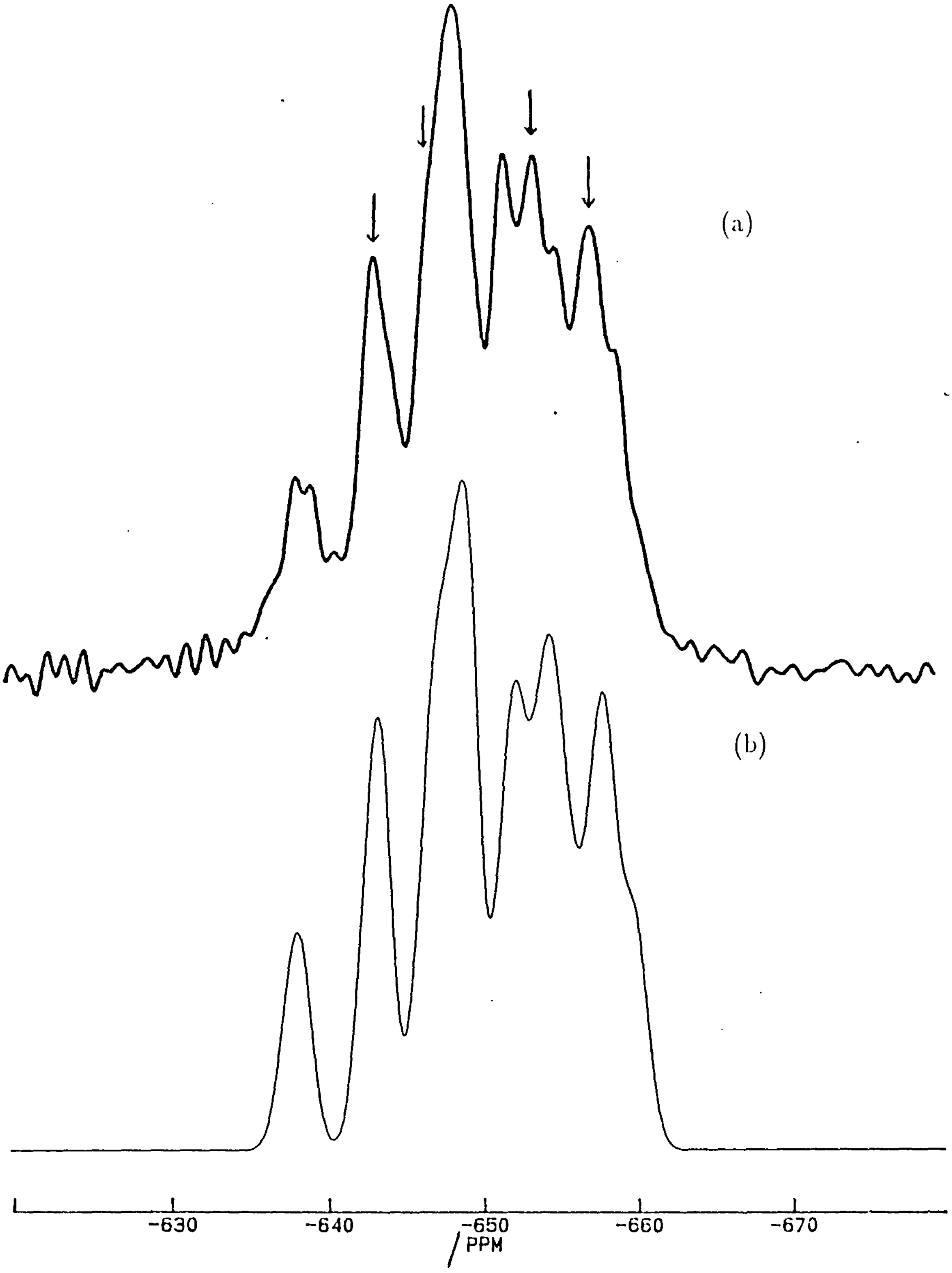

Figure 5.2.14: (a) ^{119}Sn CPMAS spectrum of (bzac)$_2$SnCl$_2$ obtained at 74.63 MHz (centreband only). Spectrometer operating conditions: contact time 3ms; recycle delay 30s; number of transitions 2550; spinning speed 3500 Hz. The lines indicated by arrows are the invariable lines as in Figure 5.2.10. (b) Simulated powder pattern, with $|J^{iso}| = 270$ Hz and $D'\chi = -3.3\times10^{9}$ Hz^{2}.

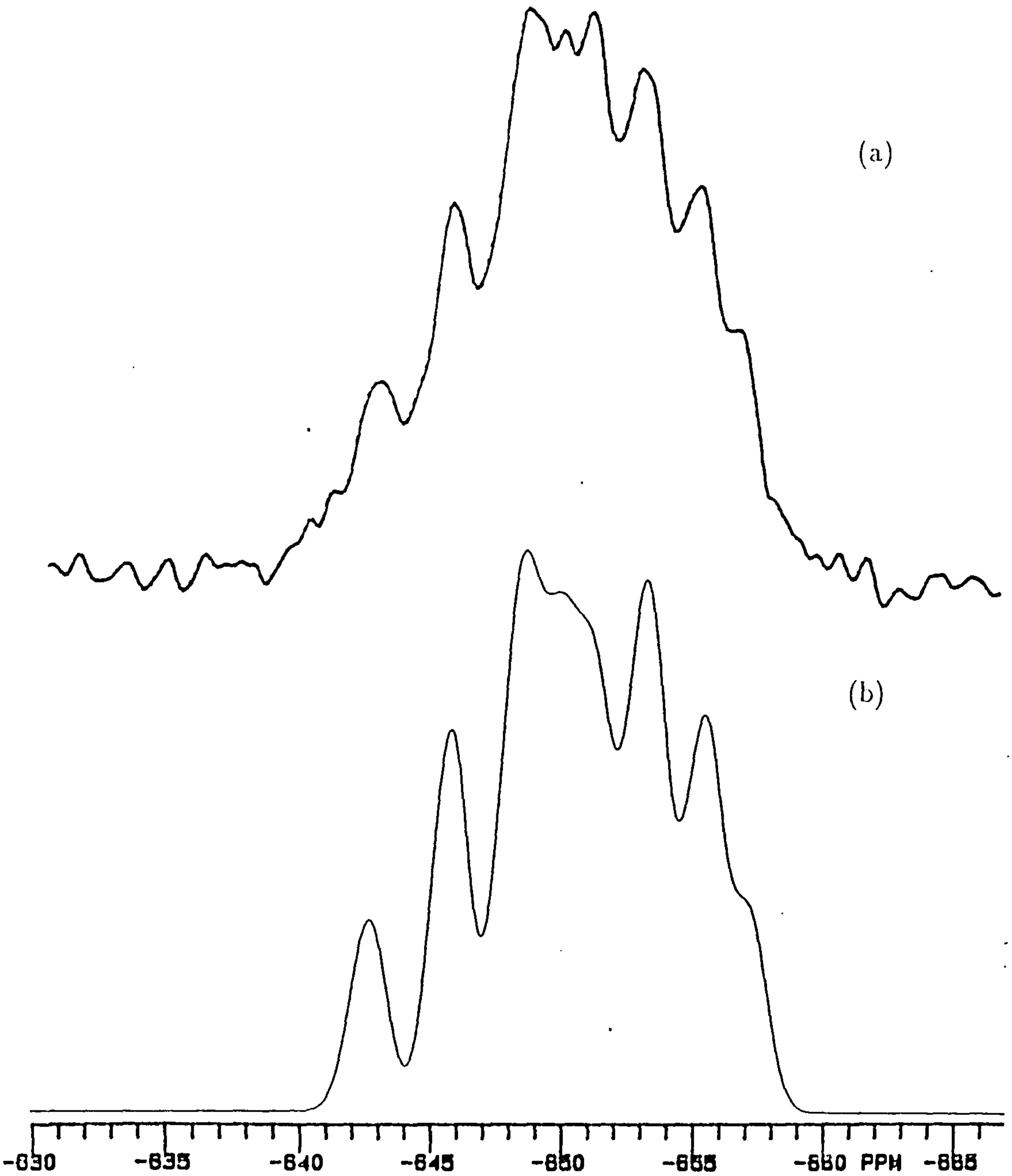

Figure 5.2.15: (a) ^{119}Sn CPMAS spectrum of (bzac)$_2$SnCl$_2$ as for Figure 5.2.13, but obtained at 111.86 MHz (centreband only). Spectrometer operating conditions: contact time 3ms; recycle delay 2s; number of transitions 2000; spinning speed 4520 Hz. (b) Simulated powder pattern, with $|J^{iso}| = 270$ Hz and $D'\chi = -3.3\times10^{9}$ Hz^2.

giving $|J^{iso}|$ = 270 ± 10 Hz, which is almost the same as for $(acac)_2SnCl_2$. When the same value of $D'\chi = -3.3 \times 10^9$ Hz^2 is used and twice as much Gaussian linebroadening is applied, the simulated spectrum (Figure 5.2.14 (b)) is very close to the experimental pattern. The same values are used to calculate the spectrum at 111.86 MHz, which is also similar to the experimentally obtained spectrum (Figure 5.2.15). Much wider Gaussian linebroadening is needed to fit the $(bzac)_2SnCl_2$ spectrum, which may imply that this molecule is more rigid. The tin-119 chemical shift for the benzoylacetonato compound in the solid-state is – 650.5 ± 0.5 ppm. The data for the two tin dichloride compounds are written in Table 5.2.1.

Table 5.2.1: Tin-119 data for $(acac)_2SnCl_2$ and $(bzac)_2SnCl_2$

compound	δ_{Sn} /ppm	$|J^{iso}|$ /Hz	$D'\chi$ /$\times 10^9$ Hz^2	ΔJ /Hz	Gaussian linebroadening /Hz
$(acac)_2SnCl_2$	−642.2	276	−3.3	−1270	30
$(bzac)_2SnCl_2$	−650.5	270	−3.3	−1270	62
Estimated error	±0.5	±10	±0.3	±25	–

5.2.4 The shielding anisotropies

The spinning sidebands in Figure 5.2.8 were analyzed by iterative fitting to extract the effective shielding anisotropies and asymmetries of the tin nucleus (see Chapter 7). The results are shown in Table 5.2.2, and Figure 5.2.16 exhibits one of the fitting results for this compound. The intensity of each sideband was measured as the height of each peak. Since there are some line overlappings in the spectrum, it is likely that this measurement is not very accurate. However, it is certain that the shielding tensors are not axially symmetry. The anisotropies of the nine spinning sideband manifolds are very close, ranging from ca. 102 ppm to ca. 107 ppm.

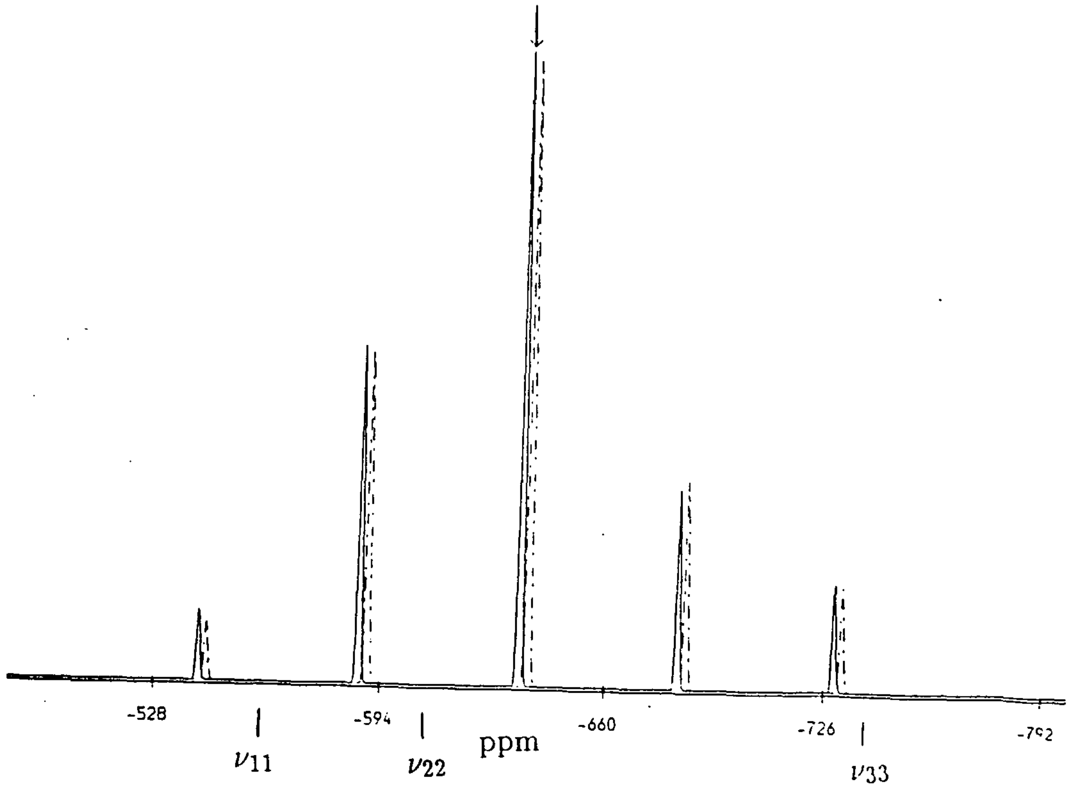

Figure 5.2.16: Fitting result of one of the sideband manifolds ($\delta = -634.9$ ppm) of Figure 5.2.8. Results: anisotropy = 103 ppm and asymmetry = 0.43.

It has been shown in Chapter 4 that the anisotropies, of the subspectra of a spin-$\frac{1}{2}$ nucleus coupled to two equivalent spin-$\frac{1}{2}$ nuclei, depend upon D′, the pseudo-dipolar coupling constant. When $D' = 0$, the anisotropies of the three subspectra would be equal. The larger the value of D′, the greater the differences in anisotropies. If this tendency is regarded as general, and used for $(acac)_2SnCl_2$, the small differences in anisotropies among the nine subspectra indicate that the value of D′ is very small. Since the $(acac)_2SnCl_2$ system is much more complicated than the penta-coordinate R_3SnF, an accurate expression for the anisotropies of the subspectra is very difficult if not impossible. However, the conclusion that the value of D′ is small resulting from this analogous discussion is consistent with the data ($D' =$ ca. 84 Hz) obtained through the residual dipolar coupling calculation.

Table 5.2.2: The shielding anisotropies and asymmetries for $(acac)_2SnCl_2$

N	δ_{Sn} /ppm	$\beth$ /ppm	η
1	−629.9	104	0.45
2	−634.9	103	0.43
3	−638.7	104	0.56
4	−640.0	104	0.54
5	−643.6	106	0.49
6	−645.7	107	0.48
7	−647.3	106	0.53
8	−649.4	108	0.46
9	−651.4	102	0.73
Estimated error	± 0.5	± 5	± 0.2

5.3 ^{119}Sn NMR Studies of Hexachlorostannate compounds $(NH_4)_2SnCl_6$, $(MeNH_3)_2SnCl_6$, $(Ph_4P)_2SnCl_6$, K_2SnCl_6

The ^{119}Sn NMR spectrum of $(NH_4)_2SnCl_6$ (I), obtained by CPMAS and high-power proton-decoupling at 74.63 MHz and ambient temperature, is shown in Figure 5.3.1. It is surprising to observe a single broad band with twelve equally spaced peaks superimposed, given the complicated ^{119}Sn spectra of $(acac)_2SnCl_2$ which is coupled to just two chlorines. The linewidth of the band is ca. 1450 Hz, and the splitting between each peak is found to be 302 ± 8 Hz. It is also interesting to notice that there are some line broadening on the right side of the lineshape. The reasons for this asymmetric broadening are discussed in detail later in this section. The complete lack of spinning sidebands in the spectrum indicates that the shielding anisotropy at the tin nucleus is very small (if any) as is expected, given the octahedral geometry of the anion, with bonding of tin to six atoms of

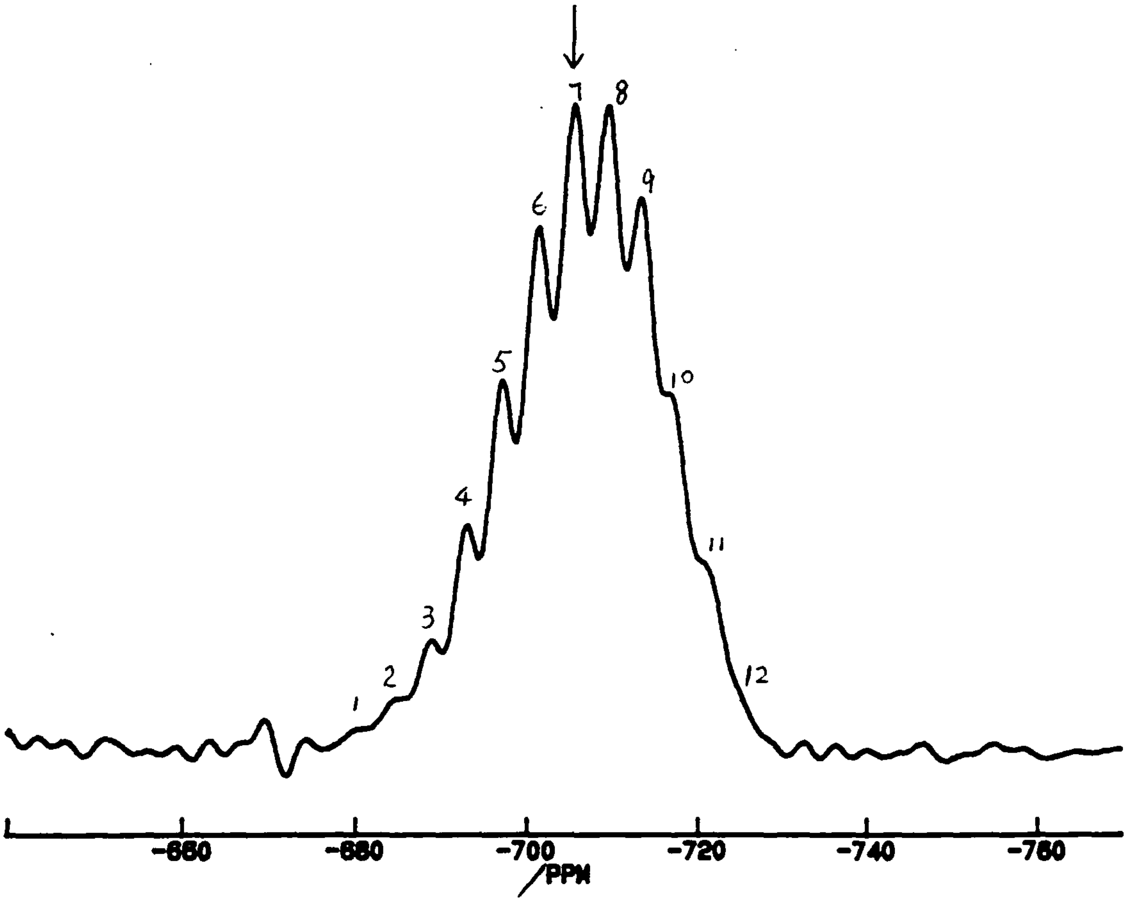

Figure 5.3.1: ^{119}Sn CPMAS spectrum of $(NH_4)_2SnCl_6$ (I) obtained at 74.63 MHz and ambient temperature. The numbers indicate the peaks which could possibly be identified. The arrow represents the position of the chemical shift. Spectrometer operating conditions: contact time 3ms, recycle delay 5s, number of transitions 11340, spinning speed 5000 Hz.

the same element (Figure 5.3.3).

The chemical shift cannot be determined for certain unless the sample is also studied at a different magnitude of applied field, since chemical shifts are independent of the strength of the magnetic field (in the units of ppm). Moreover, multi-field studies can also reveal scalar couplings as they remain constant (in the units of Hz) at different magnitudes of applied field. Hence, a spectrum of the same compound was also obtained at 111.86 MHz on a VXR-300 spectrometer as shown in Figure 5.3.2 (a).

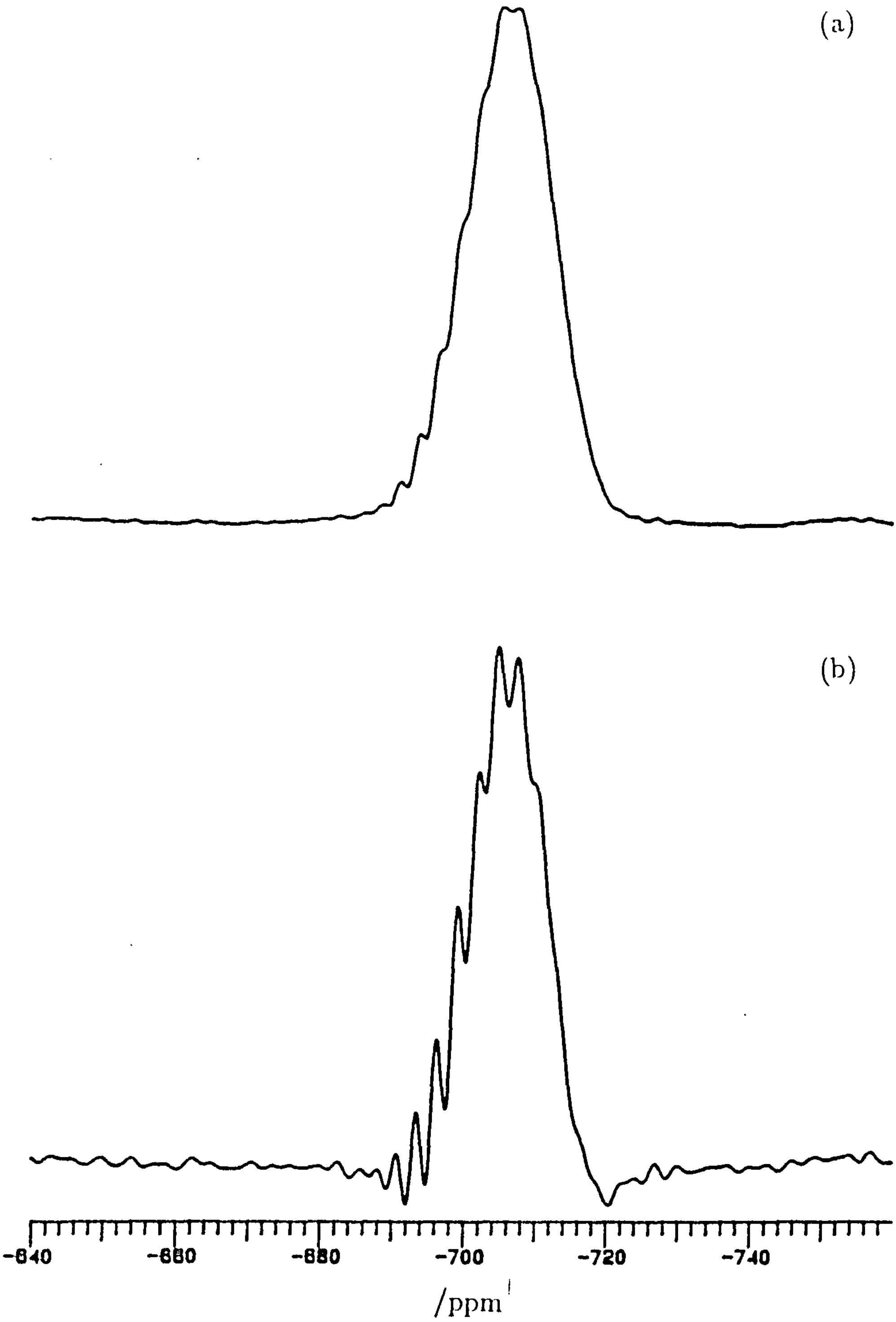

Figure 5.3.2: (a) ^{119}Sn CPMAS spectrum of compound (I) as in Figure 5.3.1, but obtained at higher field (111.86 MHz). Spectrometer operating conditions: contact time 3ms, recycle delay 2s, number of transitions 4000; spinning speed 5000 Hz. (b) After resolution enhancement.

The high-field spectrum exhibits a much less resolved broad line with linewidth of ca. 1600 Hz, and figure 5.3.2.(b) demonstrates the spectrum after resolution enhancement. Comparison of the two spectra, obtained at two different fields, shows that the peak at −705.0 ± 0.5 ppm is the only chemical shift, since this line is the one which occurs in both spectra. The distance between each peak in Figure 5.3.2 (b) also appears to be constant with the value of 314 ± 20 Hz, which is the same as that obtained from the low-field spectrum, within experimental error. Therefore, the two-field studies prove that there is only one tin site present in the molecule, and the splittings are due to tin-chlorine indirect dipolar coupling.

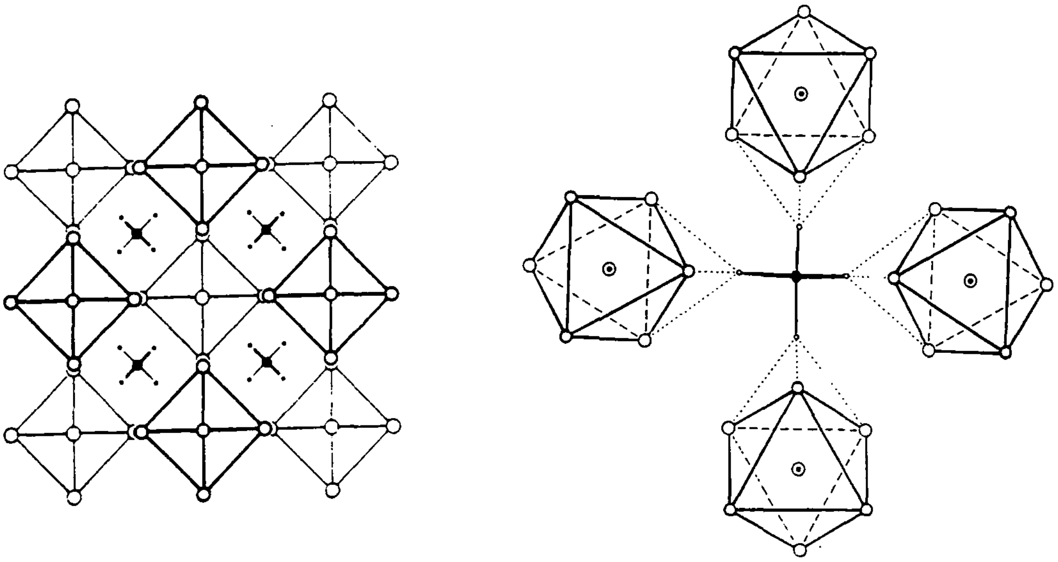

Figure 5.3.3: Crystal structure of ammonium hexachlorostannate, $(NH_4)_2SnCl_6$ [24].

Ammonium hexachlorostannate, $(NH_4)_2SnCl_6$, has been studied by X-ray crystallography [24,25], and its structure is depicted in Figure 5.3.3. The compound has a cubic lattice with space group of Fm3m. Each (NH_4^+) ion is coordinated by twelve Cl neighbours, three from each of four $SnCl_6{}^{2-}$ ions. The $SnCl_6{}^{2-}$ ion has a regular octahedral conformation which implies that all the six chlorine nuclei are equivalent. The Sn–Cl distance is reported as 2.421 Å. This value leads to a dipolar coupling constant (D) of −310 Hz.

An NQR study of $(NH_4)_2SnCl_6$ was carried out by Brill and co-workers [26]. It was found that only a single ^{35}Cl NQR frequency is observed, in agreement with the X-ray research. It was also believed that the electric field gradient at each chlorine is axially symmetric. The quadrupolar resonance frequency $\nu_Q(^{35}\mathrm{Cl})$ for $(NH_4)_2SnCl_6$ is found to be 15.45 MHz, at room temperature. Consequently the quadrupolar coupling constant $|\chi|$ is calculated to be 30.90 MHz ($\chi = 2\nu_Q$).

The presence of a single tin site with no asymmetry is consistent with the ^{119}Sn NMR data giving one chemical shift and no spinning sidebands. It is also suggested that the observed splittings in the ^{119}Sn spectra are contributed by interactions between tin (spin-$\frac{1}{2}$) and six equivalent chlorines (spin-$\frac{3}{2}$). Such interactions may have two possible types: (1) the dipolar coupling, and (2) the indirect dipolar (scalar) coupling, and it is likely that both types may exist in a given system. The detailed discussion of dipolar interactions influenced by the quadrupole nature of chlorine has been given in section 5.2. According to Equation 5.2.3, the maximum frequency shift caused by residual dipolar coupling is $n \times \frac{3D'\chi}{10\nu_s}$, where n refers to the number of equivalent quadrupole nuclei (spin-$\frac{3}{2}$) coupled to the spin-$\frac{1}{2}$ nucleus. For $SnCl_6{}^{2-}$ ions, this shift would be $\frac{9D'\chi}{5\nu_s}$. However, the spectrum obtained shows no such shift at all.

This lack of quadrupolar effect may be due to the high symmetry of the $SnCl_6{}^{-2}$ ion, which possesses a regular octahedral form. As described earlier the second-order effect of one spin-$\frac{3}{2}$ quadrupolar nucleus on the spectrum of a spin-$\frac{1}{2}$ nucleus is a function of $\sin^2\theta\cos^2\theta$, where θ is the angle between the external field ($\mathbf{B}_0$) and the z-direction of the PAS of the quadrupolar tensor. When the Sn nucleus is symmetrically coupled to six equivalent Cl atoms, any θ value of one chlorine atom will correspond to a $-\theta$ value of another chlorine atom, wherever the orientation of $\mathbf{B}_0$ is in the molecule. Therefore the second-order effect of one chlorine nucleus will be counteracted by that of another chlorine, since the constant $\frac{D'\chi}{\nu_s}$ for the six chlorine atoms is the same. The net effect of the chlorines thus will be zero. That is why no quadrupolar effect is observed in the ^{119}Sn spectrum of $SnCl_6^{-2}$ ions. Similar ions PCl_6^- have been studied by solid-state NMR, where a quadrupolar effect was observed, but small [17]. However, the structure of the PCl_6^- ions is not as highly symmetric as that of $SnCl_6^{2-}$, and in fact is a distorted octahedron. Four chlorine atoms are at 2.11 Å from the central phosphorus atom, and two are at slightly larger distance (2.13 Å and 2.16 Å). Hence the constant $\frac{D'\chi}{\nu_s}$ for the six chlorines will be different. Not surprisingly, the quadrupolar effect was detected.

In the case of $(NH_4)_2SnCl_6$, a purely (Sn,Cl) indirect coupling will lead to a symmetric pattern of lines, equally spaced by $|J^{iso}|$, whose intensity ratios are:

1: 6: 21: 56: 120: 216: 336: 456: 546: 580: 546: 456: 336: 216: 120: 56: 21: 6: 1

In total there are nineteen lines, the chemical shift being the central line. The relative intensities of the six outermost peaks compared to the highest intensity is about 0.2 %, 1.0 %, 3.6 % and 3.6 %, 1.0 %, 0.2 % respectively. These lines will almost certainly disappear into noise, given the limiting signal-to-noise ratio in the spectra. Subtracting these lines, thirteen lines remain with normalized percentage intensity ratios of:

1.4: 3.0: 5.3: 8.3: 11.3: 13.5: 14.4: 13.5: 11.3: 8.3: 5.3: 3.0: 1.4

In the spectrum, only twelve lines are observed. This is understandable since the line broadening on the right side of the lineshape is likely to cause the rightmost peak to disappear. Deconvolution of Figure 5.3.1 suggests that the intensity ratio of the high-frequency part of the spectrum, which is not influenced by line broadening, is:

1.2: 2.0: 4.1: 6.5: 11.2: 15.4: 19.3

This ratio is not quite the same as the above calculated intensity ratio for a spin-$\frac{1}{2}$ nucleus influenced by pure indirect coupling to six equivalent spin-$\frac{3}{2}$ nuclei. It seems that the pattern of the multiplet (the relative intensities of the peaks) has changed from the usual multiplet feature, where only isotropic spin-spin interaction is involved. Zalewski et al. showed [27] that such an intensity change would happen to centrebands (also spinning sidebands) of MAS spectra, when the dipolar coupling (D) or/and the J coupling anisotropy (ΔJ) are involved. Hence, it is believed that Figure 5.3.1 is not only influenced by isotropic spin-spin coupling but also by dipolar or/and anisotropic spin-spin interactions.

The line broadening mechanism could be due to the possible significant differences in relaxation times of the various chlorine spin states. A similar situation was observed for Si–Al couplings reported by Wossner and Trewelle [28]. The temperature-dependence was found for the chlorine relaxation time of the $SnCl_6{}^{2-}$ ion [29,30], and it was concluded that the ion undergoes reorientation at temperatures above 250 K. This value is lower than the room temperature at which thedspectra were taken. Reorientation of an ion changes the orientation of the electric field gradient tensor axes of at least some of the Cl atoms in $SnCl_6{}^{2-}$, and thus changes their relaxation times. This is because the relaxation rate of each spin depends upon the value of the angle between the directions of the z axis of the electric field gradient tensor before and after the reorientation. Since some of the six chlorine nuclei may be reorientated, the combination of the six chlorines may produce different relaxation times among the chlorine spin states. This could be regarded as the cause of the line broadening of some parts of the spectrum.

Measurement of the spectrum at temperatures lower than 250 K may help to confirm this explanation. Such a spectrum should show a much more symmetric splitting pattern due to the lack of reorientation of the molecules. On the other hand, if the anion motion goes even faster, for example due to an increase in temperature, then the chlorines may undergo 'self-decoupling' (see next section). As a result, the J coupling between tin and chlorines will disappear. Hence a spectrum obtained at certain high temperature will probably show only one sharp line at

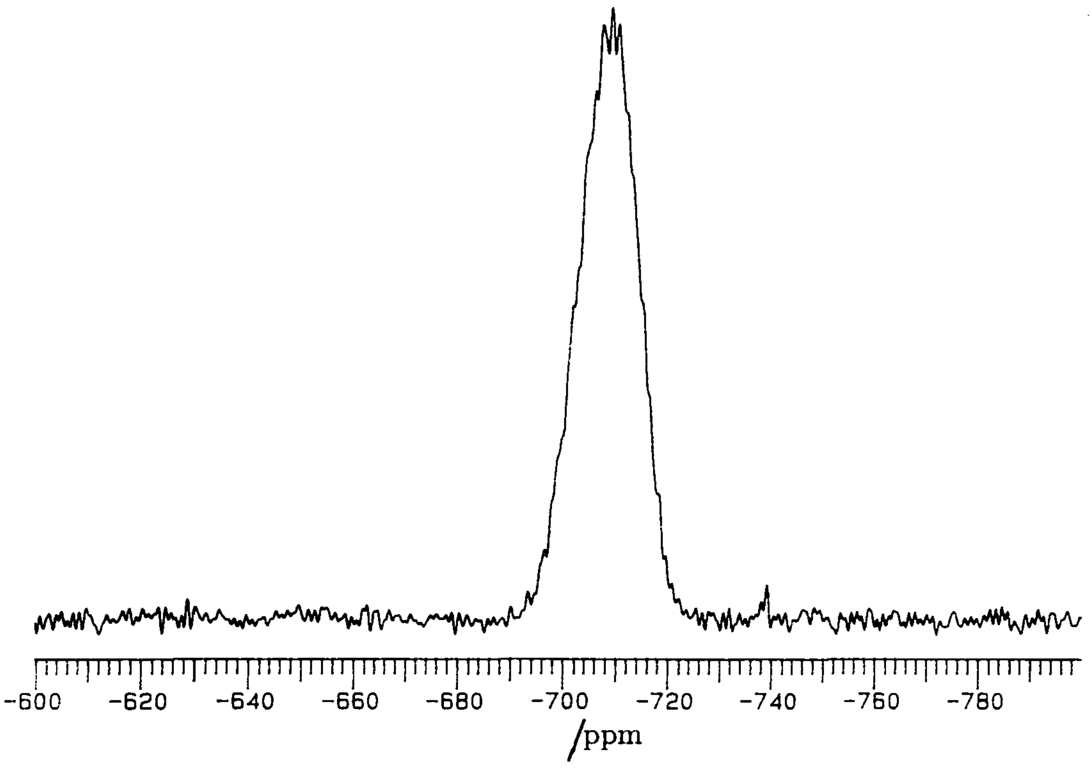

Figure 5.3.4: ^{119}Sn spectrum obtained at 100° C and on a VXR-300 spectrometer (111.86 MHz). The spectrometer operating conditions are as for Figure 5.3.2(a).

the chemical shift. Effort was made to perform high temperature experiments, and Figure 5.3.4 shows the spectrum obtained at 100° C. However, even at this temperature, the linewidth has not changed, comparing with Figure 5.3.2(a). One may surpose, then, that a higher temperature would be required to produce a noticeable change in linewidth.

Sn-119 NMR spectra were also obtained for compounds $(MeNH_3)_2SnCl_6$(II), $(Ph_4P)_2SnCl_6$(III) and K_2SnCl_6 (IV) at 74.63 and 111.862 MHz on the CXP-200 and VXR-300 spectrometers respectively. The results shown in Figures 5.3.5, 5.3.6 and 5.3.7 were obtained at 74.63 MHz. Compound (II) has an almost identical

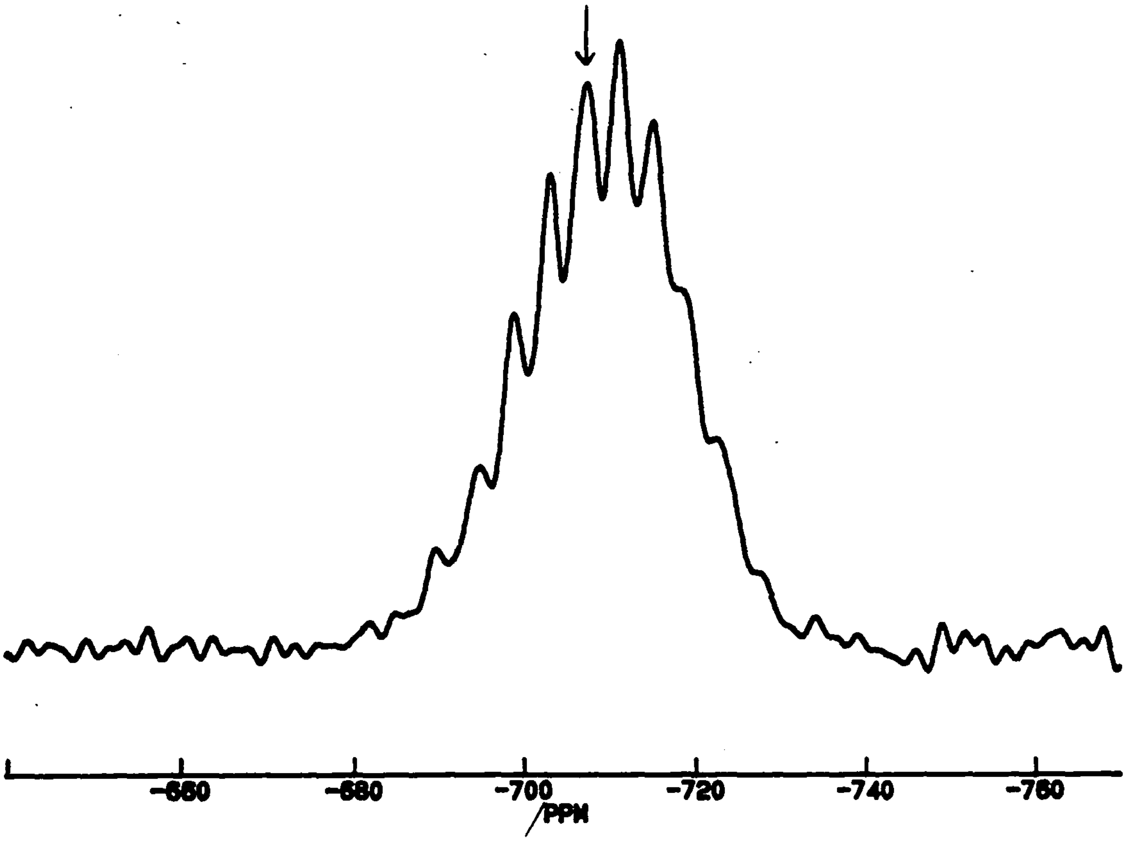

Figure 5.3.5: ^{119}Sn CPMAS spectrum of $(MeNH_3)_2SnCl_6$ obtained at 74.63 MHz. The arrow indicates the position of the chemical shift. Spectrometer operating conditions: contact time 3ms, recycle delay 10s, number of transitions 5970, spinning speed 3430 Hz.

pattern to $(NH_4)_2SnCl_6$. The spectrum of sample (III) demonstrates a similar line shape though less resolved. The spectrum of K_2SnCl_6, which was obtained by magic-angle spinning but without cross-polarization since the compound contains no protons, gives a single broad line with no splittings. The linewidth of this line is similar to those of other compounds, being ca. 1570 Hz. Resolution enhancement has been used but no splitting was observed. The spectrum obtained at higher field supplies no extra information regarding the patterns. However, the chemical shifts were identified and the results are summarized in Table 5.3.1.

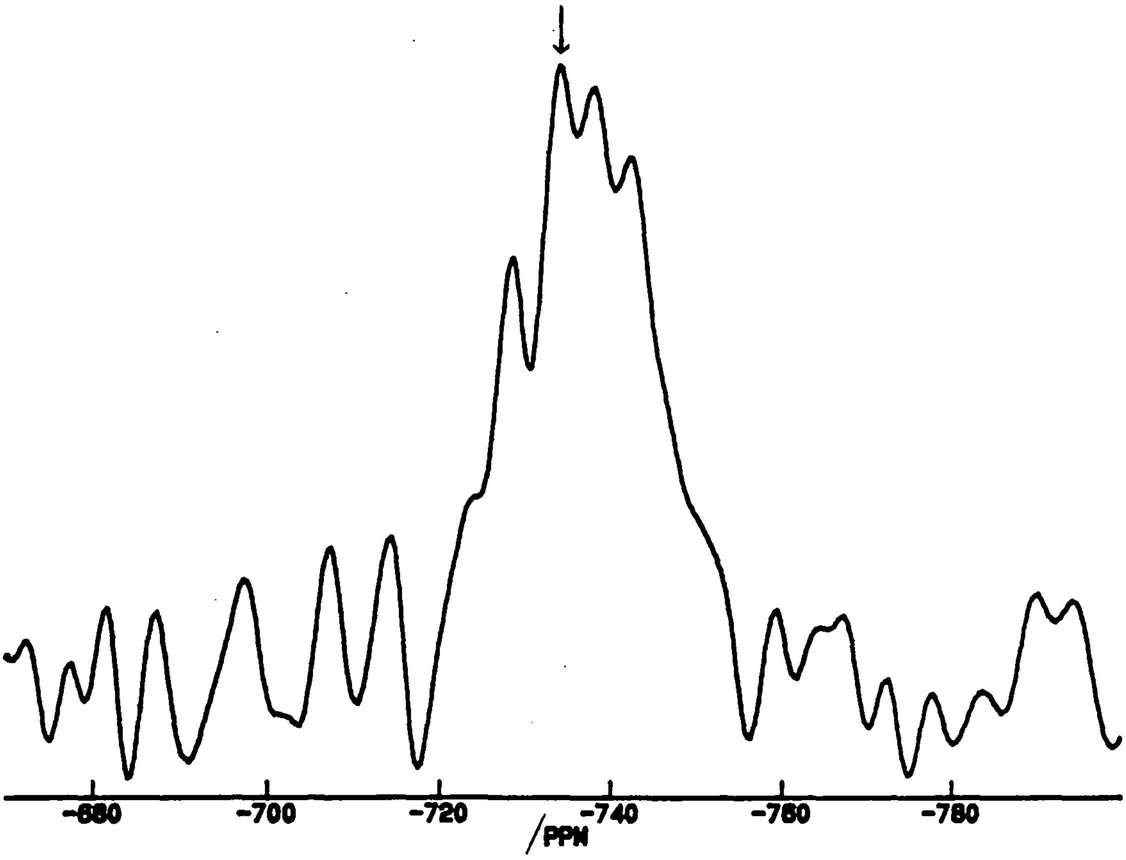

Figure 5.3.6: ^{119}Sn CPMAS spectrum of $(Ph_4P)_2SnCl_6$ obtained at 74.63 MHz. The arrow indicates the position of the chemical shift. Spectrometer operating conditions: contact time 10ms, recycle delay 60s, number of transitions 1212, spinning speed 6100 Hz.

The given data show that there are slight differences in chemical shifts of compounds (I), (II) and (IV). This may be attributed to the different cation each of these samples has. The shielding at tin for compound (III) is ca. 30 ppm larger than the others. This is due to the phenyl groups present in the cation $(Ph_4P)^+$. The total linewidths and (Sn,Cl) isotropic coupling constants of these four samples are almost the same, indicating that the octahedral ions $SnCl_6{}^{2-}$ in this group of compounds experience the same magnitude of tin-chlorine interaction and thus have similar geometries.

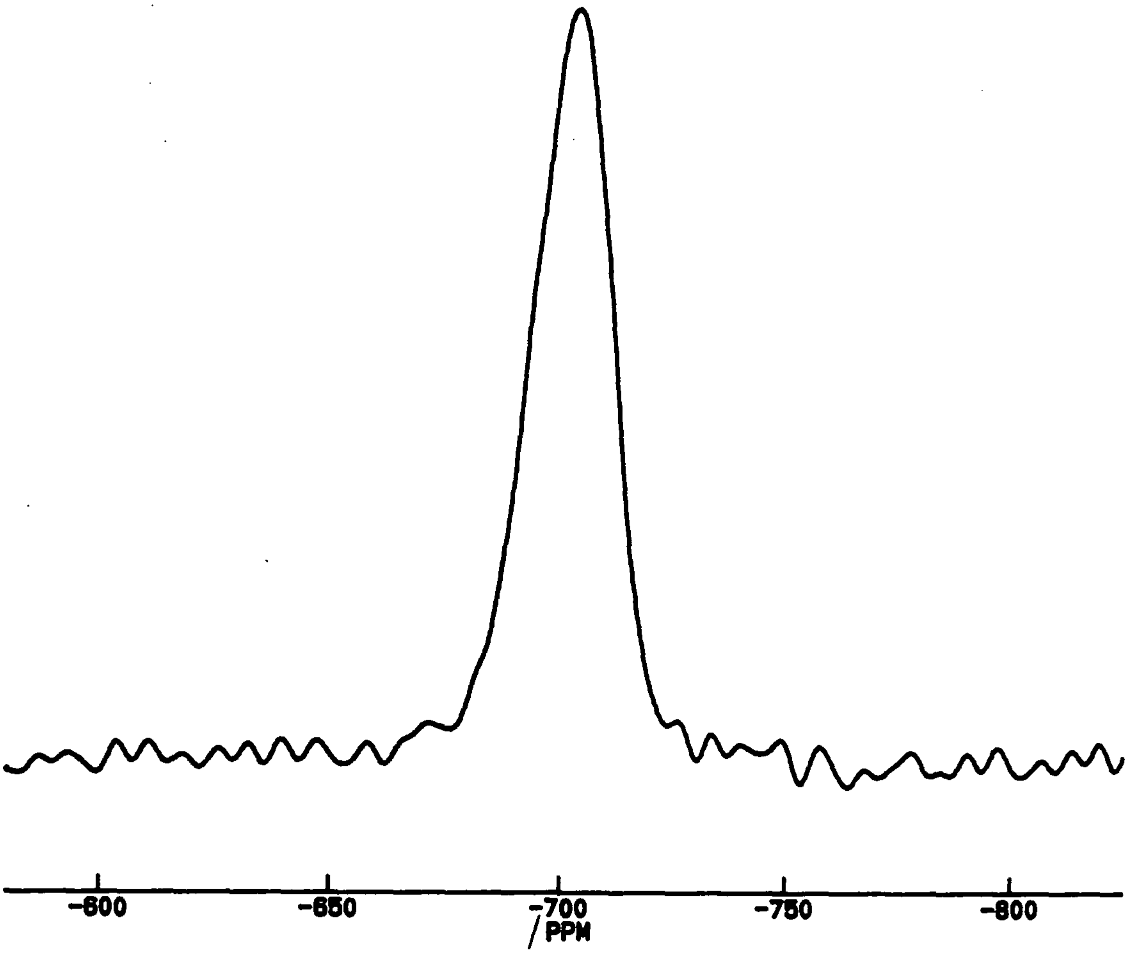

Figure 5.3.7: ^{119}Sn MAS spectrum of K_2SnCl_6 obtained at 74.63 MHz. Spectrometer operating conditions: recycle delay 10s; number of transitions 5970; spinning speed 3430 Hz.

Compounds containing the hexachlorostannate ion $SnCl_6{}^{2-}$ have been studied extensively by both nuclear quadrupole resonance and X-ray techniques. It was suggested that the $SnCl_6{}^{2-}$ octahedra are on the whole quite regular. Hence as expected the NMR spectra obtained for them have the same pattern and similar magnitudes of tin-chlorine interaction. However, it is possible that the $SnCl_6{}^{2-}$ octahedral structure may in fact have a more complicated arrangement as stated in reference [24], but this suggestion cannot be confirmed on the NMR time scale.

Table 5.3.2: Tin-119 NMR data of hexachlorostannate containing compounds

compound	δ_{Sn} /ppm	$\|J^{iso}\|$ /Hz	Linewidth /Hz
$(NH_4)_2SnCl_6$	−704.9	308	1450
$(MeNH_3)_2SnCl_6$	−707.3	305	1450
$(Ph_4P)_2SnCl_6$	−733.3	300	1570
K_2SnCl_6	−702.5	-	1650
Estimated error	± 0.5	± 20	± 20

5.4 ^{119}Sn NMR Study of $(Bu_4N)_2SnCl_6$

Though this sample belongs to the same series of compounds discussed in the previous section, it shows a remarkable difference in its NMR spectrum. So it is discussed alone in this section. Figure 5.4.1 shows the ^{119}Sn CPMAS spectra of this compound at both 74.63 MHz and 111.862 MHz. Contrary to the other spectra, they give three main sharp lines with linewidths of ca. 30 Hz. The − 736.4 ppm peak observed at higher field was not detected when the spectrum was recorded at 74.63 MHz two weeks later, but the three lines with higher intensities remained. Moreover, as the sample was rerun at 111.862 MHz several months later, that peak was again not obtained. Hence minor chemical changes in the sample are believed to be the cause of the peak disappearance.

Examination of the two spectra reveals that the three lines are in fact due to chemical shifts, showing that three types of tin sites are present in the asymmetric unit. The lack of splitting due to scalar coupling and residual dipolar coupling in the spectra may well indicate that some sort of anionic motion exists. It should be borne in mind that splitting can only be observed provided the relaxation rate of ^{35}Cl spin states is sufficiently long. If, on the other hand, the transitions between the different spin states of the chlorine nuclei are very rapid, the ^{119}Sn nucleus will only "see" an average chlorine spin state. Dipolar coupling (also scalar coupling)

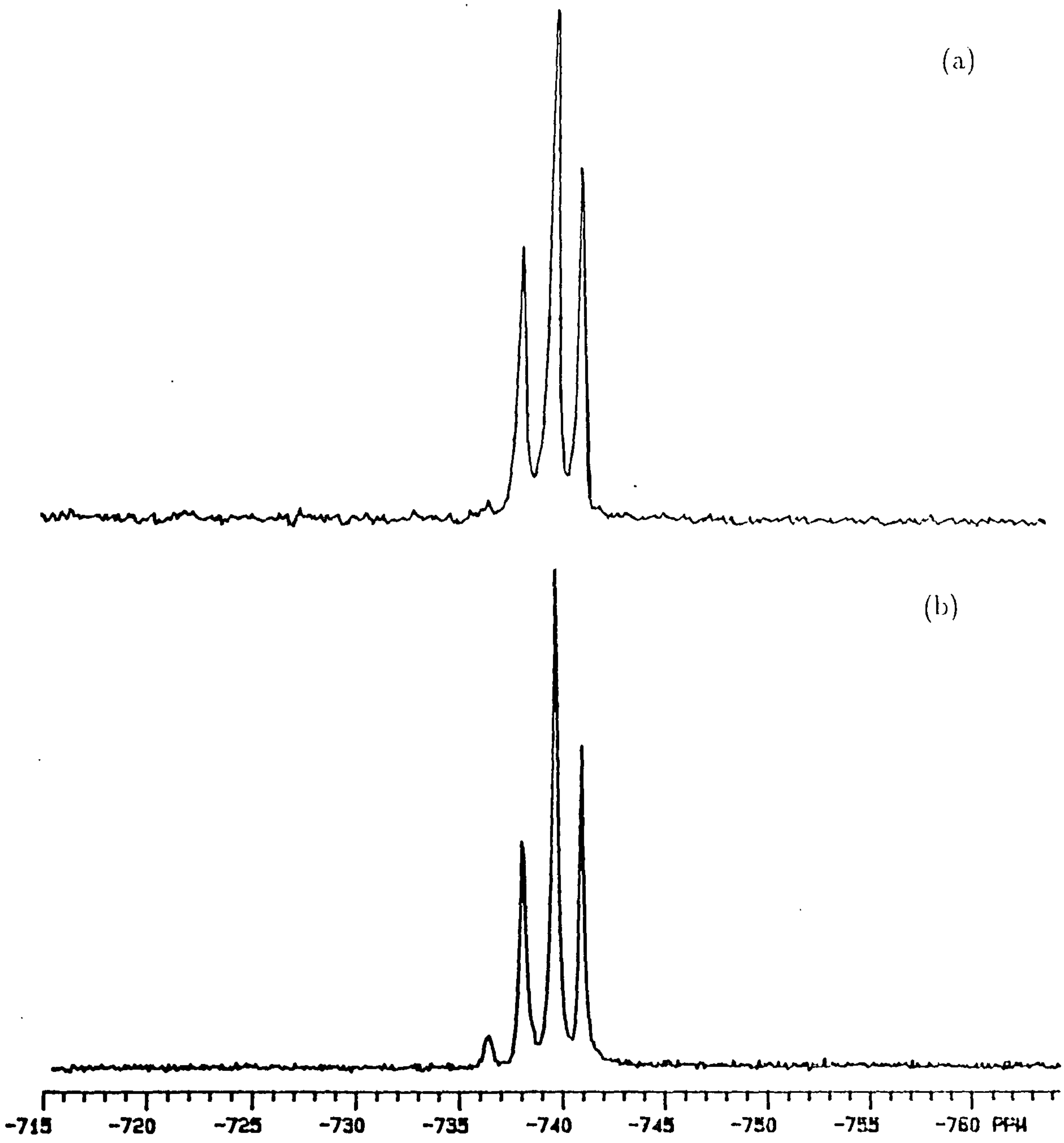

Figure 5.4.1: ^{119}Sn CPMAS spectra of $(Bu_4N)_2SnCl_6$, obtained at room temperature, and (a) 74.63 MHz and (b) 111.86 MHz. Spectrometer operating conditions: contact time 3ms (both); recycle delay 5s (both); number of transitions 1160 (a) and 604 (b); spinning speed 4410 (a) and 5000 (b) Hz.

of tin-chlorine will then be averaged out. This phenomenon is known as "self-decoupling" [31]. If motion of the anion is fast enough to induce "self-decoupling" of chlorine, the ^{119}Sn spectrum will only represent the chemical shift. This is understood to be the case for $(Bu_4N)_2SnCl_6$.

Low temperature measurements may be able to confirm this suggestion. Figure 5.4.2 illustrates the variable temperature experiments at between 0° and −50° C on a VXR-300 spectrometer (111.86 MHz). It is found that the chemical shifts move towards higher frequency by ca. 0.5 ppm every time the temperature decreases by 10° C. As the temperature decreases, all the three peaks become broader, indicating that as the anionic motions slow down the coupling between tin and chlorines gradually takes place. It is clear that the linewidth of the middle peak increases much quicker than those of the other two lines, suggesting that the three tin sites in the asymmetric unit undergo different degrees of motion. At $T = -30°$ C, the pattern of the middle peak becomes similar to those of other $SnCl_6{}^{2-}$ ions at ambient temperature (last section), where scalar coupling between tin and six equivalent chlorine atoms exists.

Since the linewidth of the split peak (due to scalar coupling) is much greater than the chemical shift differences among the three lines, line overlappings would be unavoidable. Therefore, a detailed analysis of the splitting pattern is impossible. Nevertheless, the low temperature measurements affirm the existence of fast molecular motion, and hence "self-decoupling" in this compound. The slight chemical shift differences at various temperatures are attributed to a temperature-dependent factor.

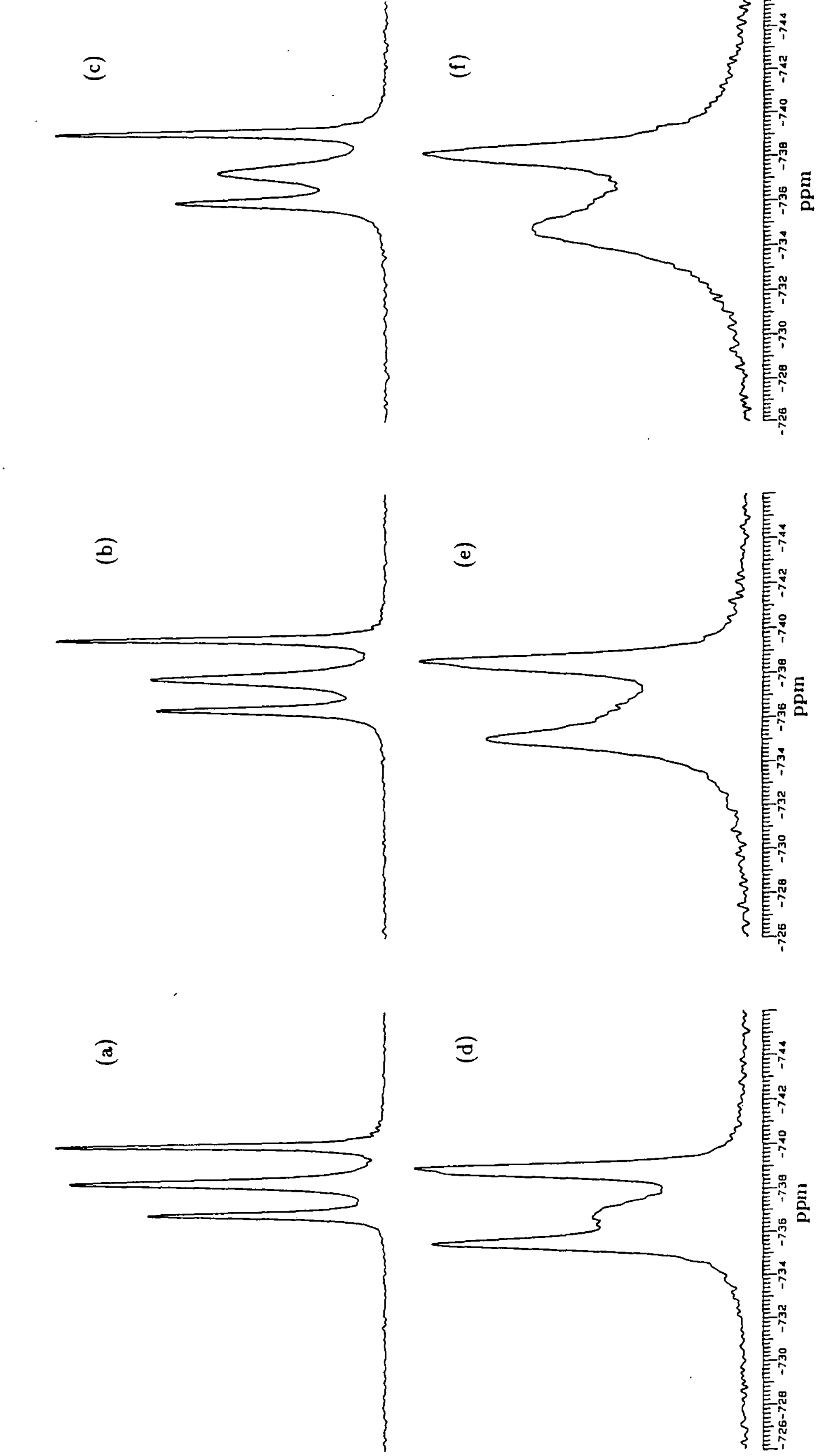

Figure 5.4.2: ^{119}Sn variable temperature spectra obtained at 111.86 MHz, and (a) 0° C; (b) −10° C; (c) −20° C; (d) −30° C; (e) −40° C; (f) −50° C.

References

1. I. E. Kundla and M. Alla, *Proc. XX Cong. Ampere*, Tallinn, E.I. Kundla, E.T Lippmaa and T. Saluvere (ed.), Springer, (1979)
2. S.J. Opella, M.H. Frey and T.A. Cross, *J. Amer. Chem. Soc.*, **101**, 5856 (1979).
3. C.J. Groombridge, R.K. Harris, K.J. Packer, B.J. Say and S.F. Tanner, *J. Chem. Soc. Chem. Commun.*. **4**, 174 (1980).
4. M.H. Frey and S.J. Opella, *J. Chem. Soc., Chem. Commun.*, **11**, 474 (1980).
5. J.G. Hexem, M.H. Frey and S.J. Opella, *J. Amer. Chem. Soc.*, **103**, 224 (1981).
6. A. Naito, S. Ganapathy, K. Akasaka and C.A. McDowell, *J. Chem. Phys.*, **74**, 3190 (1981).
7. A. Naito, S. Ganapathy and C.A. McDowell, *J. Chem. Phys.*, **74**, 5393 (1981).
8. N. Zumbulyadis, P.M. Henrichs and R.H. Young, *J. Chem. Phys.*, **75**, 1603 (1981).
9. S.J. Opella, J.G. Hexem, M.H. Frey and T.A. Cross, *Philos. Trans. R. Soc. London A*, **299**, 665 (1981).
10. J.G. Hexem, M.H. Frey and S.J. Opella, *J. Chem. Phys.*, **77**, 3847 (1982).
11. A. Naito, S. Ganapathy and C.A. McDowell, *J. Magn. Reson.*, **48**, 367 (1982).
12. J. Bohm, D. Fenzke and H. Pfeifer, *J. Magn. Reson.*, **55**, 197 (1983).
13. A.C. Olivieri, L. Frydman and L.E. Diaz, *J. Magn. Reson.*, **75**, 50 (1987).
14. A.C. Olivieri, *J. Magn. Reson.*, **81**, 201 (1989).

15. E.M. Menger and W.S. Veeman, *J. Magn. Reson.*, **46**, 257 (1982).

16. J.W. Diesveld, E.M. Menger, H.T. Edzes and W.S. Veeman, *J. Amer. Chem. Soc.*, **102**, 7935 (1980).

17. R.K. Harris and A. Root, *Moleculer Phys.*, **66**, 993 (1989).

18. R.K. Harris, *J. Magn. Reson.*, **78**, 389 (1988).

19. E.A.C. Lucken, *Nuclear Quadrupolar Coupling Constants*, Academic Press, (1969).

20. G.A. Miller and E.O. Schlemper, *Inorg. Chim. Acta*, **30**, 131 (1978).

21. R.K. Harris, A. Sebald, D. Furlani and G. Tagliavini, *Organomet.*, **7**, 388 (1988).

22. P.G. Huggett, R.J. Lynch, T.C Waddington and K. Wade, *J. Chem. Soc. Dalton*, 1164 (1980).

23. P. Jonsen, Private communication.

24. O. Knop, T.S. Cameron, M.A. James and M. Falk, *Can. J. Chem.*, **61**, 1620 (1983).

25. J.A. Lerbscher and J. Trotter, *Acac. Cryst.*, **B32**, 2671 (1976).

26. T.R. Brill, R.C. Gearhart and W.A. Welsh, *J. Magn. Reson.*, **13**, 27 (1974)

27. P. Chu, J.H. Lunsford and D.J. Zalewski, *J. Magn. Reson.*, **87**, 68 (1990).

28. D.E. Woessner and J.C. Trewlla, *J. Magn. Reson.*, **59**, 352 (1984).

29. R.J.C. Brown, B.K. Hunter, M. Mackowiak and S. Segel, *J. Magn. Reson.*, **50**, 218 (1982).

30. J.J. Van Derklink and C. Dimitropoulos, *J. Mol. Struct.*, **58**, 359 (1980).

31. H.W. Spiess, U. Haeberlen and H. Zimmermann, *J. Magn. Reso.*, **25**, 55 (1977).

Chapter VI

Multinuclear magnetic resonance studies of solid state organooxotin compounds

6.1 Introduction

In this chapter, solid-state NMR techniques used to investigate some new structural forms of organooxotin compounds, recently discovered by R. R. Holmes et al. [1-8], are discussed. The formation of these new classes of organotin materials utilize the interaction of an aryl- or alkyl-stannonic acid with either a carboxylic acid or a phosphorus-containing acid. In fact, as early as 1922, Lambourne reported that reactions of alkylstannonic acids with carboxylic acids resulted in organotin derivatives based on the formula $[MeSn(O)O_2CR]_3$ [9]. However, the possible structural features of these derivatives were not revealed until recently by Holmes and co-authors.

The structures of these compounds were determined by X-ray studies. It was found that a variety of compositions is present, which can be mainly classified as 'drum': $[RSn(O)O_2CR']_6$; 'cube': $[RSn(O)O_2PR'_2]_4$; 'ladder' or 'open-drum': $[(RSn(O)O_2CR')_2(RSn(O_2CR')_3)]_2$, 'butterfly': $[RSn(OH)(O_2PR'_2)_2]_2$ and 'oxygen-capped': $[(RSn(OH)O_2PR'_2)_3O][R'_2PO_2]$, where R and R′ refer to alkyl groups. Their common structural characteristic was described as having hexacoordinated tin atoms in a four-membered stannoxane ring $(-Sn-O-)_2$. The individual crystal structures are described in sections 3 - 6.

Solution NMR was also used by the authors of references [1-8] to investigate the structural interconversions among some of these organooxotin compounds. For example, a ladder formulation may undergo transformation to form a drum by a hydrolysis reaction. Furthermore, a drum may be opened up to yield a ladder form in the presence of excess acid. Equation 6.1.1 illustrates this interconversion. A transformation may also occur between cube and oxygen capped forms as demonstrated by Equation 6.1.2:

$$[(RSn(O)O_2CR')_2RSn(O_2CR')_3]_2 + 2H_2O \longleftrightarrow [RSn(O)O_2CR']_6 + 4RCO_2H \qquad 6.1.1$$

$$[RSn(O)O_2PR']_4 + 2H_2O \longleftrightarrow [(RSn(OH)O_2PR'_2)_3O][R'_2PO_2] + RSn(O)OH \qquad 6.1.2$$

From the above two equations it may be concluded that, hydrolytically, drum forms are more stable than ladders, and oxygen-capped cluster arrangements are more stable than cube compositions.

Although solution NMR has been widely used to investigate these classes of materials, solid-state NMR data have not been seen reported so far. What follows in this chapter is a résumé of the solution-state NMR studies followed by the report of an investigation of four powder samples having the compositions of drum, cube and oxygen-capped. These samples were kindly provided by Professor Holmes.

6.2 Solution NMR data

The solution NMR results, which appeared in the literature [1–8], are summarised in Table 6.2.1. The data chosen here include only four structural formations which are associated with the work presented in this thesis. It was revealed that the ^{119}Sn chemical shift is especially diagnostic of the type of structure present, since the values for each formation fall in a rather narrow chemical shift range, with no overlap between ranges, thus giving an unambiguous assignment. It was also found that the compounds retain their structures in the solution-state. Hence the data given in Table 6.2.1 can be used as an index for the assignments of the NMR spectra in the solid-state.

Table 6.2.1: Ranges of ^{119}Sn NMR data for n-butyloxotin clusters in $CDCl_3$

Cluster	δ_{Sn} /ppm	$^2J(^{119}Sn\text{-}O\text{-}^{31}P)$ /Hz	$^2J(^{119}Sn\text{-}O\text{-}^{117}Sn)$ /Hz
Drum $[RSn(O)O_2CR']_6$	−485 ∼ −490	-	-
Ladder $[(RSn(O)O_2CR')_2$ $(RSn(O_2CR')_3)]_2$	−520 ∼ −529 −546 ∼ −552 −606 ∼ −632	-	-
Cube $[RSn(O)O_2PR'_2]_4$	−460 ∼ − 475	109 ∼ 125	-
Oxygen-capped $[(RSn(OH)O_2PR'_2)_3O]$ $[O_2PR_2']$	−497 ∼ −509	127 ∼ 132	202

It should be noted that the data given in the above table are valid only when n-butyl groups are attached to tin atoms. The appearance of a methyl group bonded to tin would increase the ^{119}Sn chemical shift, for example, by ca. 15 ppm for a drum form. This is possibly associated with the relatively low electron-releasing nature of the methyl group (see Chapter 4). Also, the values for drum and ladder forms are for those which do not contain phosphorus atoms. The chemical shift values of these six-coordinated tin atoms are much lower than those of the penta-coordinated tin nuclei discussed in Chapter 4 (ca. 400 ppm). This fact provides further evidence that, when the coordination number at tin increases, a significant change of ^{119}Sn chemical shift to lower frequencies takes place. Crystallographic analysis found that the tin atoms are equivalent for drum, cube and oxygen-capped compositions, whereas ladder compositions have three chemically inequivalent types of Sn atoms in the molecule. The NMR results, which show one resonance signal for drum, cube and oxygen-capped formations but three signals for ladder forms, are thus in agreement with the X-ray work.

6.3 Drum $[MeSn(O)O_2CMe]_6$

Organooxotin derivative $[MeSn(O)O_2CMe]_6$ (I), the product of a reaction between methylstannonic acid and glacial acetic acid, is an insoluble white powder. X-ray analysis [4,7] showed it to possess a drum-shaped arrangement with an idealized S_6 molecular symmetry as shown in Figure 6.3.1 (a). The Sn–O framework of the molecule can be described as a drum with top and bottom faces each being composed of a six-membered tristannoxane ring. The sides of the drum are thus formed by six four-membered distannoxane rings. The core of each of the side rings is spanned by a carboxylate group that forms a symmetrical bridge between two tin atoms, each of which is bonded to a methyl group to produce hexacoordination at tin. However, neither the six-membered rings nor the four-membered rings are planar, but folded along the Sn–Sn vectors, so that the oxygen atoms are directed towards the interior of the cavity as illustrated in Figure 6.3.1 (b). The six Sn atoms are chemically equivalent, as are the six tricoordinate oxygen atoms.

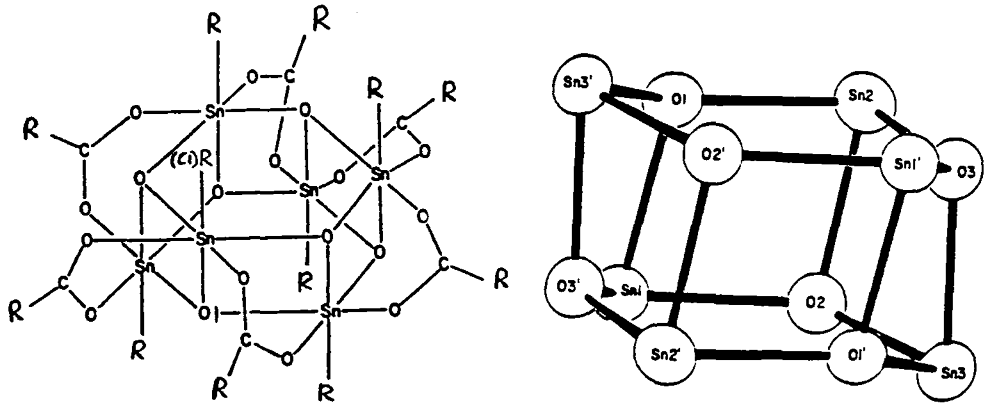

Figure 6.3.1: (a) Crystal stucture of drum $[MeSn(O)O_2CMe]_6$ when R=Me, compound (I). (b) The Sn-O framework of the molecule.

The ^{119}Sn CPMAS spectrum of this compound, obtained with high-power proton-decoupling at 74.63 MHz, is illustrated in Figure 6.3.2 (a). A single resonance is found at -471.3 ± 0.5 ppm, indicating that only one type of tin site is present in the molecule. This conclusion is consistent with that of the X-ray studies, i.e. all the tin atoms are chemically equivalent. The centreband, indicated by an arrow in the spectrum, is located by varying the speed of the magic-angle spinning. The existence of a great number of spinning sidebands implies a large shielding anisotropy at the tin atoms. The value of the chemical shift (-471.7 ppm) is ca. 15 ppm greater than the chemical shift range of a drum composition in solution (Table 6.2.1). However, considering the fact that this molecule has methyl groups bonded to tins instead of n-butyls, the chemical shift does fall in the expected drum range. This is because the substitution of butyl by methyl will reduce the electron-releasing ability of the alkyl group bonded tin, and the ^{119}Sn chemical shift thus increases.

Figure 6.3.2 (b) shows the expanded centreband. There are two pairs of satellite peaks present with coupling constants $|J^{iso}|$ 120 ± 15 Hz and 228 ± 15 Hz respectively. The splittings are assigned to the two-bond indirect coupling between the isotopic tin nuclei Sn-117 and Sn-119 through oxygen atoms, namely, the ^{119}Sn – O –^{117}Sn couplings of the top and bottom faces of the drum, and the ^{119}Sn – O –^{117}Sn couplings of the sides of the drum. It is unclear as to which of these two couplings corresponds to each value of the coupling constant obtained in the NMR spectrum. However, it is usually true that a shorter bond distance is related to a larger value of J coupling, which implies that the couplings of the tristannoxane rings have the value of 228 Hz, wheras those of the distannoxane rings have the value of 120 Hz.

The spinning sideband manifold has been analyzed by an iterative fitting program (see Chapter 7) to extract the values for the anisotropy and asymmetry of the shielding tensor at tin. The results, together with their reproducibility, are displayed in Table 6.3.1, and a typical plot of the fitting is presented in Figure 6.3.3.

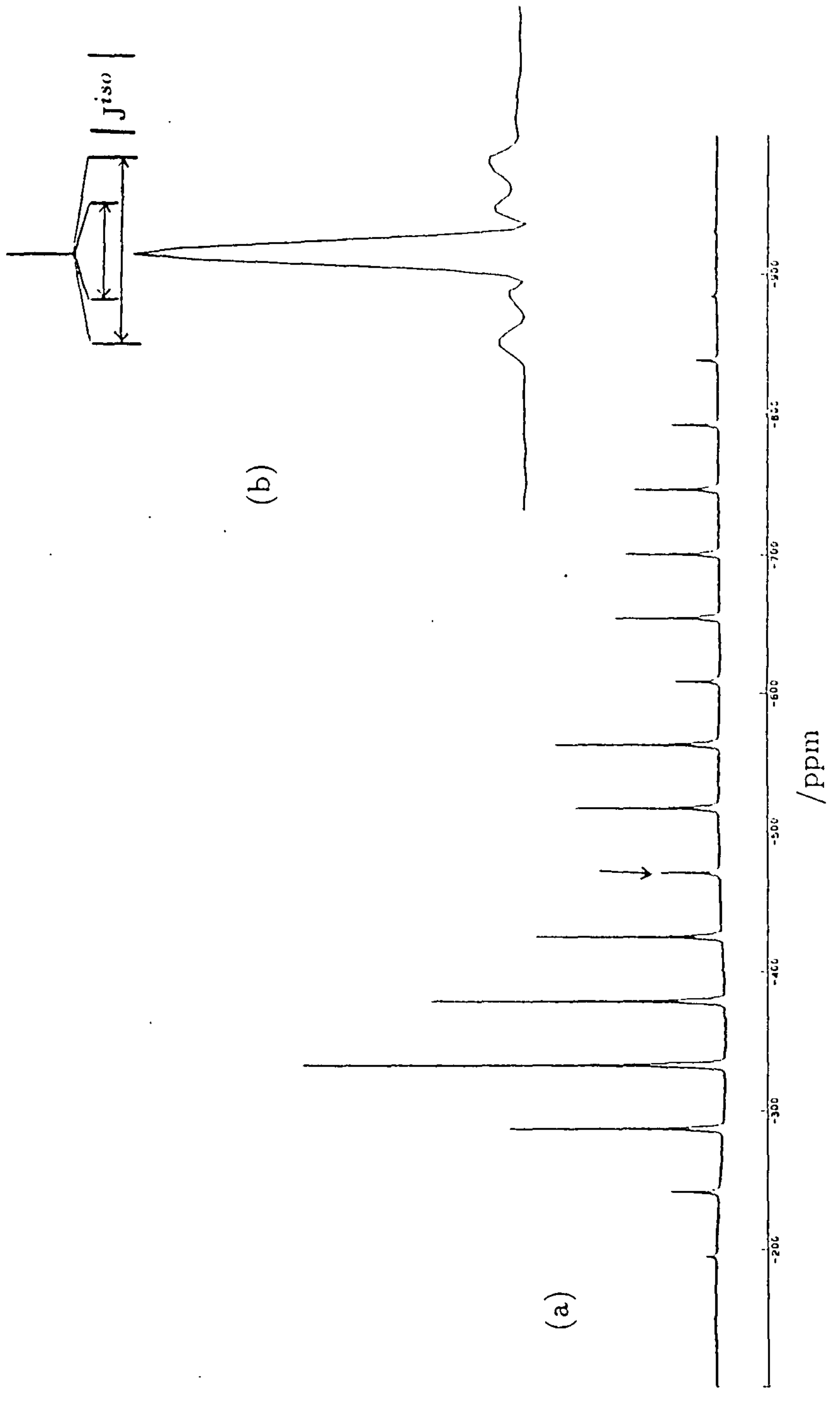

Figure 6.3.2: (a) ^{119}Sn CPMAS spectrum of compound (I), obtained at 74.63 MHz, and the centreband is indicated by an arrow. Spectrometer operating conditions: contact time 5ms; recycle delay 15s; number of transitions 3840; spinning speed 3260 Hz. (b) The expanded centreband after resolution enhancement.

It is shown that the tin nuclei are in an apparently axially symmetric system, although this cannot be exactly true. The orientation of the tensor may be inferred from the molecular symmetry, which suggests that the unique axis lies parallel to the C1–Sn–O1 direction (Figure 6.3.1). This is because the angle C1–Sn–O1 is 177.6° ± 2° (almost a straight line) and the other four oxygen atoms bonded to tin are nearly in a plane perpendicular to this line (the angles range from 77.7° to 101.5°) [7]. On the NMR scale, this structural formation will probably give an axial symmetry for tin atoms.

Table 6.3.1: Shielding tensor components at tin for drum $[MeSn(O)O_2CMe]_6$

spinning speed /Hz	δ_{Sn} /ppm	$\beth$ /ppm	η	σ_{11} /ppm	σ_{22} /ppm	σ_{33} /ppm
3430	−471.3	369	0.00	287	287	840
3500	−472.1	364	0.00	290	290	836
3260	−471.7	374	0.00	285	285	846
Average	−471.7 ± 0.4	369 ± 5	0.00	287 ± 3	287 ± 3	841 ± 5

Figure 6.3.4 is the ^{13}C CPMAS spectrum which shows three carbon resonances, with the linewidth of each being ca. 20 Hz. The signals marked with * are spinning sidebands. The peak at 7.0 ± 0.5 ppm is assigned to the methyl groups coupled to tin atoms. This assignment can be justified by the existence of the $^{117/119}Sn$ satellites due to the indirect coupling between the methyl carbon and the tin nucleus. The doublets of the satellite peaks, which are expanded in the Figure, result from the tin isotope nuclei ^{117}Sn and ^{119}Sn. This is because the value of J coupling between two nuclei is proportional to their magnetogyric ratios. With slightly different magnetogyric values (^{117}Sn being -9.578×10^7 and ^{119}Sn being -10.021×10^7 rad T^{-1} s^{-1}), their couplings to carbons will be slightly different accordingly. The coupling constant of 1140 ± 10 Hz is allocated to ^{117}Sn–^{13}C

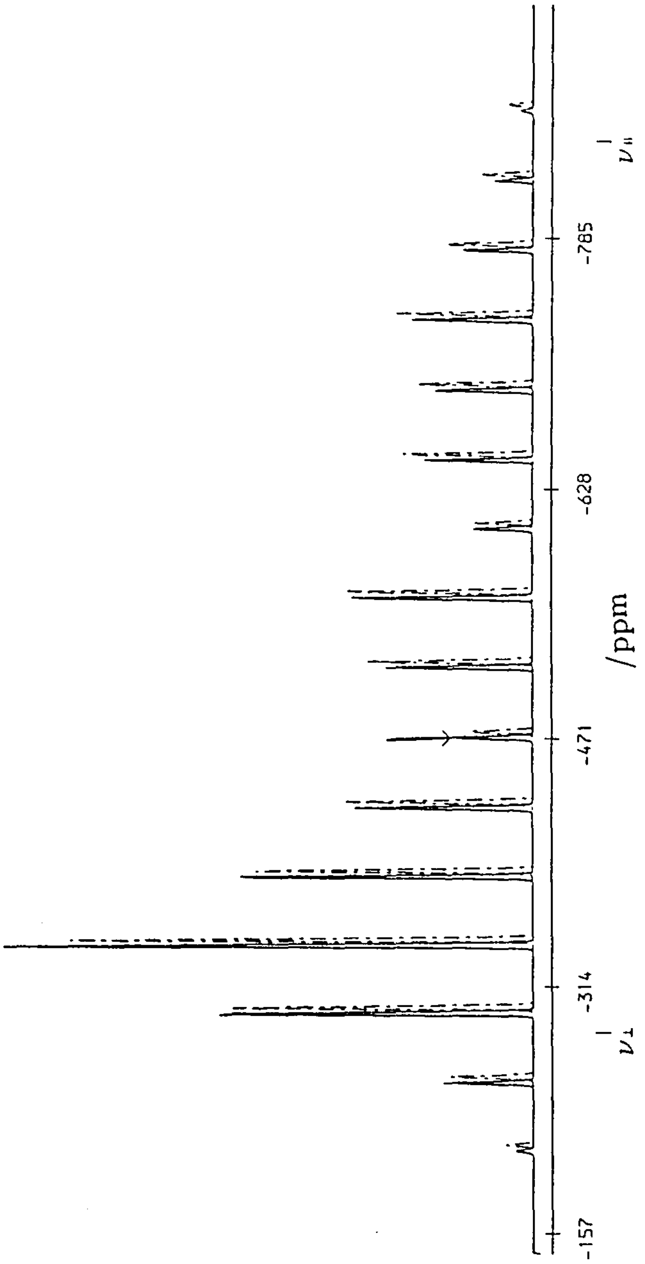

Figure 6.3.3: Fitting result of Figure 6.3.2. The arrow denotes the centreband, and $\nu_{\|}$, $\nu_{\perp}$ represent the positions of the shielding tensor components. Results: anisotropy = 374 ppm and asymmetry = 0.00.

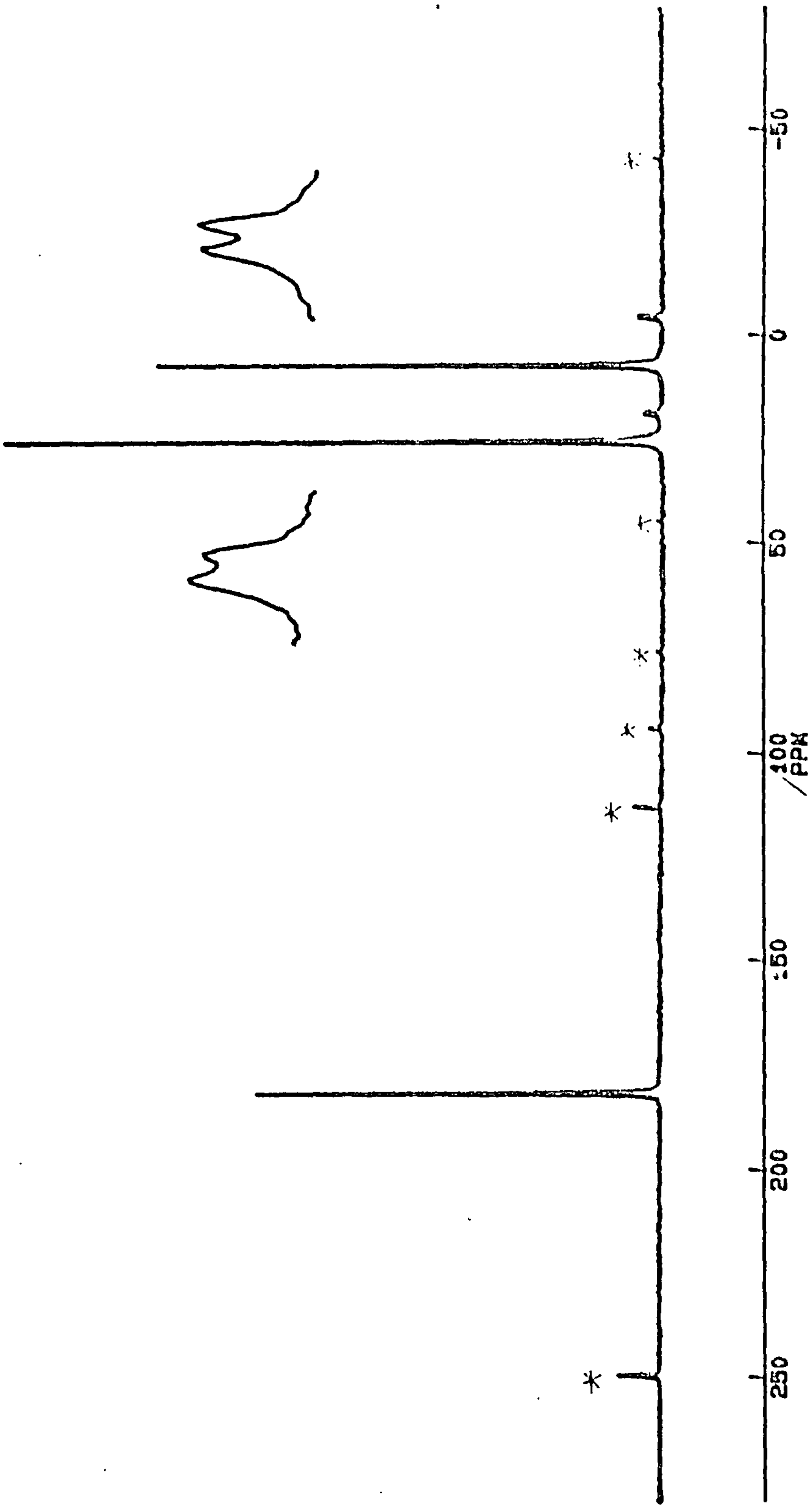

Figure 6.3.4:^{13}C CPMAS spectrum of compund (I) obtained at 50.32 MHz. The peaks marked with $*$ are the spinning sidebands, the magnified doublets are shown above. Spectrometer operating conditions: contact time 1ms; recycle delay 10s; number of transitions 2000; spinning speed 3440 Hz.

coupling, and that of 1180 ± 10 Hz to ^{119}Sn–^{13}C coupling.

It is clear that the signal at 25.2 ± 0.5 ppm is due to the methyl carbons bonded to the bridging carboxylates, while the resonances of the carbons in the carboxylate groups are at 180.9 ± 0.5 ppm. All the three peaks have narrow linewidths, implying that the compound is highly crystalline.

6.4 Drum $[n\text{-BuSn(O)O}_2\text{CMe}]_6$

Drum compound $[n\text{-BuSn(O)O}_2\text{CMe}]_6$ (II) has almost identical structural features to those of $[\text{MeSn(O)O}_2\text{CMe}]_6$ (I), discussed in the previous section. The only difference is that n-butyl groups, instead of methyl groups, are coupled to tin atoms. Both compounds have the same Sn–O framework, so Figure 6.3.1 can also be regarded as the structure of compound (II) apart from the alkyl groups (R) bonded to Sn atoms.

This compound is soluble in chloroform solution; the solution ^{119}Sn NMR spectrum, taken by Holmes, is shown in Figure 6.4.1 [10]. One resonance with two pairs of satellites is observed as for the solid-state spectrum of compound (I) (Fig.6.3.2). The chemical shift is at −486.0 ± 0.5 ppm, falling in the range for the drum composition. The two coupling constants $|^2J(^{117}\text{Sn} - \text{O} - ^{119}\text{Sn})^{iso}|$, one is related to the top and bottom faces of the drum, and the other one is related to the sides of the drum, are measured as ca. 70 and ca. 250 Hz, slightly different from those for solid compound (I).

Although the solution-state of compound (II) was proved to be pure drum, the corresponding solid-state was found to be much more complicated. Figure 6.4.2 demonstrates the ^{119}Sn CPMAS spectrum of compound (II) in the solid-state, obtained at 74.63 MHz on a Bruker CXP-200 spectrometer. The three arrows indicate the three centrebands located by variable spinning speed experiments. They are not equally spaced, showing that these signals are influenced by chemical shifts rather than any splittings due to indirect couplings. This suggestion is

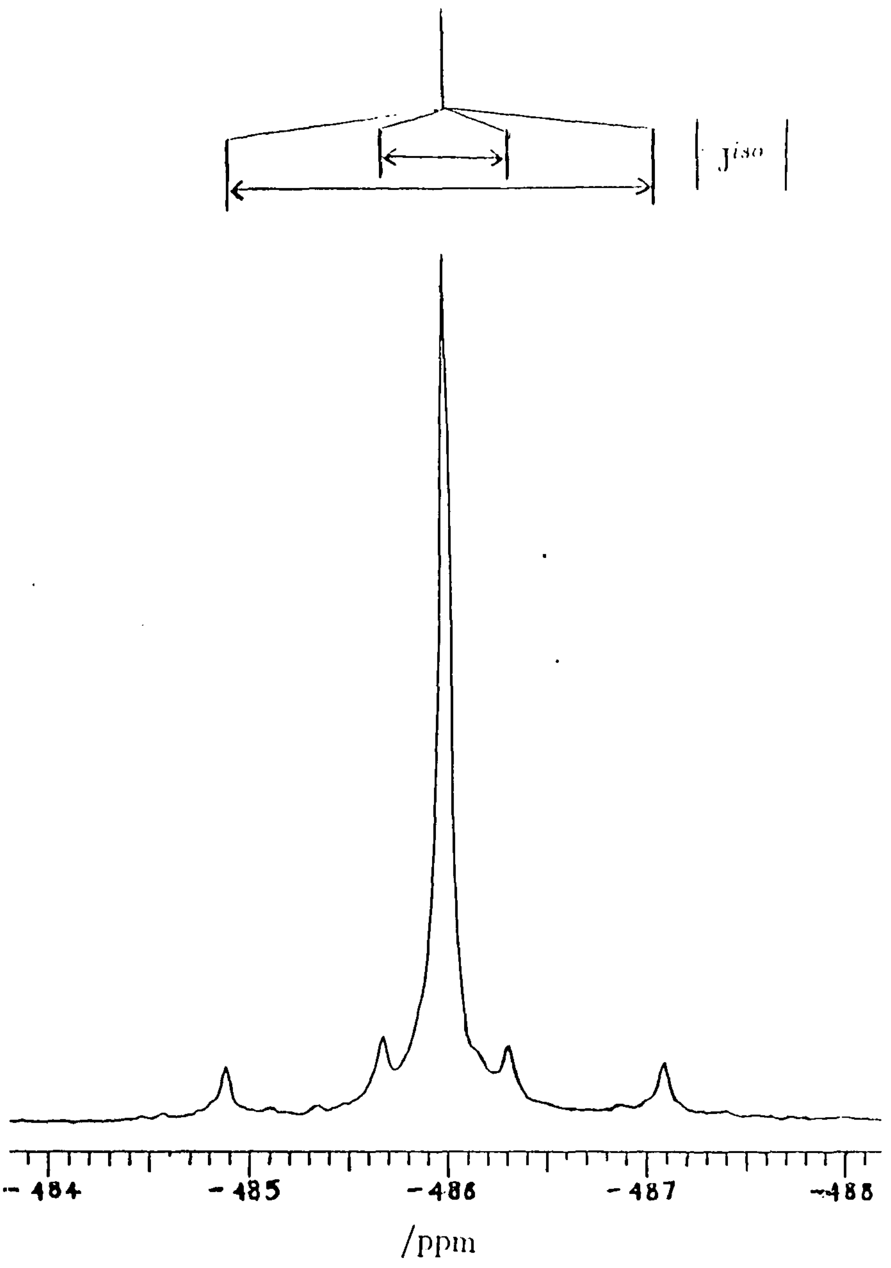

Figure 6.4.1: ^{119}Sn solution NMR spectrum of [n-BuSn(O)O$_2$CMe]$_6$, compound (II), obtained at 111.86 MHz [10].

supported by the spectrum taken at a different magnetic field (111.86 MHz), as displayed in Figure 6.4.3.

The expanded centrebands from both fields show further splittings, but they too appear to be due to chemical shifts. This is because both fields give essentially

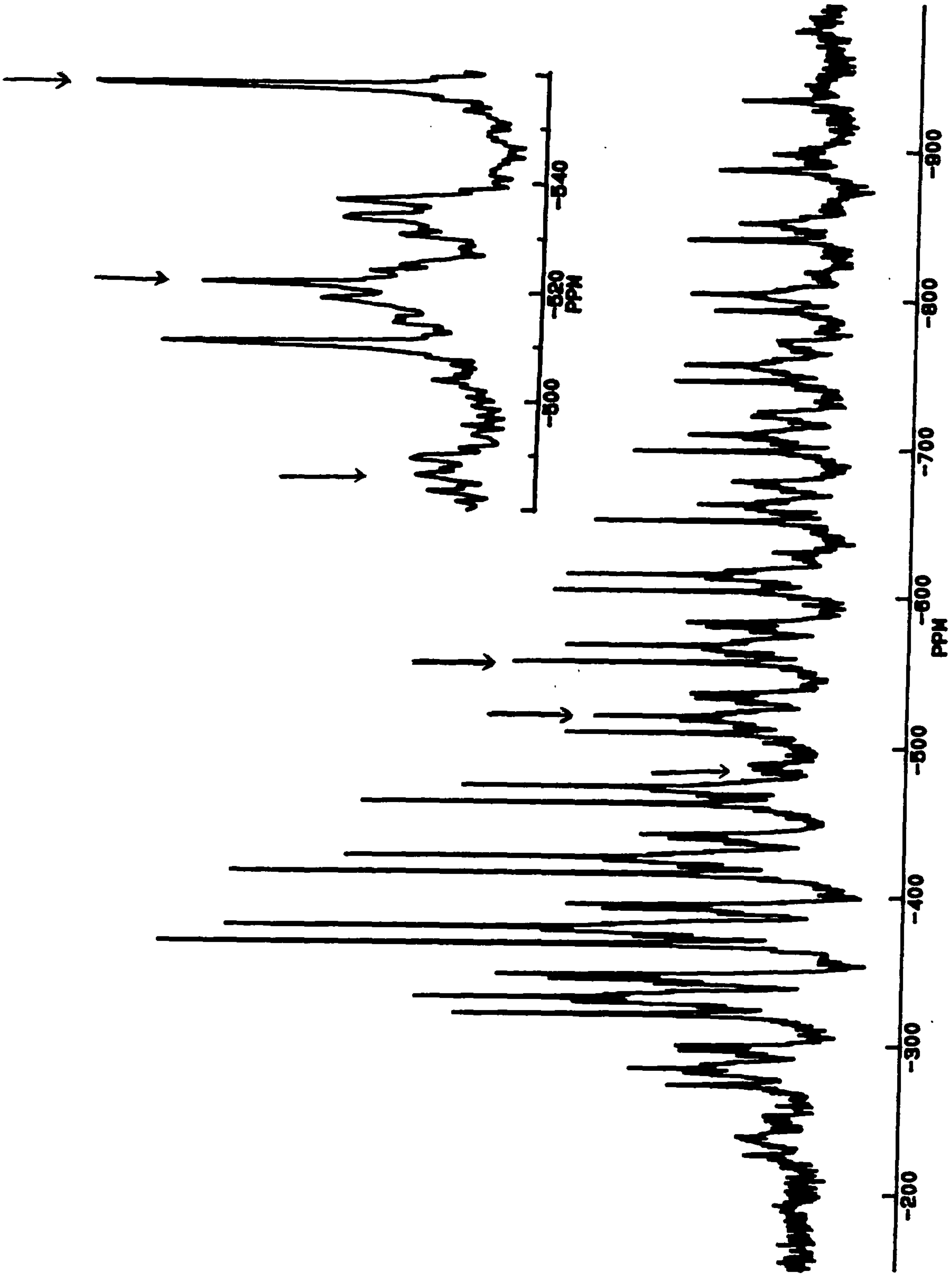

Figure 6.4.2: ^{119}Sn solid-state CPMAS spectrum of compound (II) obtained at 74.63 MHz. The centreband region is expanded on the right corner, and the centrebands are indicated by arrows. Spectrometer operating conditions: contact time 5ms; recycle delay 20s; number of transitions 2332; spinning speed 3520 Hz.

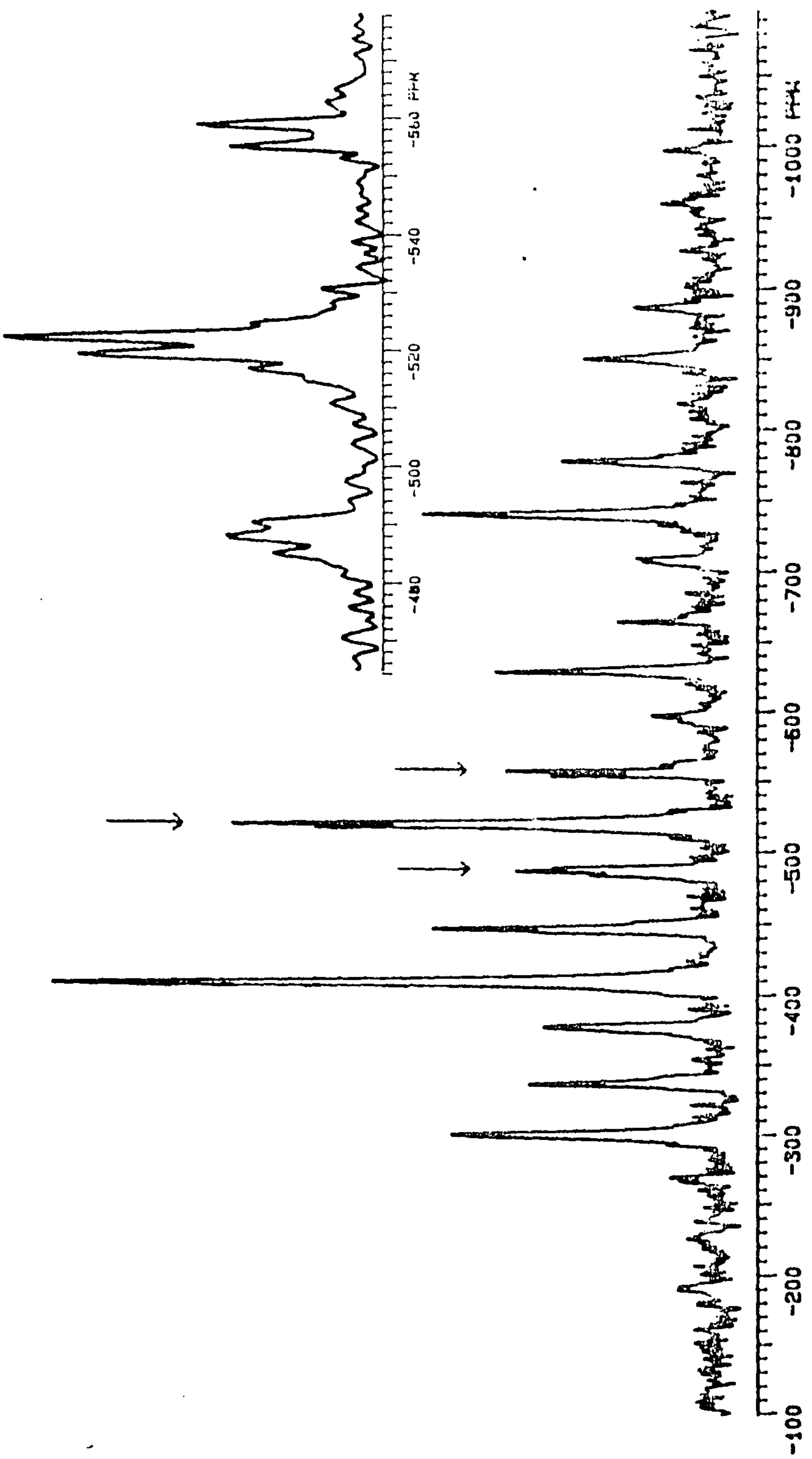

Figure 6.4.3: ^{119}Sn solid-state CPMAS spectrum of compound (II) as for Figure 6.4.2, but obtained at higher field (111.86 MHz). The centrebands are indicated and expanded on the right corner. Spectrometer operating conditions: contact time 5ms; recycle delay 20s; number of transitions 2800; spinning speed 12100 Hz.

the same values in units of ppm for each of the signals. The chemical shifts of the highest frequency peaks (−483, −486 and −489 ppm) may be associated with the drum structure (Table 6.2.1). One of these peaks, at −486 ppm, corresponds to the solution signal, but the origin of the other two peaks is unclear. The lower frequency signals near −521 and −557 ppm are within the range of the ladder compositions. The components of the band at −521 ppm are −518, −521 and −523 ppm while the components of the band at −557 ppm are −555, −557, −559 and −562 ppm.

The crystal structure of ladder formulation, produced by Holmes et al., is presented in Figure 6.4.4 [3]. The ladders have crystallographic C_i symmetry, which corresponds to the idealized molecular symmetry. Therefore, three chemically nonequivalent types of tin atoms (labelled as Sn1, Sn2 and Sn3 in Figure 6.4.4) exist in the molecule, which should result in three different ^{119}Sn chemical shifts. Atoms Sn1 and Sn2 are both hexacoordinated and have distorted octahedral geometry, whereas terminal atom Sn3 is seven-coordinated and has a pentagonal bipyramidal geometry. The Sn–O framework for the ladder is shown in Figure 6.4.4 (b). The four-membered stannoxane ring formed by Sn1, O1, Sn1′ and O1′ is planar, and the O2 atoms lie very nearly in this plane. Sn2 and Sn3 atoms lie outside this plane in opposite directions. The tricoordinate oxygen atoms tend toward planarity.

The appearance of bands was also observed in solution-state ^{119}Sn spectra for drum compound [n-BuSn(O)$O_2CC_6H_{11}$]$_6$ (V) [5] and for ladder compound [(n-BuSn(O)O_2CPh)$_2$(n-BuSn(O_2CPh)$_3$)]$_2$ (VI) [7]. The reason for the occurrence of multiplets is not clear. However, these multiplets may imply the existence of closely related drum forms and ladder compositions, which could not be revealed by X-ray analysis.

The low frequency signal assignable to the pair of terminal tin atoms of the ladder, in the range of −606 to −632 ppm was not detected for the solid state. This lack of low frequency peaks was also reported for a solution spectrum of ladder

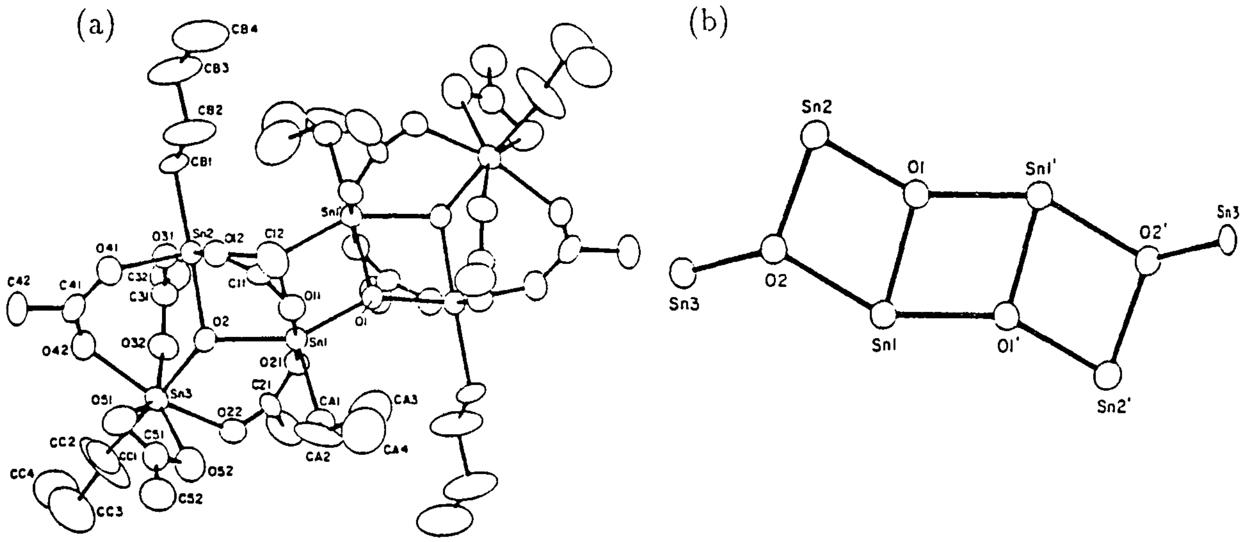

Figure 6.4.4: (a) Crystal structure of $[(\text{n-BuSn(O)O}_2\text{CMe})_2\text{-n-BuSn(O}_2\text{CMe})_3]_2$. (b) The Sn–O framework of the structure [3].

compound $[(\text{n-BuSn(O)O}_2\text{CMe})_2(\text{n-BuSn(O}_2\text{CMe})_3)]_2$ (VII) [3]. A rather broad line in this range was obtained for the ladder compound (VI). These observations lead one to suggest that the combination of bands with large linewidths and the likely line overlapping with the sidebands may be the reason which causes the low frequency resonances to be unobservable in the solid-state, especially given the poor signal-to-noise ratio of the spectrum. Thus, it seems likely that the compound as supplied was a mixture, rather than a pure composition.

The ^{13}C NMR spectrum of this compound was obtained at 50.32 MHz. The spectrum shows a very complicated pattern, as expected for a mixture. The highest frequency signals are assigned to the carboxylate carbons, whereas the other two groups of peaks are assigned to n-butyl carbons and methyl carbons respectively, as indicated in Figure 6.4.5. It is not feasible to allocate these resonances in any detail.

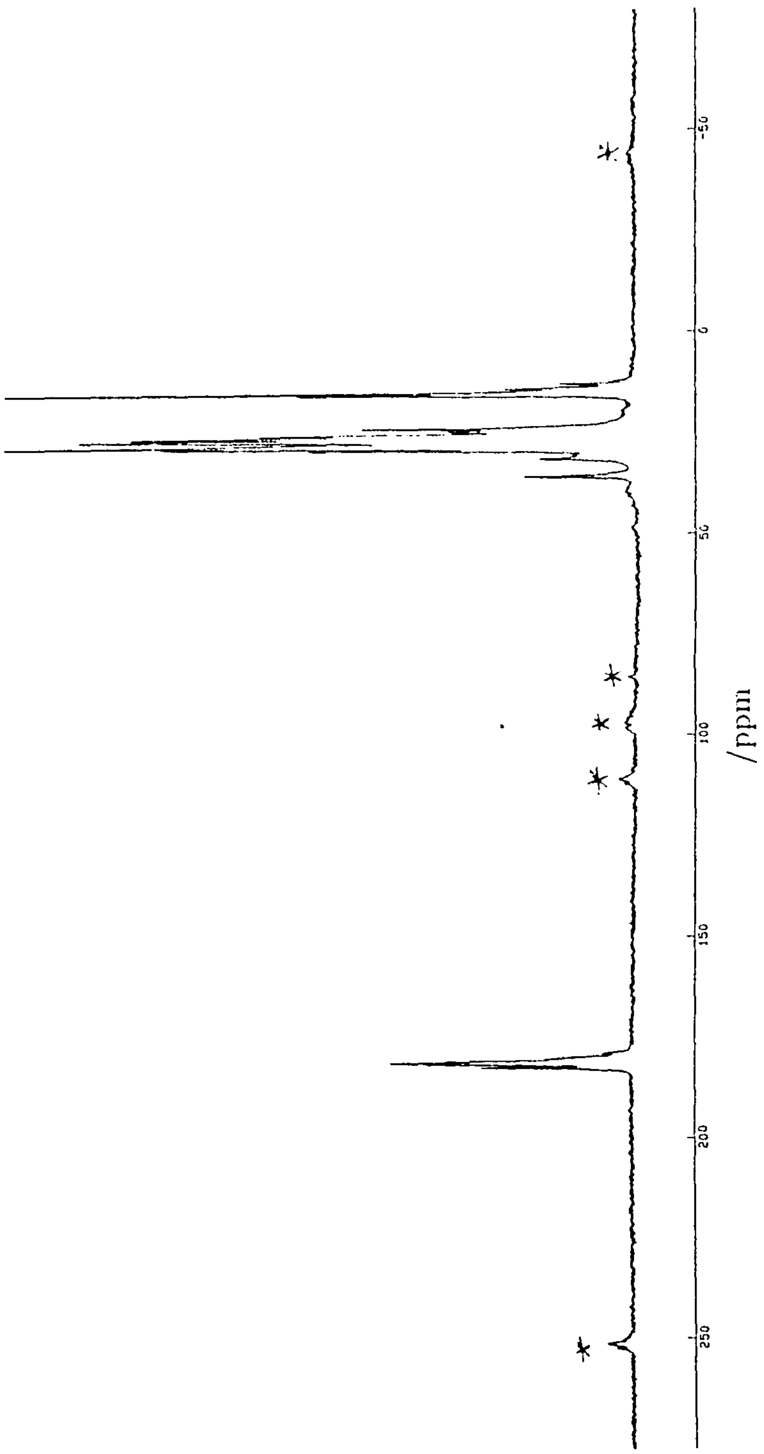

Figure 6.4.5: ^{13}C solid-state CPMAS spectrum of compound (II) obtained at 50.32 MHz. The peaks marked with * are the spinning sidebands. Spectrometer operating conditions: cantact time 1ms; recycle delay 10s; number of transitions 1450; spinning speed 3530 Hz.

6.5 Cube $[n\text{-BuSn(O)O}_2\text{P}(\text{C}_6\text{H}_{11})_2]_4$

Cube compositions are those obtained with phosphorus-based acids, and contain four tin atoms in a molecule. $[n\text{-BuSn(O)O}_2\text{P}(\text{C}_6\text{H}_{11})_2]_4$ (III) results from the reaction of n-butylstannoic acid with dicyclohexylphosphinic acid: its X-ray structure is shown in Figure 6.5.1 [4]. The molecule has a crystallographic D_2 symmetry in which each of the two crystallographically independent phosphorus atoms (PA, PB) is constrained to lie on a twofold axis, and all the tin atoms are chemically equivalent. The atoms of the asymmetric unit in the structure are those with unprimed labels, whereas the coordinates of atoms labelled as ′ and ″ etc. can be generated with the symmetry operators.

The core of the molecule is made up of four six-coordinated tin atoms and four trivalent oxygen atoms, which occupy the corners of a distorted cube. Each face is defined by a four-membered (–Sn–O–Sn–)$_2$ stannoxane ring. The top and bottom faces of the cube are open, but each of its side faces is bridged diagonally by a phosphinate between two tins, and the phosphinate bridges are symmetrical. As in the drum form, the (–Sn–O–Sn–) rings are not planar but bent so that the oxygen atoms are directed toward the interior of the cube.

Figure 6.5.2 displays the Tin-119 NMR spectrum for this cube compound in solid-state. A large number of spinning sidebands, each of which has a triplet pattern, are observed. The resonance signal (centreband) is at -465.5 ± 0.5 ppm, found by varying the magic-angle spinning speed. The value of the chemical shift is in the range associated with the cube formation (Table 6.2.1), confirming a cube form. The presence of a single chemical shift is consistent with the X-ray analysis, which shows that all Sn are equivalent. The triplet is due to the indirect coupling between tin and two equivalent phosphorus atoms, contrary to the fact that the phosphorus atoms (PA, PB) are actually not equivalent. The coupling constant is found to be 114 ± 3 Hz. The ^{119}Sn solution NMR [4] gave a triplet resonance at ca. -466.7 ppm with a $|^2J(^{119}\text{Sn} - \text{O} -^{31}\text{P})^{iso}|$ coupling constant of ca. 116

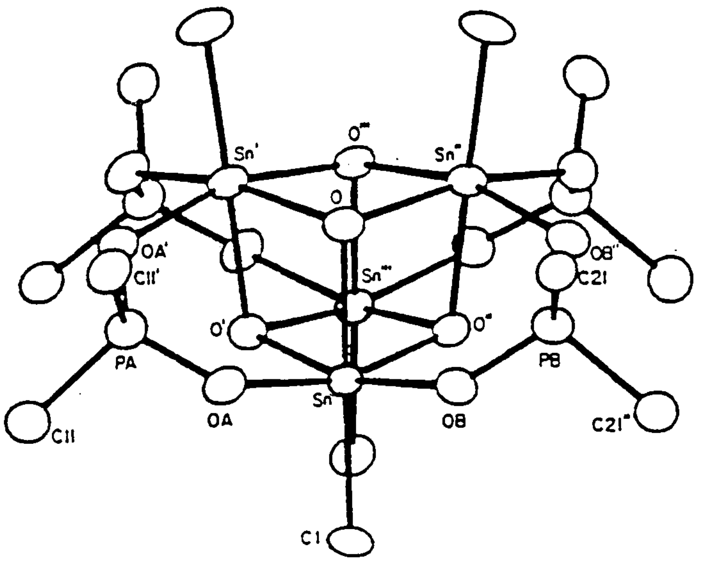

Figure 6.5.1: Crystal structure of cube [n-BuSn(O)$O_2P(C_6H_{11})_2]_4$, compound (III). All pendant carbons of the cyclohexyl and n-butyl groups are omitted for reason of clarity [4]. C1 refers to the n-Bu group; C11 and C21 represent the cyclohexyl groups.

Hz. The results are almost the same as those obtained from the solid-state. It is therefore comfirmed that the compound retains its structual integrity in solution.

Spinning sideband analysis was carried out for spectra spinning at different speeds, and the averaged results and the reproducibility are given in Table 6.5.1. The plot of one of the fittings is shown in Figure 6.5.3. It is revealed that the Sn atoms are in a nearly axial symmetric system. (The program is unable to distinguish between axial and near axial symmetry). The unique axis σ_{33} is probably lying close to the C1–Sn–O direction, i.e. the edge of the cube (Figure 6.5.1). This suggestion may be supported by the molecular symmetry and by the fact that C1–Sn–O nearly forms a straight line (angle C1–Sn–O = 178.2° ± 4°).

The ^{31}P MAS NMR spectrum (Figure 6.5.4), obtained with high-power proton decoupling and single pulses at 121.4 MHz, shows two triplets, with the same intensity, centred at 56.9 ± 0.5 ppm and 55.3 ± 0.5 ppm respectively, suggesting two types of phosphorus atoms present in the molecule. These two triplet patterns were

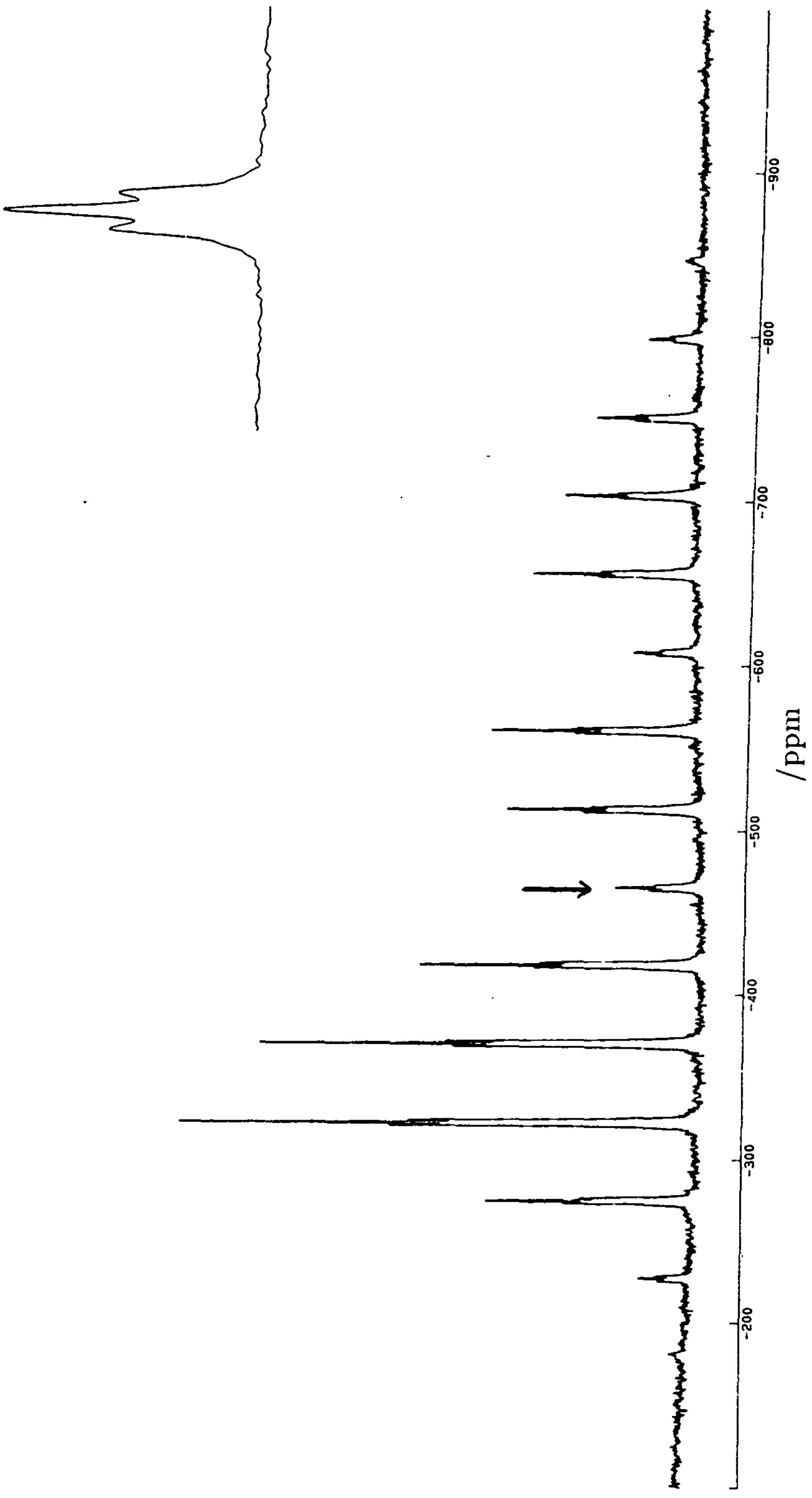

Figure 6.5.2: ^{119}Sn CPMAS spectrum of compound (III) in solid-state obtained at 74.63 MHz. The arrow indicates the centreband, which is expanded on the right corner. Spectrometer operating conditions: contact time 5ms; recycle delay 15s; number of transitions 4614; spinning speed 3550 Hz.

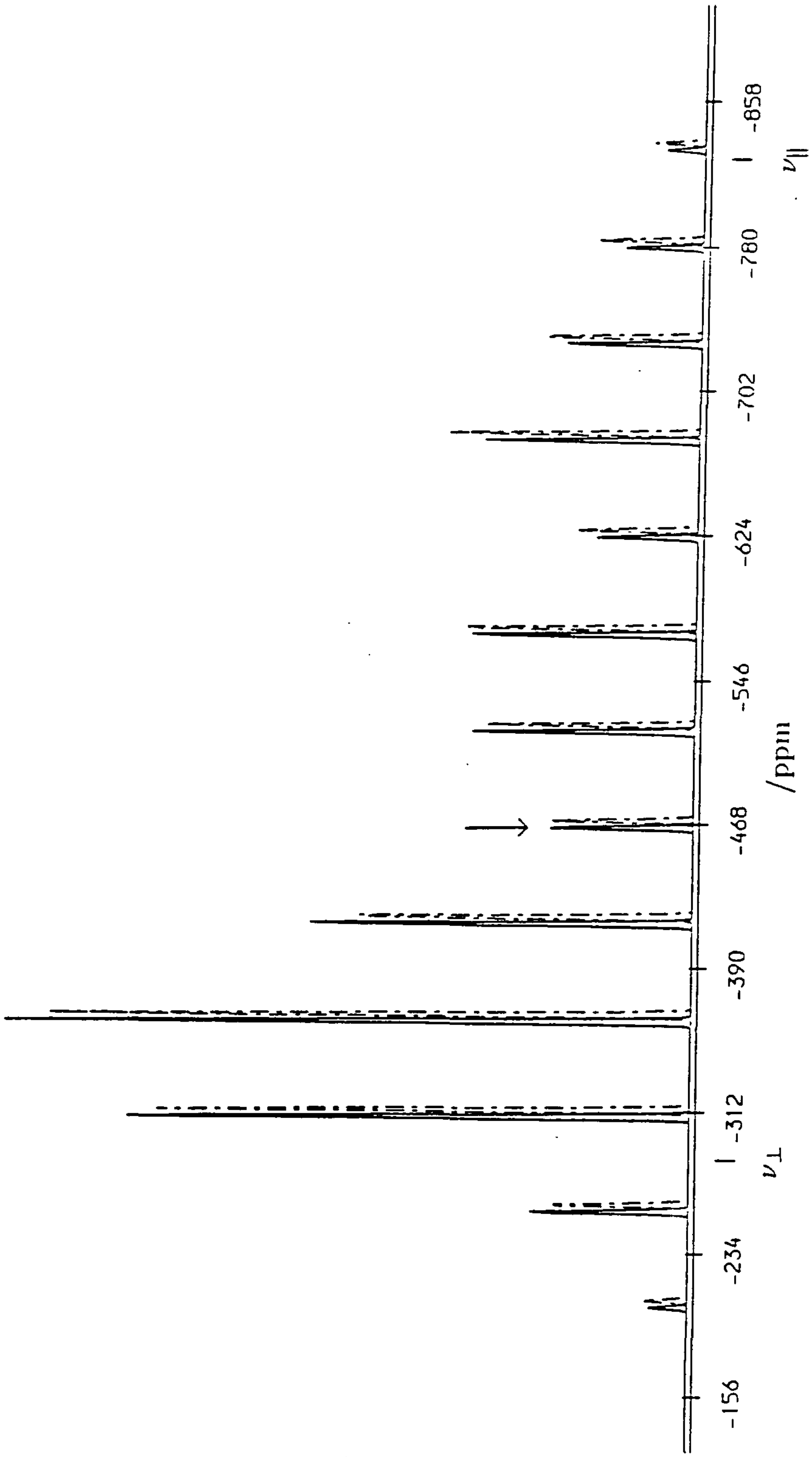

Figure 6.5.3: Fitting result of Figure 6.5.2: $\beth$ = 360 ppm and η = 0.00.

confirmed by the spectrum obtained at 81.01 MHz. Judging from the structure and the relative intensities of the peaks, it is apparent that the couplings are due to the two-bonded interactions between phosphorus and tin nuclei through oxygen atoms: ^{31}P–O–$^{117/119}$Sn. The values of the two coupling constants are 113 and 117 Hz respectively, and can be regarded as identical within experimental error (the digital error is 3 Hz), and also equal to the value obtained from the ^{119}Sn spectrum.

Thus, NMR studies are in conformity with the X-ray results that all the tin atoms are chemically equivalent, whereas two chemically different phosphorus atoms exist in the molecule. However, the indirect coupling constants of Sn–PA and Sn–PB happen to be the same (ca. 115 Hz). This fact explains the ^{119}Sn spectrum (Figure 6.5.2) which shows one triplet instead of two doublets. It is not clear, however, as to which signal should be assigned to which of the two phosphorus atoms. This is partially because the two chemical shifts are very close and partially because so far there has been little data available for comparison.

Table 6.5.1: Shielding tensor components at tin for cube $[\text{n-BuSn(O)O}_2\text{P(C}_6\text{H}_{11})_2]_4$

spinning speed /Hz	δ_{Sn} /ppm	$\beth$ /ppm	η	σ_{11} /ppm	σ_{22} /ppm	σ_{33} /ppm
3550	−465.5	360	0.05	282	282	822
3900	−466.0	361	0.00	286	286	827
Average	−465.8 (±0.3)	361 (±1)	0.02 (±0.03)	284 (±2)	284 (±2)	825 (±3)

The data in parentheses are the estimated errors.

The ^{13}C CPMAS spectrum as shown in Figure 6.5.5 gives support to the argument that two different phosphorus atoms exist. The signal at 13.9 ± 0.5

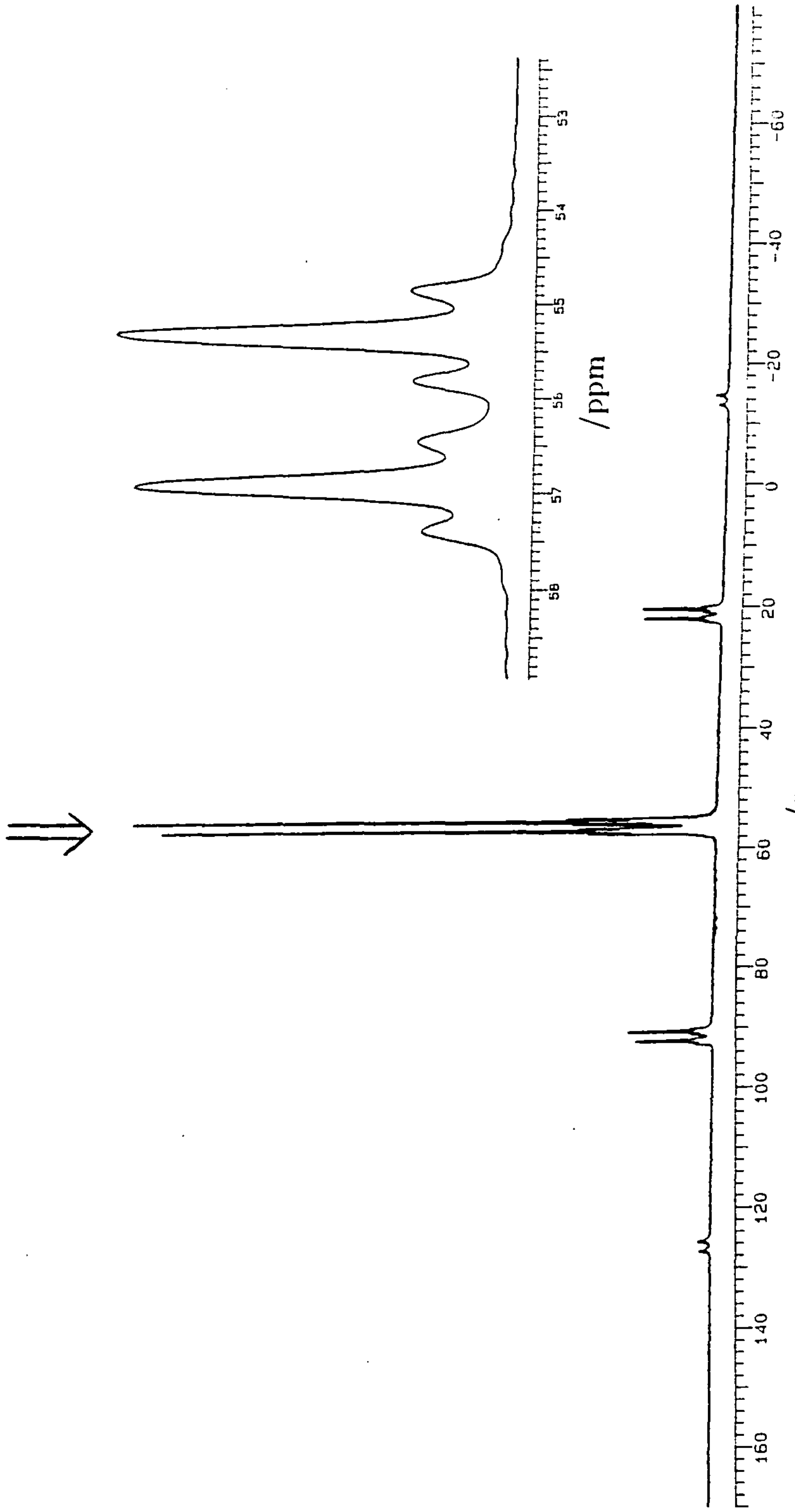

Figure 6.5.4: ^{31}P MAS NMR spectrum of compound (III) in solid-state obtained at 121.42 MHz. The centrebands are indicated by an arrow and expanded above. Spectrometer operating conditions: recycle delay 120s; number of transitions 50; spinning speed 4230 Hz.

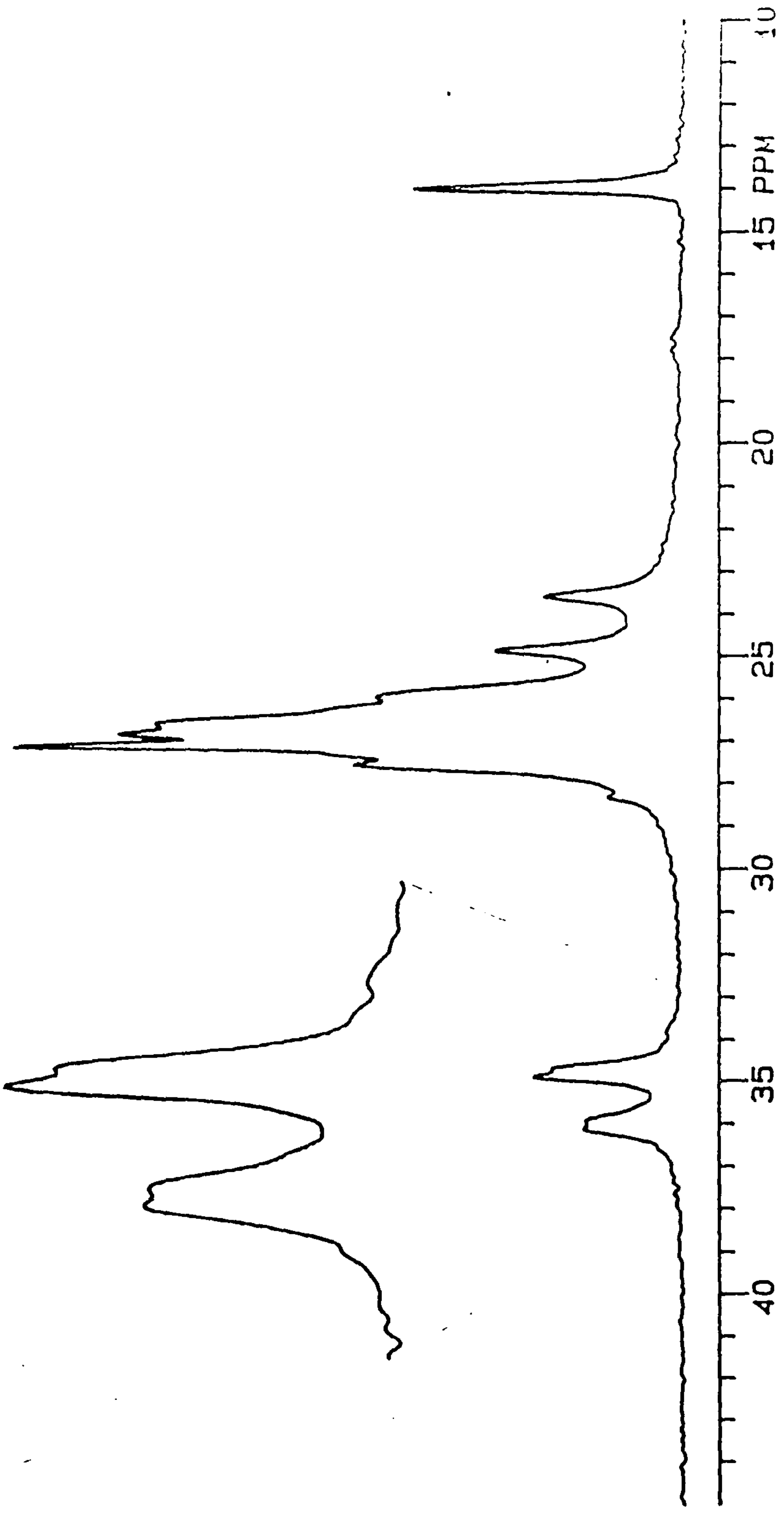

Figure 6.5.5: ^{13}C CPMAS spectrum of compound (III) in solid-state obtained at 75.43 Mhz. Spectrometer operating conditions: contact time 1ms; recycle delay 2s; number of transitions 200; spinning speed 4750 Hz.

ppm is obviously due to the CH_3 in n-butyl groups. The group of peaks ranging from 23.5 ppm to 28.5 ppm may be assigned to the CH_2 carbons from the n-butyl and the C_6H_{11} groups. The chemical shifts of the CH carbons (in C_6H_{11} groups) should be in the range 30 to 40 ppm. In this range, two peaks are observed, each with a doublet splitting (expanded above). It is not difficult to notice that the linewidths of these two signals are twice as wide as those of others. Hence these doublet splittings do in fact exist and do not arise from noise. Considering the fact that this carbon is bonded to a phosphorus nucleus, it is believed that J couplings between carbon and phosphorus atoms are the cause of the splittings. Since there are two crystallographically independent cyclohexyl groups present (one bonded to PA, another bonded to PB), two different chemical shift values are expected.

Two ways of assignments are possible: (1) the splitting between line 1 and line 2 (see Figure 6.5.5) (and line 3 and line 4) is the J^{iso} coupling constant, which gives $|J^{iso}| = 13.5 \pm 0.6$ Hz; (2) the splitting between line 1 and line 3 (and line 2 and line 4) is the coupling constant, which gives $|J^{iso}| = 93.0 \pm 0.6$ Hz. Of the two assignments, the first one seems more likely, since the intensities and the shapes of line 1 and line 2 (and line 3 and line 4) are very similar whereas those of line 1 and line 3 (and line 2 and line 4) are not. If so, the chemical shifts of the CH carbons in the two chemically distinct cyclohexyl groups will be at 34.8 ± 0.1 and 36.0 ± 0.1 ppm respectively, their couplings to ^{31}P atoms are the same with magnitude of 13.5 ± 0.6 Hz.

6.6 Oxygen–capped $[(n\text{-}BuSn(OH)O_2PPh_2)_3O][Ph_2PO_2]$

Figure 6.6.1 shows the crystallographic structure of oxygen–capped composition $[(n\text{-}BuSn(OH)O_2PPh_2)_3O][Ph_2PO_2]$ [2]. The synthesis of this product can be described by the following equation:

$$3n\text{-}BuSn(O)OH + 4Ph_2PO_2H \longrightarrow$$

$$[(n - BuSn(OH)O_2PPh_2)_3O][Ph_2PO_2] + 2H_2O \qquad (6.6.1)$$

The basic framework of this structure comprises a tristannoxane ring in a cyclohexane chair arrangement, forming three distannoxane ring units. These three four-membered rings may be regarded as a portion of a cube, hydroxyl groups comprising the oxygen components of the ring system. It is believed that one tricoordinate oxygen atom caps one side of the framework while three diphenylphosphinate groups span between two adjacent tin atoms. The three tin atoms are hexacoordinated and are chemically equivalent. There are also hydrogen-bonding interactions present between the Sn–OH framework and the anionic phosphinate ($Ph_2PO_2^-$) group.

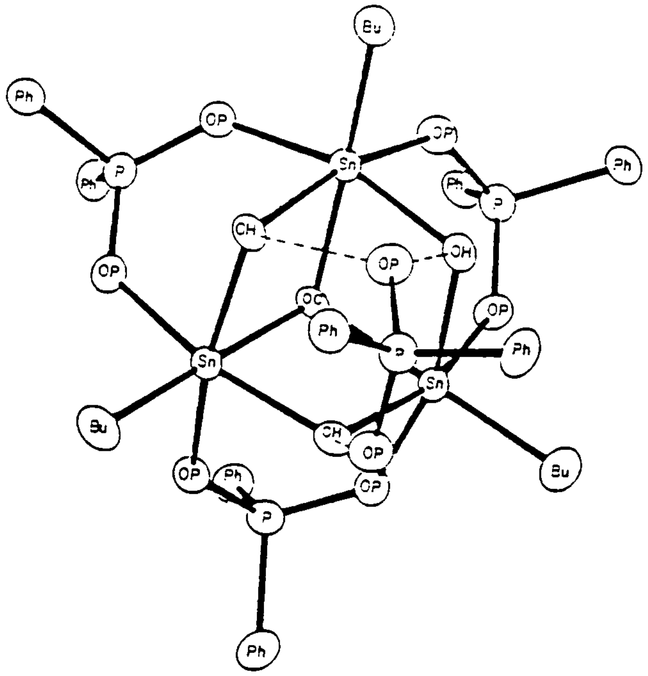

Figure 6.6.1: Crystal structure of $[(n\text{-}BuSn(OH)O_2PPh_2)_3O][Ph_2PO_2]$, compound (IV) [2]. Pendant atoms of the three n-Bu groups and of the eight Ph groups are omitted for purpose of clarity. The dashed lines show the hydrogen-bonding interaction.

The solution-state ^{119}Sn NMR spectrum for the oxygen–capped cluster shows a single resonance with triplet character centred at -497.0 ± 0.5 ppm (Fig 6.6.2), and having a coupling constant of $|^2J(^{119}Sn - O - ^{31}P)^{iso}| = 132.0 \pm 5$ Hz. This

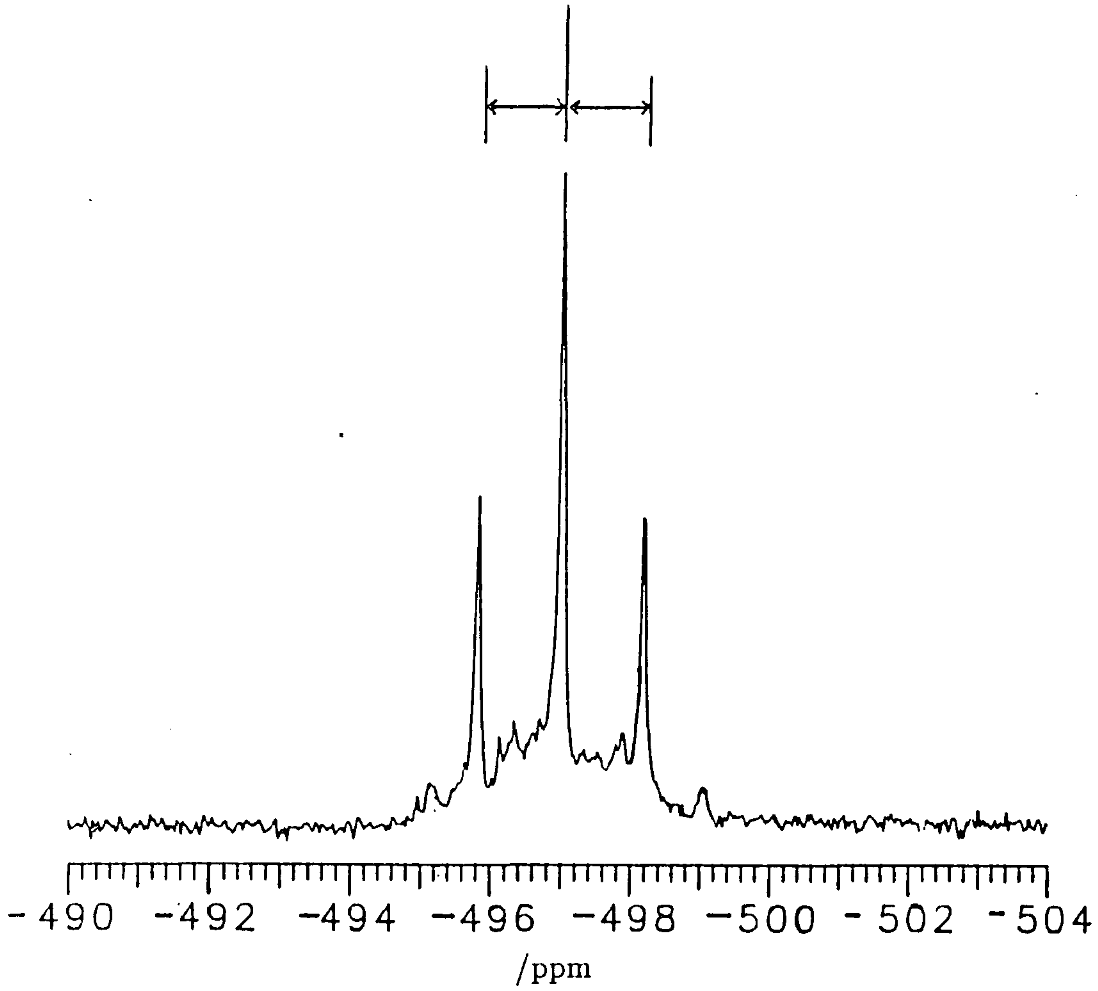

Figure 6.6.2: ^{119}Sn NMR spectrum of compound (IV) in solution-state obtained at 111.86 MHz [10].

observation is consistent with the structural characterization described above.

Figure 6.6.3 exhibits the ^{119}Sn CPMAS spectrum for the solid-state at 74.63 MHz. As with other organooxotin compounds, a great number of spinning sidebands was observed, each having a linewidth of ca. 550 Hz, which is much broader than those of the other organooxotin compounds. The spectrum resolution is not so good despite the fact that the experimental conditions had been optimized and 8900 scans were accumulated. The centreband was found at −498.8 ± 0.5 ppm, confirming the presence of the oxygen-capped form. The same chemical shift values for solution and solid states suggest that the compound retains its structural character in solution. The ^{119}Sn spectrum obtained at a higher field (111.86 MHz) presents virtually the same pattern as that obtained at 74.63 MHz, so no extra information could be achieved. The spinning sideband analysis of Figure 6.6.3 has been performed and the results are: anisotropy = 400 ppm and asymmetry = 0.00.

The study of other nuclei such as ^{31}P and ^{13}C may provide some more information. The ^{31}P spectrum of the compound, obtained at 121.4 MHz, is illustrated in Figure 6.6.4. The centrebands, indicated by arrows, are expanded in Figure 6.6.5 (a), whereas Figure 6.6.5 (b) exhibits the centrebands after resolution enhancement. Four peaks with satellites are observed and the chemical shifts and their corresponding coupling constants are given in Table 6.6.1. The couplings are the results of the two-bonded indirect interactions between ^{31}P and ^{119}Sn nuclei through oxygen atoms. The two single peaks at 20.2 ± 0.5 and 21.3 ± 0.5 ppm are assigned to the phosphinate anions, due to their lack of coupling to the tin atoms. The four peaks with satellites may indicate that four different molecules are present. Their chemical shifts are very similar, so the structures must be closely related. This observation may help to explain the surprisingly broad lines in the ^{119}Sn spectrum which, according to the ^{31}P study, should be the superposition of at least four triplets with close chemical shift values.

Four methyl carbon signals (at ca. 13.0, 13.9, 15.0 and 16.0 ppm respectively) are observed in the CPMAS ^{13}C spectrum, obtained for this sample (Figure 6.6.6), in agreement with the existence of four different molecules as concluded from the ^{31}P study. The centrebands are expanded above, and the lines marked with * in the spectrum are spinning sidebands. The bands at between 22.0 and 30.0 ppm are due to methylene carbons of butyl groups, and the bands at around 130 ppm are those arising from the aromatic groups in the molecules. However, a clear assignment of the peaks is not possible, since there are many slightly different

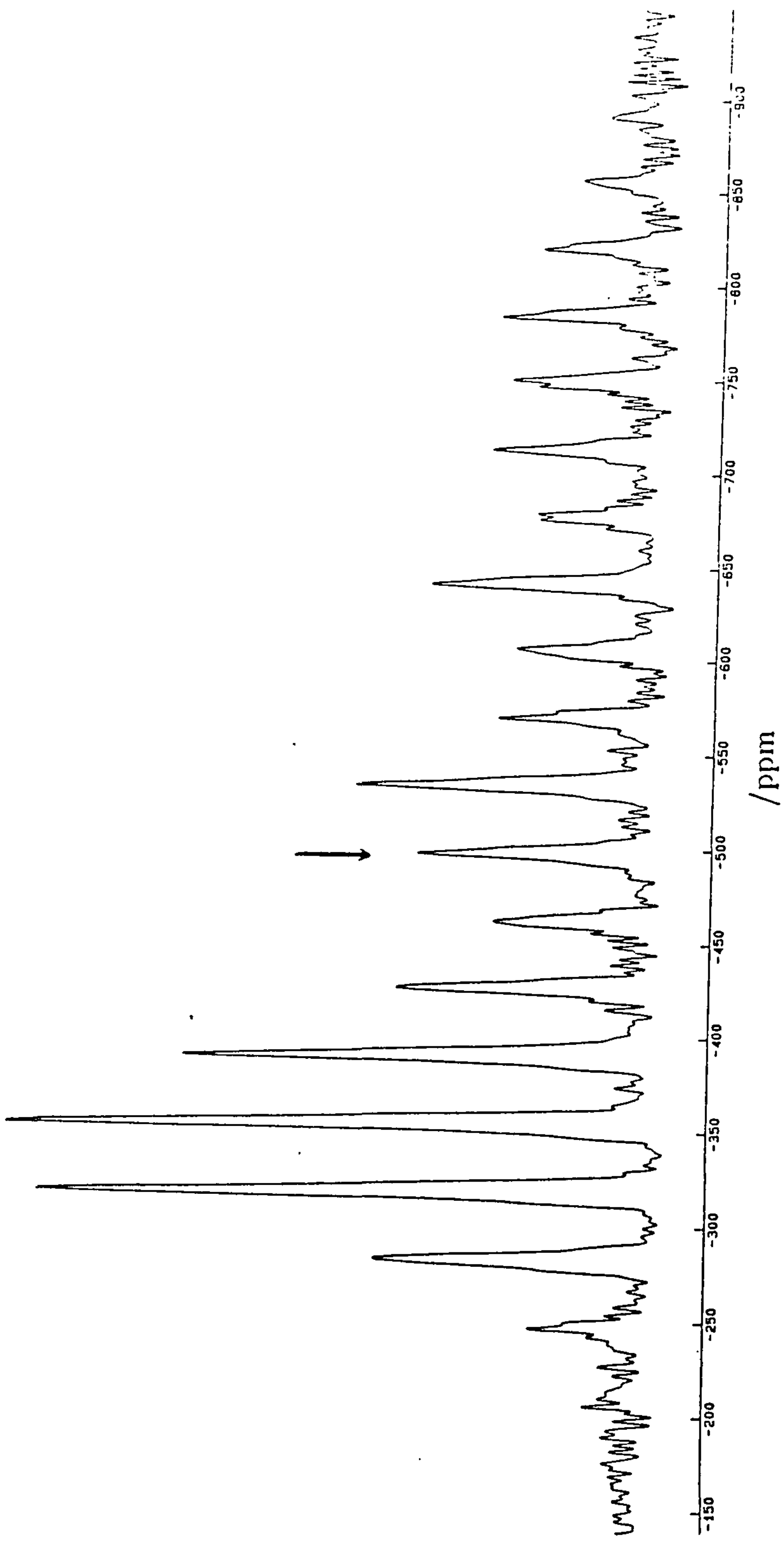

Figure 6.6.3: ^{119}Sn CPMAS spectrum of compound (IV) in solid-state obtained at 74.63 MHz. Spectrometer operating conditions: contact time 5ms; recycle delay 5s; number of transitions 8936; spinning speed 2665 Hz.

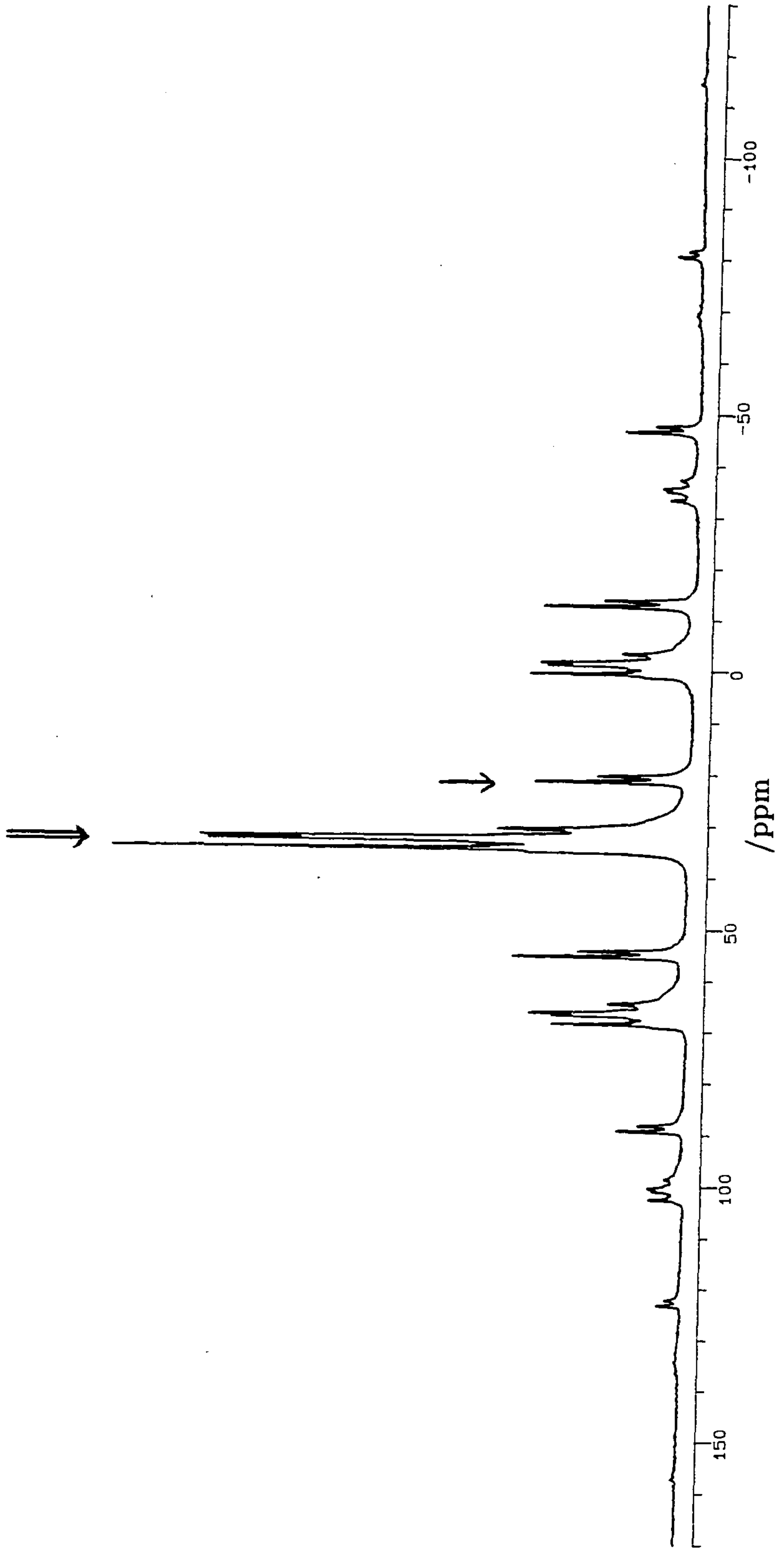

Figure 6.6.4: ^{31}P CPMAS spectrum of compound (IV) in solid-state obtained at 121.42 MHz. The centrebands are indicated by arrows. Spectrometer operating conditions: contact time 5ms; recycle delay 5s; number of transitions 100; spinning speed 4130 Hz.

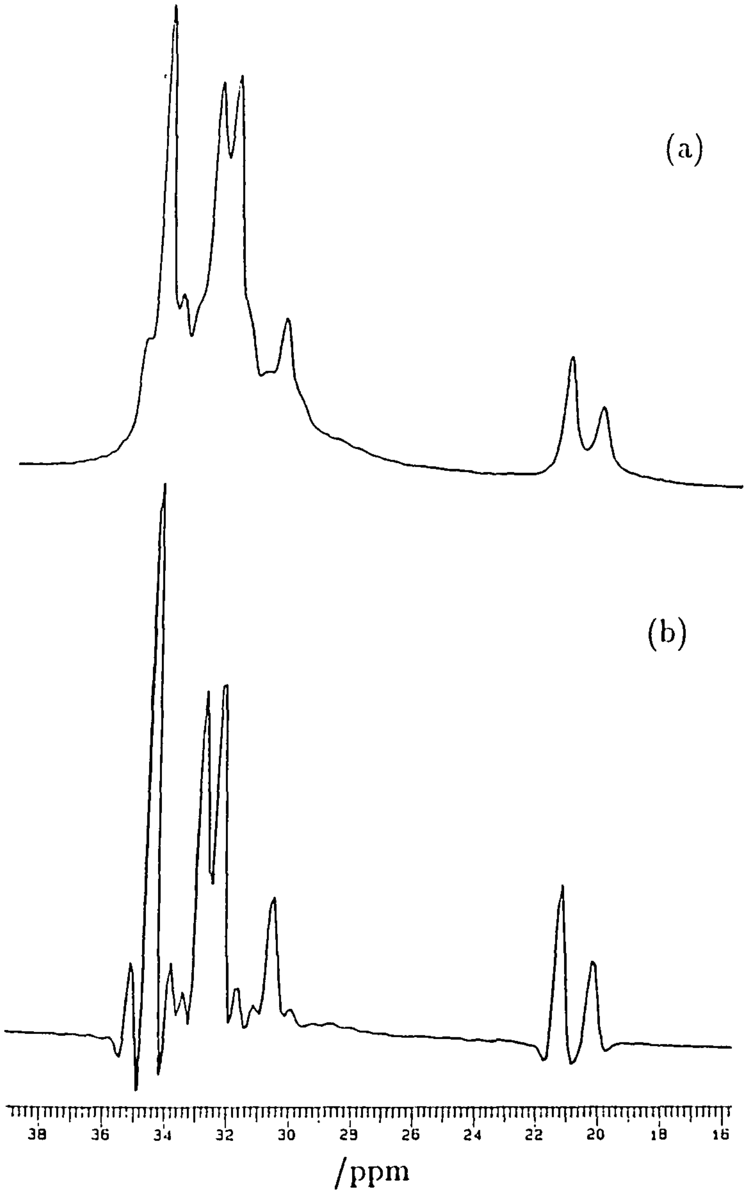

Figure 6.6.5: (a) Expanded centreband of Figure 6.6.4. (b) same centreband after resolution enhancement.

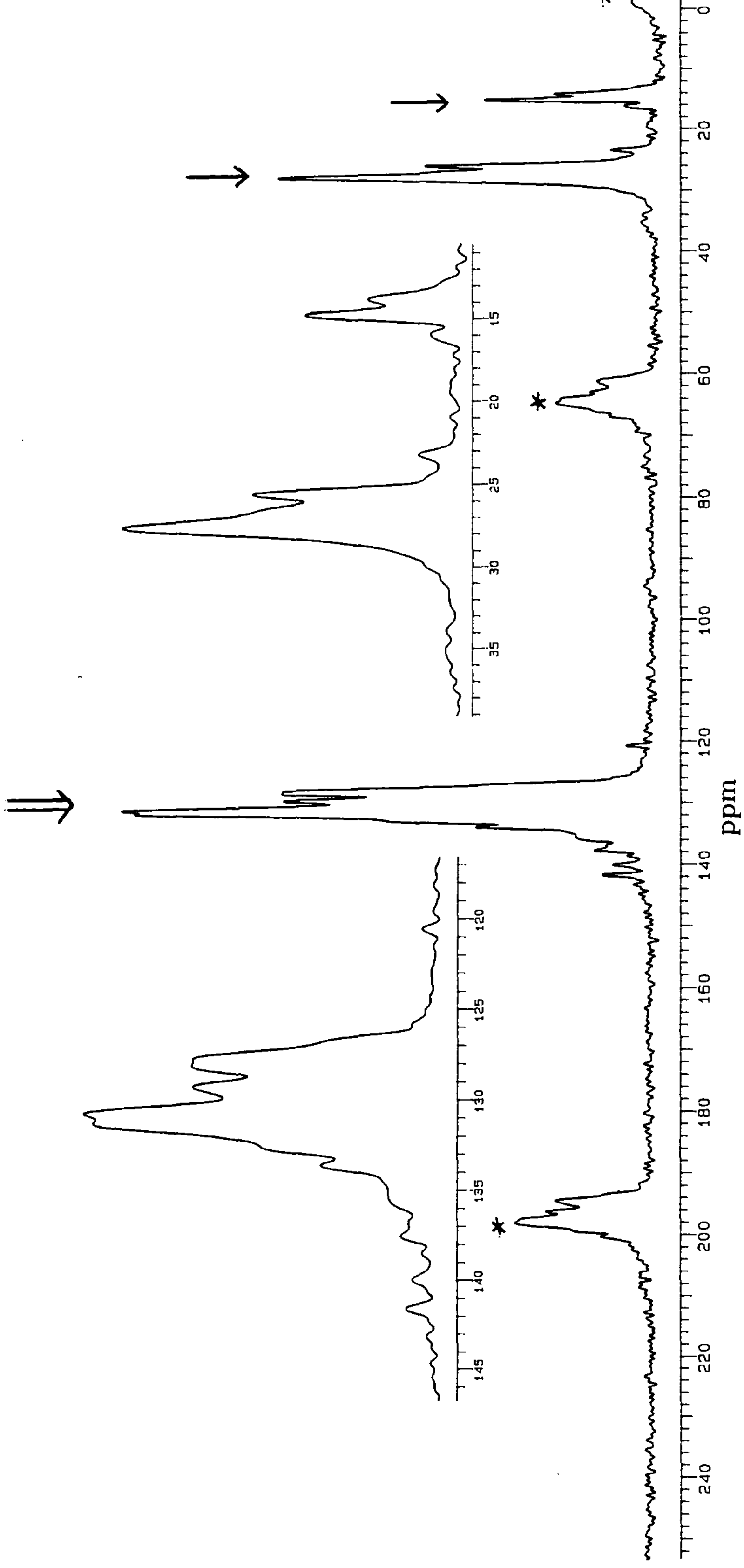

Figure 6.6.6: ^{13}C CPMAS spectrum of compound (IV) in solid-state obtained at 75.43 MHz. THe centrebands are marked by arrows, and are expanded on the right corner. Spectrometer operating conditions: contact time 1ms; recycle delay 5s; number of transitions 500; spinning speed 5050 Hz.

Table 6.6.1: ^{31}P chemical shifts and coupling constants for oxygen-capped $[(n\text{-}BuSn(OH)O_2PPh_2)_3O][Ph_2PO_2]$[(a)]

δ_P / ppm	$^2J(^{31}P\text{-}O\text{-}^{117/119}Sn)$ / Hz
34.5	152
32.8	138
32.3	146
30.5	141
(± 0.5)	(± 10)

(a) The data in parentheses are the estimated errors.

phenyl and n-butyl groups present. NQS experiments were also carried out, but like the CPMAS spectrum, they are too complicated to assign as well.

References

1. V. Chandrasekhar, R.O. Day and R.R. Holmes, *Inorg. Chem.*, **24**, 1970 (1985).
2. R.O. Day, J.M. Holmes, V. Chandrasekhar and R.R. Holems, *J. Amer. Chem. Soc.*, **109**, 940 (1987).
3. R.R. Holmes, C.G. Schmid, V. Chandrasekhar, R.O. Day and J.M. Holmes, *J. Amer. Chem. Soc.*, **109**, 1408 (1987).
4. K.C.K. Swamy, R.O. Day and R.R. Holmes, R. Holems *J. Amer. Chem. Soc.*, **109**, 5546 (1987).
5. V. Chandrasekhar, C.G. Schmid, S.D. Burton, J.M. Holems R.O. Day and R.R. Holmes, *Inorg. Chem.*, **26**, 1050 (1987).

6. R.R. Holmes, K.C.K. Swamy, C.G. Schmid and R.O. Day, *J. Amer. Chem. Soc.*, **110**, 7060 (1988).

7. R.O. Day, V. Chandrasekhar, K.C.K. Swamy, J.M. Holmes, S.D. Burton and R.R. Holmes, *Inorg. Chem.*, **27**, 2887 (1988).

8. R.R. Holmes, *Acc. Chem. Res.*, Vol. **22**, 190 (1989).

9. H. Lambourne, *J. Chem. Soc.*, **121**, 2533 (1922).

10. R.R. Holmes, Private communication.

Chapter VII

Shielding tensor analysis by slow magic-angle spinning

7.1 Introduction

The shielding (chemical shift), as described in Chapter 2, arises from the electronic screening of the nucleus by the surrounding electrons. Such screening is usually three-dimensional and thus the shielding will be anisotropic. The term used to represent this three-dimensional shielding is a second rank tensor σ, i.e. the (chemical) shielding tensor. σ may be expressed in terms of a 3×3 matrix, which can be converted to a diagonal form with three principal elements σ_{11}, σ_{22} and σ_{33} by a suitable choice of coordinate system. These three components reflect the local chemical environment of the nucleus being studied. In solution, the shielding tensor is averaged by rapid isotropic molecular motion to an isotropic value σ_{iso}, given by the trace of the tensor. However, the three principal elements may be contained in solid-state spectra since the molecules are not generally free to move. Therefore, in principle, solid-state NMR contains much more molecular information regarding structure and bonding than solution-state NMR.

The shielding is said to be characteristic of the nucleus in a particular orientation of the molecule with respect to the magnetic field, i.e. different orientations of the molecule to the applied field $\mathbf{B}_o$ will give rise to different shielding constants. For a single crystal containing crystallographically equivalent sites, a sharp line will be observed and the positon of this line will change as the orientation of the crystal to $\mathbf{B}_o$ varies. For a polycrystalline sample, the random distribution of the orientations in the powder will result in a broad line, known as the powder pattern, which is the superposition of the signals for all orientations of the crystallites, as demonstrated in Figure 7.1.1. The shape of the powder pattern depends on the principal elements of the shielding tensor. A schematic representation of the shape is shown in Figure 7.1.2, where the three principal components are indicated. However, it is not generally possible to obtain the directions of the three principal axes in the molecular axis system from the spectrum alone. Figure 7.1.2 (a) depicts a general asymmetric case whereas Figure 7.1.2 (b) presents an axially symmetric situation where two components are identical.

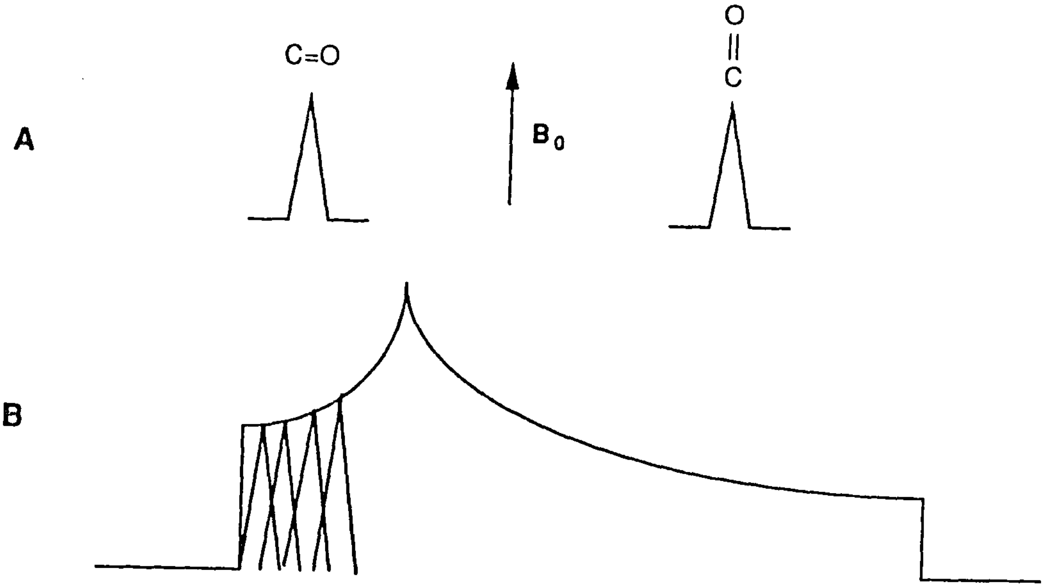

Figure 7.1.1: Schematic diagram of solid-state ^{13}C NMR shieldings of a carbonyl functionality: (a) two possible extreme orientations of the functionality in a magnetic field B_0; (b) the superposition of all orientations giving the chemical shift anisotropy pattern.

Two different conventions regarding the shielding tensor information have been suggested [1,2]. The convention used in this chapter and throughout this thesis is that of Haeberlen [1]. The shielding anisotropy $\sqsupseteq$ and the shielding asymmetry η are defined as in Equations (7.1.1) and (7.1.2):

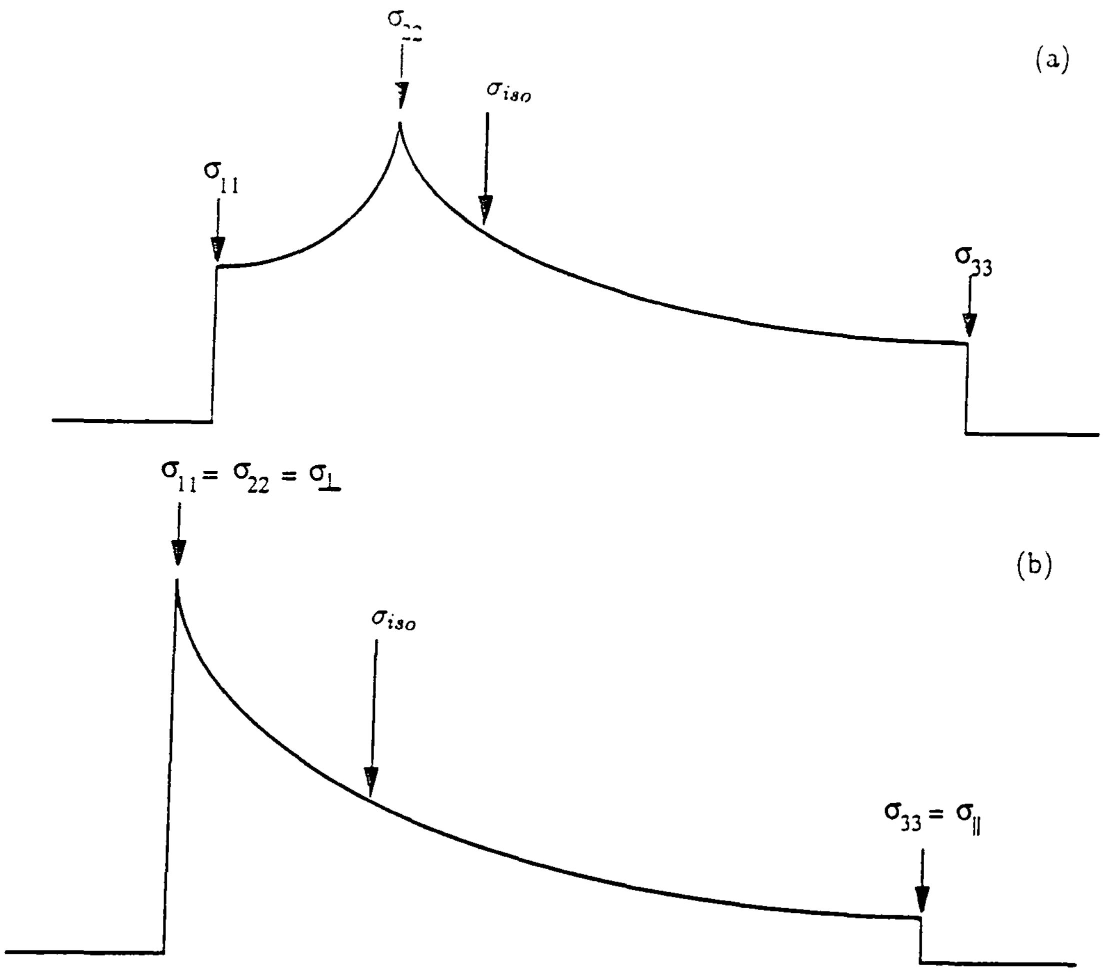

Figure 7.1.2: Schematic powder patterns caused by shielding anisotropy: (a) lower symmetry; and (b) axial symmetry.

$$\beth = \sigma_{33} - \sigma_{iso} \tag{7.1.1}$$

$$\eta = \frac{\sigma_{22} - \sigma_{11}}{\sigma_{33} - \sigma_{iso}} \tag{7.1.2}$$

The isotropic shielding σ_{iso} has always been given as:

$$\sigma_{iso} = \frac{1}{3}(\sigma_{11} + \sigma_{22} + \sigma_{33}) \tag{7.1.3}$$

The three tensor elements σ_{11}, σ_{22} and σ_{33} are assigned in the following form:

$$|\sigma_{33} - \sigma_{iso}| \geq |\sigma_{11} - \sigma_{iso}| \geq |\sigma_{22} - \sigma_{iso}| \tag{7.1.4}$$

It may be worthy of mention that the value of σ_{iso} is actually the negative value of the chemical shift, i.e. $\sigma_{iso} = -\delta_{cs}$. Once the anisotropy ($\beth$) and the asymmetry

(η) are determined, together with the isotropic chemical shift value (δ_{cs}), the three principal components (σ_{11}, σ_{22}, σ_{33}) of the tensor will be immediately derived through Equations (7.1.1)–(7.1.3).

In practice, a number of methods have been proposed to obtain the shielding tensor information. NMR studies on single crystals provide the most satisfactory means for the determination of the shielding tensor, since not only the values of the elements but also the orientation of the principal axes of the shielding tensor in the molecular frame may be obtained [3]. For polycrystalline materials the principal components of the shielding tensor may be measured directly from the powder pattern, provided only one chemically and magnetically distinct species is present [4]. If more than one type of nucleus exists, substantial overlap of the anisotropy patterns will occur, thus severely restricting the use of this method [5]. This limitation, however, may be overcome by some other methods such as: (1) slow magic-angle spinning experiments [6,7], followed by analysis of the spinning sideband manifold; (2) off-angle fast spinning [8], resulting in a scaling down (and therefore a separation) of the anisotropy patterns; (3) two-dimensional experiments to obtain the complete anisotropy patterns in one of the dimensions [9]. Of these methods, slow MAS is probably the most widely-used approach. One fact which must be emphasized here is that the above-mentioned methods do not usually supply any information regarding the orientation of the principal elements with respect to the molecular coordinate system; such information can only be obtained readily from other techniques, for instance, from single crystal studies and from molecular symmetry.

There have been two methods developed to extract the shielding tensor from a slow MAS spectrum. One of them is known as the moment method and the other is the graphic method. Both approaches have been applied to many cases and are proved to be reliable in general. Their merits and drawbacks have been investigated, and may be found in references [10-13]. Because of the problems associated with these two methods, the use of simulation of slow spinning MAS spectra became prominent. In addition, simulations of the MAS spectra provide a useful means to refine the tensor components. In fact, Maricq and Waugh suggested the use of computerized simulation in one of their original papers concerning the moment method [6]. There have been reports about the numerical simulations of spinning sideband manifolds to check and refine the shielding tensors obtained from either the moment method or the graphic method. Furthermore, Merwin [14] wrote a simulation algorithm to actually fit a spinning sideband pattern and accurately determine the tensor components. In his thesis, he gave a full discussion about this fitting program and the author of the present thesis found that his work provided a useful basis for further development. It is understood that iterative computer fitting of MAS NMR spectra is probably the best way to accurately derive the shielding elements, especially for spectra with less satisfactory signal-to-noise ratios.

The main focus of this chapter is to extend the application of the use of iterative fitting for extraction of the anisotropy and asymmetry of a shielding tensor to a large number of organotin and organolead compounds. A simple mathematical description of a spinning sideband spectrum outlined by Maricq and Waugh will first be discussed followed by the description of simulation and fitting computer programs based on those of Merwin. The estimated errors of the results will be examined and finally a number of examples of the use of the fitting program will be given.

7.2 Theoretical Description of a slow MAS spectrum

Magic-angle rotation provides an excellent method to achieve line narrowing in solid-state NMR [15-17], yielding a single peak at the isotropic chemical shift from each anisotropy pattern. At spinning speeds much lower than the spread of the anisotropy pattern the sharp peak at the chemical shift will be surrounded by a series of equally sharp sidebands spaced at the spinning frequency. Moreover, the intensities of these sidebands contain the information about the chemical shift anisotropy and provide an opportunity to recover the shielding components. This phenomenon is known as slow magic-angle spinning, and was first observed by Lippmaa et al. [18] and independently by Stejskal and co-workers [19].

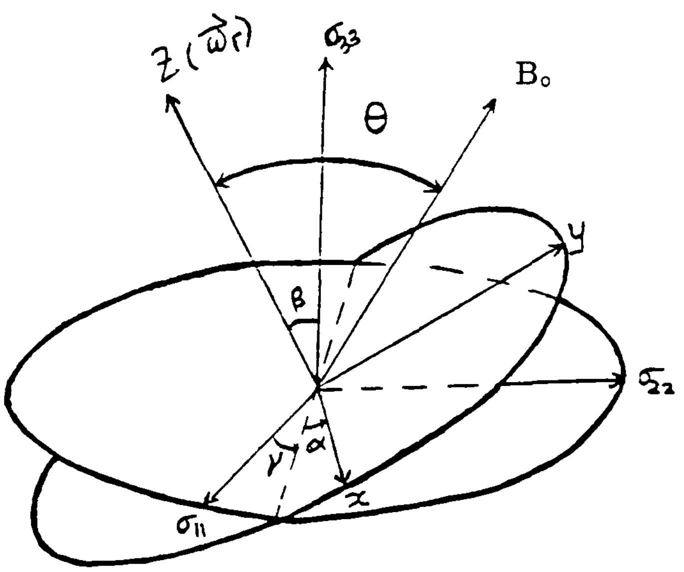

Figure 7.2.1: Schematic representation of the coordinate system. σ_{11}, σ_{22} and σ_{33} represent the principal axis system of the shielding tensor. x, y, z refer to the rotor-fixed system, with y, z and $\mathbf{B}_0$ in the same plane. θ is the magic-angle and α, β, and γ are the Euler angles.

The complete mathematical expression for a sideband spectrum has been addressed by Maricq & Waugh [6] and by Herzfeld and Berger [7]. It will not be useful to repeat the entire derivation here, but the resulting formulae are essential to the understanding of the origin of spinning sidebands and are shown below, all the expressions being quoted from reference [6]. For a sample containing only one type of chemically distinct nucleus and spinning at the magic-angle, the normalized free induction decay (FID) may be written in the form:

$$g(t) = \exp[i\omega_o\sigma_{iso}t]\sum_k \exp[i\omega_o \beth \int_0^t \xi_k(t')\,dt'] \tag{7.2.1}$$

where ω_o is the Larmor frequency of the nucleus; σ_{iso} refers to the isotropic trace of the shielding tensor; $\beth$ is defined as the shielding anisotropy; $\xi_k(t)$ is the time-dependent term of the k^{th} crystallite, induced by the two transformations among the coordinate systems: from the laboratory frame to a rotor-fixed system and from the rotor-fixed frame into the principal axis system (PAS) of the shielding. The transformations may be easily understood from Figure 7.2.1. The form of $\xi(t)$ may be expressed as:

$$\xi(t) = C_1\cos\omega_r t + S_1\sin\omega_r t + C_2\cos 2\omega_r t + S_2\sin 2\omega_r t \tag{7.2.2}$$

where

$$C_1 = \frac{1}{2}\sin 2\theta\sin\beta[\cos\beta(\eta\cos 2\gamma - 3)\cos\alpha - \eta\sin 2\gamma\sin\alpha] \tag{7.2.3}$$

$$S_1 = \frac{1}{2}\sin 2\theta\sin\beta[\cos\beta(3 - \eta\cos 2\gamma)\sin\alpha - \eta\sin 2\gamma\cos\alpha] \tag{7.2.4}$$

$$\begin{aligned} C_2 =& \frac{1}{2}\sin^2\theta[[\frac{3}{2}\sin^2\beta + \frac{\eta}{2}\cos 2\gamma(1+\cos^2\beta)]\cos 2\alpha \\ &- \eta\cos\beta\sin 2\gamma\sin 2\alpha] \end{aligned} \tag{7.2.5}$$

$$\begin{aligned} S_2 =& \frac{1}{2}\sin^2\theta[-[\frac{3}{2}\sin^2\beta + \frac{\eta}{2}\cos 2\gamma(1+\cos^2\beta)]\sin 2\alpha \\ &- \eta\cos\beta\sin 2\gamma\cos 2\alpha] \end{aligned} \tag{7.2.6}$$

η is the asymmetric parameter of the shielding; θ is the angle between the rotor axis and the magnetic field $\mathbf{B}_o$, i.e. the magic-angle 54.7°; ω_r is the rotor spinning frequency, and ω_rt is the azimuthal angle of the x axis of the rotor-fixed frame with respect to $\mathbf{B}_o$; α, β, γ are the three Euler angles of the rotor-fixed frame in the PAS of the shielding tensor.

The first exponential term of Equation 7.2.1, exp[i$\omega_o\sigma_{iso}$t] only represents the isotropic nature and contains no information regarding the anisotropy and asymmetry. Hence for the purpose of simplicity, it may be dropped as long as the centreband is regarded as the isotropic chemical shift. In a polycrystalline or amorphous sample, random distributions of the crystallites in the powder over all possible orientations occur. Each orientation ($\alpha\beta\gamma$) gives rise to its own contribution to powder pattern in the spectrum. The intensity each orientation contributes to the pattern is proportional to sinβ. A complete powder spectrum thus is the superposition of the contributions from all of these crystallites. This requires the summing over all k, which is characterised by the three Euler angles ($\alpha\beta\gamma$). The resulting expression for the FID following the above discussion is:

$$FID(t) = g(t) = \sum_{\alpha}\sum_{\beta}\sum_{\gamma}[\exp[i\omega_{o} \sqsupset \int_0^t \xi(\alpha,\beta,\gamma,t')\,dt']]\sin\beta \tag{7.2.7}$$

The time-dependent integral may be calculated as:

$$\int_0^t \xi(\alpha,\beta,\gamma,t')\,dt' = -\frac{1}{\omega_r}[S_1 + \frac{1}{2}S_2 + C_1\sin\omega_r t - S_1\cos\omega_r t$$

$$+\frac{1}{2}(C_2\sin 2\omega_r t - S_2\cos 2\omega_r t)] \tag{7.2.8}$$

Equations (7.2.7) and (7.2.8) describe the NMR signals in the time domain. Since after one full period of rotation of the sample the system returns to its initial state, one rotary echo of the FID (t: 0 $\rightarrow$ $2\pi/\omega_r$) will contain all of the frequency and intensity information for the sideband manifold, and the full decay of the train of the rotational echos only determines the linewidth of the sidebands [20]. Hence, the result of the Fourier transformation of one FID rotary echo will give an entire anisotropic sideband pattern, whose linewidth may be measured from the experimental spectrum.

7.3 Description of the computer programs

7.3.1 The operation of the simulation and fitting programs

The approach to actually simulate a MAS spectrum, expressed by Equations (7.2.7) and (7.2.8), can be summarized as: Firstly, input the values of the constants $\sqsupset$, η, σ_{iso}, ω_o and ω_r (their definitions are given in the previous section). Secondly, numerically evaluate Equation (7.2.8) for a series of t-values over a rotational period for each orientation $(\alpha\beta\gamma)$; the FID is generated by summing over all the orientations. Thirdly, the FID echo is Fourier transformed by a library subroutine (NAG routine C06FCF [21]) to produce the frequency-domain spectrum. Finally, each sideband is convoluted with a Gaussian function with linewidth measured from the experimental spectrum; the intensities of the spinning sidebands are then normalized.

The simulation program may be found in the appendix. In order to compare between experimental and simulated spectra, a code was added to the program to calculate the sum of the squares of the intensity differences (SSD) between the corresponding sidebands, i.e. if IC(n) and IE(n) represent the intensities of the n^{th} experimental and calculated sidebands respectively, the SSD can be expressed as:

$$\mathrm{SSD} = \sum_{n}[\mathrm{IC}(n) - \mathrm{IE}(n)]^2 \tag{7.2.9}$$

The total number of orientations chosen for each Euler angle here is 20, leading to a 9° angle increment for each step [17]. The Gaussian convolution is performed at the end of the program in order to keep the processing time to a minimum.

Iteratively fitting a given spectrum involves varying the parameters $\sqsupset$ and η until the intensity difference between the experimental and simulated spectra (SSD) reaches a minimum value. The flowchart (schematic diagram) of the iterative fitting procedure is represented in Figure 7.3.1. The program starts by simulating the sideband intensities based on the initial estimated values of $\sqsupset_o$ and η_o. The sum

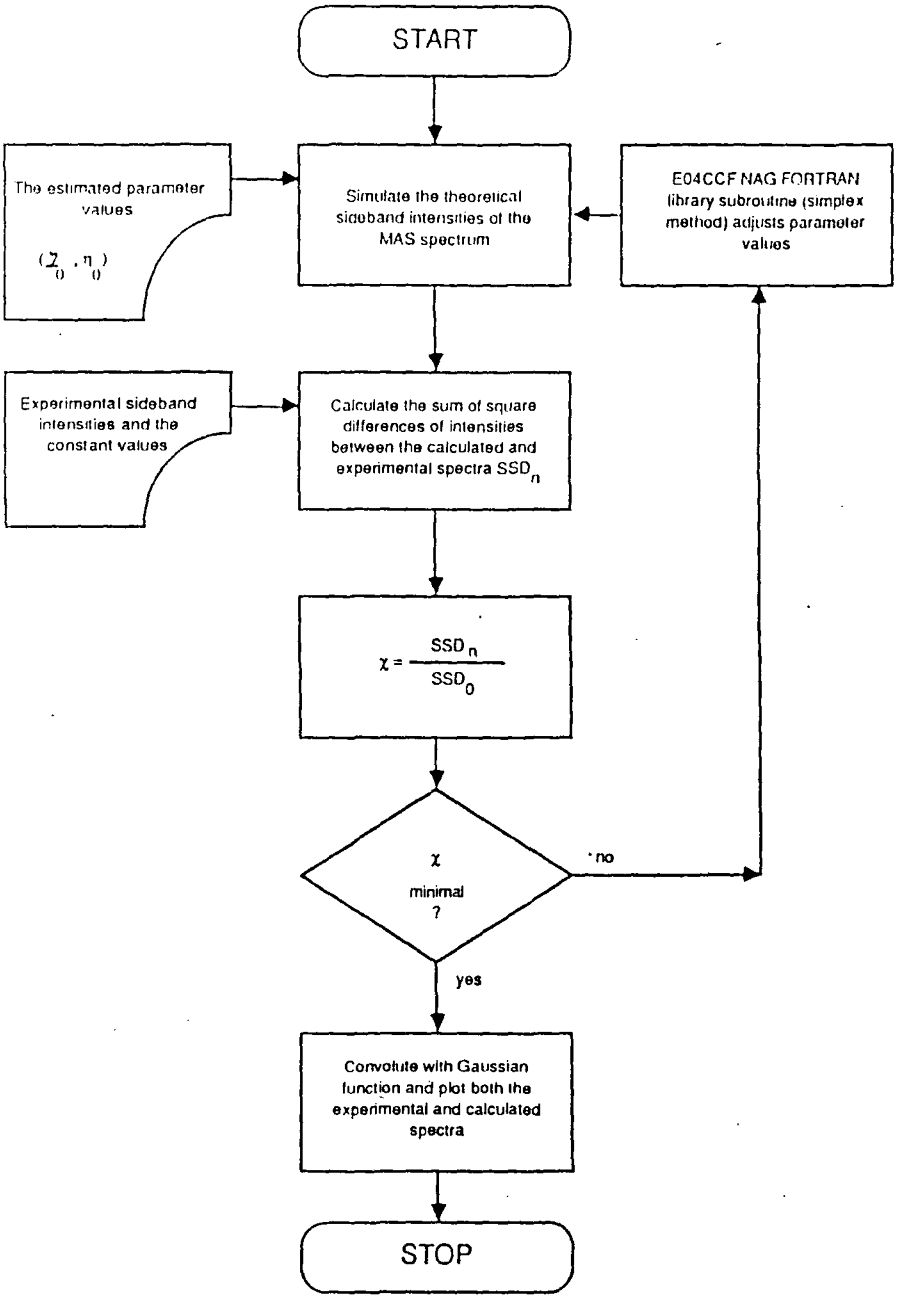

Figure 7.3.1: Flowchart describing the operation of the iterative fitting computer program (FITSB).

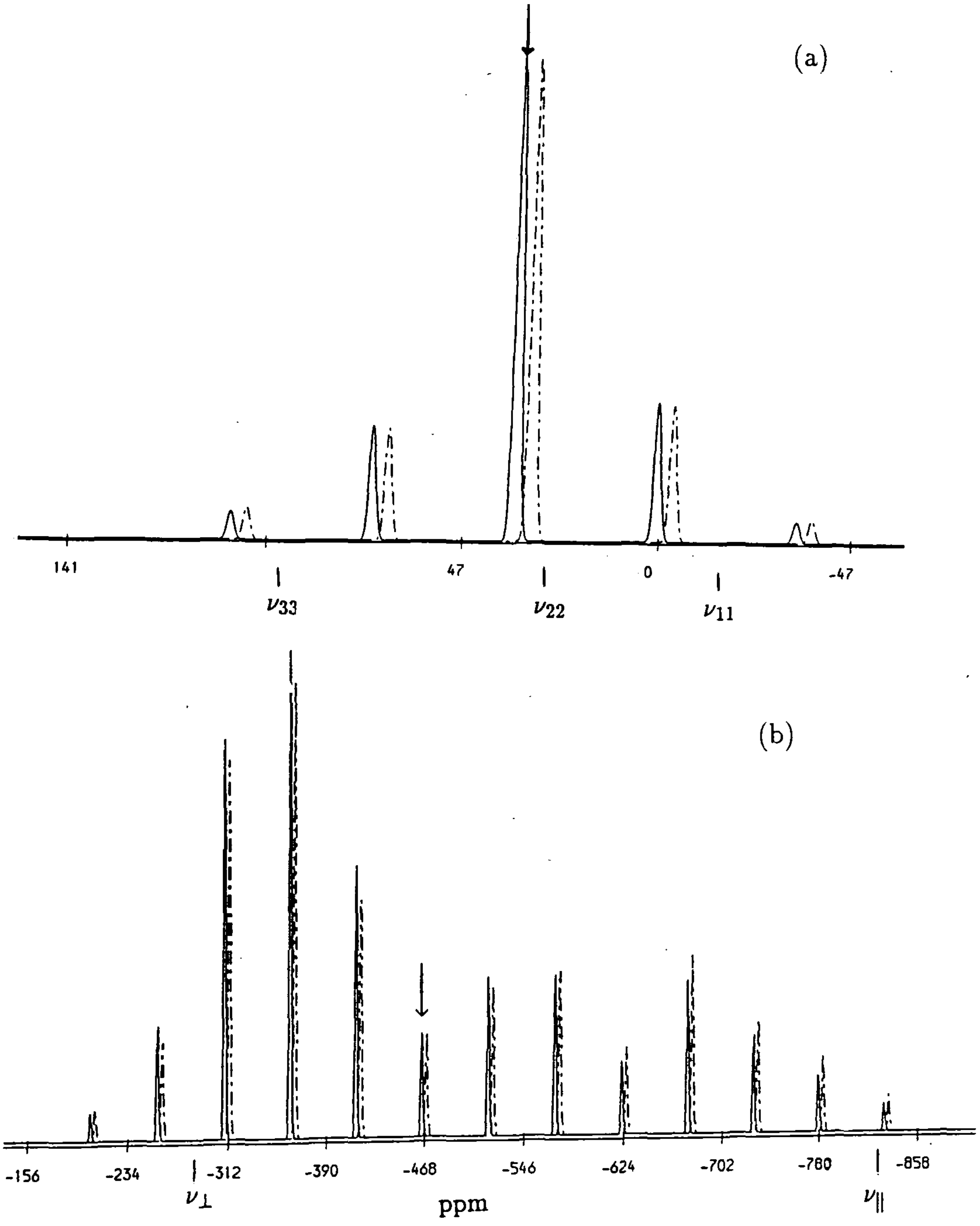

Figure 7.3.2: Typical results of the spinning sideband analysis, with (a) asymmetric shielding; and (b) axially symmetric shielding. The solid lines represent (a) the experimental ^{31}P spectrum of $[(n\text{-}BuSn(OH)O_2PPh_2)_3O][Ph_2PO_2]$ (Figure 6.6.4); and (b) the experimental ^{119}Sn spectrum of $[(n\text{-}BuSn(O)O_2P(C_6H_{11})_2]_4$ (Figure 6.5.2). The dashed lines represent the calculated spectra. The arrows indicate the centrebands. (a) ν_{11}, ν_{22} and ν_{33} denote the positions of the three shielding tensor components. Results: anisotropy = −56.6 ppm and asymmetry = 0.74. (b) $\nu_{\perp}$ and $\nu_{\parallel}$ denote the positions of the shielding tensor components respectively. Results: anisotropy = 361 ppm and asymmetry = 0.00.

of the squares of the intensity differences SSD_o is then calculated. The minimization NAG library subroutine E04CCF [21] adjusts a parameter set ($\beth$, η), and the sideband intensities for this set of values is calculated, followed by derivation of the SSD_n (the current value of SSD). The value of χ ($\chi = SSD_n/SSD_o$), which is the criterion for the minimization, is then calculated. The above procedure is repeated and each time the library subroutine adjusts a new set of ($\beth$, η), the value of χ is judged until it reaches its minimum value. The values of $\beth$, η corresponding to the smallest value of χ are thus regarded as the result of the iterative fitting. The MAS spectrum derived from these two values is then convoluted with a Gaussian function to produce a spectrum comparable to the experimental one.

The completion time of this program depends on the behaviour of the function FID(t) and the distance of the starting point from the minimum. The large number of orientations undoubtedly consumes considerable time, but this is essential for the accuracy of the fitting. The starting point ($\beth_o$ and η_o), however, can be chosen properly to speed up the fitting. This is achieved by a small computer program (appendix I) based on the moment method, which calculates $\beth$ and η using the experimental sideband intensities. These two values are then treated as the initial point for the fitting. Typical results of the fitting are shown in Figure 7.3.2. Throughout the thesis, the height of each sideband is regarded as its intensity since it is believed that the linewidths of all the sidebands have the same value.

7.3.2 The accuracy of the program – Error estimation

To explore the behaviour of the fitting program, graphs were produced of SSD (the sum of the squares of the intensity difference) against one of the variables ($\beth$ and η) while the other variable is kept constant. Such plots are displayed in Figures 7.3.3 and 7.3.4 for asymmetric and axial symmetric cases respectively. It is apparent that there is a minimum SSD value for both $\beth$ and η in the case of asymmetry. However, for the axial symmetric case, though a minimum value of SSD is found for $\beth$, it is clear that below $\eta = 0.15$, the change of SSD is too

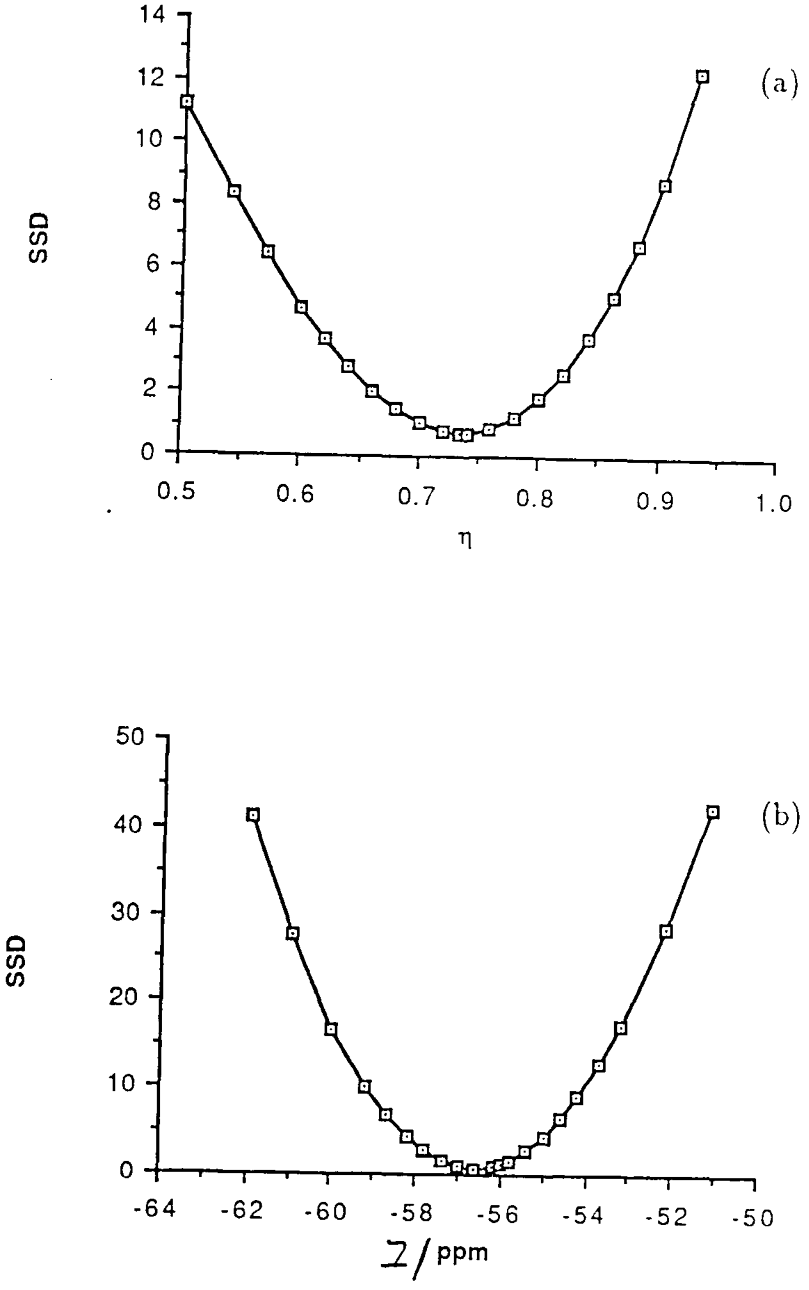

Figure 7.3.3: Graphs showing SSD (sum of the squares of the intensity difference between experimental and calculated spectra, as described in Equation (7.2.9)) as a function of (a) η while ב fixed at -56.6 ppm; (b) ב while η fixed at 0.74, for an asymmetric case. The experimental data used are as in Figure 7.3.2(a).

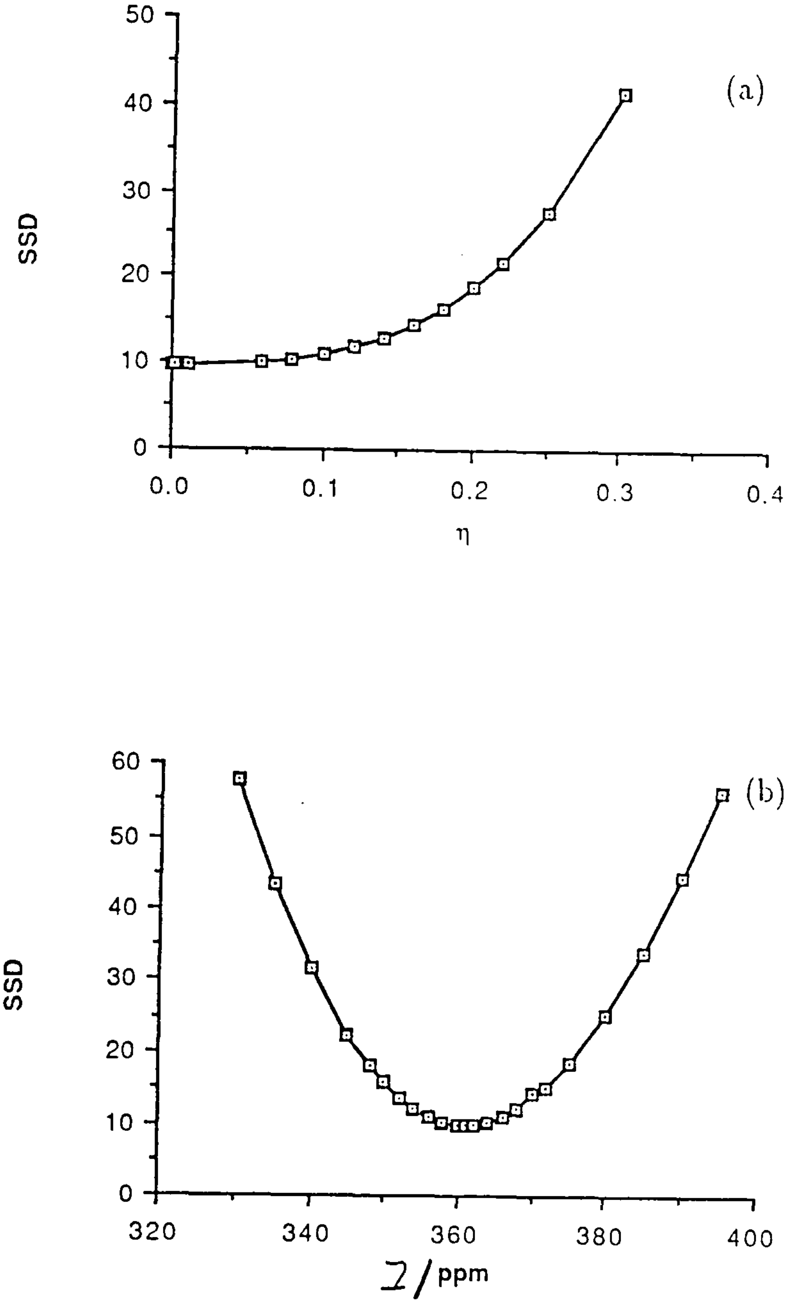

Figure 7.3.4: Graphs showing SSD (sum of the squares of the intensity difference between experimental and calculated spectra, as described in Equation (7.2.9)) as a function of (a) η while ℶ fixed at 361.0 ppm; (b) ℶ while η fixed at 0.00, for an axial symmetric case. The experimental data used are as in Figure 7.3.2(b).

small to be observed. Such a result suggests that an actual distinction between an axial and a near axial system is not possible. This conclusion is in agreement with previous studies [10,14]. It is obvious that the values of $\sqsupset$ and η corresponding to the minimum values of SSD in these plots are equal to the values obtained from the iterative fittings varying both $\sqsupset$ and η. This fact shows that the fitting program performs as required.

Once the fitting is established, it is important to estimate the accuracy which the program can offer. However, there is no accepted method for obtaining reliable error estimates in nonlinear least-squares fitting procedures [22]. The method used in this thesis is to investigate the percentage changes in sideband intensities, for a theoretical spectrum (as contrasted with an experimental case), as $\sqsupset$ (or η) varies. Suppose IC(n) and IS(n) represent the n^{th} sideband intensity of the currently calculated spectrum and that of the resulting spectrum of the fitting respectively; then the % change may be written as:

$$\%\text{change} = \sum_{n}[\text{IC}(n) - \text{IS}(n)]^2 \tag{7.2.10}$$

The above equation is valid because the sideband intensities have already been normalized in percentage terms. Figures 7.3.6 and 7.3.7 show how the % change as defined above varies as a function of the asymmetry (η) and anisotropy ($\sqsupset$) for asymmetric and axial symmetric systems respectively. These plots are then used to examine the $\sqsupset$ (and η) values that would yield the change of the intensities by 2%, 5%, 10% and 15% respectively. For example, Figure 7.3.6 shows that a 2% change in intensity would result in differences of η to ± 0.08 and of $\sqsupset$ to ± 1.0 ppm. This same procedure was repeated, and all the results are given in Table 7.3.1.

Intuitively the smaller the change of $\sqsupset$ and η due to the change in sideband intensity then the smaller will be the error in the determination of the best-fit $\sqsupset$ and η values. It is clear that for an asymmetric system, the anisotropy ($\sqsupset$) and

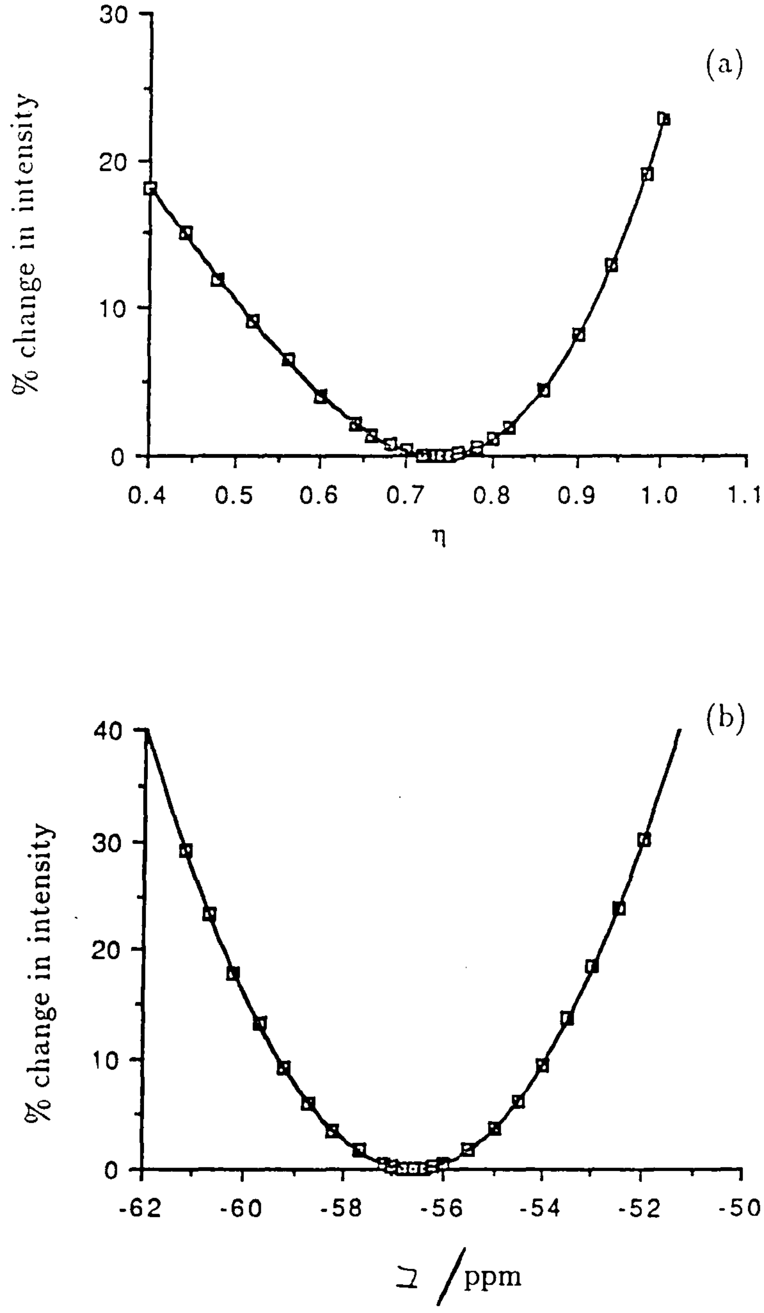

Figure 7.3.5: Graphs showing the % change of the sideband intensities for a theoretical spectrum, as described in Equation 7.2.10, with an asymmetric shielding tensor. (a) % change as a function of η while ℶ fixed at −56.6 ppm; (b) % change as a function of ℶ while η fixed at 0.74.

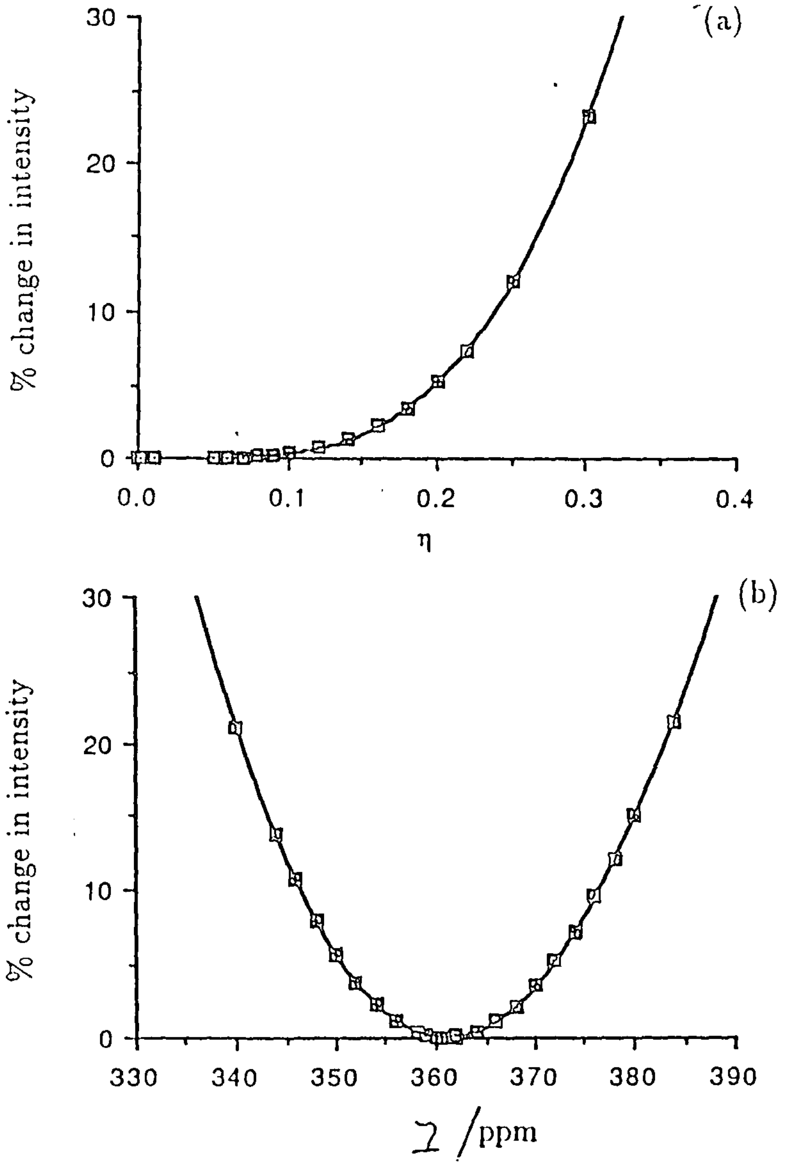

Figure 7.3.6: Graphs showing the % change of the sideband intensities for a theoretical spectrum, as described in Equation 7.2.10, with an axially symmetric shielding tensor. (a) % change as a function of η while ℶ fixed at 361.0 ppm; (b) % change as a function of ℶ while η fixed at 0.00.

Table 7.3.1: The estimated errors of anisotropy and asymmetry as the spinning sideband intensities vary

Graph	δ_{cs} /ppm	% change in intensity	⊐ /ppm	η
Figure 7.3.5	−34.5	0 %	−56.6	0.74
		2 %	± 1.0	± 0.08
		5 %	± 2.0	± 0.15
		10 %	± 3.0	± 0.20
		15 %	± 4.0	± 0.25
Figure 7.3.6	466.0	0 %	361.0	0.00
		2 %	± 6.0	± 0.15
		5 %	± 11.0	± 0.20
		10 %	± 15.0	± 0.24
		15 %	± 20.0	± 0.26

asymmetry (η) are relatively insensitive to changes in the sideband intensities. A 5 % change in intensity leads to only small differences in ⊐ (± 2.0 ppm) and η (± 0.15). Therefore, the shielding tensors derived from slow-spinning experiments are reasonably reliable for asymmetric systems, giving the errors as ± 2.0 ppm for ⊐ and ± 0.15 for η (assuming 5 % error in the measuring of the sideband intensities). On the other hand, however, the axially symmetric system presents a very different picture: both ⊐ and η are sensitive to changes in the sideband patterns. The same 5 % change in intensity would give an estimated error of ± 11.0 ppm for ⊐ and ± 0.20 for η: That is to say that the intensity differences between axial ($\eta = 0.0$) and near axial ($\eta = 0.2$) systems are so small that no measurable difference in the sideband patterns can be achieved. This result is unsurprising and indeed confirms the argument that to actually distinguish between axial and near axial symmetries is impossible. The above discussion also indicates that the accuracy of the fitting mainly depends on the accuracy of the measurement of the sideband intensities, i.e. the signal-to-noise ratio of the spectrum. The better the signal-to-noise ratio, the more accurate the fitting will be.

7.4 Shielding tensor analysis for some lead compounds

The principal components of shielding tensors are one of the most informative NMR parameters in the solid state since they exactly reflect the local environment of the nucleus in question. Therefore, it is extremely important to be able to precisely derive the values of these parameters. Solid-state ^{207}Pb NMR spectra usually have modest to large anisotropies, making them a good example to demonstrate the usefulness of iterative fitting analysis. Moreover, these analyses were also useful for program verification purposes. A number of Pb–207 slow spinning spectra were analyzed in order to extract their shielding tensors using the iterative fitting program. Some of the spectra studied in this section were taken by the author of this thesis; others, indicated individually, were obtained by a previous member of the research group (A. Sebald). The reference used in this chapter for ^{207}Pb chemical shifts is $PbPh_4$.

Figure 7.4.1(a) displays the spectrum of $Ph_2Pb(SCH_2)_2$, having a very good signal-to-noise ratio and in fact is the best among the spectra studied in this section. Therefore, the error for measuring the intensities should be small; hence a good fit is expected. The resulting fit is shown in Figure 7.4.1(b), not surprisingly exhibiting a very small difference between the experimental and the calculated spectra. The anisotropy ($\beth$) is found to be $-$ 312 ± 1 ppm and the asymmetry (η) to be 0.24 ± 0.08. The errors are estimated to be reasonably low due to the good signal-to-noise ratio of the spectrum, and the excellent fit of the calculated sideband pattern with the experimental one. A less favorable case is the spectrum of lead tetradecanoate, $(C_9H_{19}CO_2)_4Pb$, shown in Figure 7.4.2(a). The fit (Figure 7.4.2(b)) gave the shielding anisotropy as 415 ppm and the asymmetry as 0.27, with the estimated errors being ± 3 ppm and ± 0.2 respectively. These values are similar to those roughly calculated from the moment method, giving $\beth = 424$

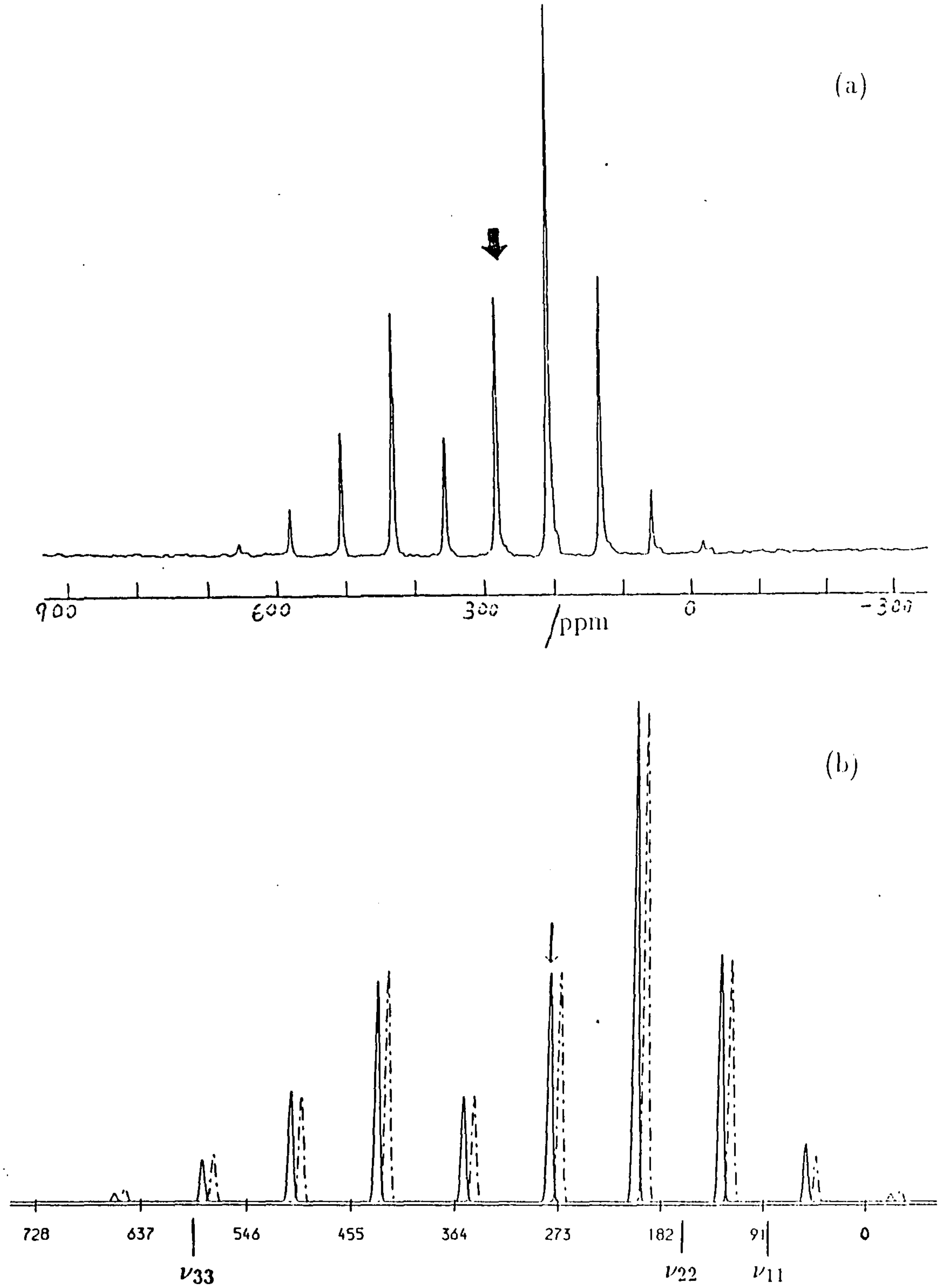

Figure 7.4.1: (a) The ^{207}Pb spectrum of $Ph_2Pb(SCH_2)_2$ obtained at 41.87 MHz (taken by Sebald). The arrow indicates the centreband. Spectrometer operating conditions: contact time 5ms; recycle delay 10s; number of transitions 4400; spinning speed 3175 Hz. (b) Fitting result: anisotropy = -312 ppm and asymmetry = 0.24. The solid lines represent the experimental spectrum while the dashed lines represent the calculated spectrum.

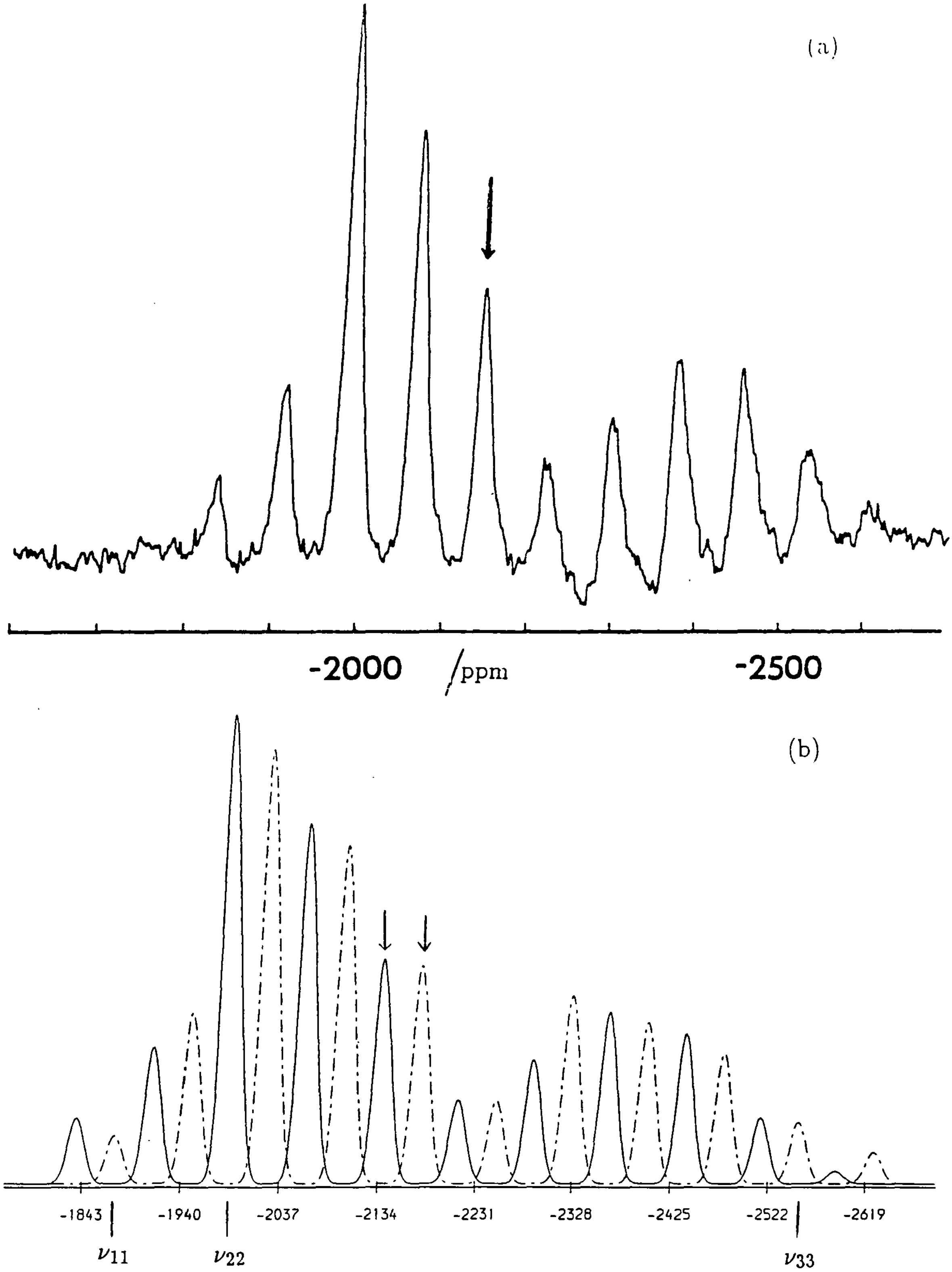

Figure 7.4.2: (a) The ^{207}Pb spectrum of $(C_9H_{19}CO_2)_4Pb$ at 41.87 MHz (taken by Sebald). The arrow indicates the centreband. Spectrometer operating conditions: contact time 5ms; recycle delay 10s; number of transitions 7400; spinning speed 3150 Hz. (b) Fitting result: anisotropy = 415 ppm and asymmetry = 0.27. The solid lines represent the experimental spectrum while the dashed lines represent the calculated spectrum.

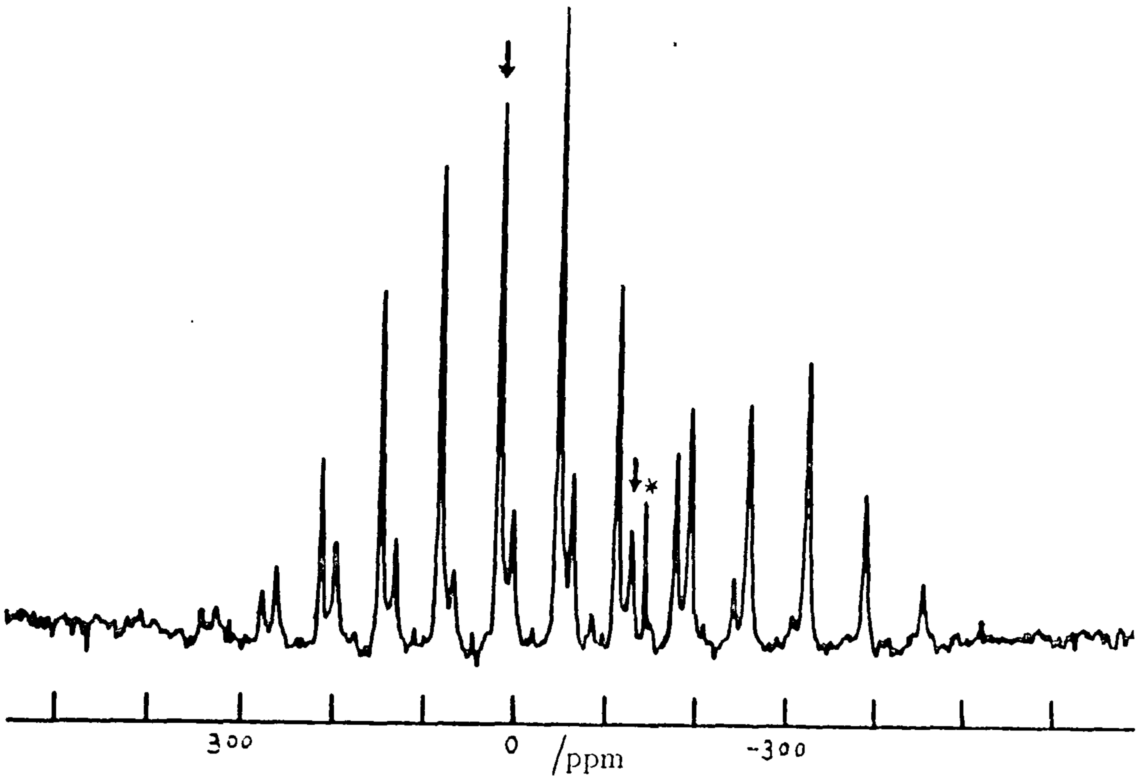

Figure 7.4.3: ^{207}Pb spectrum of Ph$_6$Pb$_2$ obtanied at 41.87 MHz. Spinning speed 2720 Hz. The spectrum was obtained by Dr. Sebald.

ppm and $\eta = 0.1$ [23].

The spectrum of hexaphenyldilead, Ph$_6$Pb$_2$, shows two sets of spinning sideband manifolds, implying that two types of Pb atoms exist in the molecular asymmetric unit (Figure 7.4.3). The centrebands, at $-$ 131.8 ± 0.5 and 14.5 ± 0.5 ppm respectively, are indicated by the arrows, and the peak marked with * is an impurity. The sidebands were analyzed separately for each anisotropic pattern, and the resulting spectra are shown in Figures 7.4.4(a) and (b). The fit of the higher frequency resonance (14.5 ppm) is relatively better, reflecting the fact that the higher frequency sideband manifold has smaller errors in the intensity measurement, due to the large magnitude of the intensities compared with the noise level. Measuring the lower intensity peaks, however, involves a greater error, due to the noise level being of significant magnitude compared with the peak heights; in this case the fit is less impressive. The spinning sidebands of ^{207}Pb spectra of $C_6H_5O_2Pb$ and

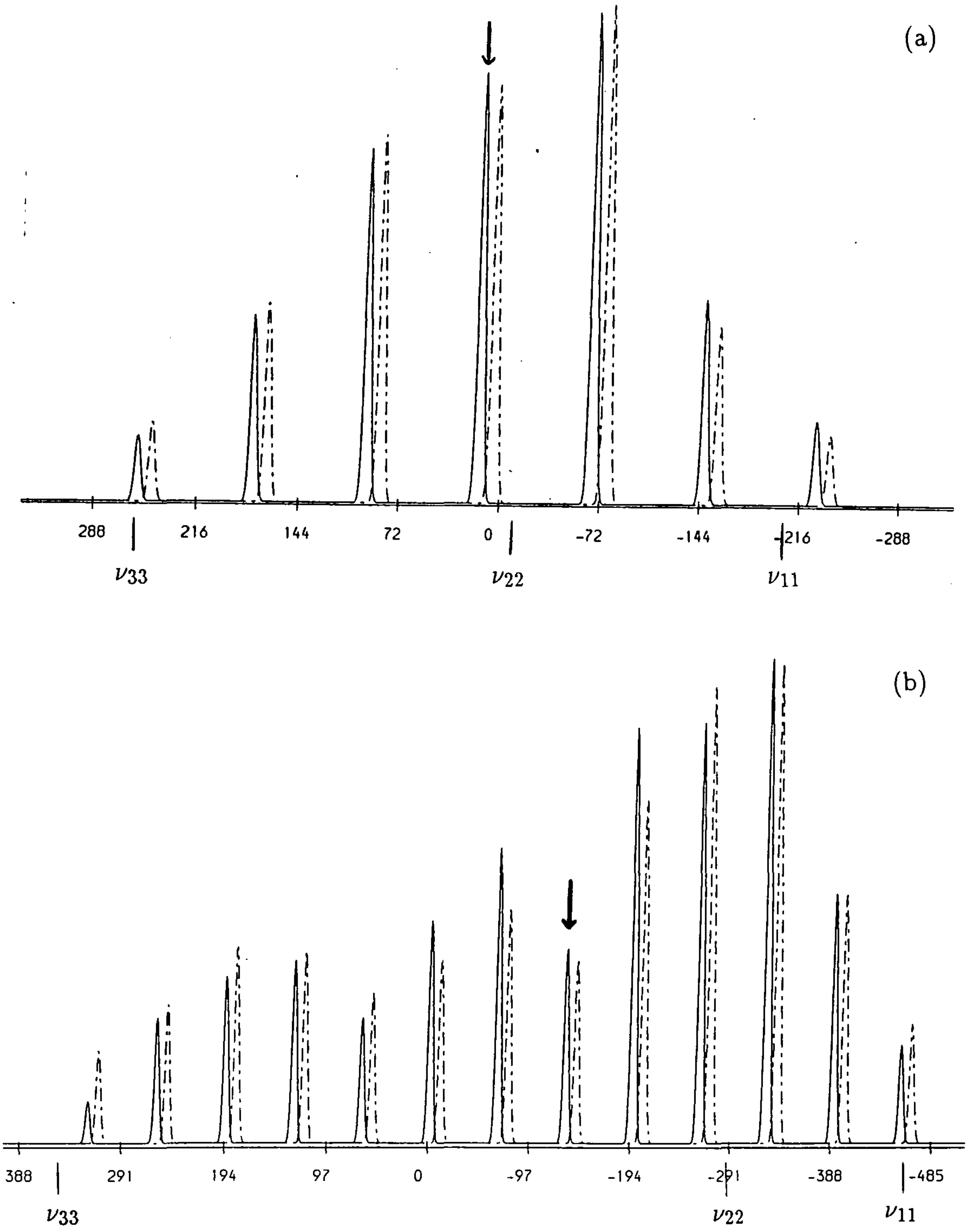

Figure 7.4.4: Fitting results of Figure 4.7.3. (a) Higher frequency resonance (δ = 14.5 ppm): anisotropy = −242 and asymmetry = 0.85; (b) Lower frequency resonance (δ = −134.8 ppm): anisotropy = −483 ppm and asymmetry = 0.35.

Table 7.4.1 ^{207}Pb spinning sideband analysis results for some organolead compounds

compounds	ν_r /Hz	δ_{Pb} /ppm	$\sqsupset$ /ppm	η	σ_{11} /ppm	σ_{22} /ppm	σ_{33} /ppm
$Ph_2Pb(SCH_2)_2$	3175	280.6	−312	0.24	−87	−163	−592
		(± 0.5)	(± 1)	(± 0.08)	(± 1)	(± 1)	(± 1)
$(C_9H_{19}CO_2)_4Pb$	3150	−2138	415	0.27	1874	1987	2553
		(± 0.5)	(± 3)	(± 0.2)	(± 3)	(± 3)	(± 3)
Ph_6Pb_2	2720	−131.8	−483	0.35	459	288	−351
		(± 0.5)	(± 2)	(± 0.15)	(± 2)	(± 2)	(± 2)
	2720	14.5	−242	0.85	210	4	−256
		(± 0.5)	(± 3)	(± 0.2)	(± 3)	(± 3)	(± 3)
$C_6H_5O_2Pb$	4500	−89.5	548	0.5	−323	−46	637
		(± 0.5)	(± 3)	(± 0.2)	(± 3)	(± 3)	(± 3)
$Ph_2Pb(OAc)_2$	3270	−226.4	793	0.22	−257	−83	1019
		(± 0.5)	(± 4)	(± 0.25)	(± 4)	(± 4)	(± 4)

The data in parentheses are the estimated errors.

$Ph_2Pb(OAc)_2$, both were taken by Sebald, were also analyzed. The fitting results, together with the estimated errors, are summarized in Table 7.4.1.

^{207}Pb NMR spectra of even chain-length lead carboxylates were recorded and their corresponding shielding tensor parameters were obtained. The results are given in Table 7.4.2. A typical spectrum of this group of compounds, that of lead dodecane dioate ($Pb(O_2C(CH_2)_{10}CO_2)$), is shown in Figure 7.4.5, exhibiting a very poor signal-to-noise ratio. The position of the centreband, identified by changing the speed of rotation, is found to be at $\delta = -1204 \pm 0.5$ ppm. The spinning sideband analyses were performed for two spinning speeds, and one of the fitting results is illustrated in Figure 7.4.6. As expected for such a bad signal-

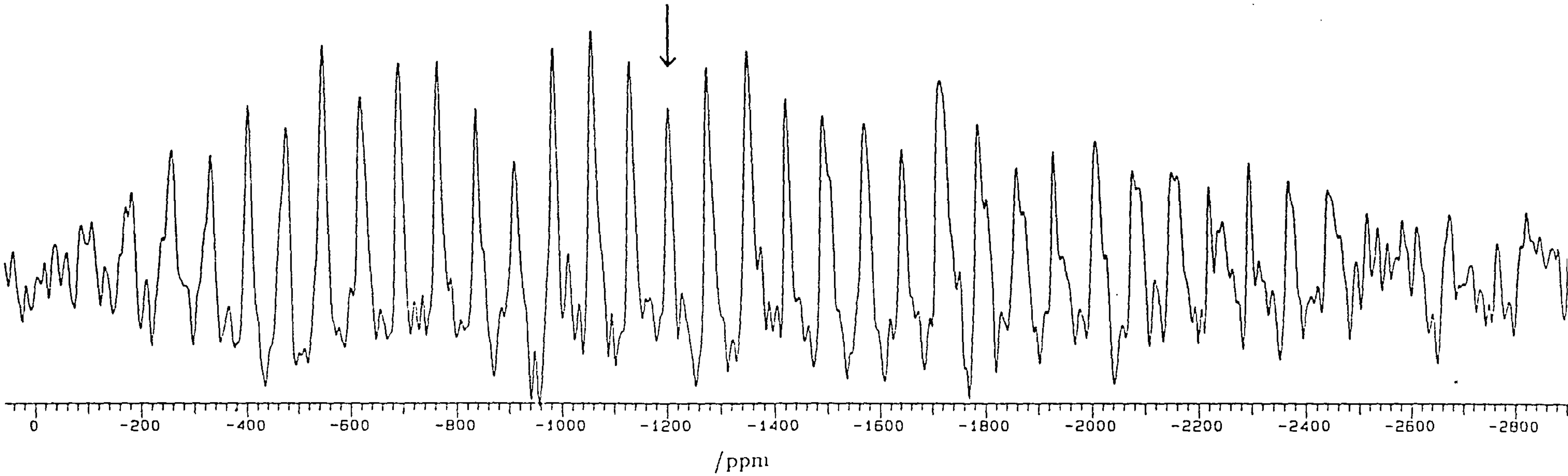

Figure 7.4.5: ^{207}Pb spectrum of $Pb(O_2C(CH_2)_{10}CO_2)$ obtained at 62.56 MHz on a VXR-300 spectrometer. The arrow indicates the centreband. Spectrometer operating conditions: contact time 5ms; recycle delay 30s; number of transitions 1900; spinning speed 4590 Hz.

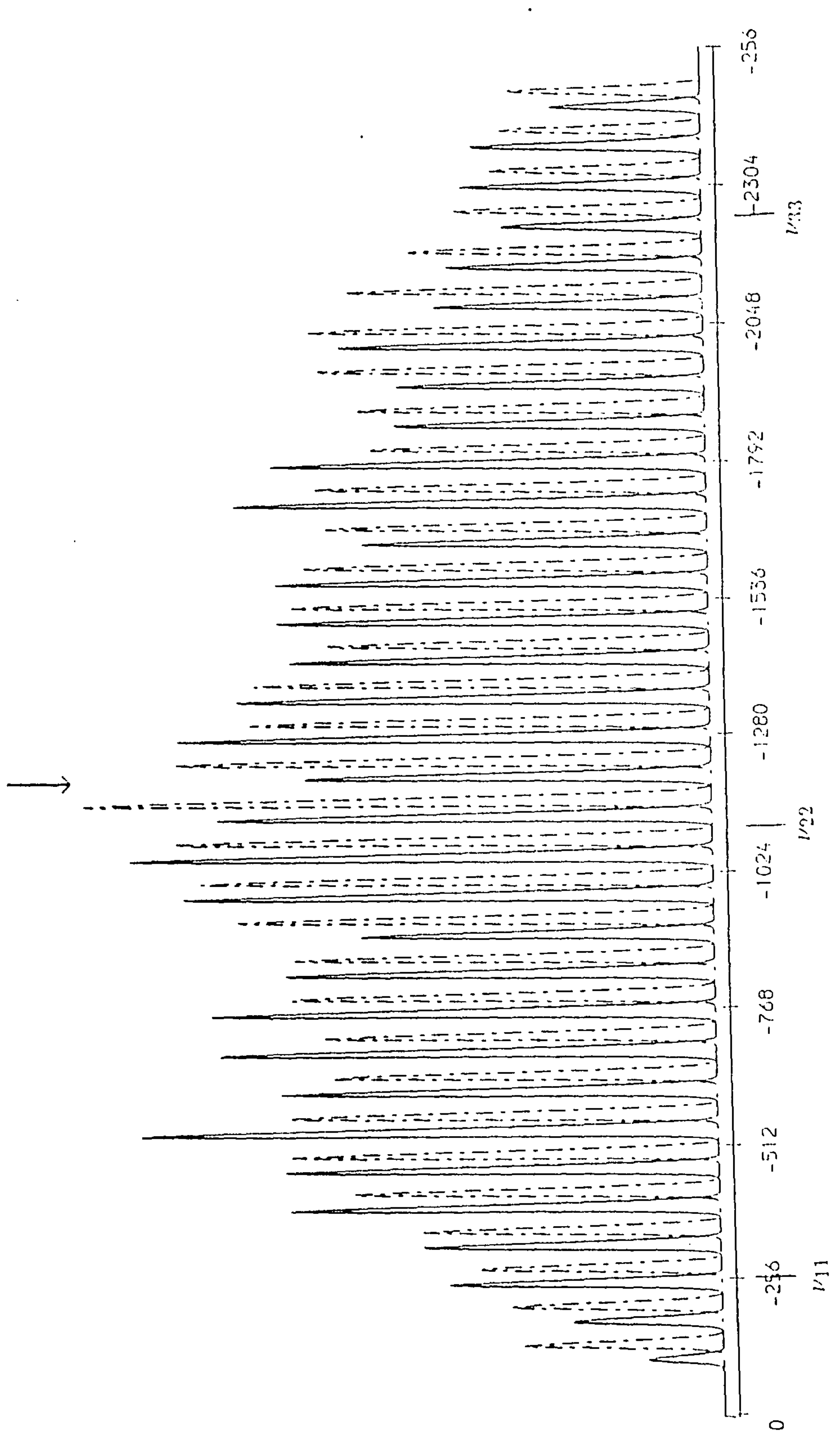

Figure 7.4.6: Fitting result of Figure 7.4.5: anisotropy = 1043 ppm and asymmetry = 0.82. The arrow indicates the centreband at −1204.2 ppm.

Table 7.4.2: ^{207}Pb shielding tensor components for even chain-length lead carboxylates

compounds	ν_r /Hz	δ_{cs} /ppm	$\beth$ /ppm	η	σ_{11} /ppm	σ_{22} /ppm	σ_{33} /pm
$Pb(O_2C(CH_2)_2CO_2)$	2900	-2441.0	445	0.68	2067	2370	2886
	3550	-2441.0	451	0.63	2073	2358	2892
	average	-2441.0	448	0.66	2070	2364	2889
		(± 0.0)	(± 3)	(± 0.03)	(± 3)	(± 6)	(± 3)
	2900	-2659.0	234	0.71	2459	2625	2893
	3550	-2659.0	237	0.66	2462	2619	2896
	average	-2659.0	236	0.69	2461	2622	2895
		(± 0.0)	(± 2)	(± 0.03)	(± 2)	(± 3)	(± 2)
$Pb(O_2C(CH_2)_4CO_2)$	4300	-1248.0	1249	0.29	442	805	2497
	4890	-1245.9	1079	0.46	458	955	2324
	average	-1246.9	1164	0.38	450	880	2411
		(± 1.0)	(± 85)	(± 0.09)	(± 8)	(± 75)	(± 86)
$Pb(O_2C(CH_2)_6CO_2)$	4000	-1255.4	1292	0.26	440	779	2547
	4513	-1254.1	1160	0.38	453	895	2414
	average	-1254.8	1226	0.32	447	837	2481
		(± 0.7)	(± 66)	(± 0.06)	(± 7)	(± 58)	(± 67)
$Pb(O_2C(CH_2)_8CO_2)$	3930	-1291.8	889	0.85	471	1224	2180
	4450	-1296.5	926	0.85	442	1225	2223
	average	-1294.2	908	0.85	457	1225	2202
		(± 2.4)	(± 19)	(± 0.0)	(± 15)	(± 1)	(±22)
$Pb(O_2C(CH_2)_{10}CO_2)$	4280	-1204.2	1121	0.82	182	1106	2325
	4590	-1204.2	1043	0.82	258	1108	2247
	average	-1204.2	1082	0.82	220	1107	2286
		(± 0.0)	(± 39)	(± 0.0)	(± 38)	(± 1)	(± 39)

to-noise ratio, the fit gives a relatively large difference between the experimental (the solid line) and calculated spectra, and the results obtained from different speeds of rotation, especially the anisotropy, $\sqsupset$, are quite different (Table 7.4.2). However, the relative error of the anisotropy, i.e. the absolute error (±39 ppm) divided by the averaged value of $\sqsupset$(1082 ppm), is still relatively small at ca.3 %. These facts indicate that reasonably accurate parameters of the shielding tensor could still be obtained, even for this rather noisy spectrum.

The cases investigated here cover a wide range of anisotropies (ca. 200 ppm to ca. 1200 ppm) and asymmetries (0.2 to 0.8). However, the structural interpretation of these data is beyond the scope of this thesis, and will not be dealt with here.

References

1. U. Haeberlen, *High-resolution NMR in Solids: Selective Averaging*, Academic Press, (1976).
2. B.R. Appleman and B.P. Dailey, *Adv. Magn. Reson.*, **7**, 231 (1974).
3. W.S. Veeman, *Prog. NMR Spectrosc.*, **16**, 193 (1975).
4. N. Bloembergen and J.A. Rowland, *Acta Metall.*, **1**, 731 (1953).
5. C.A. Fyfe, *Solid State NMR for Chemists*, C.F.C. Press, (1983).
6. M.M. Maricq and J.S. Waugh, *J. Chem. Phys.*, **70**, 3300 (1979).
7. J. Herzfeld and A.E. Berger, *J. Chem. Phys.*, **73**, 6021 (1980).
8. S.J. Opella and M.H. Frey, *J. Amer. Chem. Soc.*, **101**, 5854 (1979).
9. A. Bax and N.M. Szeverenyi, *J. Magn. Reson.*, **52**, 400 (1983).
10. N.J. Clayden, C.M. Dobson, L. Lian and D.J. Smith, *J. Magn. Reson.*, **69**, 476 (1986).

11. H.J.M. DeGroot, S.O. Smith, A.C. Kolbert, J.M.L. Courtin, C. Winkel, J. Lugtenberg, J. Herzfeld and R.G. Griffin, *J. Magn. Reson.*, **91**, 30 (1991).

12. H.J. Jakobson, P.D. Ellis, R.R. Inners and C.F. Jensen, *J. Amer. Chem. Soc.*, **104**, 7442 (1982).

13. P.S. Marchetti, P.D. Ellis and R.G. Bryant, *J. Amer. Chem. Soc.*, **107**, 8191 (1985).

14. L. Merwin, *Ph.D. Thesis*, Univ. of Durham, (1987).

15. E.R. Andrew, A. Bradbury and R.G. Eades, *Nature*, London, **182**, 1659 (1958).

16. I.J. Lowe, *Phys. Rev. Lett.*, **2**, 285 (1959).

17. E.R. Andrew, M. Firth, A. Jasinski and P.J. Randall, *Phys. Lett.*, **31A**, 446 (1970).

18. E. Lippmaa, M. Alla and T. Turherm, *Prog. 19th Cong. Ampere Heidelberg*, 113 (1976).

19. E.O. Stejskal, J. Schaefer and R.A. Mckey, *J. Magn. Reson.*, **25**, 569 (1977).

20. M.G. Munowitz and R.G. Griffin, *J. Chem. Phys.*, **76**, 2848 (1982).

21. Numerical Algorithms Group Ltd., *NAG FORTRAN Library*, (1990).

22. G.E. Hawkes, K.D. Sales, L.Y. Lian and R. Gobetto, *Prog. R. Soc.*, London, A **424**, 93 (1989).

23. H.D. Burrows, C.G.C. Geraldes, T.J.T. Pinheiro, R.K. Harris and A. Sebald, *Liquid Crystals*, Vol. **3**, No.6/7, 853 (1985).

Chapter VIII

Solid-state NMR studies of Titania pigments

8.1 Introduction

Due to the development of high-resolution NMR techniques for solid samples, it has become feasible to utilize these sophisticated methods for surface studies. The work presented in this chapter deals with the application of solid-state NMR to the surface studies of titanium dioxide (TiO_2) pigments. Most titania pigments are made up of a TiO_2 crystalline base coated with a layer of hydrous oxides, typically P_2O_5, Al_2O_3 and SiO_2. The pigments being coated are amorphous rather than crystalline in nature. Though the coating does not alter the optical characteristics of the TiO_2 base, it does improve the durability (by reducing the catalytic activity) and dispersibility (by modifying the surface properties) of the pigments [1]. Hence the understanding of the coatings is very important for manufacturers.

The TiO_2 pigment is produced commercially in two different crystalline forms: anatase and rutile. The latter has a more compact atomic structure with far superior durability and optical properties, so much more attention has been given to rutile. The unit cell of the rutile crystal structure [2] contains two different types of Ti–O bonds, with four shorter equatorial bonds at 1.944 Å and two longer axial bonds of 1.988 Å, as shown in Figure 8.1.1. The external surface of the rutile crystal is known to be generally composed of three planes: (110), (101) and (100), among which the (110) plane (Figure 8.1.2) has the greatest abundance of 60%. The surface layers are predominantly ionic, and thus hydroxyl groups and water molecules are very easily chemically absorbed on the surfaces. The characteristics of the surface OH groups and water molecules, carried by the metal oxides, are related to the structures of the underlying surface atoms or ions. Hence

^{1}H NMR studies of the surface OH groups and H_2O molecules should lead to a better understanding of the surface chemistry of TiO_2 pigments. Moreover, NMR studies of ^{31}P, ^{27}Al and ^{29}Si nuclei will provide direct information about the surface coatings. Though many infrared studies of the surface properties of the rutile TiO_2 have been carried out [3-5], NMR studies in this area have not yet been reported.

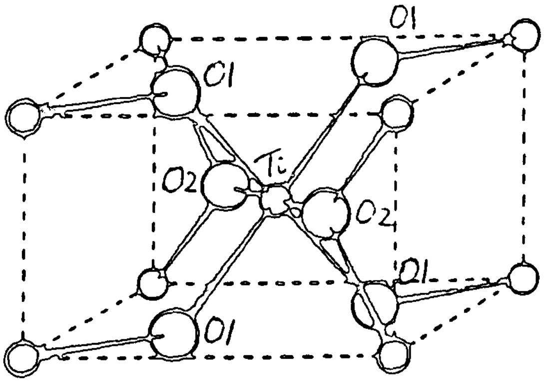

Figure 8.1.1: The unit cell of rutile crystal: Equatorial oxygens are indicated as O1 while axial oxygens are indicated as O2 [2].

This chapter describes NMR studies of four titania pigments which have different structural forms and different coatings. Their properties and compositions, together with their structures, are summarized in Table 8.1.1. However, the work reported here is only a preliminary study in this new area; neverthless, it demonstrates the potential of solid-state NMR in the study of surface science.

8.2 Handling of the samples

All the samples being investigated were provided by the Tioxide laboratories at Stockton. After being received, they were placed in a desiccator with a constant humidity mixture, which consisted of NaCl, KNO_3 and $NaNO_3$ salts. These salts were firstly dissolved in water separately to make saturated solutions and then the solutions were blended together to form a constant mixture with humidity of 30.5% at temperature 16.4°C. This mixture was made in order to keep the

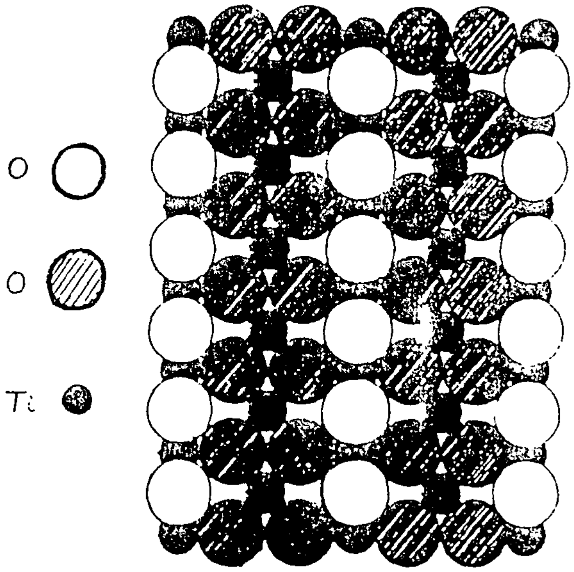

Figure 8.1.2: The (110) cleavage plane of rutile; the titanium ions and the shaded oxide ions are coplanar while the non-shaded oxide ions lie above this plane [2].

Table 8.1.1: The properties of TiO_2 pigments being investigated [6]

sample	structure	crystal size	surface area	additive
I	anatase	0.14 μm	10 m^2g^{-1}	0.6% P_2O_5, 0.4% K_2O
II	rutile	0.20 μm	3 m^2g^{-1}	0.15% P_2O_5, 0.15% K_2O
III	rutile	0.24 μm	20 m^2g^{-1}	4.4% Al_2O_3, 9.4% SiO_2
IV	rutile	0.20 μm	15 m^2g^{-1}	4.3% Al_2O_3, 0.92% organic coating

surfaces of these pigments in a constant condition. Meanwhile, a small amount of each pigment sample was put in an oven at a temperature of 220° for drying, in order to examine the adsorbed water molecules on the surfaces.

8.3 ^{1}H NMR studies of the TiO_2 pigments

^{1}H studies are one of the most established NMR techniques, and can provide a direct approach for examination of the OH groups and absorbed water on surfaces. The ^{1}H NMR spectra shown in this section are those from wideline and magic-angle-spinning methods, and were obtained using a Bruker CXP-200 spectrometer. The spectrometer has a magnetic field of 4.7 T, and accordingly the resonance frequency of protons is 200.13 MHz. ^{1}H wideline spectra are obtained in a static experiment, and are influenced by the strong dipole–dipole (e.g.^{1}H–^{1}H) interactions and shielding anisotropies, whereas MAS eliminates, to some extent, the dipolar couplings between protons and the shielding anisotropies of the nuclei. Hence the MAS results will be predominantly isotropic chemical shifts, giving much higher resolution.

The ^{1}H static spectrum of sample I gives one relatively narrow line at 0.7 ± 0.3 ppm and one wider line at 3.7 ± 0.3 ppm, with respect to TMS, as shown in Figure 8.3.1(a). Figure 8.3.1(b) shows the ^{1}H spectrum of the same sample after being dried for 16 days. It is clear that the low-frequency peak remained constant within experimental error, while the higher frequency peak appeared to split into two peaks at 5.3 ± 0.3 and 4.0 ± 0.3 ppm respectively. There is also a decrease in intensity in the high-frequency region, which is believed to be due to the reduction of surface water after drying. The resonance at ca. 5.0 ppm is assigned to the chemically absorbed water on the surface. The lines at ca. 1.0 and 4.0 ppm are both due to the surface hydroxyl groups; their intensities remain constant for different moisture content. The ^{1}H MAS spectrum (Figure 8.3.1(c)) shows three well-resolved peaks in agreement with the ^{1}H static results.

Figure 8.3.2 is the ^{1}H spectra of sample II, and the different moisture contents are indicated. The spectrum of the undried sample is dominated by the peak at 5.7 ± 0.6 ppm, while a shoulder at 1.8 ± 0.6 ppm can still be identified. The predominance of the peak assigned to water molecules suggests that sample II chemically

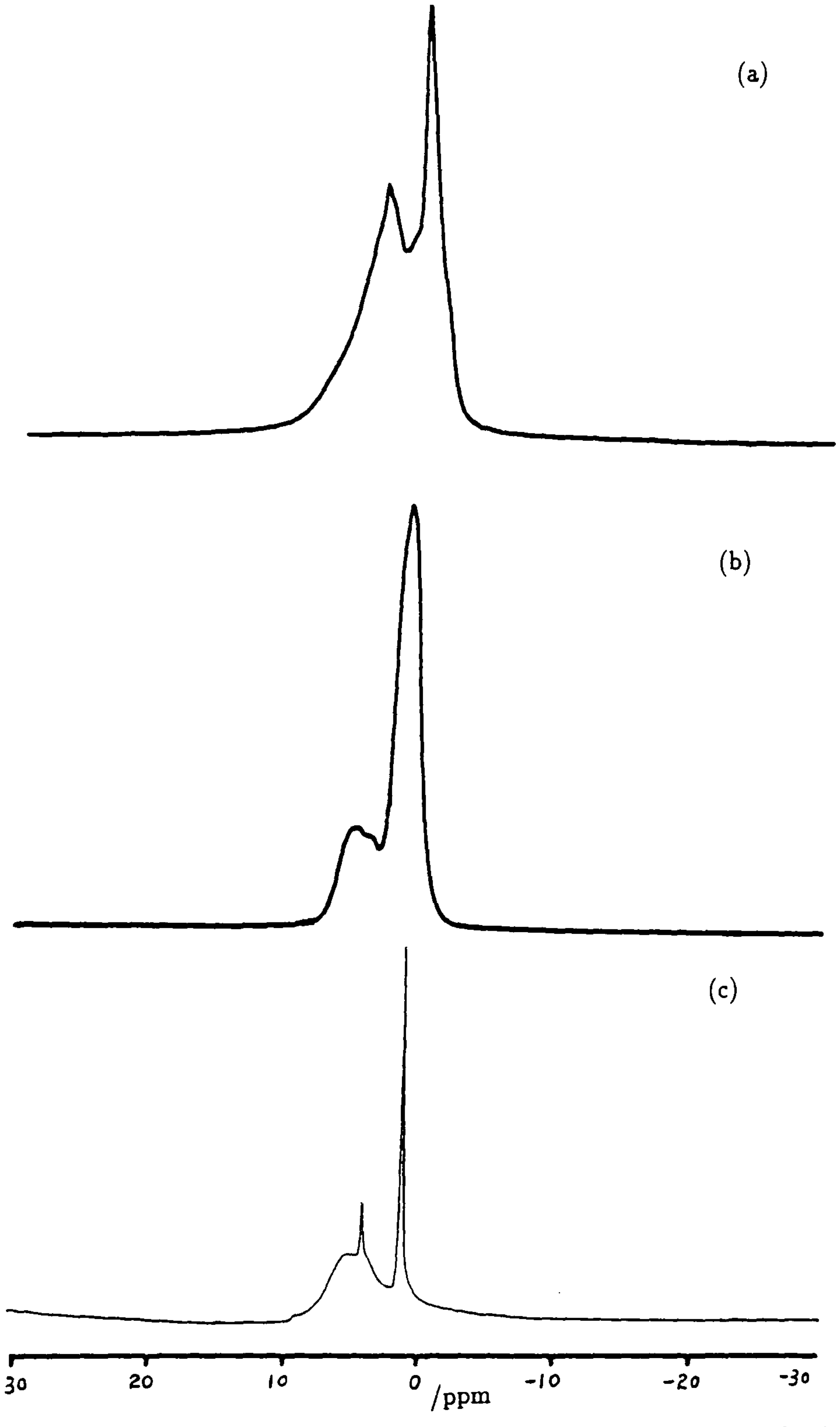

Figure 8.3.1: ^1H spectra of sample I, with anatase TiO_2 crystalline base, obtained at 200.13 MHz on a Bruker CXP-200 spectrometer. (a) static before drying; (b) static after drying for 16 days. Spectrometer operating conditions: recycle delay 3s; number of transitions 100. (c) MAS spectrum, with recycle delay 10s; number of transitions 100; spinning speed 1500 Hz.

adsorbs more water molecules than that of sample I, the two pigments have different TiO_2 structure, but both are coated with potassium phosphates. After the sample was dried in an oven for 1 day, the spectrum shows two equal intensity peaks, resulting from the intensity decrease of the peak at higher frequency. As the time for drying increases, the intensity of the high-frequency peak continues to decrease; meanwhile a line at ca. 4.3 ppm becomes more and more obvious, as shown in Figure 8.3.2(a)-(d). The ^1H MAS spectra, as displayed in Figures 8.3.3(a) and (b), exhibit two sharp lines at ca. 1.0 and ca. 4.0 ppm plus a broad peak at around 5.5 ppm, the intensity of which decreases as the moisture content decreases. This result is in accordance with that of the ^1H wideline experiments. The assignment of the three lines is the same as that for sample I, i.e. two lines related to the two types of OH groups and one related to surface water, whose amount reduces as the sample moisture content decreases.

The ^1H spectra of sample III and sample IV are very similar to those of sample II: hence their spectra will not be shown. It seems, then, that the ^1H NMR studies are unable to provide any information regarding the coatings, since the three pigments have very different coatings (though they all have rutile TiO_2 crystalline base). However, it may be concluded that pigments with anatase TiO_2 base may find it chemically more difficult to adsorb water on their surfaces than those with rutile TiO_2 base, but, these conclusions need further investigation.

8.4 Phosphorus-31 NMR studies of the TiO_2 pigments

^{31}P NMR spectroscopy is now one of the most important analytical tools for structure elucidation. This is largely due to its favorable NMR properties: spin-$\frac{1}{2}$, 100% natural abundance, and a wide range of chemical shifts (> 600 ppm) [7]. The anatase TiO_2 pigment had 0.6% P_2O_5 added, whereas one of the rutile TiO_2 samples (II) is coated with 0.15% P_2O_5. Hence ^{31}P NMR studies of the two samples are expected to show any structural difference between the two surfaces. The ^{31}P spectra were recorded at 81.01 HMz on a Bruker CXP-200 spectrometer,

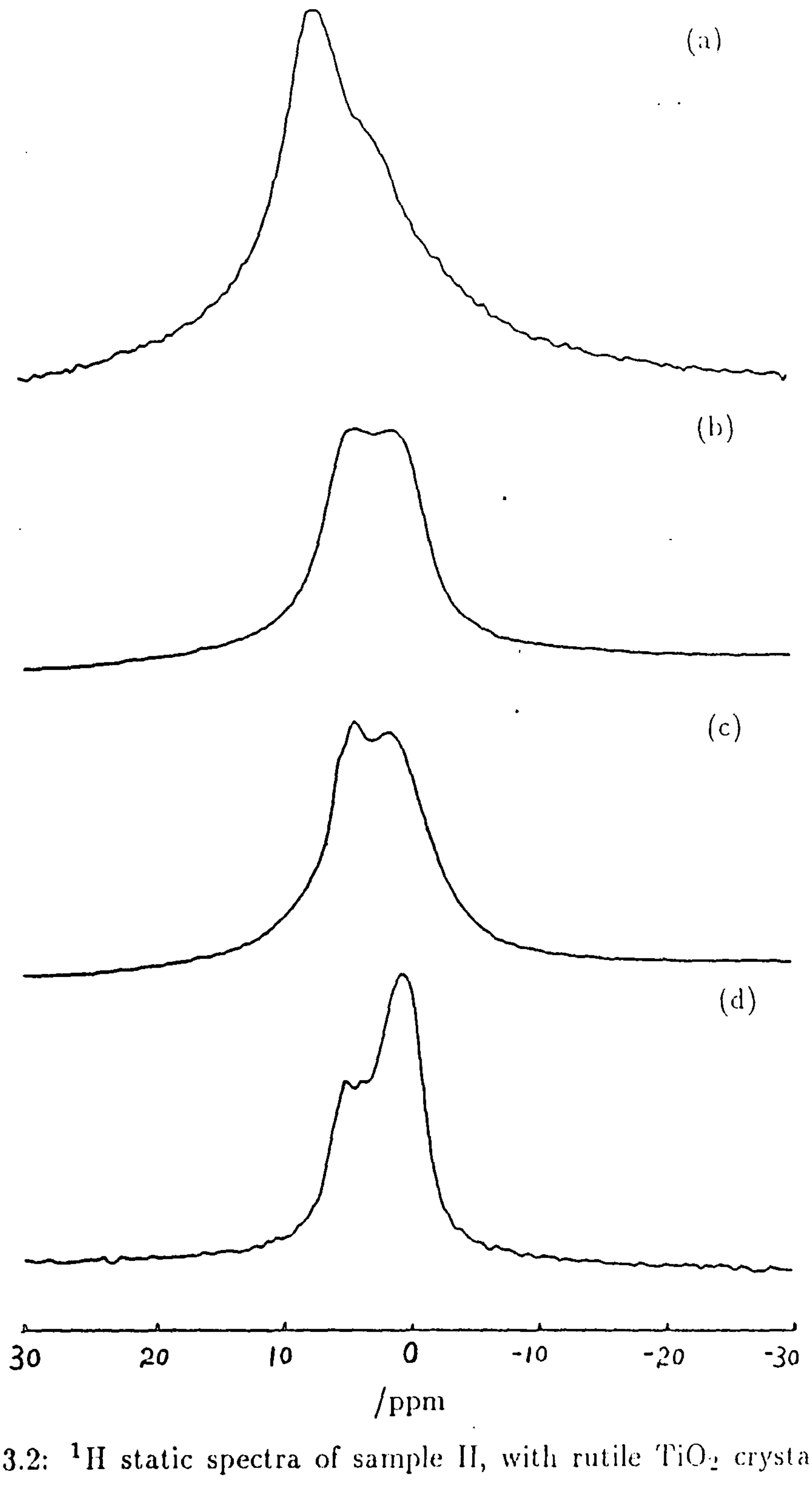

Figure 8.3.2: ${}^{1}H$ static spectra of sample II, with rutile TiO_2 crystalline base, obtained at 200.13 Mhz. Spectrometer operating conditions: recycle delay 3s; number of transitions 400. (a) undried, (b) dried for 1 day, (c) dried for 4 days, (d) dried for 100 days.

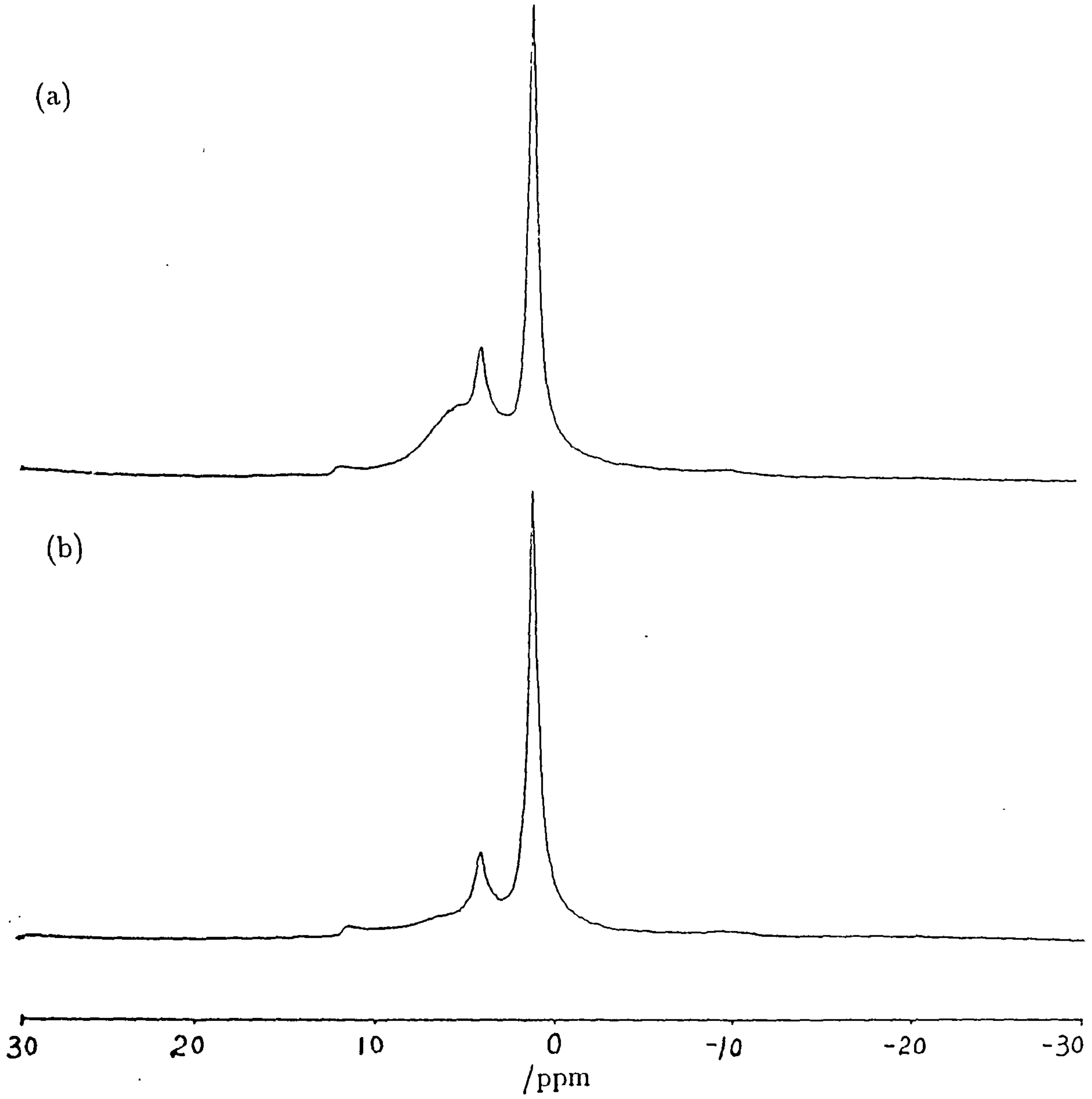

Figure 8.3.3: ^{1}H MAS spectra of sample II, obtained at 200.13 MHz. Spectrometer operating conditions: recycle delay 10s; number of transitions 100. (a) undried, (b) dried for 2 days.

and the chemical shifts are referenced to H_3PO_4 solution.

Both cross-polarization (CP) and single-pulse excitation experiments (SPE), together with magic-angle spinning, were performed on each sample. While CP discriminates in favour of phosphorus nulei close to protons, SPE favours phosphorus sites with faster relaxation rates (unless the recycle delay is sufficiently long). Thus, the comparison of CP and SPE spectra may provide information on the proximity of protons to phosphorus. The ^{31}P MAS and the ^{31}P CPMAS spectra of the anatase pigment (sample I), are shown in Figures 8.4.1(a) and (b) respectively, both with small spinning sidebands. The SPE experiment shows only one line at ca. -3.8 ppm, with linewidth of ca. 1100 Hz. For phosphorus nuclei in solids, the recycle delay needed to allow sufficient time for relaxation may be of the order of hundreds of seconds [8]. However, the recycle delay used to produce the SPE spectrum was only 5s, apparently very short. Hence, it is possible that the broad line in Figure 8.4.1 (a) is the result of superposition of several different closely related phosphorus species.

On the other hand, the CP spectrum shows two lines at ca. 1.0 and ca. -3.4 ppm respectively. The linewidth is much narrower, since for the CP experiment the recycle delay is determined by the proton relaxation time which is usually much shorter than that of phosphorus nuclei. The chemical shift of the lower frequency peak (-3.4 ppm) is very close to that of the single resonance observed in the SPE spectrum, so they may be regarded as from the same phosphate species. This phosphorus site may be assigned to the potassium phosphate (i.e. $P\text{-}O^-K^+$), since both CP and SPE experiments detected the signal. The additional peak appearing in the CP spectrum may arise from the phosphorus atoms coupled to OH groups which may be adsorbed on the surface (i.e. P-OH). Hence P-31 NMR indicates that at least two types of phosphate groups are present.

Figures 8.4.2 (a) and (b) show the ^{31}P NMR spectra of sample II, contrary to that of sample I, there is only one resonance in both MAS and CPMAS spectra.

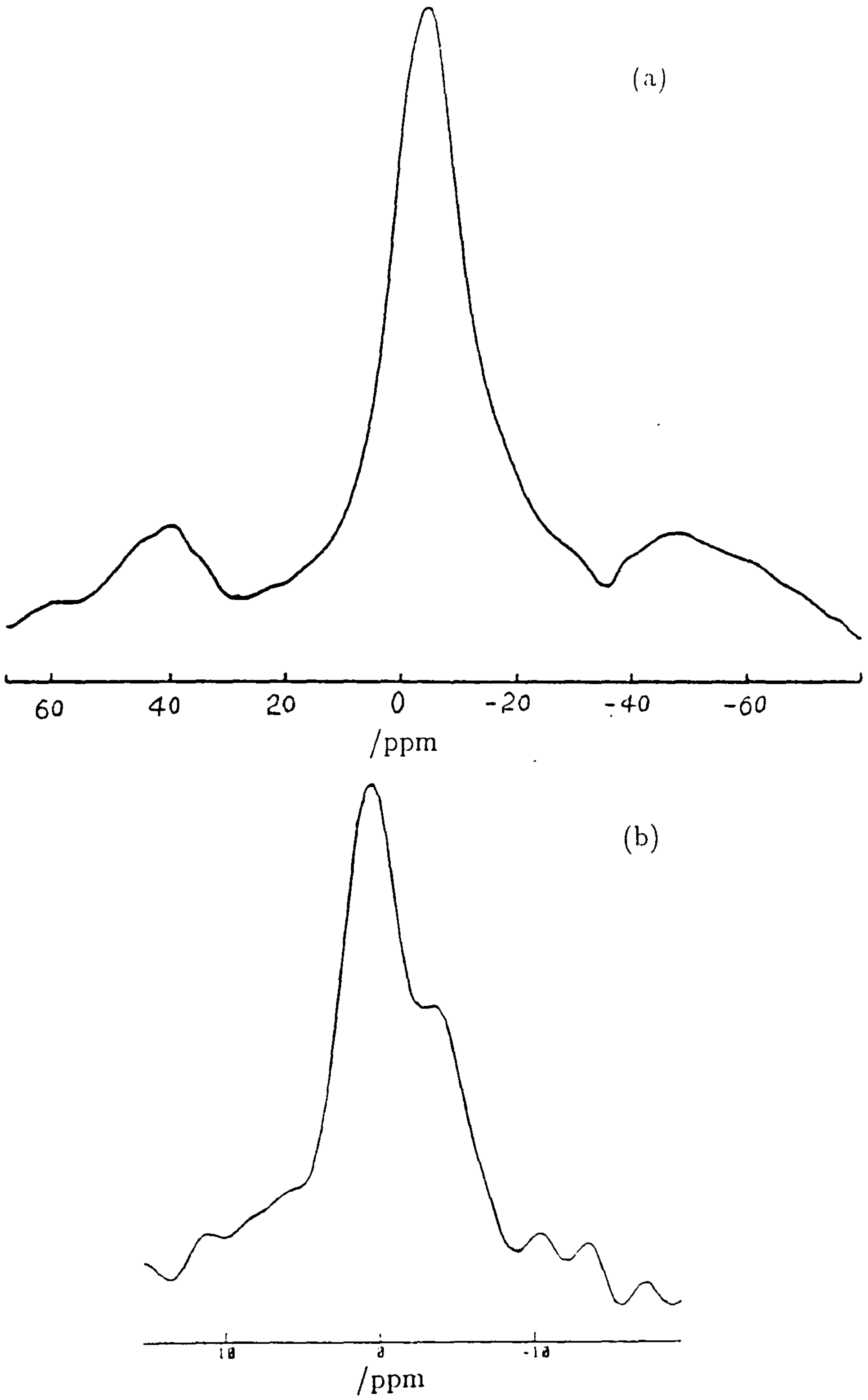

Figure 8.4.1: ^{31}P spectra of sample I obtained at 81.01 MHz. (a) MAS; and (b) CPMAS. Spectrometer operating conditions: recycle delay 5s; number of transitions 1267; spinning speed 3100 Hz; contact time 5ms.

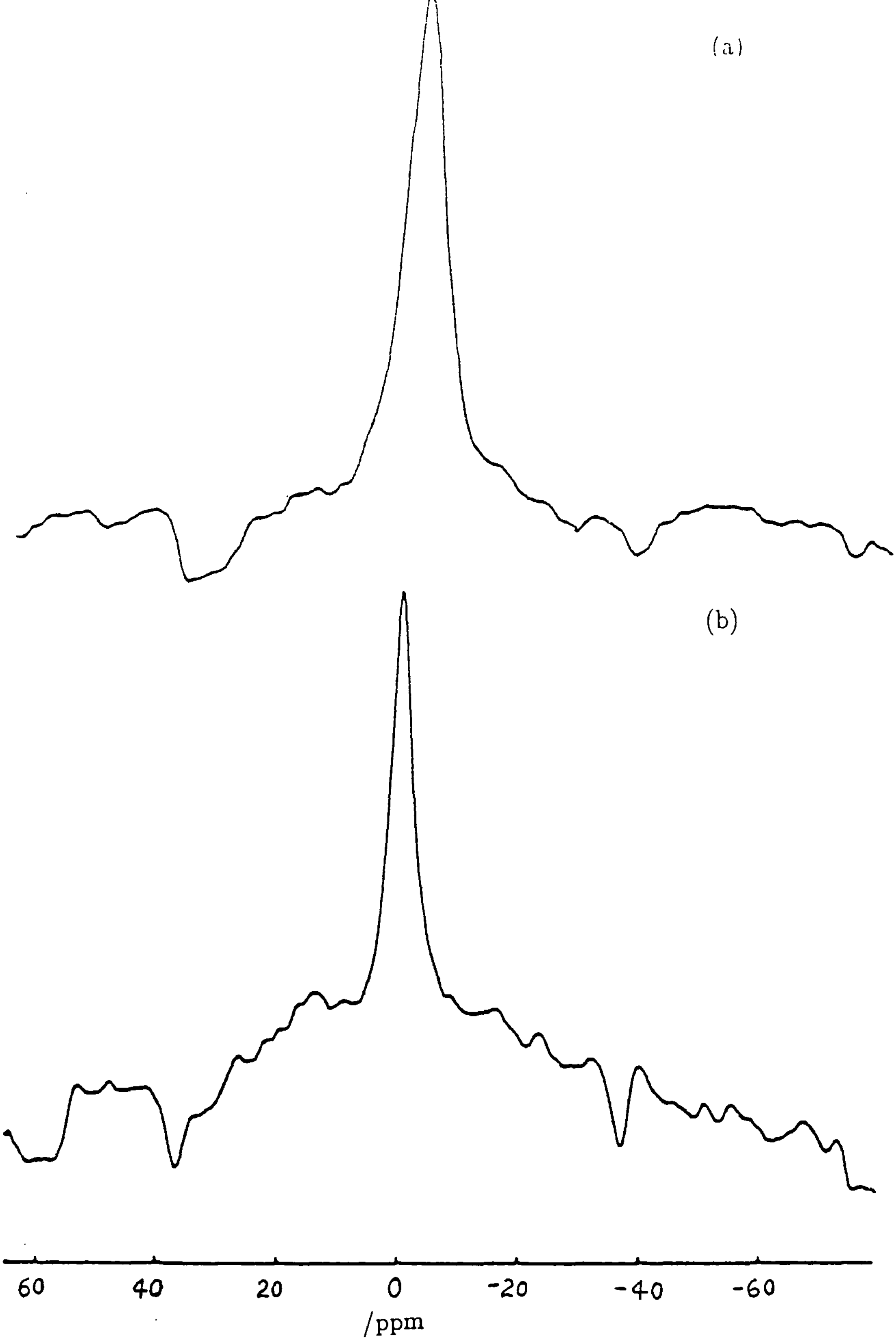

Figure 8.4.2: ^{31}P spectra of sample II, rutile TiO_2 pigment, obtained at 81.01 MHz. (a) MAS, with recycle delay 5s; number of transitions 1598; spinning speed 3000 Hz. (b) CPMAS, with contact time 5ms; recycle delay 5s; number of transitions 1598; spinning speed 3300 Hz.

The chemical shifts are ca. −0.4 ppm in SPE and ca. 0.3 ppm in CP. No resonance at around −3.4 ppm is observed, however, the SPE experiment gives a much broader linewidth than that of CP does. The reason for this could be due to the short recycle delay (5s) of the SPE spectrum, which allows the overlap of the resonances from different phosphorus species. Meanwhile, the CP spectrum, showing a much narrower linewidth, indicates that some of these species may be away from protons (since CP predominantly shows phosphorus sites near to protons). Therefore, it may be concluded that most phosphate coating in the sample is probably P–OH .

8.5 Aluminium-27 and silicon-29 studies of the pigments

Since the structure of the coatings (mainly Al_2O_3 and SiO_2) controls the pigment's surface chemistry, the application of ^{27}Al and ^{29}Si NMR to coating studies will provide important structural information about the surface. One of the most fundamental pieces of information concerning the structural environment is the number of chemically inequivalent types of Al or Si sites present in the sample under investigation. The number is directly related to the number of distinct lines in the ^{27}Al or ^{29}Si spectra. However, the possibility of distinguishing between structurally inequivalent nuclei depends on the spectral resolution (linewidth) and the chemical shift difference between the distinct atoms. For amorphous samples, including the pigments being studied, the spectra usually give broad and overlapping lines. However, valuable information as to which structural units are present may still be derived from the chemical shift range of the spectra.

^{27}Al NMR is capable of unambiguously distinguishing between tetrahedrally and octahedrally coordinated aluminium by their clear difference in chemical shift ranges. The range for AlO_4 units is 50 to 80 ppm, while AlO_6 units have a chemical shift range of about −10 to 20 ppm, with respect to $Al(H_2O)_6^{3+}$ in solution [9]. Moreover, the local environment of a SiO_4 unit is reflected with a high degree of sensitivity by the chemical shift of the central silicon atom. Figure 8.5.1 represents chemical shift reference chosen is TMS. The assignment of the ^{29}Si NMR peaks may thus be carried out by referring to this graph.

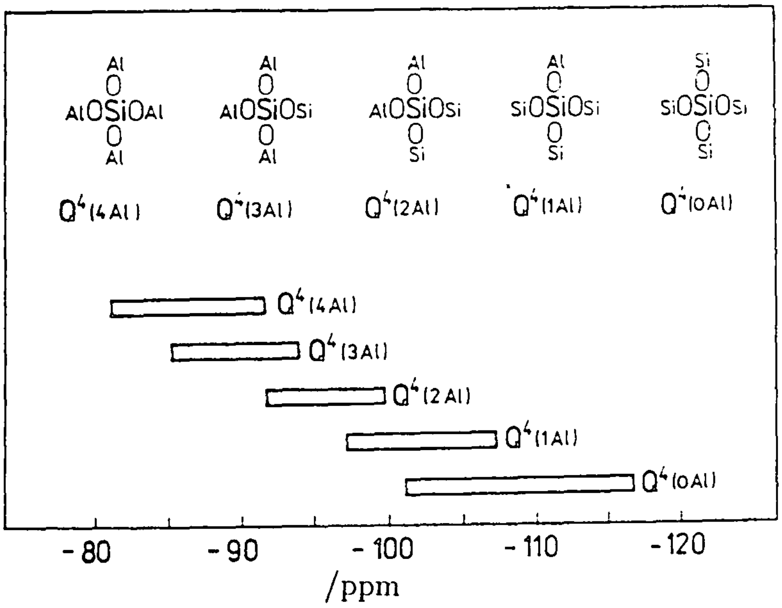

Figure 8.5.1: Ranges of ^{29}Si chemical shifts of Q^4(mAl) units in aluminosilicates [9].

Sample III is coated with both Al_2O_3 and SiO_2, so both ^{27}Al and ^{29}Si spectra have been taken. The ^{27}Al MAS spectrum (Figure 8.5.2), obtained at 78.2 MHz on a Varian VXR-300 spectrometer, exhibits a tetrahedral peak at 54.6 ± 1.0 ppm and an octahedral peak at 0.1 ± 1.0 ppm, the latter having much lower intensity. The spinning sidebands are indicated with $*$. There is also a broad line as indicated in the Figure. The origin of this peak may be due to either background or to sites of high asymmetry, given the large quadrupolar interactions of the aluminium nuclei.

Figure 8.5.3 shows the ^{29}Si MAS spectrum of sample III, obtained at 59.6 MHz. One line is observed at -94.6 ppm, with a large linewidth of ca. 20 ppm which probably results from several different types of silicon sites. The resonance is in

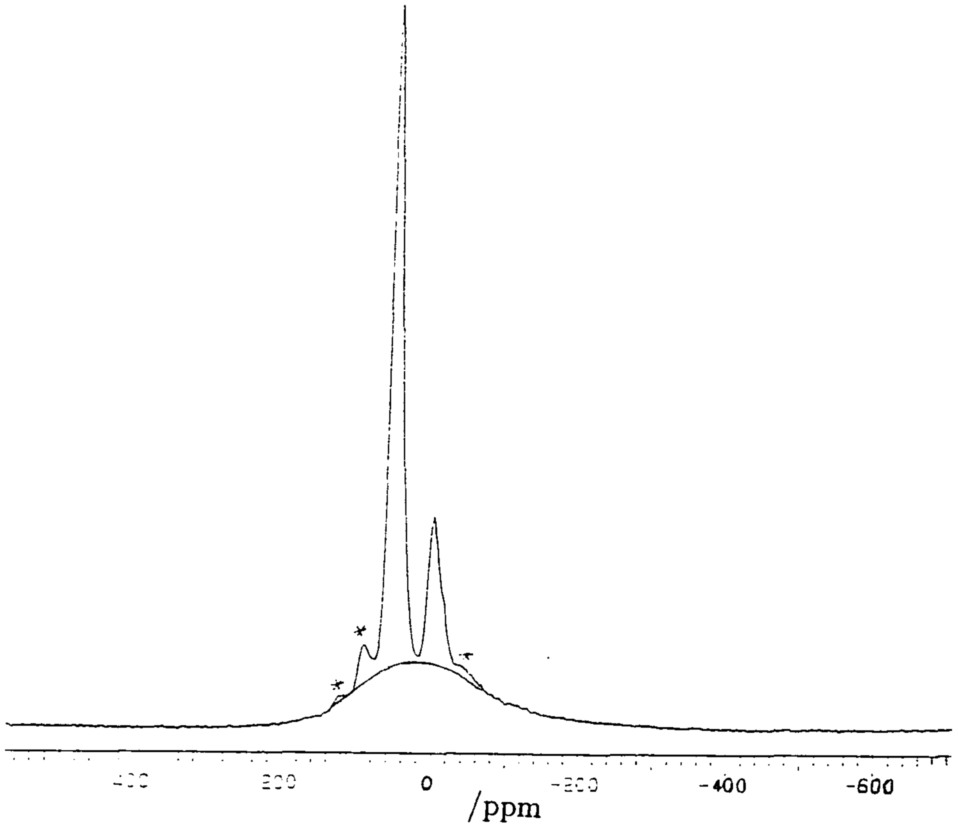

Figure 8.5.2: ^{27}Al spectrum of sample III, obtained at 78.15 MHz, with magic-angle spinning and single pulse excitation. The peaks marked with * are the spinning sidebands. Spectrometer operating conditions: recycle delay 1s; number of transitions 1000; spinning speed 2800 Hz.

probably results from several different types of silicon sites. The resonance is in the region expected for Si bonded to two OSi groups and two OAl (or OH) groups. Obviously, further studies should be carried out before any detailed structural information can be deduced.

The ^{27}Al MAS spectrum of sample IV is shown in Figure 8.5.4. The centre-band, obtained by varying the spinning speeds, is found to be 4.6 ± 1.0 ppm, lying in the region for octahedral sites. A broad line under the main peak is also

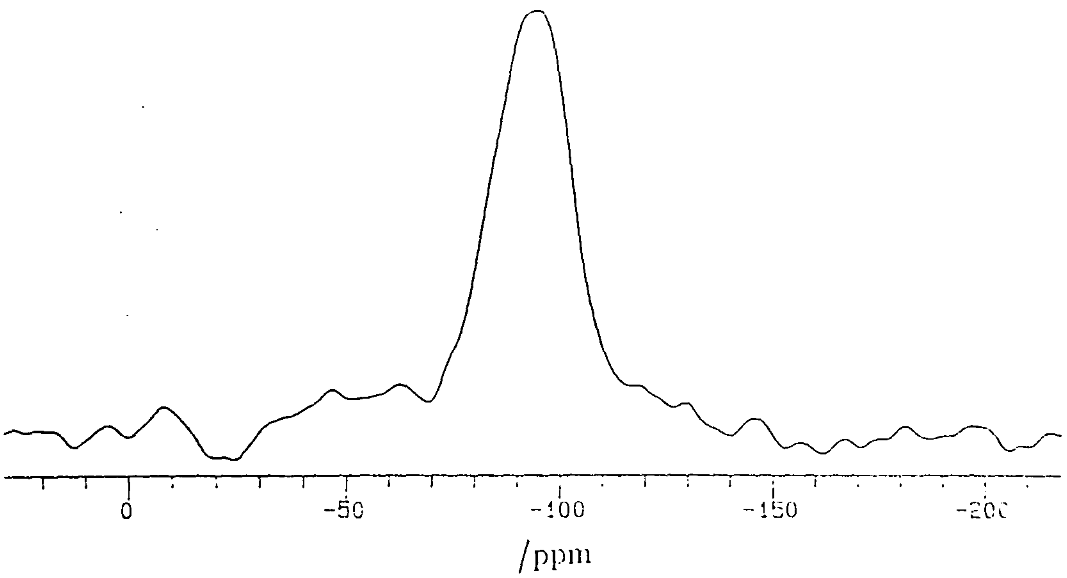

Figure 8.5.3: ^{29}Si spectrum of sample III, obtained at 59.58 MHz, with magic-angle spinning and single pulse excitation. Spectrometer operating conditions: recycle delay 10s; number of transitions 5660; spinning speed 4250 Hz.

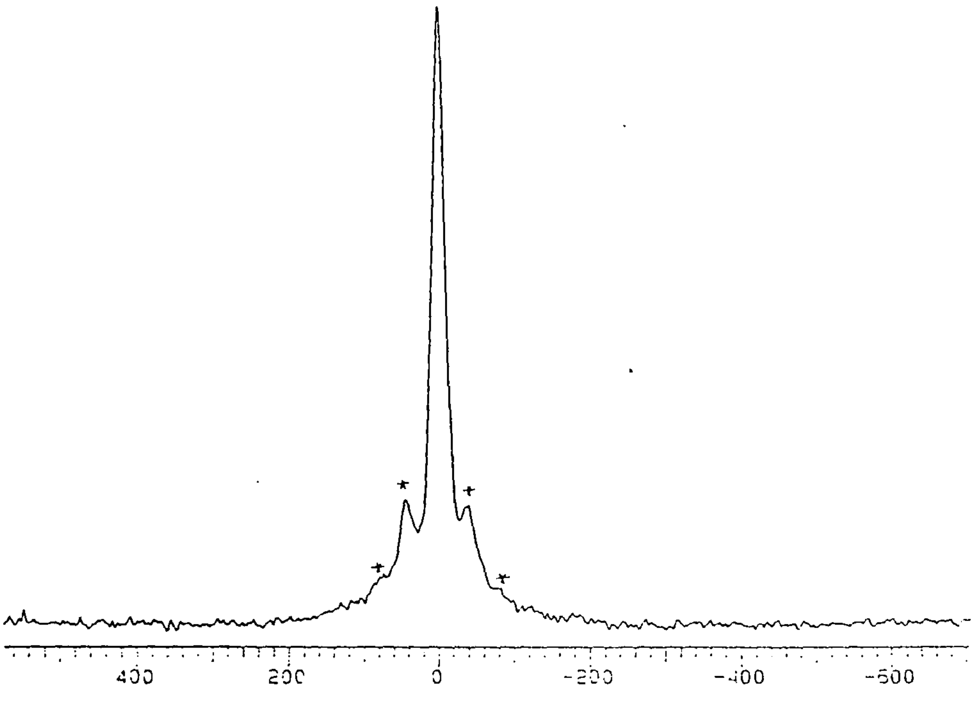

Figure 8.5.4: ^{27}Al spectrum of sample IV, obtained at 78.15 MHz, with magic-angle spinning and single pulse excitation. The peaks marked with * are the spinning sidebands. Spectrometer operating conditions: recycle delay 1s; number of transitions 1000; spinning speed 3080 Hz.

observed, possibly due to aluminium sites with high quadrupolar interactions or to background. The presence of one line suggests that there is only one type of aluminium nuclei on the surface for the pigment which is coated with Al_2O_3 but without silica.

References

1. *Tioxide pigments in airdrying glass paints*, BTP/167.
2. C.H. Rochester, *Infrared studies of absorbed species on rutile at the solid-vapor and solid-liquid interactions.*
3. P. Jones and J.A. Hockey, *Trans. Faraday Soc.*, **67**, 2679 (1971).
4. F.A. Grant, *Rev. Mod. Phys.*, **31**, 646 (1959).
5. D.K. Smith and H.W. Newkirk, *Acta. Cryst.*, **18**, 983 (1965).
6. Provided by the Tioxide Company.
7. D.G. Gorenstein, *Phosphorus-31 NMR, Principles and Applications.*
8. P.S. Belton, R.K. Harris and P.J. Wilkes, *J. Phys. chem. Solids*, Vol. **49**, No.1, 21 (1988).
9. G. Engelhardt and D. Miche, *High-resolution solid-state NMR of silicates and zeolites*, Wiley, (1987).

Appendix A

Program MOMENT

```
C                            Program MOMENT
C                          -----------------
C     Calculate the anisotropy and asymmetry of shielding tensors
C     by moment method through spinning sideband analysis
C     Haiping Bai, Dept. of Chemistry, University of Durham
C     Ref: M.Maricq and J. Waugh, J. Chem. Phys. 70, 3300 (1979)

      PROGRAM MOMENT

      IMPLICIT REAL (A-H,O-Z)
      DIMENSION SPI(-25:25), SPN(-25:25),R(3),ROOT(3),ETA(3)
      INTEGER LLIM,RLIM
      CHARACTER*80 TITL
      DATA PI /3.141592653/

C     ============ Data Input Section =====================
C     Read in sidebands and experimental parameters
C     Normalize sidebands and calculate delta and eta

      READ(5,100) TITL
  100 FORMAT(A80)
      READ(5,*) VR,SF
      READ(5,*) NSB,IH,IL
      READ(5,*) LLIM,RLIM
      SNRM=0.0
      READ(5,*) (SPI(I), I=IH,IL)
      DO 10 I=IH,IL
          SNRM=SNRM+SPI(I)
   10 CONTINUE
      DO 20 I=IH,IL
          SPN(I)=(SPI(I)*100.0)/SNRM
   20 CONTINUE
      READ(5,*) SHIF,WIDH

      SIGBAR=-SHIF
      AREA=0.0
      AM2=0.0
      AM3=0.0
      DO 30 I=IH,IL
         AREA=AREA+SPN(I)
         AM2=AM2+(I**2)*SPN(I)
         AM3=AM3+(I**3)*SPN(I)
   30 CONTINUE

C     Calculate the second and third moments CM2 and CM3,
C     Using equation X**3+A*X+B=0, R(N) is derived root,
```

```
C     the asymmetry parameter eqn.

      CM2=((VR**2)*AM2)/AREA
      CM3=((VR**3)*AM3)/AREA
      A=-15.0*CM2/4.0
      B=-35.0*CM3/8.0

      CM=2.0*SQRT(-A/3.0)
      THETA=ARCOS((3.0*B)/(A*CM))
      THETA=THETA/3.0
      R(1)=CM*COS(THETA)
      R(2)=CM*COS(THETA+(2.0*PI)/3.0)
      R(3)=CM*COS(THETA+(4.0*PI)/3.0)

      IK=0
      DO 40 I=1,3
         IF ((15.0*CM2)/(R(I)**2).LT.3.0) GO TO 40
         IK=IK+1
         ROOT(IK)=R(I)
   40 CONTINUE
      DO 50 I=1,IK
         ETA(I)=SQRT(((15.0*CM2)/(ROOT(I)**2))-3.0)
         ROOT(I)=ROOT(I)/SF
         IF(ETA(I).GT.1.0) GO TO 50
         EETA=ETA(I)
         DELP=ROOT(I)
   50 CONTINUE

C     Calculate the tensor components and set in proper order

      S33=DELP+SIGBAR
      S11=(3.0*SIGBAR-EETA*DELP-S33)/2.0
      S22=S11+EETA*DELP

      IF (ABS(S33-SIGBAR).GT.ABS(S11-SIGBAR)) GO TO 60
      TEMP=S11
      S11=S33
      S33=TEMP
   60 IF (ABS(S11-SIGBAR).GT.ABS(S22-SIGBAR)) GO TO 70
      TEMP=S22
      S22=S11
      S11=TEMP
   70 IF (ABS(S33-SIGBAR).GT.ABS(S11-SIGBAR)) GO TO 80
      TEMP=S11
      S11=S33
      S33=TEMP

C     =============== Output data ======================

   80 WRITE(6,220) DELP,EETA
  220 FORMAT(1X,'ANISOTROPY = ',F9.3,'ppm',3X,'ASYMMETRY
```

```
   1= ',F8.5,//1X)
    WRITE(6,230)
230 FORMAT(3X,'THE CORRESPONDING SHIFT TENSORS ARE :',//1X)
    WRITE(6,240) S11,S22,S33
240 FORMAT(3X,3F9.2)
    END
```

Appendix B

Program FITSB

```
C
C                          Program FITSB
C                        -----------------
C     Iteratively fits a spinning sideband pattern to extract the
C     shielding anisotropy and asymmetry
C     Haiping Bai, Dept. of Chemistry, University of Durham
C     Version 3, June 1989
C     Ref: M.Maricq and J. Waugh, J. Chem. Phys. 70, 3300 (1979)

      PROGRAM FITSB

      IMPLICIT DOUBLE PRECISION (A-H,O-Z)
      DIMENSION SPI(-25:25),SPN(-25:25),W1(2),W2(2),W3(2),W4(2)
      DIMENSION W5(3),W6(3,3),Z(2)
      INTEGER LLIM,RLIM
      COMMON Z
      COMMON /EXPI/ NSB,IH,IL,LLIM,RLIM
      COMMON /EXPR/ WR,VR,SF
      COMMON /SPEC/ SPN,SPI
      COMMON /PAR/ DELP,EETA,SHIF,SIGBAR
      COMMON /ERR/ IFAIL1,IFAIL2
      COMMON /EXPW/ WIDH
      EXTERNAL FUNCT,MONIT
      DATA N,IW,MAXCAL /2,3,100/

C     MAIN PROGRAM ************

      IFAIL1=0
      IFAIL2=0
      XAF=X02AAF(R)
      TOL=DSQRT(XAF)
      CALL INSET
      CALL E04CCF(N,Z,F,TOL,IW,W1,W2,W3,W4,W5,W6,FUNCT,MONIT,
     1MAXCAL,IFAIL1)
      CALL OUTPUT
      STOP
      END


      SUBROUTINE INSET

C     Input experimental data and set up arrays and tables

      IMPLICIT DOUBLE PRECISION (A-H,O-Z)
      DIMENSION SPI(-25:25), SPN(-25:25), Z(2), SPX(-25:25)
      DIMENSION ST(0:90),CT(0:90)
      INTEGER LLIM,RLIM
```

```
      COMMON Z
      COMMON /EXPI/ NSB,IH,IL,LLIM,RLIM
      COMMON /EXPR/ WR,VR,SF
      COMMON /SPEC/ SPN,SPI
      COMMON /CHAR/ TITL
      COMMON /TABLE/ ST,CT
      COMMON /PAR/ DELP,EETA,SHIF,SIGBAR
      COMMON /SCALE/ FSCAL
      COMMON /LIMS/ IUL,ILL
      COMMON /EXPW/ WIDH
      DATA NOR,TWOPI,PI /20,6.283185307,3.141592653/

C     DATA INPUT SECTION
C     Read in sidebands and experimental parameters and the
C     estimated delta and eta. Normalize sidebands

      READ(5,100) TITL
  100 FORMAT(A80)
      READ(5,*) VR,SF
      READ(5,*) NSB,IH,IL
      READ(5,*) LLIM,RLIM
      SNRM=0.0
      READ(5,*) (SPI(I), I=IH,IL)
      DO 10 I=IH,IL
          SNRM=SNRM+SPI(I)
   10 CONTINUE
      DO 20 I=IH,IL
          SPN(I)=(SPI(I)*100.0)/SNRM
   20 CONTINUE
      READ(5,*) SHIF,WIDH
      READ(5,*) DELP,EETA

C     Calculate sigmas and set in proper size order

      SIGBAR=-SHIF
      S33=DELP+SIGBAR
      S11=(3*SIGBAR-EETA*DELP-S33)/2
     [illegible]

     IF (ABS(S33-SIGBAR).GT.ABS(S11-SIGBAR)) GO TO 60
     TEMP=S11
     S11=S33
     S33=TEMP
  60 IF (ABS(S11-SIGBAR).GT.ABS(S22-SIGBAR)) GO TO 70
     TEMP=S22
     S22=S11
     S11=TEMP
  70 IF (ABS(S33-SIGBAR).GT.ABS(S11-SIGBAR)) GO TO 80
     TEMP=S11
     S11=S33
     S33=TEMP
```

```
C     Output starting parameters and spectrum to unit 6

   80 WRITE(6,150)
  150 FORMAT(6X,'PROGRAM FITSB : DATA AND RESULTS',///,1X)
      WRITE(6,200) TITL
  200 FORMAT(1X,A80,//,1X)
      WRITE(6,210)
  210 FORMAT(1X,'THE STARTING PARAMETERS FOR SIMULATION
     1ARE :',//1X)
      WRITE(6,220) DELP,EETA
  220 FORMAT(1X,'ANISOTROPY = ',F9.3,'ppm',3X,'ASYMMETRY
     1= ',F8.5,//1X)
      WRITE(6,230)
  230 FORMAT(3X,'THE CORRESPONDING SHIFT TENSORS ARE :',//1X)
      WRITE(6,240) S11,S22,S33
  240 FORMAT(1X,'S11 = ',F9.3,3X,'S22 = ',F9.3,3X,'S33
     1= ',F9.3,//1X)
      WRITE(6,250) VR,SF
  250 FORMAT(1X,'ROTOR SPEED= ',F8.2,' Hz    SPECTROMETER
     1FREQUENCY= ',F9.4,' MHz',//,1X)
      WRITE(6,300) SHIF
  300 FORMAT(1X,'THE CHEMICAL SHIFT = ',F9.3,' ppm',//,1X)
      WRITE(6,350) WIDH
  350 FORMAT(1X,'THE WIDTH OF PER PEAK = ',F9.3,' ppm',//,1X)
      WRITE(6,450) LLIM,RLIM
  450 FORMAT(1X,'FITTING OVER SIDEBAND RANGE: ',I3,' TO',I3,/1X)

C     Calculate angular spinning speed, initialize fitting arrays
C     Calculate sin and cos look-up tables
C     Calculate the fitting criteria

      WR=VR*TWOPI
      Z(1)=1.0
      Z(2)=EETA
      DO 90 I=0,NOR
          ARG=I*PI/NOR
          ST(I)=DSIN(ARG)
          CT(I)=DCOS(ARG)
   90 CONTINUE
      CALL SPECT(DELP,EETA,SPX)
      FSCAL=0.0
      DO 95 I=LLIM,RLIM
        FSCAL=FSCAL+(SPN(I)-SPX(I))**2
   95 CONTINUE
      FSCAL=1.0/FSCAL
      RETURN
      END


      SUBROUTINE SPECT(DELT,ETA,SPC)
```

```
C     Calculate spectrum by summing over molecular orientations

      IMPLICIT DOUBLE PRECISION (A-H,O-Z)
      DIMENSION SPC(-25:25),X(50),Y(50),WORK(50),TEMP(50)
      DIMENSION ST(0:90),CT(0:90),SUMR(50),SUMI(50)
      INTEGER LLIM,RLIM
      DOUBLE PRECISION NORC
      COMMON /EXPI/ NSB,IH,IL,LLIM,RLIM
      COMMON /EXPR/ WR,VR,SF
      COMMON /TABLE/ ST,CT
      COMMON /ERR/ IFAIL1,IFAIL2
      COMMON /LIMS/ IUL,ILL
      DATA NOR,INT /20,16/
      DATA PI,TWOPI /3.141592653,6.283185306/

C     Calculate spectrum over Euler angles and rotor period

      RP=1.0/(NSB*VR)
      DO 100 I=1,50
          X(I)=0.0
          Y(I)=0.0
  100 CONTINUE
      THEA=54.7*PI/180.0
      CONST=DSIN(2.0*THEA)
      CONST=CONST/2.0
      THD=0.5*(DSIN(THEA)*DSIN(THEA))
      DO 140 I=1, NOR
        SINA=ST(I)
        COSA=CT(I)
        SIN2A=2.0*ST(I)*CT(I)
        COS2A=CT(I)*CT(I)-ST(I)*ST(I)
        DO 130 J=1, NOR
          SINB=ST(J)
          COSB=CT(J)
          SSQB=SINB*SINB
          CO1=CONST*SINB
          CSQB=COSB*COSB
          DO 120 K=1, NOR
            SIN2C=2.0*ST(K)*CT(K)
            COS2C=CT(K)*CT(K)-ST(K)*ST(K)
            CO2=ETA*COS2C
            CO3=(1.5*SSQB+(ETA/2)*COS2C*(1+CSQB))
            C1=CO1*(COSB*(CO2-3)*COSA-ETA*SIN2C*SINA)
            S1=CO1*(COSB*(3-CO2)*SINA-ETA*SIN2C*COSA)
            C2=THD*(CO3*COS2A-ETA*COSB*SIN2C*SIN2A)
            S2=-THD*(CO3*SIN2A+ETA*COSB*SIN2C*COS2A)
            DO 110 L=1,INT
              T=(L-1)*RP
              AN=WR*T
              AN2=2.0*AN
```

```
              XI=(1.0/WR)*(S1+0.5*S2+C1*DSIN(AN)-S1*DCOS(AN)
     1          +0.5*(C2*DSIN(AN2)-S2*DCOS(AN2)))
              PT=XI*DELT*SF*TWOPI
              SUMR(L)=DCOS(PT)
              SUMI(L)=DSIN(PT)
              X(L)=X(L)+SUMR(L)*SINB
              Y(L)=Y(L)+SUMI(L)*SINB
  110         CONTINUE
  120       CONTINUE
  130     CONTINUE
  140   CONTINUE

C     Normalize FID, Perform FT,
C     Normalize real spinning sideband pattern

      NORC=0.0
      DO 150 I=1,NSB
        NORC=NORC+X(I)*X(I)+Y(I)*Y(I)
  150 CONTINUE
      NORC=DSQRT(NORC)
      DO 160 I=1,NSB
        X(I)=X(I)/NORC
        Y(I)=Y(I)/NORC
  160 CONTINUE
      CALL C06FCF(X,Y,NSB,WORK,IFAIL2)
      NORC=0.0
      DO 170 I=1,NSB
        NORC=NORC+X(I)
  170 CONTINUE
      DO 180 I=1,NSB
        X(I)=(X(I)*100.0)/NORC
  180 CONTINUE

C     Place SSB in proper order

      NCUT=IL+1
      NSTART=NSB+IH+1
      IJ=1
      DO 190 I=NSTART,NSB
        TEMP(IJ)=X(I)
        IJ=IJ+1
  190 CONTINUE
      DO 200 I=1,NCUT
        TEMP(IJ)=X(I)
        IJ=IJ+1
  200 CONTINUE
      J=1
      DO 210 I=IH,IL
        SPC(I)=TEMP(J)
        J=J+1
  210 CONTINUE
```

```
      RETURN
      END


      SUBROUTINE FUNCT(N,XC,FC)

C     Routine called from E04CCF calculates sum squared difference
C     between real and calculated SSB patterns over chosen range

      IMPLICIT DOUBLE PRECISION (A-H,O-Z)
      DIMENSION XC(N),SPN(-25:25),SPC(-25:25),SPI(-25:25)
      INTEGER N,LLIM,RLIM
      COMMON /PAR/ DELP,EETA,SHIF,SIGBAR
      COMMON /EXPI/ NSB,IH,IL,LLIM,RLIM
      COMMON /SPEC/ SPN,SPI
      COMMON /SCALE/ FSCAL
      COMMON /EXPW/ WIDH
      CDELT=XC(1)*DELP
      CETA=XC(2)
      CALL SPECT(CDELT,CETA,SPC)
      FC=0.0
      DO 10 I=LLIM,RLIM
        FC=FC+(SPN(I)-SPC(I))**2
   10 CONTINUE
      FC=FC*FSCAL
      RETURN
      END


      SUBROUTINE MONIT (FMIN,FMAX,SIM,N,IS,NCALL)

C     Subroutine to produce monitor output for the fitting routine
C     E04CCF output to unit 7

      DOUBLE PRECISION MIN,FMAX,SIM(IS,N)
      INTEGER IS,N,NCALL
      WRITE(7,100) NCALL,FMIN
  100 FORMAT (2X,'AFTER',I4,' FUNCTION CALLS, THE VALUE IS ',E14.7,
     1' WITH SIMPLEX:',/1X)
      WRITE (7,200)((SIM(I,J), J=1,N),I=1,IS)
  200 FORMAT(3(2F12.4/))
      RETURN
      END


      SUBROUTINE OUTPUT

C     Produce output of experimental and calculated parameters
C     Normalize SSB intensities.  Plot SSB patterns.

      IMPLICIT DOUBLE PRECISION (A-H,O-Z)
```

```
    DIMENSION SPN(-25:25),SPC(-25:25),SPI(-25:25),Z(2),TEMP(50)
    DIMENSION C1(50),C2(50),Z1(50),Z2(50),X1(1000),X2(1000)
    DOUBLE PRECISION MXY
    REAL MY,PDELT,PETA,PSF,PVR,PSHIF,LEFT,RIGHT,DEPTH,HEIGHT
    REAL CHARHT,SIGMA,SIGMA1,SIGMA2,SIGMA3,FNEWI,XDIV,CB,CH
    INTEGER LLIM,RLIM
    CHARACTER*80 TITL
    COMMON Z
    COMMON /EXPI/ NSB,IH,IL,LLIM,RLIM
    COMMON /EXPR/ WR,VR,SF
    COMMON /SPEC/ SPN,SPI
    COMMON /PAR/ DELP,EETA,SHIF,SIGBAR
    COMMON /CHAR/ TITL
    COMMON /ERR/ IFAIL1,IFAIL2
    COMMON /EXPW/ WIDH

    WRITE(6,100)
100 FORMAT(///,1X)
    IF (IFAIL2.EQ.1) GOTO 110
    IF (IFAIL2.EQ.2) GOTO 130
    IF (IFAIL2.EQ.3) GOTO 150
    GOTO 170
110 WRITE(6,120)
120 FORMAT(1X,'THE FT ROUTINE HAS FAILED: A PRIME FACTOR
   1OF NSB IS > 19 ',//1X)
    RETURN
130 WRITE(6,140)
140 FORMAT(1X,'FT ROUTINE HAS FAILED: NSB HAS MORE THAN
   120 FACTORS',//1X)
    RETURN
150 WRITE(6,160)
160 FORMAT(1X,'THE FT ROUTINE HAS FAILED: NSB < 1',//1X)
    RETURN
170 IF(IFAIL1.EQ.2) GOTO 180
    IF (IFAIL1.EQ.1) GOTO 200
    GOTO 300
180 WRITE(6,190)
190 FORMAT(1X,'THE ROUTINE (E04CCF) HAS REACHED THE
   1MAXIMUM NUMBER',/,1X,'OF FUNCTION CALLS WITHOUT REACHING
   1THE SPECIFIED TOLERANCE:'/,1X,'THE RESULTS OF THE LAST
   1ITERATION ARE NOTED BELOW',///,1X)
    GOTO 300
200 WRITE(6,210)
210 FORMAT(1X,'ONE OR MORE OF THE PARAMETERS FOR ROUTINE
   1E04CCF IS',/,1X,'OUTSIDE OF THE SPECIFIED RANGE: SEE
   2OUTPUT IN I/O UNIT 7',////,1X)
    RETURN

300 CDELT=Z(1)*DELP
    CETA=Z(2)
    DO 888 I=IH,IL
```

```
        SPC(I)=0.0
  888 CONTINUE

      IF(CETA.GT.-1.0.AND.CETA.LT.0.0) GO TO 890
      GO TO 895
  890 CETA=-CETA

  895 CALL SPECT(CDELT,CETA,SPC)
      S11=SIGBAR-0.5*CDELT*(1.0+CETA)
      S22=SIGBAR-0.5*CDELT*(1.0-CETA)
      S33=SIGBAR+CDELT

      SIGMA1=-S11
      SIGMA2=-S22
      SIGMA3=-S33

      WRITE(6,310)
  310 FORMAT(1X,'MASFIT HAS FIT THE SIDEBAND PATTERN TO THE
     1SPECIFIED TOLERANCE ' ,//,1X)
      WRITE(6,320) CDELT,CETA
  320 FORMAT(1X,' ANISOTROPY= ',F9.3,' ppm',3X,'ASYMMETRY
     1= ',F8.5,//1X)
      WRITE (6,340)
  340 FORMAT (1X,'THE CORRESPONDING SHIELDING TENSORS ARE:', //1X)
      WRITE(6,345) S11,S22,S33
  345 FORMAT (1X,3(3X,F9.3),//1X)
      WRITE(6,350)
  350 FORMAT (18X,'SIDEBAND INTENSITIES',//,1X,'SIDEBAND',4X,
     1'ENTERED',9X,'NORMALIZED',4X,'CALCULATED (NORMALIZED)',//)
      SDF=0.0
      DO 370 I=LLIM,RLIM
        WRITE(6,360) I,SPI(I),SPN(I),SPC(I)
        SDFF=SPN(I)-SPC(I)
        SDF=SDF+(SDFF*SDFF)
  360   FORMAT(3X,I3,3X,F11.2,9X,F9.6,8X,F9.6)
  370 CONTINUE
      WRITE(6,371) SDF
  371 FORMAT(1X,/,1X,'SUM OF SQUARED DIFFERENCES = ',1PE12.5)

C     PLOT SECTION
C     Put the spinning sidebands in proper order. Scale the
C     SSB intensities. Calculate the fitted and experimental
C     spinning sideband patterns by using Gaussian equation.

C     Note that DOUBLE PRECISION variables have been used to
C     this point because of the requirements of NAG on the MTS
C     mainframe.
C     For the GHOST-80 plot routines, REAL variables must be used
C     See type statements for a list of REAL plotting variables.

        IJ=1
```

```
       DO 440 J=IH,IL
          TEMP(IJ)=SPN(J)
          IJ=IJ+1
440    CONTINUE
       DO 450 J=1,NSB
          SPN(J)=TEMP(J)
450    CONTINUE
       IJ=1
       DO 460 J=IH,IL
          TEMP(IJ)=SPC(J)
          IJ=IJ+1
460    CONTINUE
       DO 470 J=1,NSB
          SPC(J)=TEMP(J)
470    CONTINUE
       DO 471 I=1,NSB
471    CONTINUE
    MXY=0.0
    DO 400 I=1,NSB
      MXY=DMAX1(MXY,SPN(I),SPC(I))
400 CONTINUE
    SCALER=70.0/MXY
    DO 405 I=1,NSB
       SPN(I)=SPN(I)*SCALER
       SPC(I)=SPC(I)*SCALER
405 CONTINUE
       DO 472 I=1,NSB
472    CONTINUE
    CO=1000.0/((NSB+2)*VR)
    WIDH=WIDH*SF
    LEFT=(1.5-IH)*VR/SF+SHIF
    RIGHT=SHIF-(1.5+IL)*VR/SF
    DO 410 I=1,NSB
       C1(I)=(I+0.5)*1000.0/(NSB+2)
       C2(I)=C1(I)+WIDH*CO*2.0
410 CONTINUE
    CB=SHIF
    CH=DMAX1(SPN(0),SPC(0))+1.0
    CH=CH*SCALER
    DO 420 I=1,1000
       DO 430 J=1,NSB
          Z1(J)=FLOAT(I)-C1(J)
          Z2(J)=FLOAT(I)-C2(J)
          Z1(J)=Z1(J)*Z1(J)
          Z2(J)=Z2(J)*Z2(J)
          Z1(J)=-Z1(J)*(4.0*LOG(2.0)/(WIDH*CO)**2)
          Z2(J)=-Z2(J)*(4.0*LOG(2.0)/(WIDH*CO)**2)
          Z1(J)=EXP(Z1(J))
          Z2(J)=EXP(Z2(J))
430    CONTINUE
       DO 480 J=1,NSB
```

```
            X1(I)=X1(I)+SPN(J)*Z1(J)+0.05
            X2(I)=X2(I)+SPC(J)*Z2(J)+0.05
  480     CONTINUE
  420 CONTINUE

C     Plot the calculated and experimental spinning
C     sideband patterns

      CALL PAPER(1)
      CALL PSPACE(0.01,0.99,0.10,0.80)
      CALL MAP(LEFT,RIGHT,-5.0,100.0)
      CALL POSITN(LEFT,0.5)
      DO 490 I=1,1000
         FNEWI=LEFT-(FLOAT(I)/1000.0*(LEFT-RIGHT))
         CALL JOIN(FNEWI,X1(I))
  490 CONTINUE
      CALL POSITN(LEFT,0.5)
      DO 500 I=1,1000
         FNEWI=LEFT-(FLOAT(I)/1000.0*(LEFT-RIGHT))
         CALL BROKEN(3,6,12,6)
         CALL JOIN(FNEWI,X2(I))
  500 CONTINUE

C     Write the text. Draw the scale

      CALL FULL
      CALL CSPACE(0.01,0.90,0.01,0.90)
      CALL CTRMAG(15)
      CALL CTRFNT(2)
      CALL PLACE(2,10)
      CALL TYPENC(100)
      CALL TYPENC(164)
      PDELT=CDELT
      PETA=CETA
      CALL TYPENF(PDELT,3)
      CALL PLACE(2,11)
      CALL TYPENC(106)
      CALL TYPENC(164)
      CALL TYPENF(PETA,5)
      CALL CTRFNT(1)
      CALL PLACE(2,12)
      CALL TYPECS('vr=')
      PSF=SF
      PVR=VR
      PSHIF=SHIF
      CALL TYPENF(PVR,1)
      CALL TYPECS('Hz')
      CALL PLACE(2,13)
      CALL TYPECS('sf=')
      CALL TYPENF(PSF,4)
      CALL TYPECS('MHz')
```

```
      CALL PLACE(2,14)
      CALL TYPECS('cs=')
      CALL TYPENF(PSHIF,2)
      CALL TYPECS('ppm')
      CALL CTRMAG(20)
      CALL PLACE(2,6)
      CALL TYPECS(TITL)
      CALL CTRFNT(2)
      CALL PLOTNC(CB,CH,187)
      CALL CTRMAG(10)
      XDIV=(LEFT-RIGHT)/10.0
      CALL XAXISI(FLOAT(INT(XDIV)))

C     Draw the positions of the calculated shielding components

      DEPTH=2.1
      HEIGHT=2.0
      CHARHT=2.5
      NAXIL=ABS(0.01*PDELT)
      IF (ABS(SIGMA1-SIGMA2).LT.NAXIL) GO TO 900
      CALL CTRMAG(15)
      CALL POSITN(SIGMA1,0.0-DEPTH)
      CALL JOIN(SIGMA1,0.0-DEPTH-HEIGHT)
      CALL PCSEND(SIGMA1,0.0-DEPTH-HEIGHT-CHARHT,'s')
      CALL CTRMAG(12)
      CALL TYPECS('11')
      CALL CTRMAG(15)
      CALL POSITN(SIGMA2,0.0-DEPTH)
      CALL JOIN(SIGMA2,0.0-DEPTH-HEIGHT)
      CALL PCSEND(SIGMA2,0.0-DEPTH-HEIGHT-CHARHT,'s')
      CALL CTRMAG(12)
      CALL TYPECS('22')
      CALL CTRMAG(15)
      CALL POSITN(SIGMA3,0.0-DEPTH)
      CALL JOIN(SIGMA3,0.0-DEPTH-HEIGHT)
      CALL PCSEND(SIGMA3,0.0-DEPTH-HEIGHT-CHARHT,'s')
      CALL CTRMAG(10)
      CALL TYPECS('33')
      GO TO 999
  900 SIGMA=(SIGMA1+SIGMA2)/2.0
      CALL CTRMAG(15)
      CALL POSITN(SIGMA,0.0-DEPTH)
      CALL JOIN(SIGMA,0.0-DEPTH-HEIGHT)
      CALL PCSEND(SIGMA,0.0-DEPTH-HEIGHT-CHARHT,'s')
      CALL CTRMAG(10)
      CALL TYPENC(193)
      CALL CTRMAG(15)
      CALL POSITN(SIGMA3,0.0-DEPTH)
      CALL JOIN(SIGMA3,0.0-DEPTH-HEIGHT)
      CALL PCSEND(SIGMA3,0.0-DEPTH-HEIGHT-CHARHT,'s')
      CALL CTRMAG(10)
```

```
    CALL TYPENC(208)
999 CALL GREND
    RETURN
    END
```

Appendix C

Program SIMD

```
C                        Program SIMD
C                      ---------------
C     THIS PROGRAM SIMULATES THE LINESHAPES OF A SPIN-HALF NUCLEUS
C     COUPLED TO ONE (OR TWO) QUADRUPOLAR NUCLEI (SPIN-3/2) USING
C     PERTURBATION THEORY

      PROGRAM SIMD

C     MAIN PROGRAM ************

      IMPLICIT REAL (A-H,O-Z)
      REAL MY,JCC,MAGICA
      INTEGER XA,XG,JIM
      DIMENSION QUAN(4),CONS(4),POSI(4),SPEC(4000)
      DIMENSION SPEC1(4000),SPEC2(4000),SPEC3(4000),SPEC4(4000)
      COMMON /INPUT/ DDASH,QCC,JCC,SFREQ,SPIN,WIDH
      COMMON /SCALE/ HZH,HZL,HZP,PNP,WIDTH,JIM
      COMMON /PAR/ QUAN
      DATA PI, MAGICA/3.141592,54.7/

C     Input the parameters and the frequency range ======

      READ (5,*) N,DDASH,QCC,JCC,SFREQ,WIDH
      READ (5,*) HZH,HZL

      SPIN=1.5
      JIM=1024

      QUAN(1)=-3.0/2.0
      QUAN(2)=-1.0/2.0
      QUAN(3)=1.0/2.0
      QUAN(4)=3.0/2.0

      HZP=(HZH-HZL)/(JIM-1)
      PNP=1.0/HZP
      WIDTH=4.0*LOG(2.0)/(WIDH**2)

      DO 200 M=1,JIM
         SPEC(M)=0.0
  200 CONTINUE

      IF (N.EQ.2) GO TO 40
      CEN=0.0
      CALL CONVOL(CEN,SPEC)
      GO TO 230

   40 DO 100 K=1,4
```

```
         CONS(K)=9.0*DDASH*QCC*(SPIN*(SPIN+1)-
     1   3.0*QUAN(K)**2)/(4.0*SFREQ*SPIN*(2.0*SPIN-1.0))
         CONS(K)=CONS(K)*2.0/15.0
         POSI(K)=-QUAN(K)*JCC+CONS(K)
 100  CONTINUE

      CEN1=POSI(1)
      CALL CONVOL(CEN1,SPEC1)
      CEN2=POSI(2)
      CALL CONVOL(CEN2,SPEC2)
      CEN3=POSI(3)
      CALL CONVOL(CEN3,SPEC3)
      CEN4=POSI(4)
      CALL CONVOL(CEN4,SPEC4)

      DO 220 M=1,JIM
         SPEC(M)=SPEC1(M)+SPEC2(M)+SPEC3(M)+SPEC4(M)
 220  CONTINUE

 230  DO 240 M=1,JIM
          MY=MAX1(MY,SPEC(M))
          SPEC(M)=SPEC(M)+0.1
 240  CONTINUE
      MY=MY+1.0

C     Output section =======

      CALL PAPER(1)
      CALL PSPACE(0.10,0.60,0.1,0.40)
      CALL MAP(HZH,HZL,0.0,MY)
      CALL POSITN(HZH,0.1)
      DO 400 M=1,JIM
          XM=HZH-FLOAT(M)*HZP
          CALL JOIN(XM,SPEC(M))
 400  CONTINUE
      CALL CTRMAG(15)
      XDIV=(HZH-HZL)/20.0
      CALL XAXISI(FLOAT(INT(XDIV)))

      CALL GREND
      END

C     **********************

      SUBROUTINE CONVOL(POSIT,SPC)

      IMPLICIT REAL (A-H,O-Z)
      REAL INCRAD,MY,MAGICA,JCC
      INTEGER XA,XG
      DIMENSION BETA(180),PHI(360),CONS(4),QUAN(4),Z(4)
      DIMENSION X(4,180), Y(4,180),PWD(4,4000),SPC(4000)
```

```
      COMMON /INPUT/ DDASH,QCC,JCC,SFREQ,SPIN,WIDH
      COMMON /SCALE/ HZH,HZL,HZP,PNP,WIDTH,JIM
      COMMON /PAR/ QUAN
      DATA PI,INCR/3.141592,5/

      MAGICA=54.7

      DO 20 M=1,JIM
         SPC(M)=0.0
 20   CONTINUE

      INCR=5
      INCRAD=INCR*PI/180.0
      MAGICA=MAGICA*PI/180.0

      DO 100 I=1,90
         BETA(I)=(I-1)*PI/180.0
         BET=BETA(I)
         DO 120 J=1,360,INCR
            PHI(J)=(J-1)*PI/180.0
            PH=PHI(J)
            COSTH=COS(MAGICA)*COS(BET)+SIN(MAGICA)*SIN(BET)*COS(PH)
            FREQ=COSTH**2*(1-COSTH**2)
            FREBAR=FREBAR+FREQ*INCRAD
120      CONTINUE
      FREBAR=FREBAR/(2.0*PI)

      DO 140 K=1,4
         CONS(K)=9.0*DDASH*QCC*(SPIN*(SPIN+1)-
     1   3.0*QUAN(K)**2)/(4.0*SFREQ*SPIN*(2.0*SPIN-1.0))
         X(K,I)=FREBAR*CONS(K)-QUAN(K)*JCC+POSIT
         Y(K,I)=SIN(BET)
140   CONTINUE
100   CONTINUE

      DO 200 K=1,4
         DO 220 L=1,90
            XF=X(K,L)
            XA=INT((HZH-XF)*PNP+0.5)
            DO 240 XG=1,JIM
               SPC(XG)=SPC(XG)+Y(K,L)*
     1                    EXP(-WIDTH*(FLOAT(XG-XA))**2)
240         CONTINUE
220      CONTINUE
200   CONTINUE
      RETURN

      END
```

The board of studies in Chemistry at Durham University requires that each postgraduate research thesis contains a list of:

(i) all research colloquia and research seminars and lectures arranged by the Department of Chemistry and DUCS during the author's residence as a postgraduate student;

(ii) all research conferences attended and papers presented by the author during the same period;

(iii) details of the postgraduate induction course.

Conferences attended

(i) International Society of Magnetic Resonance, Xth Meeting, Morzine, France, July 1989.

(ii) Solid State NMR: New Materials and New Techniques, RSC Symposium, Warwick, September 1990.

(iii) Graduate symposia at Durham (1988) and Newcastle (1990).

Induction Course

1. Departmental organisation.
2. Safety matters.
3. Electrical appliances.
4. Chromatography etc.
5. Atomic absorptiometry and inorganic analysis.
6. Library facilities.
7. Mass spectroscopy.
8. NMR.

UNIVERSITY OF DURHAM

Board of Studies in Chemistry

COLLOQUIA, LECTURES AND SEMINARS GIVEN BY INVITED SPEAKERS 1ST AUGUST 1987 to 31st JULY 1988

BIRCHALL, Prof. D. (I.C.I. Advanced Materials) Environmental Chemistry of Aluminium	25th April 1988
BORER, Dr. K. (University of Durham Industrial Research Labs.) The Brighton Bomb - A Forensic Science View	18th February 1988
BOSSONS, L. (Durham Chemistry Teachers' Centre) GCSE Practical Assessment	16th March 1988
BUTLER, Dr. A.R. (University of St. Andrews) Chinese Alchemy	5th November 1987
CAIRNS-SMITH, Dr. A. (Glasgow University) Clay Minerals and the Origin of Life	28th January 1988
DAVIDSON, Dr. J. (Herriot-Watt University) Metal Promoted Oligomerisation Reactions of Alkynes	November 1987
GRADUATE CHEMISTS (Northeast Polytechnics and Universities) R.S.C. Graduate Symposium	19th April 1988
GRAHAM, Prof. W.A.G. (University of Alberta, Canada) Rhodium and Iridium Complexes in the Activation of Carbon-Hydrogen Bonds	3rd March 1988
GRAY, Prof. G.W. (University of Hull) Liquid Crystals and their Applications	22nd October 1987
HARTSHORN, Prof. M.P. (University of Canterbury, New Zealand) Aspects of Ipso-Nitration	7th April 1988
HOWARD, Dr. J. (I.C.I. Wilton) Chemistry of Non-Equilibrium Processes	3rd December 1987
JONES, Dr. M.E. (Durham Chemistry Teachers' Centre) GCSE Chemistry Post-mortem	29th June 1988
JONES, Dr. M.E. (Durham Chemistry Teachers' Centre) GCE Chemistry A Level Post-mortem	6th July 1988
KOCH, Prof. H.F. (Ithaca College, U.S.A.) Does the E2 Mechanism Occur in Solution?	7th March 1988
LACEY, Mr. (Durham Chemistry Teachers' Centre) Double Award Science	9th February 1988
LUDMAN, Dr. C.J. (Durham University) Explosives	10th December 198
McDONALD, Dr. W.A. (I.C.I. Wilton) Liquid Crystal Polymers	11th May 1988
MAJORAL, Prof. J.-P. (Université Paul Sabatier) Stabilisation by Complexation of Short-Lived Phosphorus Species	8th June 1988
MAPLETOFT, Mrs. M. (Durham Chemistry Teachers' Centre) Salters' Chemistry	4th November 1987
NIETO DE CASTRO, Prof. C.A. (University of Lisbon and Imperial College) Transport Properties of Non-Polar Fluids	18th April 1988
OLAH, Prof. G.A. (University of Southern California) New Aspects of Hydrocarbon Chemistry)	29th June, 1988
PALMER, Dr. F. (University of Nottingham) Luminescence (Demonstration Lecture)	21st January 1988
PINES, Prof. A. (University of California, Berkeley, U.S.A.) Some Magnetic Moments	28th April 1988
RICHARDSON, Dr. R. (University of Bristol) X-Ray Diffraction from Spread Monolayers	27th April 1988
ROBERTS, Mrs. E. (SATRO Officer for Sunderland) Talk - Durham Chemistry Teachers' Centre - "Links Between Industry and Schools"	13th April 1988
ROBINSON, Dr. J.A. (University of Southampton) Aspects of Antibiotic Biosynthesis	27th April 1988
ROSE van Mrs. S. (Geological Museum) Chemistry of Volcanoes	29th October 1987
SAMMES, Prof. P.G. (Smith, Kline and French) Chemical Aspects of Drug Development	19th December 1987
SEEBACH, Prof. D. (E.T.H. Zurich) From Synthetic Methods to Mechanistic Insight	12th November 1987
SODEAU, Dr. J. (University of East Anglia) Durham Chemistry Teachers' Centre Lecture: "Spray Cans, Smog and Society"	11th May 1988
SWART, Mr. R.M. (I.C.I.) The Interaction of Chemicals with Lipid Bilayers	16th December 1987
TURNER, Prof. J.J. (University of Nottingham) Catching Organometallic Intermediates	11th February 1988
UNDERHILL, Prof. A. (University of Bangor) Molecular Electronics	25th February 1988

WILLIAMS, Dr. D.H. (University of Cambridge) Molecular Recognition	26th November 1987
WINTER, Dr. M.J. (University of Sheffield) Pyrotechnics (Demonstration Lecture)	15th October 1987

UNIVERSITY OF DURHAM

Board of Studies in Chemistry

COLLOQUIA, LECTURES AND SEMINARS GIVEN BY INVITED SPEAKERS
1ST AUGUST 1988 to 31st JULY 1989

ASHMAN, Mr. A. (Durham Chemistry Teachers' Centre) The Chemical Aspects of the National Curriculum	3rd May, 1989
AVEYARD, Dr. R. (University of Hull) Surfactants at your Surface	15th March, 1989
AYLETT, Prof. B.J. (Queen Mary College, London) Silicon-Based Chips:- The Chemist's Contribution	16th February, 198
BALDWIN, Prof. J.E. (Oxford University) Recent Advances in the Bioorganic Chemistry of Penicillin Biosynthesis	9th February, 1989
BALDWIN & WALKER, Drs. R.R. & R.W. (Hull University) Combustion: Some Burning Problems	24th November, 198
BOLLEN, Mr. F. (Durham Chemistry Teachers' Centre) Lecture about the use of SATIS in the classroom	18th October, 1988
BUTLER, Dr. A.R. (St. Andrews University) Cancer in Linxiam: The Chemical Dimension	15th February, 198
CADOGAN, Prof. J.I.G. (British Petroleum) From Pure Science to Profit	10th November, 198
CASEY, Dr. M. (University of Salford) Sulphoxides in Stereoselective Synthesis	20th April, 1989
CRESSEY & WATERS, Mr. D. & T. (Durham Chemistry Teachers' Centre) GCSE Chemistry 1988: "A Coroner's Report"	1st February, 1989
CRICH, Dr. D. (University College London) Some Novel Uses of Free Radicals in Organic Synthesis	27th April, 1989
DINGWALL, Dr. J. (Ciba Geigy) Phosphorus-containing Amino Acids: Biologically Active Natural and Unnatural Products	18th October, 1988
ERRINGTON, Dr. R.J. (University of Newcastle-upon-Tyne) Polymetalate Assembly in Organic Solvents	1st March, 1989
FREY, Dr. J. (Southampton University) Spectroscopy of the Reaction Path: Photodissociation Raman Spectra of NOCl	11th May, 1989
GRADUATE CHEMISTS, (Polytechs and Universities in North East England) R.S.C. Symposium for presentation of papers by postgraduate students	12th April, 1989

HALL, Prof. L.D. (Addenbrooke's Hospital, Cambridge) NMR - A Window to the Human Body	2nd February, 1989
HARDGROVE, Dr. G. (St. Olaf College, U.S.A.) Polymers in the Physical Chemistry Laboratory	December, 1988
HARWOOD, Dr. L. (Oxford University) Synthetic Approaches to Phorbols Via Intramolecular Furan Diels-Alder Reactions: Chemistry under Pressure	25th January, 1988
JÄGER, Dr. C. (Friedrich-Schiller University GDR) NMR Investigations of Fast Ion Conductors of the NASICON Type	9th December, 1988
JENNINGS, Prof. R.R. (Warwick University) Chemistry of the Masses	26th January, 1989
JOHNSON, Dr. B.F.G. (Cambridge University) The Binary Carbonyls	23rd February, 1989
JONES, Dr. M.E. (Durham Chemistry Teachers' Centre) Discussion Session on the National Curriculum	14th June, 1989
JONES, Dr. M.E. (Durham Chemistry Teachers' Centre) GCSE and A Level Chemistry 1989	28th June, 1989
LUDMAN, Dr. C.J. (Durham University) The Energetics of Explosives	18th October, 1988
MACDOUGALL, Dr. G. (Edinburgh University) Vibrational Spectroscopy of Model Catalytic Systems	22nd February, 1989
MARKO, Dr. I. (Sheffield University) Catalytic Asymmetric Osmylation of Olefins	9th March, 1989
McLAUCHLAN, Dr. K.A. (University of Oxford) The Effect of Magnetic Fields on Chemical Reactions	16th November, 1988
MOODY, Dr. C.J. (Imperial College) Reactive Intermediates in Heterocyclic Synthesis	17th May, 1989
MORTIMER, Dr. C. (Durham Chemistry Teachers' Centre) The Hindenberg Disaster - an Excuse for Some Experiments	14th December, 1988
NICHOLLS, Dr. D. (Durham Chemistry Teachers' Centre) Demo. "Liquid Air"	11th July, 1989
PAETZOLD, Prof. P. (Aachen) Iminoboranes $XB\equiv NR$: Inorganic Acetylenes?	23rd May, 1989
PAGE, Dr. P.C.B. (University of Liverpool) Stereocontrol of Organic Reactions Using 1,3-dithiane-1-oxides	3rd May, 1989
POLA, Prof. J. (Czechoslovak Academy of Sciences) Carbon Dioxide Laser Induced Chemical Reactions - New Pathways in Gas-Phase Chemistry	15th June, 1989
REES, Prof. C.W. (Imperial College London) Some Very Heterocyclic Compounds	27th October, 1988
REVELL, Mr. P. (Durham Chemistry Teachers' Centre) Implementing Broad and Balanced Science 11-16	14th March, 1989
SCHMUTZLER, Prof. R. (Technische Universitat Braunschweig) Fluorophosphines Revisited - New Contributions to an Old Theme	6th October, 1988
SCHROCK, Prof. R.R. (M.I.T.) Recent Advances in Living Metathesis	13th February, 1989
SINGH, Dr. G. (Teesside Polytechnic) Towards Third Generation Anti-Leukaemics	9th November, 1988
SNAITH, Dr. R. (Cambridge University) Egyptian Mummies: What, Where, Why and How?	1st December, 1988
STIBR, Dr. R. (Czechoslovak Academy of Sciences) Recent Developments in the Chemistry of Intermediate-Sited Carboranes	16th May, 1989
VON RAGUE SCHLEYER, Prof. P. (Universitat Erlangen Nurnberg) The Fruitful Interplay Between Calculational and Experimental Chemistry	21st October, 1988
WELLS, Prof. P.B. (Hull University) Catalyst Characterisation and Activity	10th May, 1989

Board of Studies in Chemistry

COLLOQUIA, LECTURES AND SEMINARS GIVEN BY INVITED SPEAKERS
1ST AUGUST 1989 TO 31ST JULY 1990

ASHMAN, Mr. A. (Durham Chemistry Teachers' Centre) The National Curriculum - an update	11th October, 1989
BADYAL, Dr. J.P.S. (Durham University) Breakthoughs in Heterogeneous Catalysis	1st November, 1989
BECHER, Dr. J. (Odense University) Synthesis of New Macrocylic Systems using Heterocyclic Building Blocks	13th November, 1989
BERCAW, Prof. J.E. (California Institute of Technology) Synthetic and Mechanistic Approaches to Ziegler-natta Polymerization of Olefins	10th November, 1989
BLEASDALE, Dr. C. (Newcastle University) The Mode of Action of some Anti-tumour Agents	21st February, 1990
BOLLEN, Mr. F.(Formerly Science Advisor, Newcastle LEA) Whats's New in Satis, 16-19	27th March, 1990
BOWMAN, Prof. J.M. (Emory University) Fitting Experiment with Theory in Ar-OH	23rd March, 1990
BUTLER, Dr. A. (St. Andrews University) The Discovery of Penicillin: Facts and Fancies	7th December, 1989
CAMPBELL, Mr. W.A. (Durham Chemistry Teachers' Centre) Industrial catalysis - some ideas for the National Curriculum	12th September, 1989
CHADWICK, Dr. P. (Dept. of Physics, Durham University) Recent Theories of the Universe (with Reference to National Curriculum Attainment Target 16)	24th January, 1990
CHEETHAM, Dr. A.K. (Oxford University) Chemistry of Zeolite Cages	8th March, 1990
CLARK, Prof. D.T. (ICI Wilton) Spatially Resolved Chemistry (using Natures's Paradigm in the Advanced Materials Arena)	22nd February, 1990
COLE-HAMILTON, Prof. D.J. (St. Andrews University) New Polymers from Homogeneous Catalysis	29th November, 1989
CROMBIE, Prof. L. (Nottingham University) The Chemistry of Cannabis and Khat	15th February, 1990
DYER, Dr. U. (Glaxo) Synthesis and Conformation of C-Glycosides	31st January, 1990
FLORIANI, Prof. C. (University of Lausanne, Switzerland) Molecular Aggregates - A Bridge between homogeneous and Heterogeneous Systems	25th October, 1989
GERMAN, Prof. L.S. (USSR Academy of Sciences - Moscow) New Syntheses in Fluoroaliphatic Chemistry: Recent Advances in the Chemistry of Fluorinated Oxiranes	9th July, 1990
GRAHAM, Dr. D. (B.P. Reserch Centre) How Proteins Absorb to Interfaces	4th December, 1989
GREENWOOD, Prof. N.N. (University of Leeds) Novel Cluster Geometries in Metalloborane Chemistry	9th November, 1989
HOLLOWAY, Prof. J.H. (University of Leicester) Noble Gas Chemistry	1st February, 1990
HUGHES, Dr. M.N. (King's College, London) A Bug's Eye View of the Periodic Table	30th November, 1989
HUISGEN, Prof. R. (Universität München) Recent Mechanistic Studies of [2+2] Additions	15th December, 1989
IDDON, Dr. B. (Univeristy of Salford) Schools' Christmas Lecture - The Magic of Chemistry	15th December, 1989
JONES, Dr. M.E. (Durham Chemistry Teachers' Centre) The Chemistry A Level 1990	3rd July, 1990
JONES, Dr. M.E. (Durham Chemistry Teachers' Centre) GCSE and Dual Award Science as a starting point for A level Chemistry - how suitable are they?	21st November 1989
JOHNSON, Dr. G.A.L. (Durham Chemistry Teachers' Centre) Some aspects of local Geology in the National Science Curriculum (attainment target 9)	8th February, 1990
KLINOWSKI, Dr. J. (Cambridge University) Solid State NMR Studies of Zeolite Catalysts	13th December 1989
LANCASTER, Rev. R. (Kimbolton Fireworks) Fireworks - Principles and Practice	8th February, 1990
LUNAZZI, Prof. L. (University of Bologna) Application of Dynamic NMR to the Study of Conformational Enantiomerism	12th February, 1990
PALMER, Dr. F. (Nottingham University) Thunder and Lightning	17th October, 1989

PARKER, Dr. D. (Durham University) Macrocycles, Drugs and Rock 'n' roll	16th November, 1989
PERUTZ, Dr. R.N. (York University) Plotting the Course of C-H Activations with Organometallics	24th January, 1990
PLATONOV, Prof. V.E. (USSR Academy of Sciences - Novosibirsk) Polyfluoroindanes: Synthesis and Transformation	9th July, 1990
POWELL, Dr. R.L. (ICI) The Development of CFC Replacements	6th December, 1989
POWIS, Dr. I. (Nottingham University) Spinning off in a huff: Photodissociation of Methyl Iodide	21st March, 1990
RICHARDS, Mr. C. (Health and Safety Executive, Newcastle) Safety in School Science Laboratories and COSHH	28th February, 1990
ROZHKOV, Prof. I.N. (USSR Academy of Sciences - Moscow) Reactivity of Perfluoroalkyl Bromides	9th July, 1990
STODDART, Dr. J.F. (Sheffield University) Molecular Lego	1st March, 1990
SUTTON, Prof. D. (Simon Fraser University, Vancouver B.C.) Synthesis and Applications of Dinitrogen and Diazo Compounds of Rhenium and Iridium	14th February, 1990
THOMAS, Dr. R.K. (Oxford University) Neutron Reflectometry from Surfaces	28th February, 1990
THOMPSON, Dr. D.P. (Newcastle University) The role of Nitrogen in Extending Silicate Crystal Chemistry	7th February, 1990